UNIVERSITY OF CAPE TOWN
IYUNIVESITHI YASEKAPA • UNIVERSITEIT VAN KAAPSTAD

BLAST IMPACT AND SURVIVABILITY RESEARCH UNIT

Study of Dynamic Behaviour of Multi-Layered Structures Subjected to Blast Loading

Muhammad Saeed Ahmad

Thesis presented in fulfillment of the requirements of
the degree of Doctor of Philosophy

Department of Mechanical Engineering, University of Cape Town,
Rondebosch, South Africa
2011

This thesis is dedicated to
Maryam Saeed
and
Sara Saeed

Declaration

I, Muhammad Saeed Ahmad, hereby:

(a) Grant the University free license to reproduce this thesis, entitled "**Study of Dynamic Behaviour of Multi-Layered Structures Subjected to Blast Loading**", in whole or in part, for the purpose of research.

(b) Declare that:

(i) This thesis is my own unaided, both in conception and execution, and that apart from the normal guidance of my supervisor; I have received no assistance apart from that stated in the "Acknowledgements" section of the thesis.

(ii) This thesis or any part of this thesis has not been submitted in past, or is being, or is to be submitted in this or any other form for a degree at the University of Cape Town or any other University according to best of my knowledge.

(iii) I am now presenting this thesis entitled "**Study of Dynamic Behaviour of Multi-Layered Structures Subjected to Blast Loading**"for examination for the degree of PhD in Mechanical Engineering.

Muhammad Saeed Ahmad
September 2011

Abstract

The objective of this research work is to assess the response of multi-layered plates in comparison to single plates to gain physical understanding of different phenomena taking place at micro level during localized blast loading. Since layered plates have been shown to give improved ballistic performance under certain circumstances, it is useful to ascertain and understand the influence of layering on blast performance. This investigation is carried out both experimentally and numerically. A finite element model was developed to design the blast experiments for two different steels of various thicknesses. The following are the main objectives of this research work

- To understand the response and failure characteristics of multi-layered and equivalent mass single steel plates to localized blast loading
- To answer the hypothesis that multi-layered plates exhibit improved blast performance compared to their equivalent mass counterparts
- To determine if multi-layered plates exhibit failure modes that have more ductile characteristics, thus absorbing more energy prior to rupture

Metallographic study of both materials was carried out before and after the blast tests to investigate the changes in microstructure during blast loading. The fractured surfaces of single and multi-layered plates of Domex 700MC after blast loading were analyzed and results were compared in terms of micro-void morphology. Different micro-void morphologies were revealed during fractography of the torn plates at various charge masses. The ductile nature of fractures was noted in layered plates whereas the single plates exhibited comparatively less ductile fracture behaviours. Equiaxed dimples were found in front fractured plates whereas the elongated dimples were noted in back fractured plates.

In the current project, two different HSLA steels namely Domex 550MC and Domex 700MC were considered to study the effect of localized blast loading of single and multi-layered structures. Two configurations having total thickness of 4mm, namely “4mm single” and “double (2+2)mm” were subjected to localized blast loading and the results of both configurations of Domex 550MC and Domex 700MC were compared. Four configurations having total thickness of 6mm, namely “6mm single” and “double (3+3)mm”, “double (4+2)mm” and “triple (2+2+2)mm” were subjected to localized blast loading and the results were compared with each other of all configurations of Domex 700MC.

For the 4mm thick configurations, the single plates performed better than the double plates of Domex 550MC and Domex 700MC as the double (2+2)mm plates configuration failed at lower charge mass.

For 6mm configurations, the performance of double plates is better than single and triple plate configurations. The protection level of 6mm configurations decreases from No. 1 to No. 4 in the series given below.

1. Double plate (3+3)mm
2. Double plate (4+2)mm
3. Single plate (6mm)
4. Triple plate (2+2+2)mm

The maximum protection is provided by double (3+3)mm followed by double (4+2)mm of 6mm configurations. The lowest protection level was observed in case of the triple plate configurations.

Acknowledgements

First of all I want to express my gratitude to Almighty Allah who bestowed on me the strength and courage to take up this task.

I would like to express my sincere thanks to all of the people who have assisted me in my efforts towards receiving a PhD degree at University of Cape Town, South Africa.

I am grateful to Professor G.N. Nurick (Director, Blast Impact Survivability Research Unit), my PhD supervisor in his support and for giving me the opportunity to perform this work. I wish to thank him for his confidence in me. Without his continuous guidance and support, this work was not possible.

I would also like to thank my co-supervisor, Associate Professor Genevieve Langdon who is an invaluable source of knowledge concerning responses of materials subjected to blast loadings and blast test methods. I appreciate her time, patience and valuable guidelines regarding experimental and summing up this work throughout the study.

The author also wishes to thank all members of the Blast Impact and Survivability Research Unit (BISRU) for all their assistance and support. I am grateful for the friendships I have made with all of the graduate students and research scientists at BISRU.

Others that deserve my gratitude include the Centre for Materials Engineering for providing necessary experimental facilities to complete my work, especially Mrs. P. Park-Ross for her assistance with the tensile testing and metallography. Many thanks go to the workshop staff in the Department of Mechanical Engineering for their efforts in manufacturing and preparation of specimens.

I also acknowledge the Institute of Industrial Controls Systems (IICS), Islamabad, Pakistan for providing me the PhD fellowship. I would also like to thank Dr. Syed Wilayat Husain and my colleagues at IICS for releasing me and taking over my duties during my entire studies.

Finally, special thanks go to my parents and family, for putting up with my ups and downs throughout the course of my studies at University of Cape Town, South Africa. Their continuous encouragement and belief in me and my work has been a great support during this period.

S. Ahmad

Contents

List of figures

List of tables

Nomenclature

A	loaded area
a	charge radius
b	plate width
c	capped
d	average grain diameter
E	Young's modulus
e	engineering strain
F	force
f	natural frequency
g	gravitational constant
H	plate thickness
h	charge height
I	impulse
K	pressure decay constant
l	length
m	mass
P	pressure
R	plate radius
S	engineering stress
T, T^*, T_m, T_{ref}	temperature, homologous, melting, reference
t	time
V	volume
v	impact velocity

$\boldsymbol{\varepsilon}$	true strain
$\boldsymbol{\varepsilon}_{eq}$	equivalent plastic strain
$\dot{\boldsymbol{\varepsilon}}$	strain rate
Φ_q	dimensionless impulse (quadrangular plates)
Φ_c	dimensionless impulse (circular plates)
η	inelastic heat fraction
ρ	density
μ_T	shear modulus
σ	true stress
δ	midpoint deflection
υ	poisson's ratio
τ	loading time
V_b	burn velocity
$\boldsymbol{\sigma_o}$	static yield stress

c_p	specific heat
HV	vickers hardness
P_n	natural period
P_o	ambient pressure
P_m	peak overpressure
I_s	specific impulse

Cap Ø	diameter of torn fragments (cap)
cp	crack percentage

Mode I	large inelastic deformation
Mode Ia	large inelastic deformation with necking at partial boundary
Mode Ib	large inelastic deformation with necking around entire boundary
Mode II	tearing (tensile failure)
Mode IIa	complete tearing with increasing midpoint deflection
Mode IIb	complete tearing with decreasing midpoint deflection
Mode II*	large inelastic deformation with partial
Mode III	transverse shear failure

C_1, C_2, C_3, C_4, C_5, C_6, β, β_0, β_1, σ_a, α_0, α_1	material constants (Zerilli-Armstrong, Goldthorpe)
A, B, C, n, m,	model constants (Johnson-Cook)
D, q	model constants (Cowper and Symonds)
K_n	constant of plate geometry

Abbreviations

BP	Bodner-Partom
HSLA	High strength low alloy
HPB	Hopkinson Pressure Bar
JWL	Jones-Wilkins-Lee equation of state
MVC	Micro Void Coalescence
UTS	Ultimate tensile stress
VDLOAD	vectorised user defined pressure load subroutine (ABAQUS)

J-C	Johnson-Cook
KH	Khan-Huang
ZA	Zerilli-Armstrong
PE	plastic explosive
FEM	finite element modelling
TTT	Time-Temperature Transformation
TNT	Trinitrotoluene

Chapter 1

1 Introduction

1.1 Background

It has been estimated that more than 100 million active mines are scattered over sixty countries in the world [1] and every month more than 2000 people are maimed or killed by mines [2;3]. Most of these mines buried in roads and tracks are able to damage landmine detection armoured vehicles. Peace keeping troops and law enforcement agencies are engaged in minimizing terrorist activities in the hot spots of the world. These agencies are using armoured vehicles for the transportation of personnel to the location of interest and hence these vehicles need to be fast and safe. To ensure the safety of the personnel inside, these vehicles have traditionally been protected by various types of armour steel plates of different thickness. The main threats to these vehicles can broadly be divided into two categories: high velocity projectiles and blast loading from landmines. The upper portion of these armoured vehicles, namely the turret, is targeted by high velocity projectiles whereas the lower part, including the hull and bottom/base, has to face landmines and blast explosions.

Conventionally, High Strength Low Alloy (HSLA) steels are considered as a basic construction material for the armour system. These steels have been used in the form of multi-layered or single target plates in armour applications for a long time. The response of single and multi-layered targets against various types of the projectile was studied by many researchers. The response of multi-layered plates against different types of projectiles at various muzzle velocities has been comprehensively studied [4-12].

Marom and Bodner [8] performed ballistic tests on layered targets of aluminium alloy (6061-T) in various configurations by using 0.22 calibre projectiles at a velocity of 375 m/s and found that multi-layered beams were more effective in resisting perforation than single beams of the same weight. Corran et al. [5] showed experimentally that a double/triple-layered shield was superior in ballistic resistance to a single plate if the total thickness exceeded a critical value. Target plates of mild steel, stainless steel and aluminium were impacted at sub-ordnance velocity by various projectiles. Woodward and Cimpoeru [11] carried out an experimental study on layered 2024-T351 aluminium plates impacted by 6.35 mm diameter, 3.83g mass, blunt and conical projectiles. Targets having two plates of equal thickness provided the highest ballistic limit for both nose shapes.

Contradictory results on layered targets are also reported in open literature. Radin and Goldsmith [13] reported results from normal impact tests on multi-layered targets of different thickness and showed that the ballistic resistance of the metallic single target was greater than that of several adjoining plates of the same thickness.

Almohandes et al. [14] reported the results of layered steel plates of thickness (1-8)mm in various configurations impacted by 7.62 mm standard bullets. Single plates were found more effective than laminated targets of the same total thickness. The effectiveness of the laminated targets was increased by decreasing the number of laminates. Zukas et al. [15]

reported that layering of target plates dramatically weakened thin and intermediate thickness targets.

Teng et al. [10] reported results from a numerical study on the protection performance of double-layered metal shields against different projectile using ABAQUS/Explicit. The study indicated improved ballistic resistance of 8–25% by using double-layer configuration against flat-nose projectile. Dey [7] reported the results from double-layering the target and observed an increase of 40 - 50% in ballistic limit velocity (V_{50}) compared to a single target of equal thickness when impacted by blunt projectiles. In case of ogival nose projectile, the single target showed a better protection, but the difference in perforation resistance was only 10–15% [7].

The reason for the improved performance of multi-layered plates subjected to projectile impact is attributed to the difference in failure mode by Dey [7]. The multi-layered plates exhibited more ductile failure, absorbing more energy than thicker single target plates which exhibited brittle failure in the form of shear plugging as indicated in Figure 1-1 and Figure 1-2.

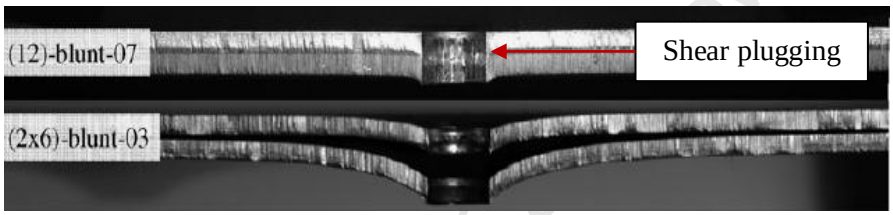

Figure 1-1: Photographs of the sectioned single and layered plates perforated by blunt projectiles [7]

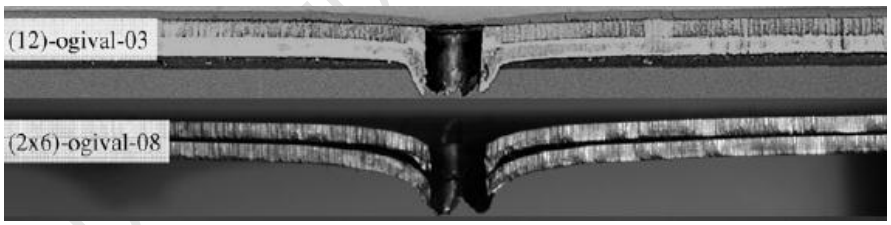

Figure 1-2: Photographs of the sectioned single and layered plates perforated by ogival projectiles [7]

This assumption is also supported by the relative improvement being dependent upon the geometry of the projectile (which significantly influenced the type of failure exhibited).

The response of single target plates subjected to blast loading can be found in the literature [16;17]. There is a need to work on multi-layered target plates subjected to blast loading as the author unaware of work published on the performance of multi-layered steel plates subjected to localized blast loading.

It is postulated that multi-layered targets may also perform better than single targets subjected to localized blast loading but this is yet to be confirmed by published investigations. The drawback of using heavy monolithic steel armours is that it gives rise to an extremely heavy

structure which then creates logistic problems in transporting the vehicles [18]. A possible solution to producing armour with the weight characteristics required for rapid transportation involves the use of multi-layered plates.

The work reported in this thesis is concerned with the evaluation of multi-layered target plates subjected to localized blast loading and the understanding of phenomenon associated with blast induced failure of multi-layered structures. This thesis reports on the results of experimentation, metallurgical investigations and finite element simulations. The response of multi-layered plates is compared to that of equivalent mass single plates for a range of plate thickness and two different steel alloys (Domex 550MC and Domex 700MC).

1.2 Objective

The objective of this research work is to gain physical understanding of different phenomena taking place during localized blast loading and to assess the response of multi-layered plates in comparison to single plates when subjected to similar experimental conditions. The investigation is carried out both experimentally and numerically. A finite element model was developed to design the blast experiments for two different steels and a successful numerical model would offer a better understanding of the response of multi-layered structures to localized blast loading. Following are the main objectives of this research work

- To understand the response and failure characteristics of multi-layered and equivalent mass single steel plates subjected to localized blast loading.
- To answer the hypothesis that multi-layered plates exhibit improved blast performance compared to their equivalent mass counterparts.
- To determine if multi-layered plates exhibit failure modes that have more ductile characteristics, thus absorbing more energy prior to rupture.

1.3 Thesis outline

The research work contains a literature review regarding the blast loading of structures, responses of layered plates, material testing and designing of structures. The blast loading experiments were conducted based on the results obtained by numerical simulations. Fractured surfaces were analyzed and compared with each other to investigate the failure modes morphologies. Finally, the results were discussed and correlated with the previous studies available in open literature. This work has been arranged in the following manner.

Chapter 2: This chapter contains literature review, describing responses of the steel plates subjected to uniform and localized blast loadings. Various failure modes and their fractured surfaces are discussed. This chapter will give the overall introduction to the reader regarding the responses of metal structures subjected to blast loading and about fractured surfaces morphologies subjected to various applied loads.

Chapter 3: The introduction of the materials used in blast experiments is given in this chapter. Experimental work to determine the basic material properties like ultimate tensile

strength, yield strength, elongation is presented and explained in terms of stress-strain diagrams. The fractured surfaces of Domex 700MC tensile samples at different strain rates were studied and analyzed.

Chapter 4: Introduces two of the most commonly used constitutive relations presented in the literature, which can represent the mechanical response of materials subjected to high strain rates. Johnson–Cook parameters were determined for design the experiments to be used in ABAQUS/Explicit simulations. Johnson-Cook (J-C) and Cowper-Symonds models were used for the simulation of the blast experiments. The simulated results for the Domex 550MC and Domex 700MC are described in this chapter and used to design the experiments.

Chapter 5: This chapter contains the experimental methods and results of the blast loaded plates of various configurations. Two configurations of 4mm thickness (4mm single and double(2+2)mm) and four configurations of 6mm thickness (6mm single, double (3+3)mm, double (4+2)mm and triple (2+2+2)mm) were considered. The midpoint deflections are given in tabular formats up to Mode I failures. Photographs of the deformed, cracked and torn plates are given.

Chapter 6: Analysis of deformed plates of Domex 550MC and Domex 700MC for the Mode I failure is given in this chapter. The results of the micro-structural study are discussed. Effect of impulse on the grain size of micro-structure and fracture path (inter-granular or trans-granular) is discussed.

Chapter 7: Analysis of fractured plates (Mode II), in terms of deformation profiles of fractured plates, threshold impulse and fractography is reported. The fractographic analysis of the blast loaded torn plates are presented. Various micro-void morphologies at different strain rates are presented and compared with each other. The effect of the charge mass on the dimple morphology of fractographs is discussed.

Chapter 8: This chapter contains the discussion on the comparison of various configurations, displacement versus impulse and nature of fractured surfaces. The experimental and numerical results are discussed and compared with each other.

Chapter 9: This chapter contains conclusions drawn from this research work and makes recommendations for future work.

Chapter 2

2 Literature review

2.1 Explosives and blast waves

Explosive materials are classified as low or high explosives according to their rates of decomposition. These materials are chemically unstable and undergo the explosion process by rapid chemical reaction. During the explosion process, the explosive materials convert into a gas with a discharge of high temperature and an enormous amount of heat causing variations in nearby air pressures. These gases expand outward and generate shock waves in the adjacent air, known as a blast wave. According to Baker [19], in "an explosion process, a large amount of energy is rapidly released in the form of light, heat, sound, and takes place in a volume to produce pressure wave, known as a blast or shock wave". Marchand and Alfawakhiri [20] defined explosion as a rapid release of stored energy characterized by a bright ash and an audible blast, released in the form of heat, light, sound and a shock wave in the surrounding air. The blast wave is a shock wave that moves through air [21] and consists of highly compressed air, travels outward from its origin at very high velocities and interacts with any object in its path. The blast wave induces impulsive or dynamic pressure loading on the structures it encounters. The response of these objects depends on their mechanical properties, metallurgical properties and the intensity of interacting blast waves.

Jacinto et al. [22] presented a typical pressure-time curve of the blast load shown in Figure 2-1, obtained from the detonation of 10 kg of Gelamon VF8 explosives in air at a stand-off distance of 90m. Four tests with different amounts of explosives were carried out in order to measure the overpressure generated by the shock waves by using pressure sensors. Dynamic response of the plates was measured by using three accelerometers. Similar pressure-time curves were also recorded by Cloete et al. [23] by using a Hopkinson Pressure Bar (HPB) on detonating 3g charge mass at a stand-off distance of 13mm as shown in Figure 2-2.

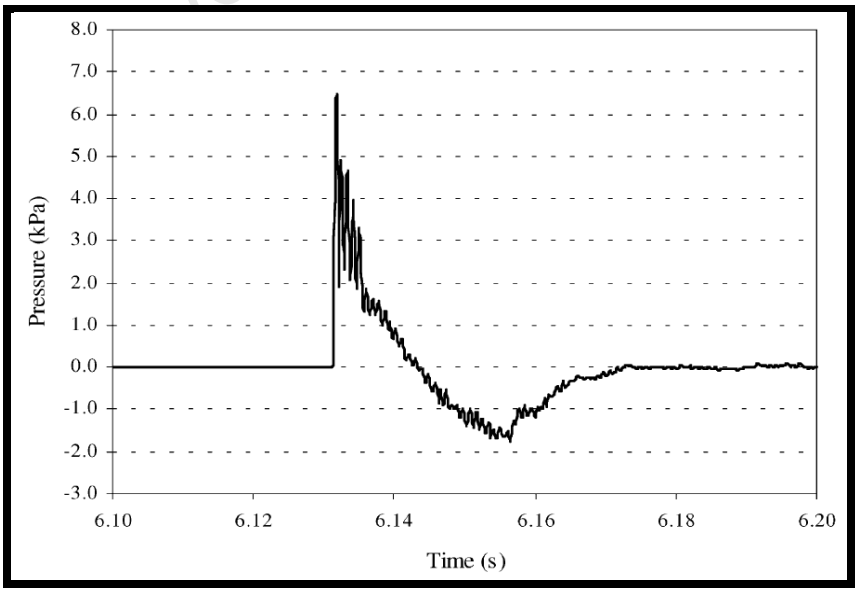

Figure 2-1: Pressure time history of air pressure generated from explosive devices [22]

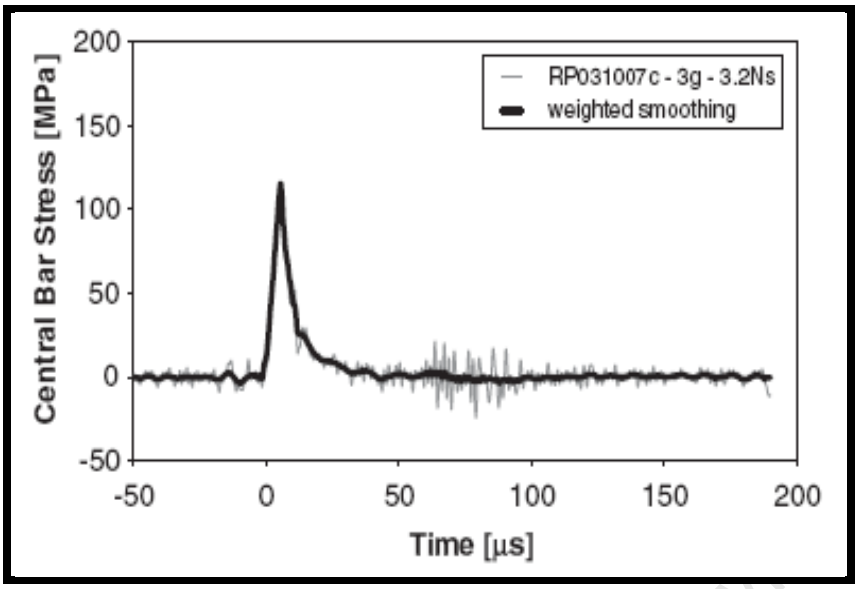

Figure 2-2: Centrally localized blast load pressure time history using a HPB [23]

The Steel Construction Institute [24] defined impulsive loads as those in which the duration of loading is significantly shorter than the natural period of the structure experiencing the load. This implies that the structure cannot show any significant response during the loading application. This interaction imposes dynamic or impulsive loads on the objects causing plastic deformation or destruction. When the shock wave arrives at a point of interest it originates a dynamic pressure that is proportional to the square of the wind velocity and the density of the air behind the shock front. When the incident blast wave impinges on a denser medium, it is reflected. The peak value of the reflected pressure depends on the peak of the incident wave, the angle at which it strikes the surface and the nature of the surface [22]. This is in contrast to quasi-static loading in which the period of loading is much longer than the natural period of the structure. The load duration regime in between impulsive and quasi-static loading is referred to as dynamic. Young [25] gives an equation for calculating the natural period (P_n) of circular plates fixed at the boundary shown in Equation 2-1.

$$\boldsymbol{P_n} = \frac{\boldsymbol{2\pi}}{\boldsymbol{K_n R^2}\left(\frac{\boldsymbol{EH^3}}{\boldsymbol{12(1-\nu^2)\rho V}}\right)^{\boldsymbol{0.5}}} \qquad 2\text{-}1$$

Where

E	Young's modulus	K_n	10.2 (constant for plate geometry)
H	plate thickness	R	plate radius
ν	Poisson's ratio	ρ	plate density
V	plate volume		

The blasting of explosives may occur accidently or deliberately by detonating plastic explosives. The effect of blast loading on the objects is generally characterized by the pressure pulse. In such explosions, high pressures are generated instantaneously that decay exponentially as shown in Figure 2-3. There are two regions, namely, a positive phase and negative phase. Large peak defined a region of over-pressure that decays exponentially with time followed by a region of negative pressure where the pressure acts in a direction away from the face of the structure. The pressures in negative phase are typically small and are not takes into account in the analysis of structures under blast loading [26].

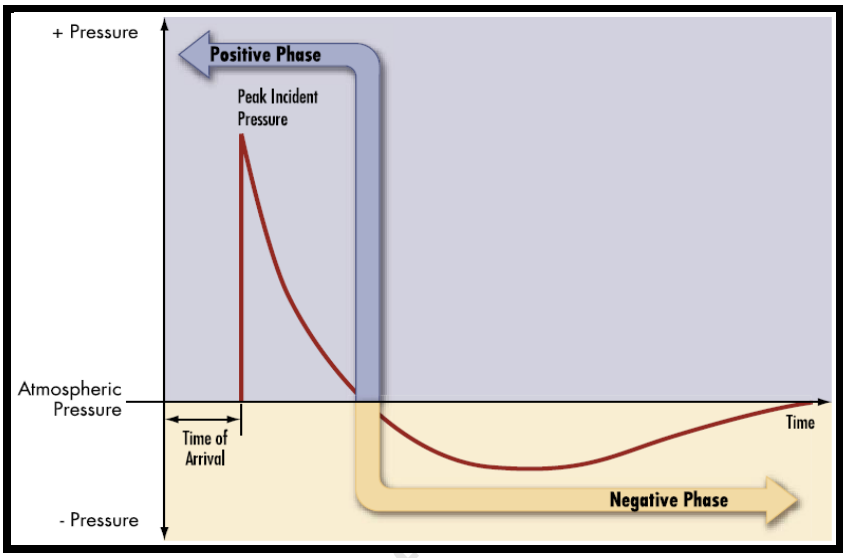

Figure 2-3: A typical pressure-time history on a structure under blast loading [27]

Apart from overpressure and time of arrival another significant blast wave parameter is the specific impulse of the wave during the positive phase I_s, as given in Equation 2-2.

$$\boldsymbol{I_s = \int_{ta}^{ta+td} P(t)\, dt} \qquad 2\text{-}2$$

Blast wave velocity increases with increasing peak overpressures at the shock front. As the blast wave progresses outward, the pressure at the shock front decreases and the velocity decreases, for example at long ranges, once the overpressure decreases to 7 KPa, the velocity of the blast wave approaches the ambient speed of sound. The duration of the overpressure phase increases with the energy of the explosive yield and the distance from the explosion. The instantaneous pressure of the positive phase of an ideal air blast wave is given by the Friedlander [26] as in Equation 2-3.

$$\boldsymbol{P(t) = P_o + P_m \left[1 - \left(\frac{t}{t_d}\right) e^{-\alpha t / t_d}\right]} \qquad 2\text{-}3$$

Where "P_o" is the ambient pressure, "t" is the instantaneous time; "t_d" is the positive duration of the pressure pulse and "α" is called waveform parameter that depends upon the peak overpressure "P_m" of the shock wave. The waveform parameter α is regarded as an adjustable parameter which is selected so that the overpressure–time relationships provide suitable values of the blast impulse.

According to Zhu and Lu [28] the blast loading can be qualified based on the charge weight and stand-off distance. Generally, the amount of explosive charge in terms of weight is converted to an equivalent value of TNT weight (known as TNT equivalency) by a conversion factor. In other words, the TNT is employed as a reference for all explosives. The TNT equivalence factor for various explosives are given in reference [29]. For example, PE4 has a TNT equivalency of 1.37 [30].

2.2 Ballistic pendulum

A ballistic pendulum system can be used to obtain impulse imparted to various structures subjected to air blast explosion. When a charge is detonated in front of the pendulum, blast pressure is exerted on a structure attached to the pendulum, causing the pendulum to displace. The imparted impulse can be calculated from the measured displacement of the centre of mass and the distance from the rotation/translation centre. Hanssen et al. [31] used a two-cable pendulum shown in Figure 2-4a which can be applied to measure the impulse imparted by several kilograms of TNT. Nurick et al. [32-34] used four-cable ballistic pendulum for explosive loading studies of steel and composite plates for a number of years, as shown in Figure 2-4b.

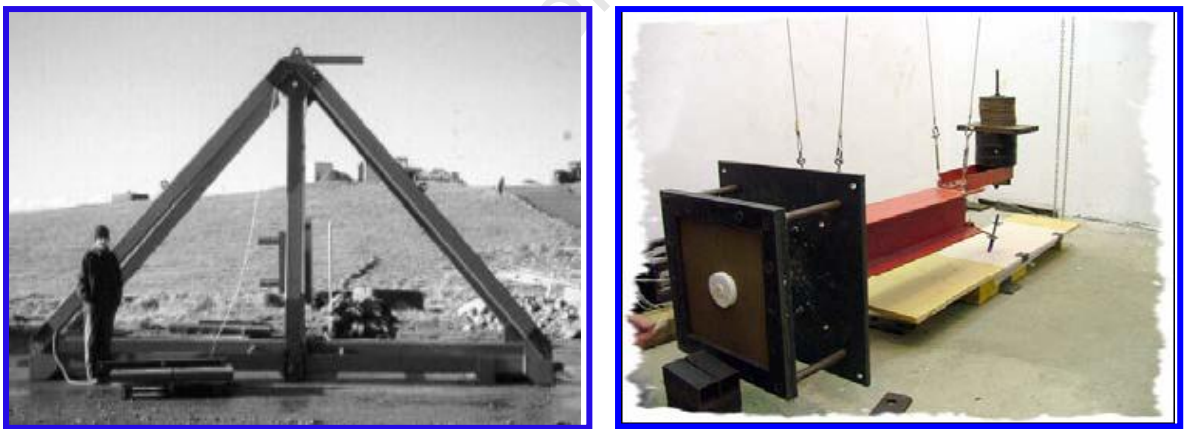

(a) A two-cable pendulum [31] (b) A four-cable pendulum [35]

Figure 2-4: Photographs of two types of ballistic pendulums

2.3 Blast loading conditions from experiments

Various loading conditions can be achieved by changing the shape and stand-off distances of explosives as discussed by Nurick et al. [16;17]. Marchand and Alfawakhiri [20] suggested guidelines for the assumption of uniform blast load over a structure. When the angle of incidence between the explosive charge and structural edges exceeds 45°, there is a

significant reduction in the resultant pressure and impulse impinging on a structure. If the charge stand-off exceeds one-half of the width or height of the structure, then loads can be reasonably averaged over the structure provided the charge is centrally located [20]. For instance, if explosive is laid out at a stand-off distance more than 50mm (which is greater than one-half of circular plate of diameter 100mm) the blast load can be considered as uniform over the entire plate area [36].

Schematics of uniformly and locally blast loaded plates with plastic explosive are shown in Figure 2-5a and b respectively [37].

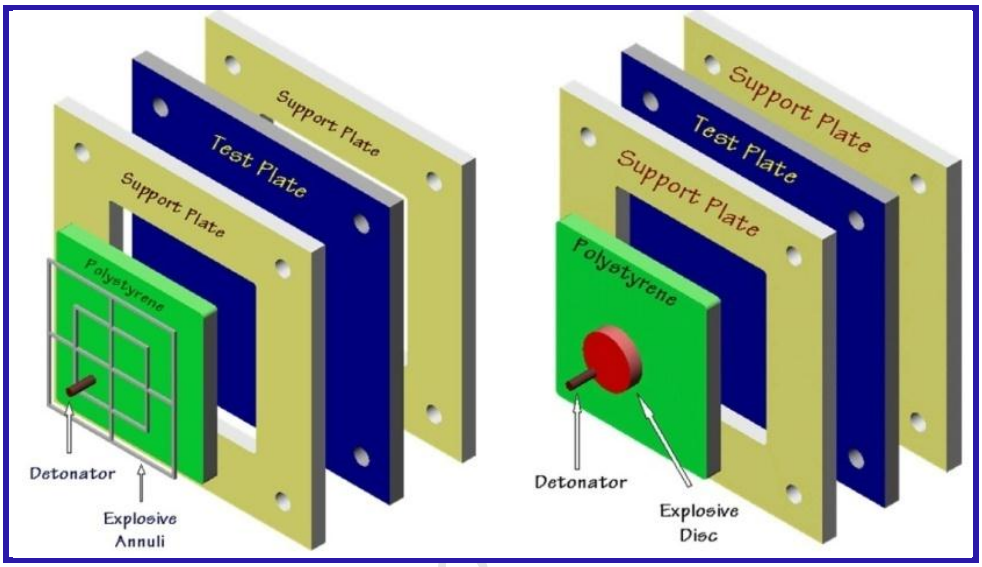

(a) Uniform blast load (b) Localised blast load

Figure 2-5: Schematics of blast loading conditions [37]

2.4 Response of single structures to blast loading

Extensive experimental studies have been carried out to understand the large permanent ductile deformation and rupture of plates, beams and shells. The response of thin plates clamped at the outer edges and built-in plates subjected to both uniform and localized blast loading conditions have been studied for a number of years. Jones [38] and Nurick and Martin [16;17] presented overviews of the theoretical and experimental results of plates subjected to blast loads. The results reported discuss the geometrical effects of circular, square and rectangular plates.

2.5 Modes of failure

The failure modes of structures subjected to uniformly distributed blast loading were first classified by Menkes and Opat [39] for fully clamped aluminium alloy beams at various impulse levels. Three distinct failure modes were observed at various intensities of impulse classified as

Mode I: Large inelastic deformation of the entire beam
Mode II: Tearing (tensile failure) of the beam material at the support
Mode III: Transverse shear failure of the beam material at the support

The transition from failure Mode I to a Mode III with increasing impulse is shown in Figure 2-6.

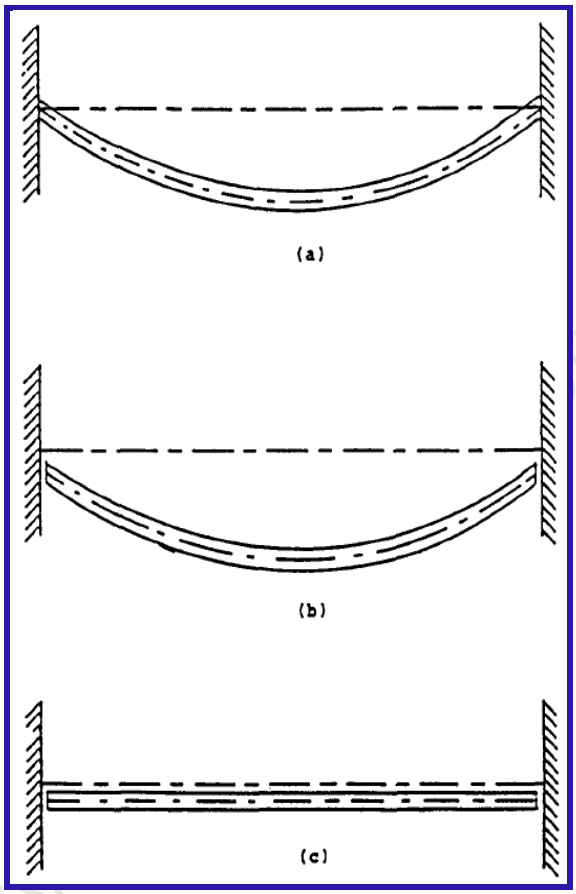

Figure 2-6: Schematics of failure Modes (a) Mode I; (b) Mode II; (c) Mode III [39]

Similar failure modes were also observed by Teeling-Smith and Nurick [40] for clamped circular plates subjected to uniform blast loads and Nurick and Shave [34] and Olson et al. [41] for square plates subjected to uniform blast loads. Nurick et al. [42] further redefined failure Mode I to describe necking. Some experimental results for Mode I failure have also been reported by Houlston and Slater [43] and Nurick and Conolly [44].

Mode I - large inelastic deformation without necking at the boundary
Mode Ia - large inelastic deformation with necking at partial boundary
Mode Ib - large inelastic deformation with necking around entire boundary

Nurick and Shave[34] redefined failure Mode II to describe partial tearing as follows.

Mode II* - partial tearing at the boundary
Mode IIa - complete tearing with increasing midpoint deflection
Mode IIb - complete tearing with decreasing midpoint deflection

These failure modes were also observed by Nurick and Martin [16;17]. The range of failure modes observed [45] for localized blast loading were large inelastic deformation (Mode I) to complete tearing at the boundary (Mode II). Shearing at the boundary (Mode III) was not observed for thin plates, but shear has been observed in thicker plates [45]. Fragments, referred to as caps, were produced from plates at higher impulses due to tearing of a central ring of material. The capping failure mode was further subdivided by Nurick and Radford [33] as mentioned below.

Mode I - large inelastic response
Mode Itc - large inelastic response with thinning in central area
Mode Ib - large inelastic response with thinning at the boundary
Mode II*c - partial tearing in the central area
Mode IIc - complete tearing in the central area - capping
Mode II - complete tearing at the boundary

If the impulse is increased beyond the onset of Mode IIc, the plate tears in a "petalling" fashion. Cloete et al. [23] presented experimental investigations of deformation and shear failure in peripherally clamped centrally supported (PCCS) blast loaded circular plates. Timing of shear failure events and the associated magnitude of the shear forces were reported. The plates exhibited three distinct modes of failure: Mode I (large ductile deformation), Mode II (boundary failure after large deformation) and Mode III (boundary failure prior to large deformation). An expression for dimensionless impulse, applicable to annular and PCCS plates was derived. Satisfactory correlation between the experimental data and analytical predictions was found. Jacob et al. [36] summarised the failure modes for different loading conditions given in the Table 2-1.

Table 2-1: Modes of failure for plates subjected to uniform and localised blast loads [36]

Failure Modes	Description	Uniform loading	Localized loading
Mode I	large inelastic deformation	✓	✓
Mode Ia	large inelastic deformation with necking around part of the boundary	✓	
Mode Ib	large inelastic deformation with necking around the entire boundary	✓	✓
Mode Itc	large inelastic deformation with thinning in the central area		✓
Mode II*	large inelastic deformation with partial tearing around part of the boundary	✓	
Mode II*c	partial tearing in the central area		✓
Mode II	tensile tearing at the boundary	✓	✓
Mode IIa	increasing midpoint deflection with increasing impulse with complete tearing at the boundary	✓	
Mode IIb	decreasing mid-point deflection with increasing impulse with complete tearing at the boundary	✓	
Mode IIc	Complete tearing in the central area - capping		✓
Mode III	transverse shear failure at the boundary	✓	
Petalling			✓

2.6 Response of single plates to uniform blast loading

The failure of circular plates subjected to uniform blast loads was investigated by Teeling-Smith and Nurick [40]. It was reported that permanent midpoint deflection increased with increased impulse, causing thinning at the boundary. Further increase in impulse led to partial tearing along the plate boundary, followed by complete tearing. The midpoint deflection decreased as impulse was increased beyond the threshold of complete tearing as the failure tended towards complete shear at the boundary edges. The transition in plate midpoint deflection with increasing impulse is shown in Figure 2-7. Similar behaviour was also reported by Nurick and Shave [34] for clamped mild steel square plates subjected to impulsive loads as shown in Figure 2-8. Olson et al. [41] reported that tearing of the plate occurred first at the middle of the boundary edge and then progressed towards the corners as the impulse increased in uniformly loaded clamped square plates. As impulse increased some of the corners were torn out, and the plates rotated about the remaining corners. Pulling-in of the sides of the plates during Mode II failure was also noted. Midpoint deflection reached a

maximum point as the impulse increased, and then decreased in the same way as observed for circular plates. The spring back effect was also noted to decrease with increased impulse[37].

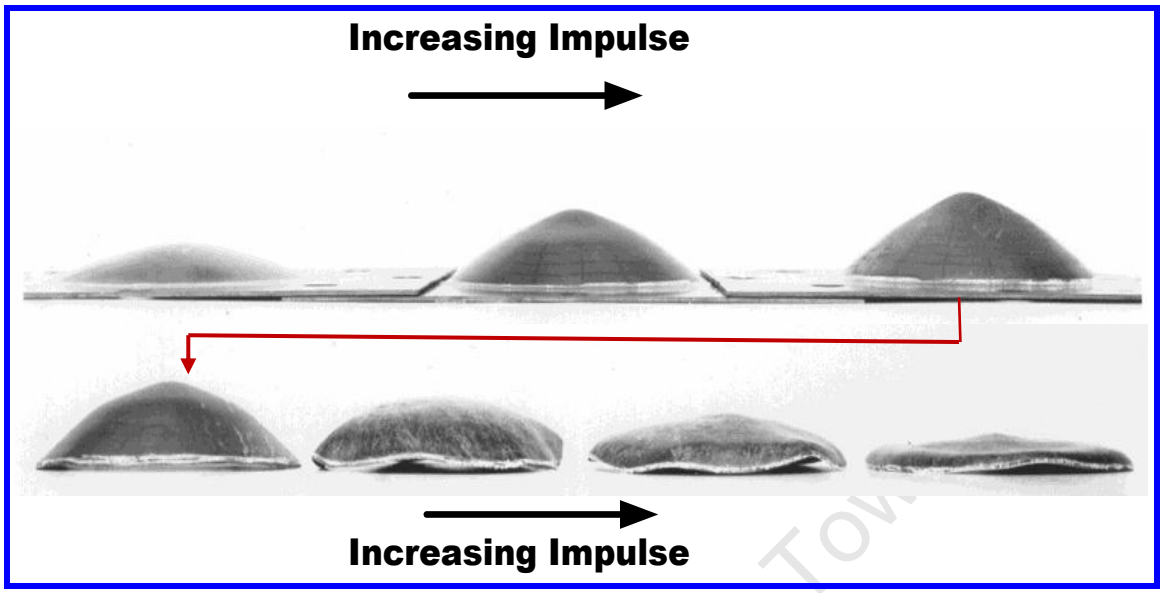

Figure 2-7: Photographs of uniformly loaded circular plates, showing change in midpoint deflection for increasing impulse [40]

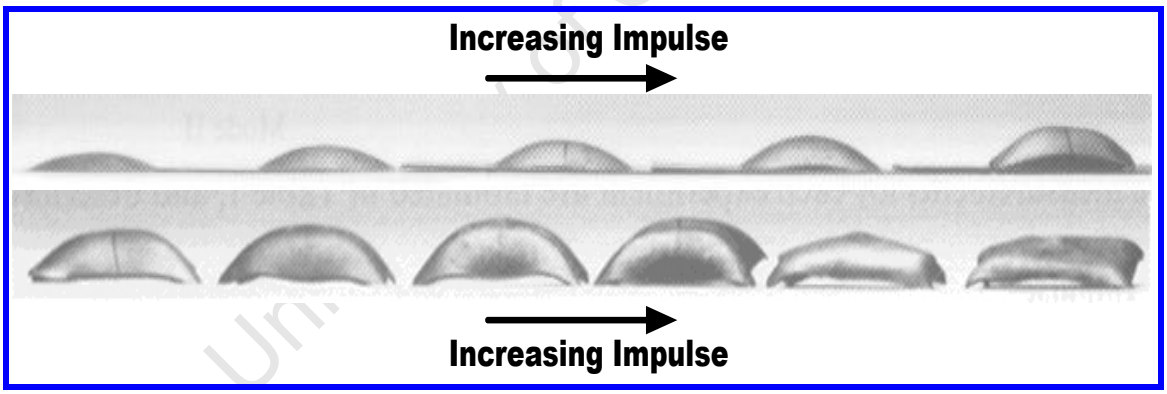

Figure 2-8: Photographs of square plates subjected to uniformly distributed blast loading, showing change in midpoint deflection for increasing impulse [34]

2.7 Response of single plates to localized blast loading

Wierzbicki and Nurick [46] investigated the response of thin clamped plates subjected to a localized impulsive load to determine the location of tearing and critical impulse to failure. Over 40 tests were performed with four different loading conditions of radii and the impulse. "Dish like" deflection profiles were produced and measured. Smaller loading radii led to a more localized bulging and uniform load produced tearing at the clamped boundary. Theoretically the plate was modeled as a rigid-plastic membrane. Good correlation was obtained between the predicted and measured normalized deflection profile[46].

Experiments on fully clamped circular mild steel plates subjected to localized blast loads were reported by Nurick and Radford [33]. The plate deformation was characterized by an inner dome superimposed on a larger global dome. The inner dome diameter was proportional to the load diameter. At higher impulses, thinning in the central region and at the plate boundary was observed. Tearing in the central area of the plate occurred with further increases in impulse after the onset of thinning. The tearing observed was characterized by a cap torn away from the plate. The diameter of the cap was proportional to the load diameter. A reduction in thickness of the plate at the centre, smaller than the load diameter was reported by Chung Kim Yuen and Nurick [45] during the study of a built-in circular plate subjected to localized blast load. Thinning in the form of necking occurred at the edge of the inner dome that ultimately led to capping failure with an increase of impulse [45]. The thicker plates subjected to smaller load diameters showed "petalling" response rather than capping failure. The inner dome was less apparent for the thicker plates [45]. Tearing at the boundary was observed where load-plate diameter ratios exceeded 0.4. Various failure modes of locally blast loaded built-in circular plates are shown in Figure 2-9.

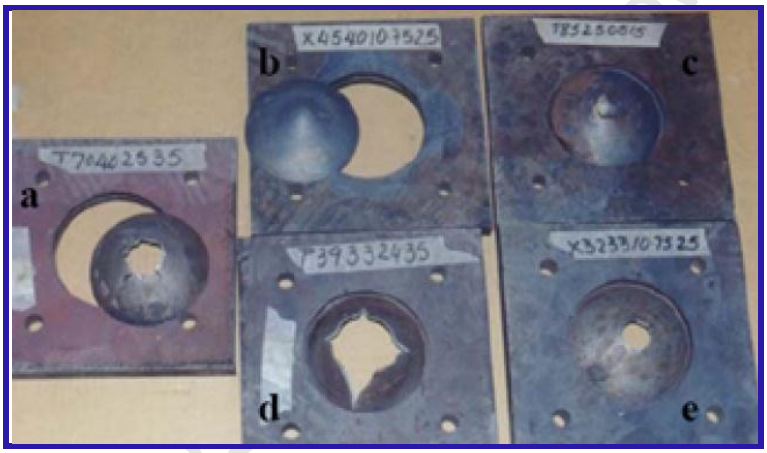

Figure 2-9: Photographs of locally blast loaded circular plates, showing failure modes (a) Mode II (with capping), (b) Mode II, (c) Mode II*c, (d) Petalling and (e) Mode IIc [45]

Figure 2-10: Photographs of cross-sections from blast loaded rectangular plates (length/width= 2.3) for a load diameter of 32mm [47]

Jacob et al. [47] reported the results of clamped mild steel quadrangular plates of various thicknesses (1.6, 2, 3)mm and 4mm subjected to localized blast load. Disc shaped explosive

(PE4) was centrally positioned on target plates. The response was studied by varying charge diameter-to-plate width ratios (0.2-0.37) and charge heights (1.8–14mm). Three series of experiments were conducted. Series I considered the effect charge height on a constant charge diameter with different plate thicknesses. Series II considered the effect of charge diameter with a constant charge height with different plate thickness. Series III considered the effect of varying plate length–width ratio (l/b) and varying charge height with a constant charge diameter–plate width ratio on plates of constant thickness. It was concluded that for a constant charge diameter, impulse increased with increasing charge height; for a constant charge height, impulse was increased by increasing charge diameter [47]. Photographs of typical circular and quadrangular plate responses to localized blast load are shown in Figure 2-9 and Figure 2-10 respectively.

The influence of experimental set-up on the impulse imparted to a plate was studied by Bonorchis and Nurick [48]. The experimental results of a series of test showed that the impulse measured by a ballistic pendulum depends on the height of the boundary or clamps. The impulse was found to increase as the height of the clamps increases. Further, it was found that the additional impulse due to the clamps height did not influence the deformation of the plate [48].

2.8 Stiffened target plates

Chung Kim Yuen and Nurick [37] studied experimentally and numerically the behaviour of mild steel quadrangular plates with different stiffener configurations subjected to blast loading. All the plates exhibited a uniform global dome with a peak displacement at the centre. The addition of stiffeners to the plates resulted in lower central displacements. The single stiffened plates were less effective than double-cross stiffened plates.

Nurick et al. [32] conducted experiments on fully built-in steel stiffened plates. The results indicated that in Mode I failure, the midpoint deflection increases with an increase in the applied impulse. Tollner and Nurick [49] reported the numerical predictions for clamped stiffened circular plates subjected to uniform blast loading. The numerical results were compared with the experimental results obtained by Nurick and Lumpp [50] Mode I behaviour was suitably predicted by the numerical results for the individual components.

An experimental study on single and double clamp-stiffened rectangular plates subjected to uniform blast loading was carried out Nurick and Conolly [44]. The plates suffered tearing of the long side whereas stiffened plates exhibited tearing along the short side. It was concluded that plate tearing was related to plate deflection rather than applied impulse.

Veldman et al. [51;52] studied the effects of static pre-pressurization on the blast response of clamped reinforced square aluminum alloy plates. Bare spherical explosive charges of C4 were detonated at various stand-off distances. Experimental and numerical predictions of the dynamic plate response were determined using finite element analysis. No significant increase in plate deflection was observed as static pressurization increased from 0.0 to 62.1 KPa. Good correlation was found between experimental and predicted values.

Other experimental results for stiffened plates have also been reported by Schubak et al. [53;54], Schleyer et al. [55;56], and Pan and Louca [57]. Schubak, et al. [58] investigated the response of T-beam stiffened steel plate (DRES panel) to blast loads. Longitudinal edges of

the panel slipped inward during the blast while the maximum permanent displacement occurred at the middle of the panel.

Schleyer et al. [55] carried out experimental work on stiffened plates subjected to blast loading. It was concluded that in-plane restraint was responsible for reducing the maximum transient deflections in the stiffened plates up to 50% and permanent deformations by more than a factor of 4. There was also no sign of lateral buckling in the stiffeners.

Wiehahn et al. [59;60] examined the response of stiffened square plates subjected to localize impulsive loading. Temperature dependent material properties were also included in a numerical model of circular plates subjected to localized blast loading. It was reported that ‘‘capping’’ failure of plates associated with thermo-mechanical instability of material.

Langdon et al. [61] studied experimentally and numerically the behaviour of mild steel quadrangular plates of different stiffener configurations subjected to localized blast loading. It was concluded that localized blast loading leads to higher displacements and lower tearing thresholds than uniformly blast load tests. The tearing threshold impulses were four times higher for uniformly loaded plates.

The effect of welded stiffener heights and different weld configurations subjected to localized blast loading was studied by Bonorchis and Nurick [62]. For a specific weld configuration, tearing threshold impulse was observed to decrease by increasing stiffener heights. The bulge and stiffener deflection trends are independent of the weld configuration for the same stiffener height.

2.9 Effect of various parameters on the response of target plates

2.9.1 Effect of standoff distance

The effect of stand-off distance on square plates subjected to air blast loading was reported by Akus and Yildirim [63]. The results indicated maximum midpoint deflection at the closest stand-off distance, followed by a rapid decrease as stand-off increased. Jacob et al. [36] studied the effect of stand-off distance and charge mass on the response of fully clamped circular mild steel plates subjected to blast loads. The stand-off distance was varied from 13 to 300 mm, using different tube lengths. The blast load was considered localized at stand-off distances less than the plate radius (13-40mm), and considered uniformly distributed at stand-off distances greater than the plate radius (100-300mm). Different plate profiles were observed at various stand-off distances. An inner dome superimposed on a larger global dome was observed at stand-off distances less than a plate radius. At stand-off distances greater than the plate diameter (100 mm), response appeared similar to that of uniform loading (that is a global dome). A transition phase (global to localized) was observed at stand-off distances of 50 and 75mm. Midpoint deflections decreased from 13 to 50mm as stand-off distance increased for given charge mass. For stand-off distances ranging from 75 to 300mm, similar midpoint deflections were reported for a given charge mass.

2.9.2 Effect of boundary conditions on failure

Thomas and Nurick [64] compared fully clamped and built-in mild steel plates with different edge fixations subjected to uniform blast loads. Built-in plates were machined from 20 thick

steel plates. No significant difference in the results was found for Mode I failure whereas Mode II* failure was highly dependent on the edge condition. Partial tearing along the boundary was found to occur at lower impulses in the machined plates than in the clamped plates. Schleyer et al. [56] also examined the effect of boundary clamping on the response of mild steel plates subjected to dynamic loading. The loading took the form of a triangular pressure pulse applied over 50 ms and was not impulsive considering the long load duration with respect to the natural period of the test plates. In-plane movement along the clamped edge was observed. Nurick et al. [42] investigated the onset of thinning for different diameter circular mild steel plates clamped between frames with different edge conditions. The clamps were sharp edged or filleted with 1.5 and 3.2 mm radius. Thinning of plates was reported for all plate diameters with sharp-edged clamps. Plates secured using frames with fillets allowed larger deflections to occur before the onset of thinning and tearing. In the case of a curved edge boundary, the thinning was similar to that observed in a uni-axial tensile test. Welded boundary response was compared to responses with clamped, straight and chamfer boundaries of hot rolled mild steel plates subjected to localized blast load [65]. Similar trends were observed for the plate midpoint-deflection ratio versus dimensionless damage number for all the boundary types. The straight and chamfer boundary machined plates were found to tear at the lowest damage number. The welded plates tore at a damage number approximately 7% greater than the machined plates. The clamped plates have the highest tearing threshold at a damage number approximately 24% greater than the machined plates.

2.10 Theoretical studies of monolithic structures to blast loading

Johnson [66] proposed a dimensionless impulse (shown in Equation 2-4) and an analytical solution to predict large inelastic deformation of fully clamped circular plates loaded by a uniformly distributed velocity.

$$\boldsymbol{\alpha = \frac{\rho v_o}{\sigma_d}} \qquad 2\text{-}4$$

Where "v" is the impact velocity, "ρ" is the material density and "σ_d" is the damage stress which is taken as equal to the plate material yield stress "σ_y". This parameter does not consider plate geometry/boundary conditions, or the method of impact. Johnson's damage number [66] is applicable only when plates have similar dimensions.

Nurick and Martin [16] proposed modified dimensionless numbers for both uniformly and locally loaded circular plates. A modified dimensionless number Φ was introduced by Nurick and Martin [17] that incorporated plate dimensions and loading conditions. This dimensionless number allowed comparison of blast-loaded panels and plates of different geometries and different materials to be treated similarly. The dimensionless numbers for circular and quadrangular plates is given in Equation 2-5 [16]and Equation 2-6 [67].

$$\boldsymbol{\Phi_c = \frac{I\left\{1+\ln\left(\frac{R}{a}\right)\right\}}{\pi R H^2 (\rho\sigma_0)^{0.5}}} \qquad 2\text{-}5$$

$$\Phi_q = \frac{I}{2H^2(bl\rho\sigma_0)^{0.5}} \quad 2\text{-}6$$

Where

Φ_q	Non dimensional impulse
I	Applied impulse (Ns)
R	Plate radius (m)
a	Load radius (m)
H	Plate thickness (m)
l	Plate length (m)
b	Plate width (m)
ρ	Material density (Kg/m^3)
σ_o	Plate static yield stress (MPa)

Nurick and Martin [16] also presented an empirical relationship given in Equation 2-7, based on experimental results.

$$\left(\frac{\delta}{H}\right) = 0.48\emptyset q + 0.277 \quad 2\text{-}7$$

Where δ is a midpoint deflection

Jacob et al. [47] proposed a damage number for uniformly and locally loaded quadrangular plates, as shown in Equation 2-8.

$$\Phi_q = \frac{I\left\{1+\ln\left(\frac{lb}{\pi a^2}\right)\right\}}{2H^2(bl\rho\sigma_o)^{0.5}} \quad 2\text{-}8$$

2.11 Computational studies of monolithic structures to blast loading

The dynamic response of structures is difficult to model due to the dependence on both load history and boundary conditions. Predictions using computational analysis have been reported widely in the literature for the large deformation of symmetrical structural components and subsequent tearing as a result of a blast load. The solutions employ nonlinear finite element analysis. Jones proposed a plastic hinge model [68;69] to calculate the maximum strain at the support. Jones [68;69] defined Mode II failure as the instant when the maximum strain reached the rupture strain obtained from a uniaxial static tensile test. Good correlation was reported in Mode I failure domain while Mode II failure was limited to predicting the initiation of failure only. Radford and Nurick [70] and Farrow et al. [71] modeled circular plates with axi-symmetric cross sections. Nurick et al. [32] and Fagnan [72] used a strain-based model to predict Mode II failure numerically.

Rudrapatna et al. [73;74] developed a model to predict the modes of failure of blast loaded clamped square and stiffened plates using an interactive failure criterion for bending, tension and transverse shear. Good comparison between the experimental and predicted results was obtained. The influence of shear on the failure mechanism for Mode II and Mode III was reported [73]. During deformation of plate, 90% of the plastic work is converted into heat [75] causing an increase in the temperature in a localized area. The heat, generated by the plastic deformation at high strain-rate, flows and causes thermal softening. If the deformation occurs slowly, such as in quasi-static loading conditions, most of the generated heat is conducted away from the slowly deforming regions and the body remains in an isothermal condition. At the other extreme, when deformations occur rapidly, for example in high velocity impact or explosive loading, the process is essentially adiabatic, as there is not sufficient time for redistribution of the generated heat. Due to short response time of the plate, no significant heat conduction occurs between elements.

Wiehahn et al. [59;60] included temperature dependent material properties in a numerical model to predict tearing of a circular plate subjected to a localized blast load. Localized shear bands decreased in the simulations, provided new insights into the tearing mechanism through the thickness of the plate undergoing deformation at strain rates in the range of 10^2–10^4 s^{-1}. "Capping" failure of centrally loaded plates was shown to be associated with thermo-mechanical instability of material.

Numerical analysis of single mild steel plates subjected to uniform and localized blast loading was conducted by Chung Kim Yuen and Nurick [37] and Langdon et al. [61]. In refs [37;61], ABAQUS/Explicit version 5.8 was used by incorporating non-linear geometry, material effects, strain-rate sensitivity and temperature effects. The Finite Element (FE) predictions compared well with the experimental results for both large inelastic deformation and tearing. The temperature distribution and the permanently deformed profile of a flat plate subjected to localized blast load of an impulse of 9.5Ns shown in Figure 2-11. The FE analysis predicted the central peak observed in the blast tests. Figure 2-11a and b show a contour 'ring' of elevated temperature (700°C), led to predictions of tearing of a central cap. Predicted thinning along the boundary is shown in Figure 2-11c.

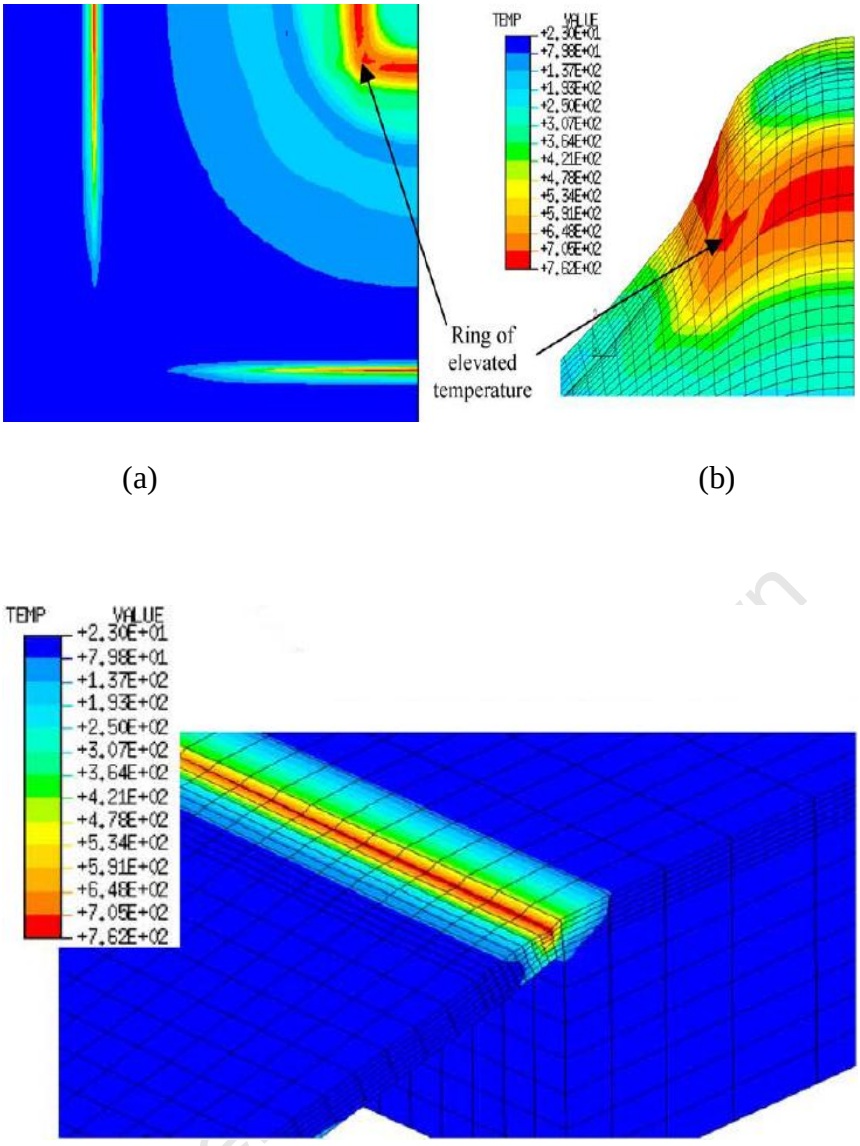

Figure 2-11: FE predictions of the response of a single plate subjected to an impulse of 9.5Ns: (a) temperature contour plot (max temp = 762 °C), (b) details of temperature profile for thinning ring, (c) thinning along the boundary [61]

Balden and Nurick [76] simulated the results of plates subjected to uniform and localized blast loading. The simulations were validated using experimental studies [40;77] including uniform and localized blast loadings. A finite element code (ABAQUS) was used to simulate the structural response of the respective blast structures, while a hydro-dynamic code (AUTODYN) was used to characterize the localized blast pressure, time and spatial history. The simulations showed satisfactory correlation with the experiments for energy input, large inelastic deformations and post-failure motion. The simulation results of uniformly loaded circular plates showed close correlation to the published study of Teeling-Smith and Nurick [40] for both failure Mode I and Mode II responses. Favorable comparison between the simulated and experimental results for the localized blast loading of parallel separated plates, as described in Nurick and Bryant [77] was also presented. Simulation results for a localized blast load are shown in Figure 2-12, which are typical of a Mode I response of the front face.

Figure 2-12a shows the actual thinning/necking of the test plate while Figure 2-12b and c show comparable predicted simulated behaviour of material necking. Figure 2-12d shows the displacement-time history for the tip of the upper face and indicates a favorable comparison of the final midpoint deflection. A typical Mode II response of the front face and Mode I response of the back face is shown in Figure 2-13. Figure 2-13a shows a sequence of images as the front plate material necks, at approximately 29 μs, and tears from the front face at approximately 30 μs. The fragment travels toward the back face with a predicted free velocity of 675 m/s, shown in Figure 2-13c. Contact between the fragment and back face was established at approximately 130 μs, seen by increasing tip deflection of the back face in Figure 2-13b. Following contact, the fragment and back face move together and reach a stop after approximately 600 μs.

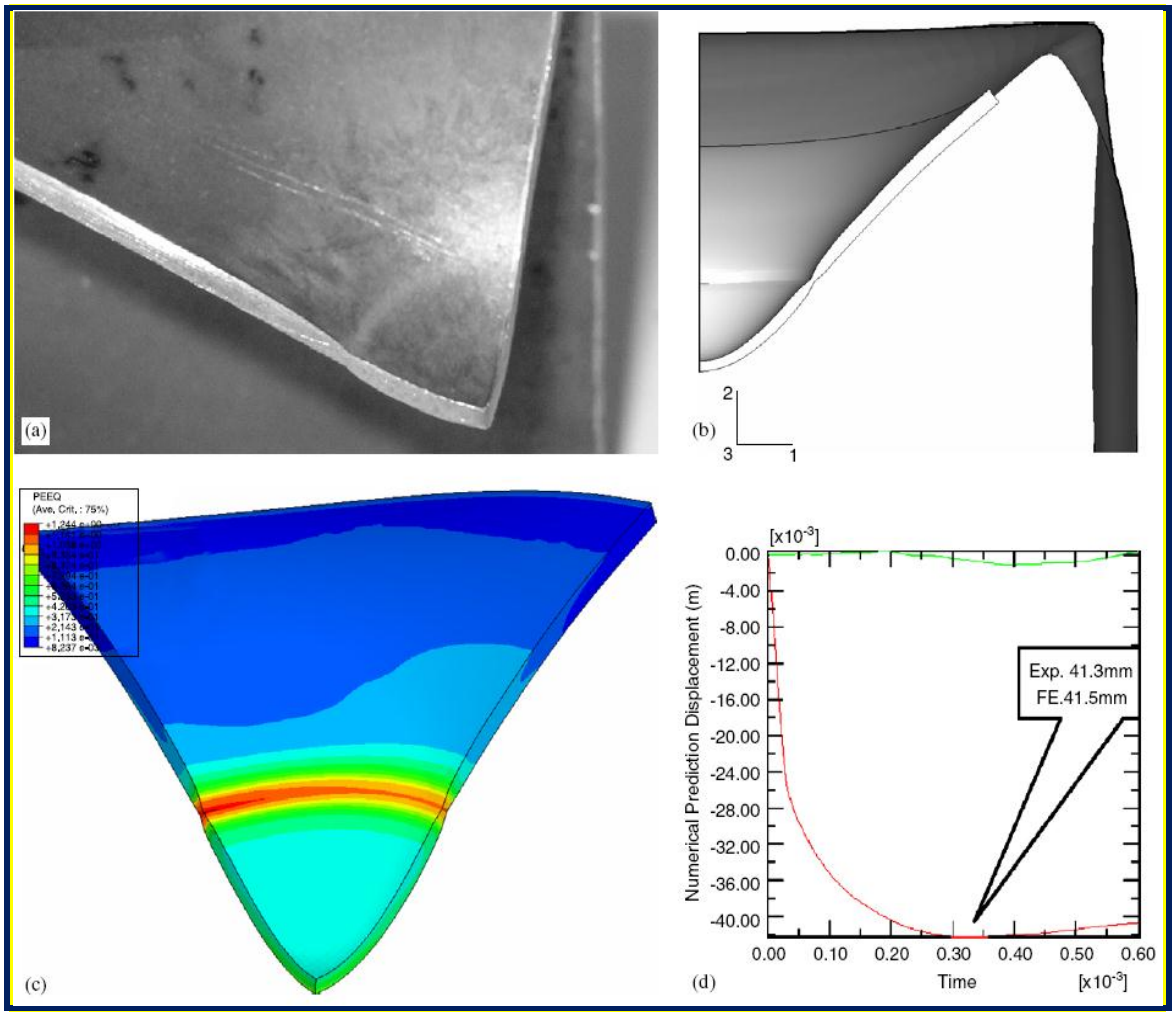

Figure 2-12: Numerical simulation results for a localized blast impulse of 14.22Ns. (a) actual photograph of tube specimen, (b) deformed plot showing localized necking, (c) contour plot of equivalent plastic strain at 22.5 ms, (d) displacement-time history plot of predicted tip deformation[76]

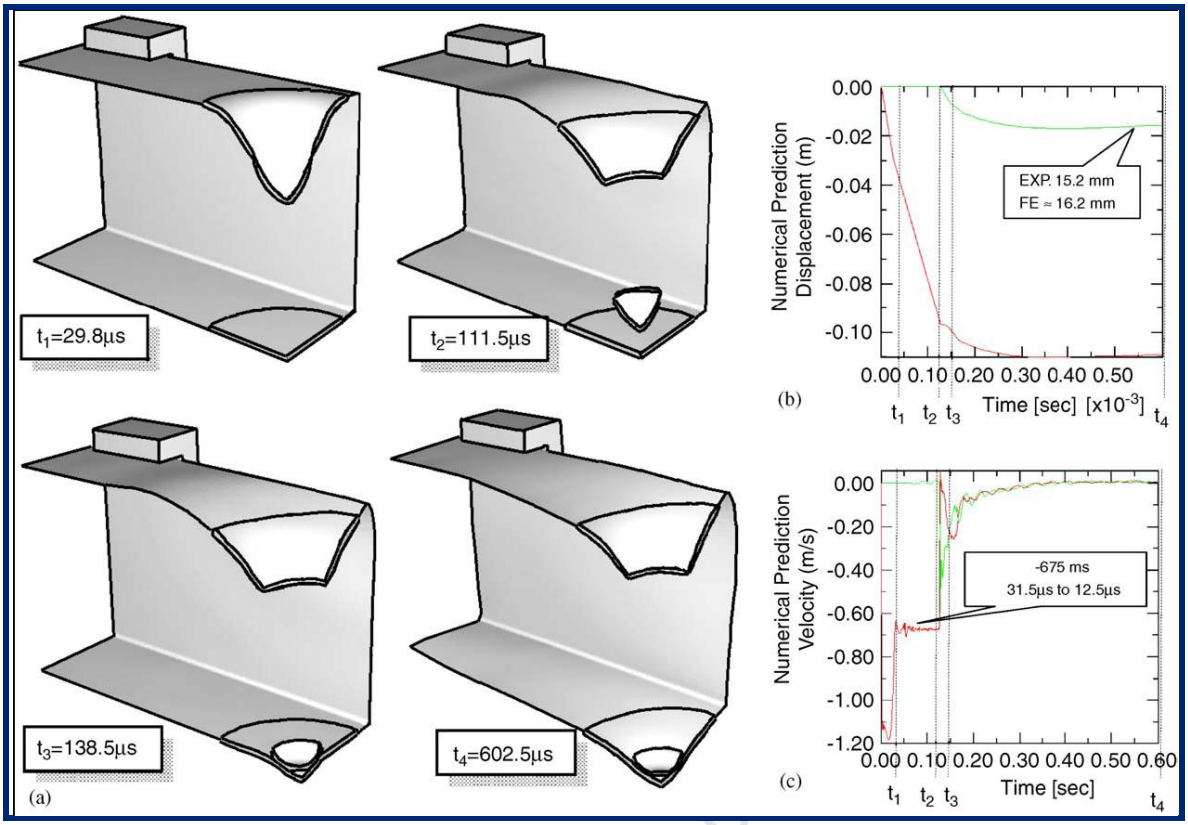

Figure 2-13: Numerical simulation results for a localized blast impulse of 17.64Ns. (a) Sequence of deformation plots showing progression of experiment, (b) time history plot of deformation of both the front and back faces, (c) time history plot of the velocity of both the front and back faces [76]

Various shapes of the pressure-time curve as shown in Figure 2-14 have been used in numerical simulations [24]. The area under the pressure-time curve is constant for the rectangular and triangular shapes as shown in Figure 2-14c and d. Farrow et al. [71] used both rectangular and triangular pressure profiles to model the plate deflections, deformation shapes, residual strains and dynamic yield stress of a circular plate subjected to uniformly distributed blast load. ABAQUS/Explicit finite element code was used for the predictions. It was reported that the results obtained from rectangular pulses were closer to experimentally obtained results [71].

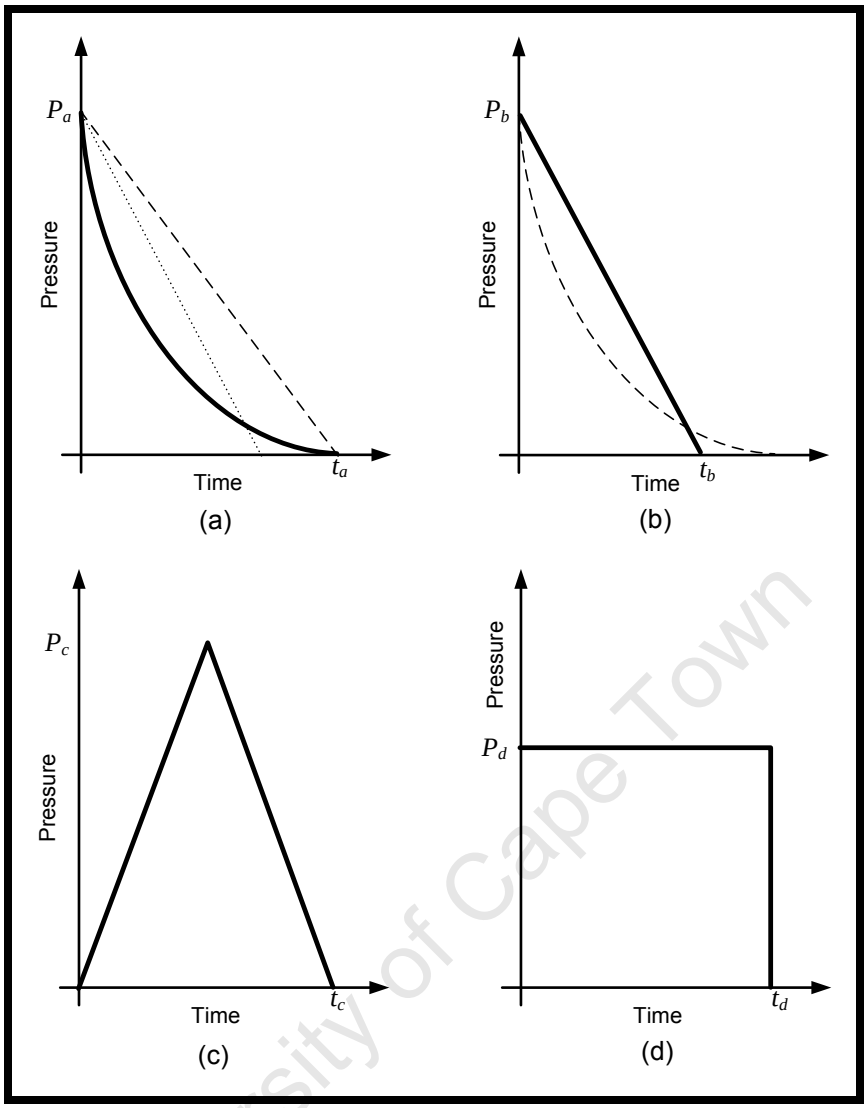

Figure 2-14: Different shapes of pressure-time loading histories [24]

2.12 Fractography

Study of fracture surfaces of materials is known as fractography and is used to determine the cause of failure of engineering structures. Fractures in metals and alloys can be classified as ductile or brittle. The main difference between ductile and brittle fractures can be attributed to the amount of plastic deformation that the material undergoes prior fracture. Ductile materials demonstrate large amounts of plastic deformation while brittle materials show little or no plastic deformation before fracture. The engineering materials always contain impurities, inclusions, second phase particles and crystalline defects and are never completely pure. Materials that contain these impurities fail at much lower strains. Figure 2-15 illustrates the difference between a completely pure material and an engineering material in a uniaxial tensile test. “The material reaches the instability point where the strain hardening cannot keep pace with loss in cross sectional area” [78]. The material reaches the instability point during a tensile test and necking starts beyond the maximum load.

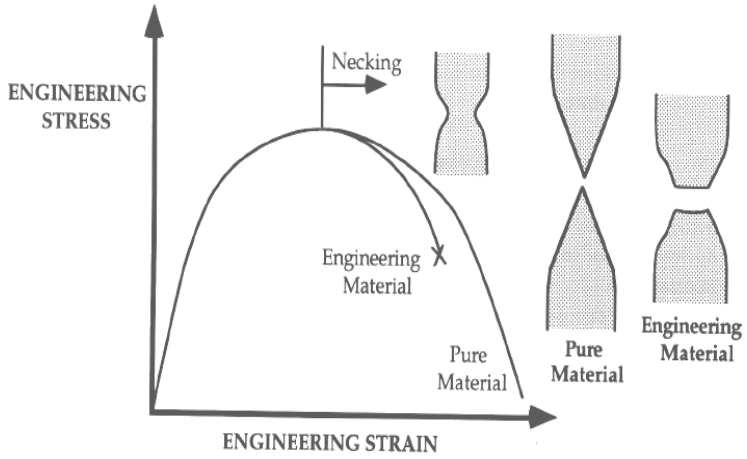

Figure 2-15: Uniaxial tensile deformation of ductile material [78]

The ductile and brittle materials show cracking in different ways. In ductile materials, the crack moves slowly and is accompanied by a large amount of plastic deformation whereas the crack spreads suddenly in brittle materials. The crack in metals and alloys can propagate by a trans-granular (through the grains) or an inter-granular (along the grain boundaries) fracture path. Trans-granular dimple rupture due to Micro Void Coalescence (MVC) is the most prevalent fracture mechanism of ductile overload failures. The most common fracture mechanisms in metals and alloys are schematically illustrated in Figure 2-16 [78;79]. Each of these modes has a characteristic fracture surface appearance and a mechanism by which the fracture propagates.

The other types of fractures include fatigue fracture (due to repetitive or cyclic loading) and decohesive rupture (result of a reactive environment)[79].

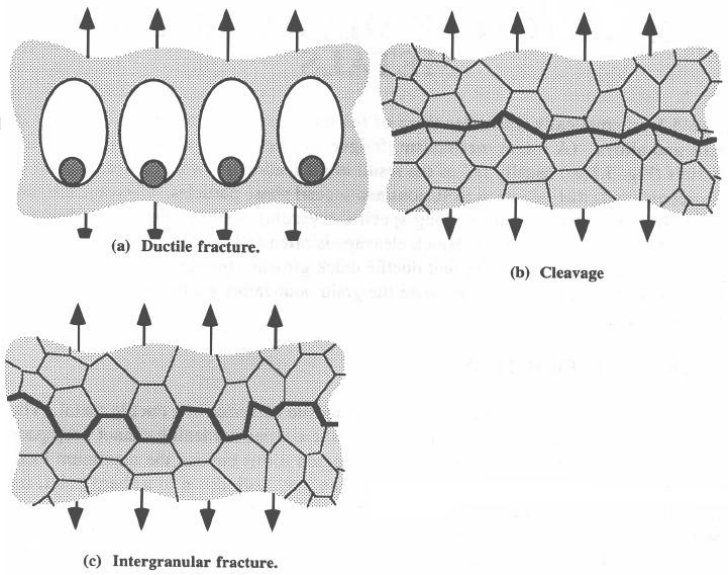

Figure 2-16: Micro-mechanisms of fracture in metals [78]

2.12.1 Brittle fracture

Cleavage is a low-energy fracture that propagates along well-defined low-index crystallographic planes known as cleavage planes. The cleavage fracture usually appears as brittle and its fracture path is granular (Figure 2-16 b). Although cleavage usually appears as brittle fracture, it can be preceded by large scale plasticity and ductile crack growth. Inter-granular fracture occurs when the grain boundaries are the preferred fracture path in the material (Figure 2-16 c). Cleavage is most likely when plastic flow is restricted [79].

Face centred cubic (FCC) metals are usually not susceptible to cleavage because there are ample slip systems for ductile behaviour at all temperatures. In these metals, a large amount of plastic deformation will occur before the stress necessary for cleavage is reached. Body centred cubic (BCC) metals and hexagonal close-packed (HCP) structures fail by cleavage at low temperatures because there are a limited number of active slip systems [78]. The metals that commonly show cleavage are Tungsten, Molybdenum, Chromium, Zinc, Beryllium and Magnesium.

Ideally, a cleavage fracture would have perfectly matching faces and be completely flat and featureless. A truly featureless cleavage is rare. The changes of orientation between grains, sub-grains and the various imperfections produce markings on the fracture surface that are characteristically associated with cleavage. A principal feature is a river pattern, which are steps between cleavages on parallel planes. River patterns always converge in the direction of local crack propagation. Another feature associated with cleavage is feather markings. The cleavage facets seen through the grains have a high reflectivity, which gives the fracture surface a shiny appearance. Figure 2-17 shows river patterns in the fractographs of brittle material. The factors that contribute to a brittle-cleavage type of fracture are (a) triaxial state of stress, (b) low temperature and (c) high strain rate.

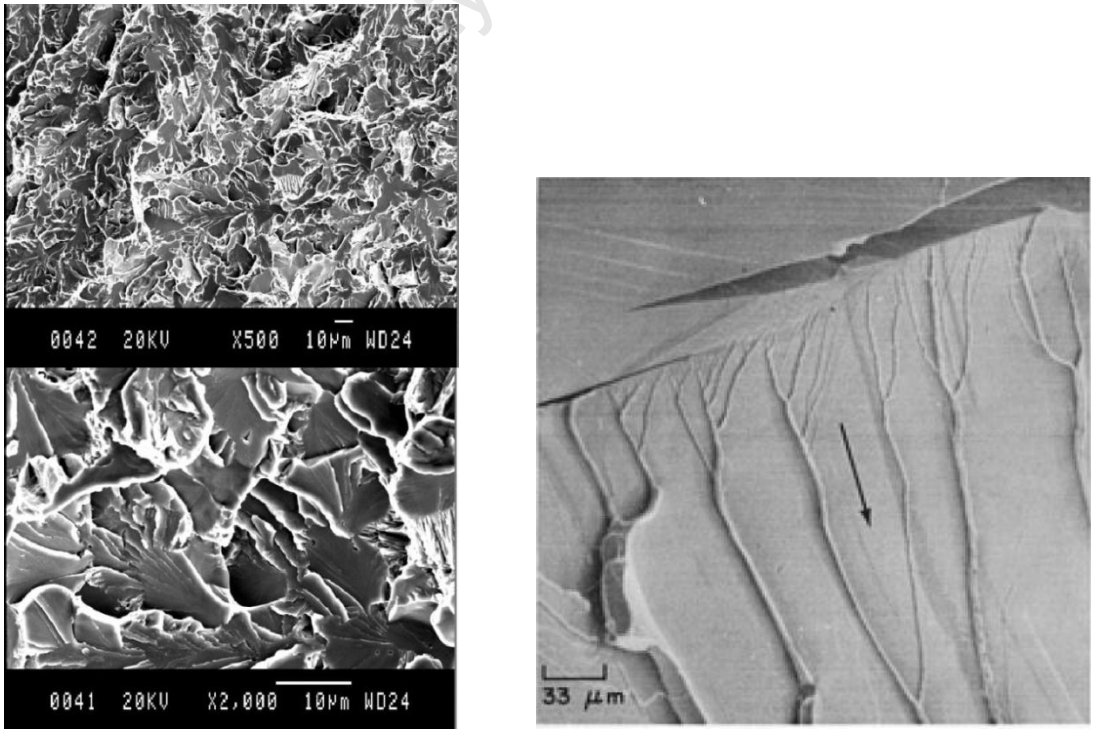

Figure 2-17: Fractographs of brittle material show river patterns [79;80]

2.12.2 Ductile fracture

Most ductile metals and alloys fail with significant macroscopic plastic deformation. The fractured surfaces exhibit micro-void morphology. This type of fracture also depends on section thickness. Significant contraction before failure occurs in thin sections whereas in the thick sections, ductile fracture may occur without noticeable contraction. In such cases the only macroscopic difference is the reflectivity of the fracture surface, which tends to be dull for a ductile fracture and shiny and faceted for a brittle fracture[78].

Ductile fracture arises from the nucleation, growth and coalescence of micro-voids that initiate at inclusions and second phase particles when subjected to plastic strain and hydrostatic tension (Figure 2-16 a). The micro-voids can nucleate at regions of localized strain discontinuity, grain boundaries and dislocation pile-ups. The ductile fracture shows several cuplike depressions that are the direct result of the micro-void coalescence. The cuplike depressions are referred to as dimples or micro-voids and the fracture mode is known as dimple rupture [81]. Both terminologies (dimples or micro-voids) are used here interchangeably in the entire study.

The size of the dimple on a fracture surface is governed by the number and distribution of micro-voids that are nucleated during application of load. When the nucleation sites are few and widely spaced, the micro-voids grow to a larger size before coalescing and the created fracture surface having larger dimples. Small dimples are formed when numerous nucleating sites are activated and adjacent micro-voids join before they have an opportunity to grow to a larger size. Extremely small dimples are often found in oxide dispersion strengthened materials. The distribution of the micro-void nucleation sites can significantly influence the fracture surface appearance [79].

When micro-voids nucleate at the grain boundaries, inter-granular dimple rupture results [79]. Ductile fracture by void growth and coalescence can occur by two modes during tensile loading. Mode-I is a plane-strain fracture, where micro-void growth and fibrous tearing occur along a crack plane that is essentially normal to the axis of the tensile load. The fracture appearance typically has a dull and fibrous look, as in the classic “cup and-cone” feature of ductile fracture in the simple cross section of a tensile testing specimen.

The other fracture mode is plane-stress fracture (Mode-II), which manifests itself as the “shear lips” in the cup and cone fracture specimens from tensile tests. During tensile loading, the fracture originates near the specimen centre, where hydrostatic stresses develop during the onset of necking and where micro-voids develop and grow. Multiple cracks join and spread outward along the plane normal to loading axis, as of Mode-I crack. When cracks reach a region near the outer surface, the mode of fracture changes to Mode-II (plane-stress) condition, where shear strain becomes the operative mode of deformation. Thus, even though the overall applied stress is still a tensile load, deformation makes a transition to the shear plane in the outer regions of the specimen [81;82].

In Mode-II region, micro-voids grow in sheets at an oblique angle (~45° to the plane of the major fracture or loading axis) to the crack plane under the influence of shear strains. This type of shear-band tearing results in the classic shear lips of a ductile cup-and-cone tensile fracture specimen. Shear-band formation also commonly occurs in deformation processing, where friction and geometric conditions produce inhomogeneous deformation, leading to local shear bands. Localization of deformation in these shear bands also results in localized

temperature increases that produce local softening. In pure metals and alloys, the material may fail by adiabatic shear-band formation, resulting in a somewhat flat fracture surface devoid of dimples [81;82].

Micro-voids nucleate in the vicinity of the crystalline defects and at inclusions and second phase particles. The voids grow together to form a microscopic flaw, which leads to fracture. In the materials where the second phase particles and inclusions are well bonded to the matrix, void nucleation is often the critical step, fracture occurs soon after the voids form. A void forms around a second phase particle or an inclusion when sufficient stress is applied to break the interfacial bonds between the particle and the matrix (Figure 2-18a and b).

Due to particle strains and hydrostatic stresses, the micro-voids around the particle nucleate (Figure 2-18c). Further growth of micro-voids leads to merging with adjacent micro-voids. Plasticity is assumed to be localised between the voids. The plastic strain is concentrated along a sheet of voids, and local necking instability develops (Figure 2-18d and e). The orientation of the fracture path depends on the stress state [78]. Experiments show that micro-voids nucleation occur more readily in a triaxial tensile stress field. The nucleation strain decreases as the hydrostatic stress increases[78].

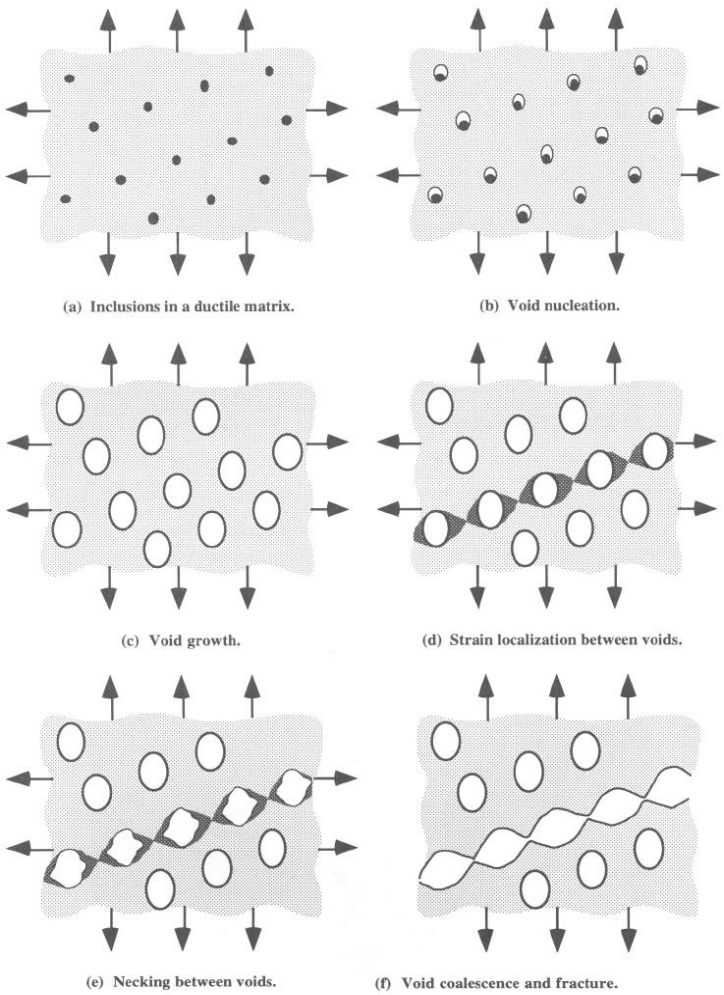

Figure 2-18: Show the void nucleation, growth and coalescence in ductile metals [78]

Figure 2-19 illustrates the formation of a cup and cone fracture surface, commonly observed in uniaxial tensile tests. The neck that produces a triaxial stress state in the centre of the specimen promotes micro-void nucleation and growth around the larger particles. Further straining leads to void coalescence, which finally results in a penny-shaped incision. The outer ring of the specimen contains relatively few micro-voids, because the hydrostatic stress is lower here than in the centre. The penny-shaped incision produces deformation bands at 45^{o} from the tensile axis. This centring of strain provides sufficient plasticity to nucleate micro-voids around the smaller particles. Since the small particles are closely spaced, instability occurs soon after formation of these smaller micro-voids. These smaller voids merge, which results in total fracture of the specimen. Since the material fractures at different stages, the cup and cone formation becomes visible [78].

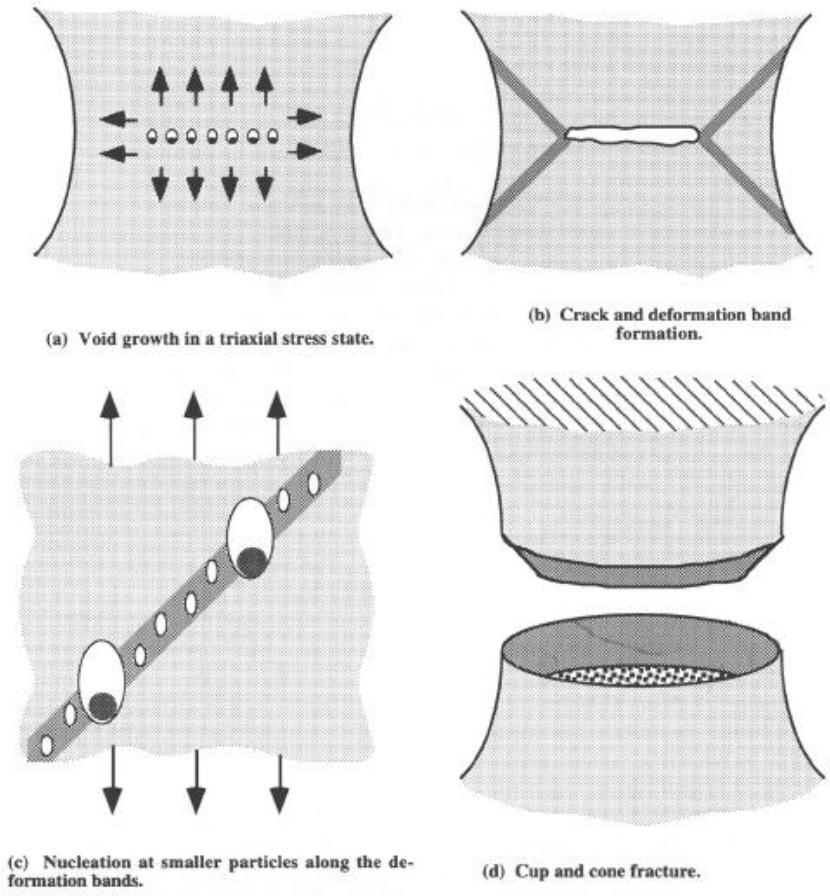

Figure 2-19: Formation of the cup and cone fracture surface in uniaxial tension with a circular cross-section [78]

Dimple shape is strongly influenced by the type of loading at the time of fracture. Fracture under uniaxial tensile loading usually results the formation of equiaxed dimples whereas the failures caused by shear stress produces elongated or parabolic shaped dimples. Various types of dimples produced by application of uniaxial tensile loading, shear and tensile tearing are shown in Figure 2-20.

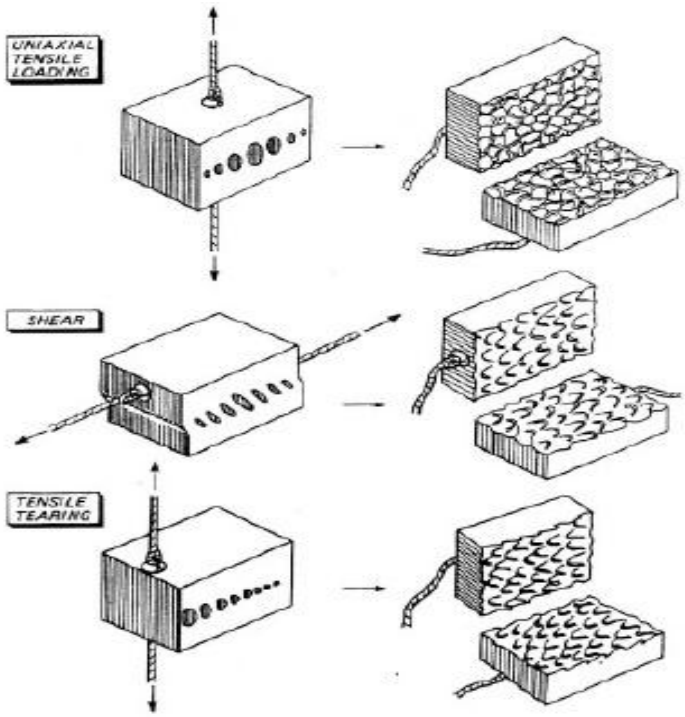

Figure 2-20: Schematic of dimple formation owing to uniaxial tensile loading, shear and tensile tearing [80]

2.12.3 Factors influencing the fracture process

The deformation and fracture process are influenced by temperature, strain rate, microstructure, phase transformation, dislocation dynamics, mechanical properties and the fracture surface morphology. The fractured surface of a material is associated with the history of entire deformation process. Dimples/micro-voids geometry and their correlation with the mechanical properties of austenitic stainless steel and HSLA steel were studied by Das et al. [83;84] and reported a systematic correlation of the mechanical properties and the dimple diameter of ductile fracture with strain rate variation. The micro-void features on the tensile fracture surfaces at various strain rates were reported by [83;85]. Higher quantities of micro-voids and lower diameter of micro-voids were observed at lower strain rates, thus the ductility was high and the strength was low. At high strain rates, the amount of micro-voids was lower and therefore, the strength was high at the expense of ductility.

The ductile fracture under high constraint, low temperatures and rapid loading at equal stress may show the lack of contraction expected for cleavage and may not exhibit any deformation before failure.

2.12.4 Single and layered plates subjected to projectiles impact

Comprehensive reviews on the response of target plates against various types of projectiles have been published by Backman and Goldsmith [86], Corbett et al. [87], Goldsmith [88] and Zukas et al. [89;90] that discuss the phenomena associated with ballistic penetration and perforation. The hardness, thickness, material density, impact methods and the target configurations are the important factors in considering the armour application.

The ability of a target to withstand projectile impact is measured by a term "ballistic limit". Ballistic limit [87] velocity is the greatest velocity a structure can withstand without perforation. Ballistic limit velocity is measured from the average of two striking velocities (highest velocity gives partial penetration and lowest velocity at complete perforation). The ballistic limit, also termed as V_{50}, critical impact velocity and plugging capacity. "All definitions of the V_{50} refer to the threshold velocity dividing penetration and non-penetration events [91]". The definition of ballistic limit depends on the interpretation of perforation [87]. Various definitions of ballistic limit velocity (army ballistic limit, protection ballistic limit and navy ballistic limit) are shown in Figure 2-21.

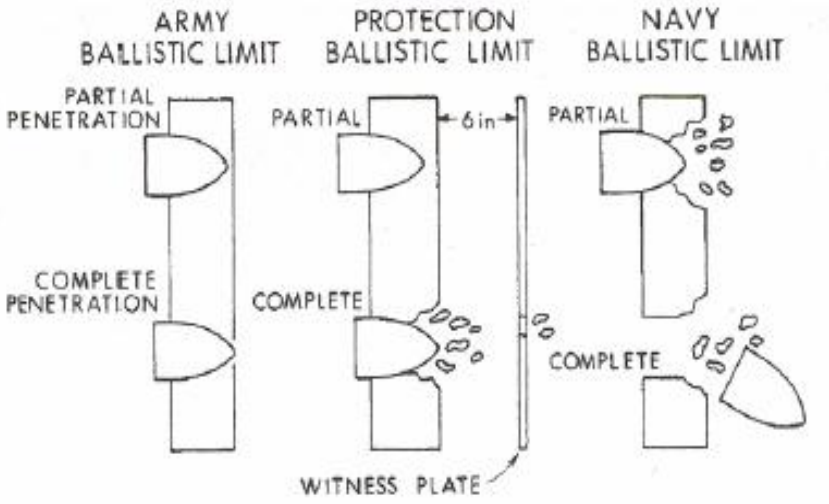

Figure 2-21: Showing various definitions of the ballistic limit velocity [86]

The target can fail by different mechanisms and the detail can be found in [86]. Backman and Goldsmith [86] identified the eight types of failure of thin or intermediate targets as shown in Figure 2-22. These failure mechanisms may occur singly or in combinations of two or more.

In the current study of localized blast loading experiments, the responses of target plates are classified as pre-threshold impulse and post-threshold impulse behaviours, since the responses are different in each group. The transition between the failure Modes-I and Mode-II was defined as Mode II* by Langdon et al [35]. The impulse at which Mode II* occurs is the threshold impulse. Backman and Goldsmith [86] divided target response into failure modes and non failure modes. The response of target plates at pre-threshold impulse is considered as non failure mode and the response of plates at post-threshold impulse was considered failure mode. The target plates were considered failed if the daylight can be seen after the threshold impulse into single plates and from the back plates of layered configurations.

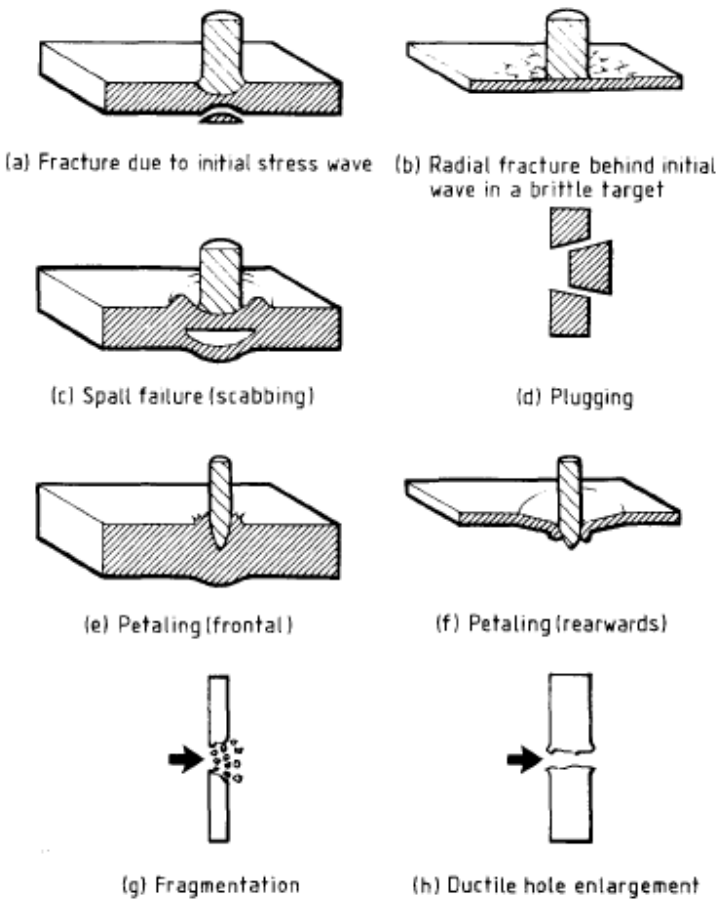

Figure 2-22: Perforation mechanisms [86;87]

The performance of single and multi-layered plates of same material against various projectiles for the optimization of areal density has been under discussion for many years. Difference of opinions in using single or multi-layered plates against projectiles can be found in the open literature. According to Radin and Goldsmith [13] and Almohandes et al. [14] the ballistic limit of a single plate was always higher than that of a multiple-layered plates of the equal thickness whereas Marom and Bodner [8] and Corran et al [5] founded multi-layered plates superior to single plates. Dey et al. [7] carried out experimental and numerical study on the perforation resistance of double-layered armour steel plates and reported an increase of 40 - 50% in ballistic limit velocity (V_{50}) compared to a single target of equal thickness when impacted by blunt projectiles. In case of ogival nose projectile, the single target showed a better protection, but the difference in perforation resistance was only 10–15% [7].

The reason for the improved performance of multi-layered plates subjected to projectile impact is attributed to the difference in failure modes of single and multi-layered plates as indicated in Figure 1-1 and Figure 1-2. The multi-layered plates exhibited more ductile failure modes and absorbing more energy than thicker single target plates which exhibited brittle failure modes in the form of shear plugging.

2.12.5 Effect of high strain rate loadings

Adiabatic shear bands in metals and alloys have been observed under high-strain-rate loading conditions [92-94] such as projectile impact and blast loading. The adiabatic shear bands are the localization of plastic deformation of a material. The strain rate domain can be divided into three main different categories [95]: low strain rates 10^{-5} to 10^{-1} s^{-1}, medium strain rates 10^{-1} to 10^{2} s^{-1}, high strain rates 10^{2} to $10^{4}s^{-1}$. The strain rates from 10^{-1} to 10^{2} s^{-1} are characteristic of vehicle collisions and strain rate sensitivity becomes pronounced at 10^{-1} s^{-1}. The behaviour of the materials resistance to impact/blast loading changes at a strain rate 10^{2} s^{-1}. The strain rates in explosive loading can be high as the order of 10^{7} s^{-1} and adiabatic shear bands are common in these circumstances [95]. Woodward [96] reported three main modes of failure in the penetration of metallic armour ductile failure, adiabatic shear plugging and discing. Adiabatic shearing is possible if the rate of thermal softening exceeds the rate of work hardening of the target material [96].

The presence of shear bands in high strain rate applications has been mentioned by Bai and Dodd [95] and Rogers and Shastry [94]. Previous study on adiabatic shear localization by Bai and Dodd [95] and Raftenberg and Krause [93] indicated shear bands that may either consist of deformed material or transformed material depending on the temperature of local area due to adiabatic heating. Deformation bands are regarded as zones of intense plastic shear whereas transformation bands are zones of intense shear in which a phase transformation has occurred.

During plastic deformation of materials, it is assumed that 90% of the plastic work is converted into heat [75] causing thermal softening and increase of temperature in the localized area. At high strain rate, there is not a sufficient time for heat conduction to nearby areas and the process becomes essentially adiabatic and could cause phase transformation in metals. The temperature of steel plates in local areas could increase such that austenite forms or increase to melting point of the material. If the temperature of the material reached to a melting point due to adiabatic heating, during cooling back, the liquid to solid state transformation can occur and the resultant structure will be dendritic as mentioned [98]. Dendritic structures generally found during liquid to solid-state transformations. Dendritic morphology is rarely seen in solid-to-solid phase transformations. Dendrites were found during solid-to-solid state phase transformations in binary alloys [99] but not seen in iron alloys. If the temperature of the steel plates reached in austenite region due to adiabatic heating, on rapid cooling, the austenite transforms into martensite and it transforms into (ferrite + pearlite) during slow cooling.

In low alloy steel, the phase transformation temperature depends on carbon content. According to the $Fe\text{-}Fe_3C$ phase diagram in Figure 2-23, steel alloys below 0.83 % carbon starts to transform into austenite when the temperature is above 723 ^{o}C. The temperature of complete transformation of (ferrite + pearlite) to austenite varies from 723 to 910 ^{o}C depending on carbon content of alloy steel.

Cooling of the material from the austenite to room temperature can lead the transformation into (ferrite + pearlite) or martensite depending on cooling rates.

(A)

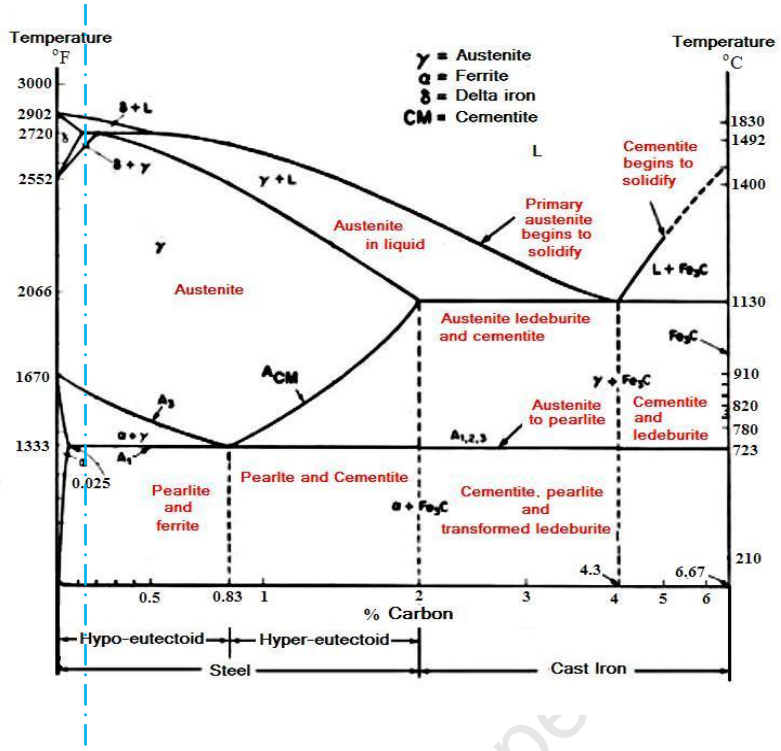

(Á)

Figure 2-23: Iron- Iron Carbide diagram[100]

The phase diagram cannot show time-dependence of the temperature. The transformation from austenite to martensite or (ferrite + pearlite) depends on cooling rate. The changes in microstructures depending on cooling rates are studied through the Time-Temperature Transformation (TTT) as shown in Figure 2-24 and Continuous Cooling Transformation diagram (CCT). Martensitic transformation is a diffusionless shear transformation occurs during cooling in a temperature range which can be precisely defined for particular steel. The reaction begins at a martensitic starting temperature (M_{start}) and finishes at martensite finishing temperature ($M_{finished}$) [101]. The rate of cooling must be sufficiently high to avoid other intermediate reactions as shown in Time-Temperature Transformation (TTT) diagrams in Figure 2-24 (plot of temperature versus the logarithm of time) for the steel of definite composition. In Figure 2-24: A, austenite; B, bainite; M, martensite; P, pearlite.

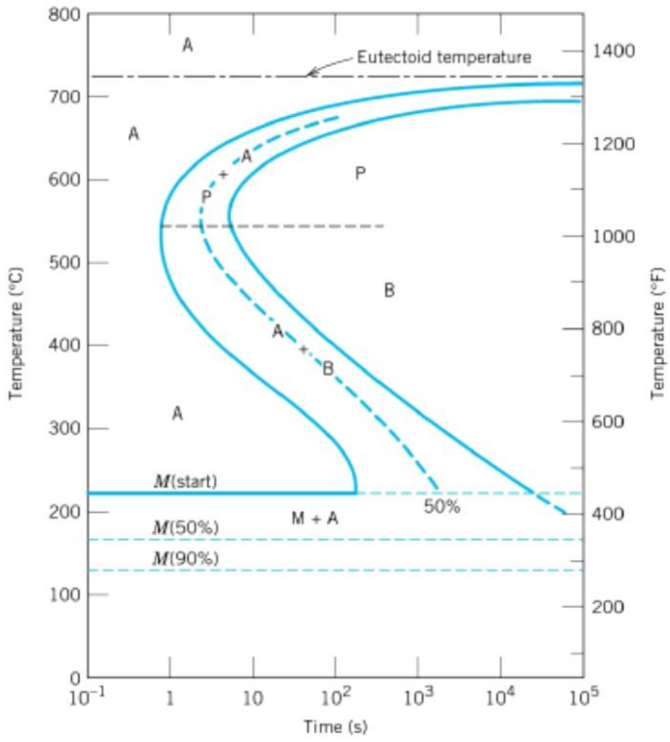

Figure 2-24: Time-Temperature-Transformation (TTT) diagram of iron – carbon alloy at eutectoid composition [102]

2.13 Summary

This literature review composed of two parts, the first part provides an overview on the response of different plate structures subjected to uniform and localized blast load whereas the second part deals with the fractography of materials.

Most published work on the response of blast loaded plates considers single plates with some additional work on stiffened plates. The influence of various parameters such as boundary conditions, stand-off distance, charge shape and loading conditions has been studied.

There is literature on ballistic impact of multi-layered steel plates that indicates, in certain circumstances, that the performance of multi-layered steel plates exceeds that of equivalent mass single steel plates. The influence of projectile geometry upon failure mode [7] determines the relative response- if ductile failure occurs in the thin multi-layered plates and shear occurs in single plates, the performance of the multi-layered system is better.

Hitherto studies on the response of multi-layered, steel target plates subjected to localized blast loading have not been reported. The effect of blast loading on the fracture surfaces of layered plates is not discussed in literature.

Hence, there is need to study the response of multi-layered target plates to localized blast load and the effect of blast loads on the fractured surface of torn plates. The multi-layered target plates may provide better resistance against localized blast loading as studies [4-12] have

indicated that multi-layered plates provide better ballistic resistance against high velocity projectiles than single target plates of equivalent mass.

In the light of these studies, the possibility of enhancing of ballistic resistance of armour against blast loads by using the multi-layered plates rather than single (plates of equal or lower mass) needs to be investigated. This research work is entirely new and will help to understand the response of multi-layered armours under localized blast loading.

Chapter 3

3 Material tests

High-strength low-alloy steels are a group of low-carbon steels that utilize small amounts of alloying elements to attain higher yield strengths in the as-rolled or normalized condition. These steels have higher strength than as-rolled carbon steels and are usually 20 to 30% lighter than carbon steel with the same strength. Their high yield strength can be obtained at lower carbon content levels. The weld-ability of many HSLA steels is comparable to or better than that of mild steel [103]. That is why the HSLA steels are used in a wide variety of applications. They are commonly used in cars, trucks, cranes, bridges, roller coasters and for high strength applications. Their properties can be tailored to specific applications by the combination of composition and structures obtained during processing. These steels have fine grain size microstructure due to micro alloying of Vanadium, Niobium and Titanium. The yield strength usually varies with grain size according to the Hall-Petch equation, given in Equation 3-1.

$$\boldsymbol{\sigma_y = \sigma_o + \frac{K_y}{\sqrt{d}}} \qquad 3\text{-}1$$

Where σ_o and K_y are constants for a particular material and d is the average grain diameter. Fine grains have larger grain boundary areas that impede dislocation motion.

Two different grades of HSLA, Domex 550 MC and Domex 700 MC (products of SAAB) were considered in the present study. Both grades are hot rolled, cold formed steel, produced by a thermo-mechanical treatment process [104] and meet the demands for steel S550MC and S700MC in EN 10149-2 [104]. The chemical compositions of Domex 550MC and Domex 700MC are listed in Table 3-1 and Table 3-2 respectively.

Table 3-1: Chemical composition of Domex 550MC steel [104]

Elements	**Wt. % age**	**Elements**	**Wt. % age**	**Elements**	**Wt. % age**
Carbon	0.12	Aluminium	0.015	Sulphur	0.010
Silicon	0.10	Vanadium	0.20	Phosphorus	0.025
Manganese	1.80	Niobium	0.09		
Iron	97	Titanium	0.15		

Table 3-2: Chemical composition of Domex 700 MC steel [104]

Elements	Wt. % age	Elements	Wt. % age	Elements	Wt. % age
Carbon	0.12	Aluminium	0.015	Sulphur	0.010
Silicon	0.10	Vanadium	0.20	Phosphorus	0.025
Manganese	2.10	Niobium	0.090		
Iron	97	Titanium	0.15		

3.1 Mechanical testing

The mechanical properties of the Domex 550 MC and Domex 700MC steels, namely yield strength and ultimate tensile strength, were determined according to ASTM standards [105]. The uniaxial tension test was used to obtain basic mechanical properties of Domex 550MC and Domex 700MC steel. Tensile tests were performed at different strain rates on dog-bone tensile test specimens at room temperature. As the flow stress is known to increase in ductile metals with increasing strain rates [106], it is important to consider the strain rate sensitivity of the material during the modelling of high stain rate events.

The Zwick Universal Testing machine (a test load capacity in tension/compression up to 200 KN) installed in the Centre for Materials Engineering at the University of Cape Town was used to determine the basic mechanical properties. A schematic diagram of the dog-bone tensile samples is shown in Figure 3-1 and the sample specifications are indicated in Table 3-3. Applied load and cross head displacement were measured during the tests.

The samples were cut from 2mm thick plates of Domex 550 MC and 3mm thick plates of Domex 700 MC in both the directions (rolling and transverse). The samples were tested at four different cross-head speeds varying from 1mm/min up to 150mm/min. A gauge length of 50mm was used for both materials. Three samples were tested at each cross-head speed. The mechanical properties of Domex 550 MC along the rolling directions are given in Table 3-4 and mechanical properties of Domex 700MC in both the directions (rolling and transverse) are given in Table 3-5 and Table 3-6 respectively. The material has similar mechanical properties in both directions.

Hardness tests were performed on samples prepared for metallographic study. The hardness of 2mm thick plates is greater than 6mm thick plates. The average hardness of Domex 550MC was 230 ± 10 HV and Domex 700MC was 320 ± 10 HV for plate thicknesses from 2mm to 6mm.

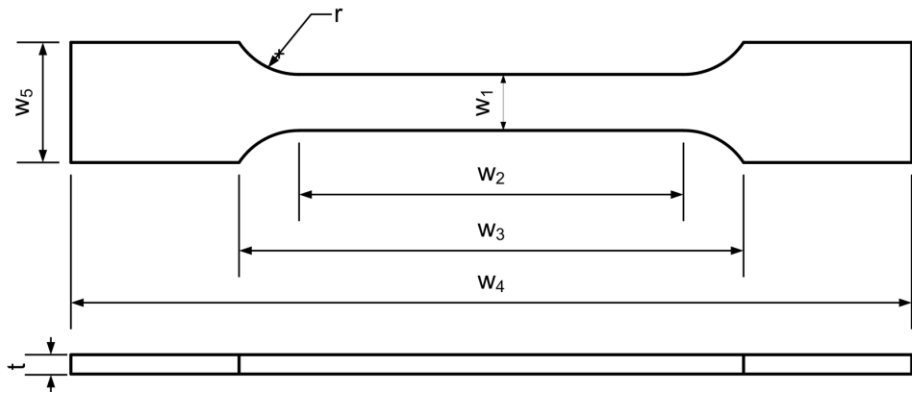

Figure 3-1: Schematic diagram of the dog-bone tensile samples

Table 3-3: Specification of tensile samples

Materials	W1 (mm)	W2 (mm)	W3 (mm)	W4 (mm)	W5 (mm)	r (mm)	t (mm)
Domex 550MC	12.5±0.01	75±0.01	100±0.01	200±0.01	25±0.01	20±0.01	2±0.01
Domex 700MC	12.5±0.01	75±0.01	100±0.01	200±0.01	25±0.01	20±0.01	3±0.01

The engineering stress-strain curves were constructed by using data obtained from the continuous load-elongation measurements during testing. The engineering stress and engineering strains were calculated using Equation 3-2 and Equation 3-3 respectively.

$$\boldsymbol{S = \frac{P}{A_0}} \qquad 3\text{-}2$$

$$\boldsymbol{e = \frac{\Delta L}{L_0} = \frac{L - L_0}{L_0}} \qquad 3\text{-}3$$

Where P is the axial load, A_0 is the original cross sectional area of the specimen and L and L_0 are final and original gauge length of the specimens.

The stress and the strain defined in Equations 3-2 and 3-3 are based on the original dimensions of the cross-sectional area of the test samples. These dimensions change

continuously during a test, meaning that the engineering stress-strain curves do not give the true behaviour of the materials. The true stress and true strain were calculated by using Equations 3-4 and 3-5. The stress strain curves were constructed by using the data up to the maximum load.

$$\boldsymbol{\varepsilon = L_n(1 + e)} \qquad 3\text{-}4$$

$$\boldsymbol{\sigma = s(1 + e)} \qquad 3\text{-}5$$

The engineering stress–strain curves of Domex 550MC and Domex 700MC at various strain rates are given in Figure 3-2 and Figure 3-4 and true stress–true strain curves of Domex 550 is given in Figure 3-3. The true stress verses plastic strain curves of Domex 700 MC is depicted in Figure 3-5. True stress and true strain curves are utilized for the determination of Johnson-Cook parameters. These parameters were used in simulation and designing of the blast experiments.

Table 3-4: Mechanical properties of Domex 550MC

Sample No.	Strain rate/second	Yield Strength (MPa)	Mean Average Yield Strength (MPa)	U.T.S (MPa)	Mean Average U.T.S (MPa)	Elongation (%)
Domex-A-001	4.16×10^{-4}	540		610		20.24
Domex-B-001	4.16×10^{-4}	540	533 ± 1	605	605 ± 1	20
Domex-C-001	4.16×10^{-4}	520		600		20.4
Domex-D-150	6.25×10^{-2}	560		630		19
Domex-E-150	6.25×10^{-2}	570	566 ± 1	640	633 ± 1	19.10
Domex-F-150	6.25×10^{-2}	570		630		18.6

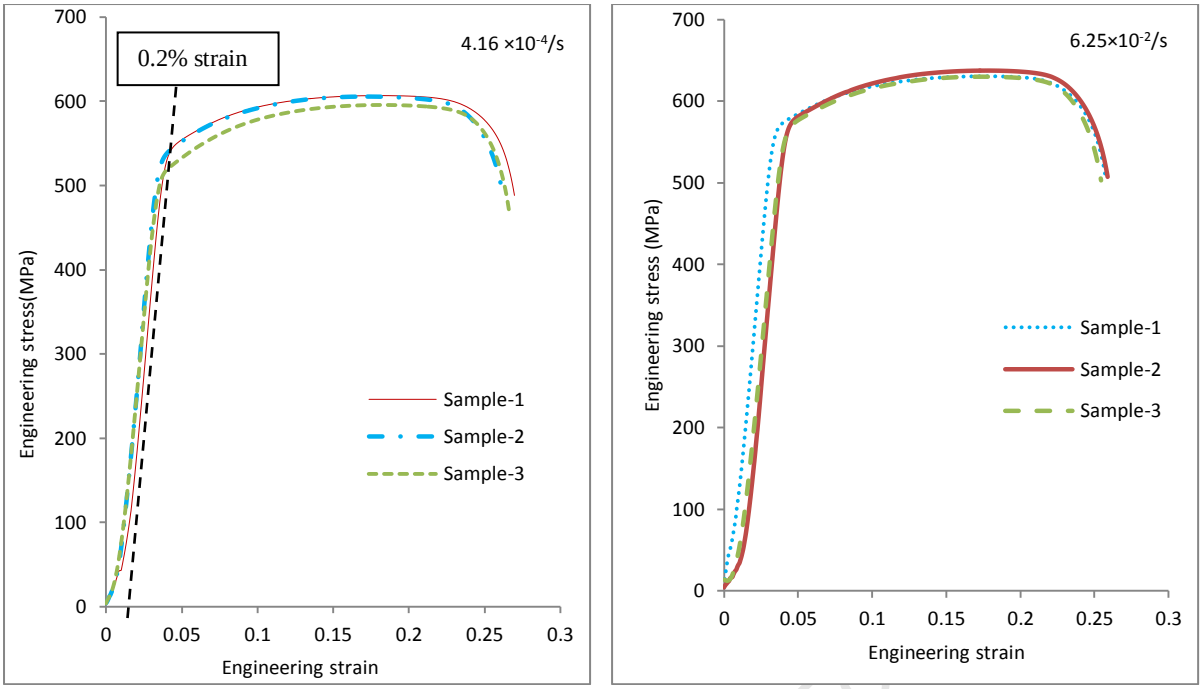

Figure 3-2: Engineering stress versus engineering strain curves of Domex 550MC at various strain rates

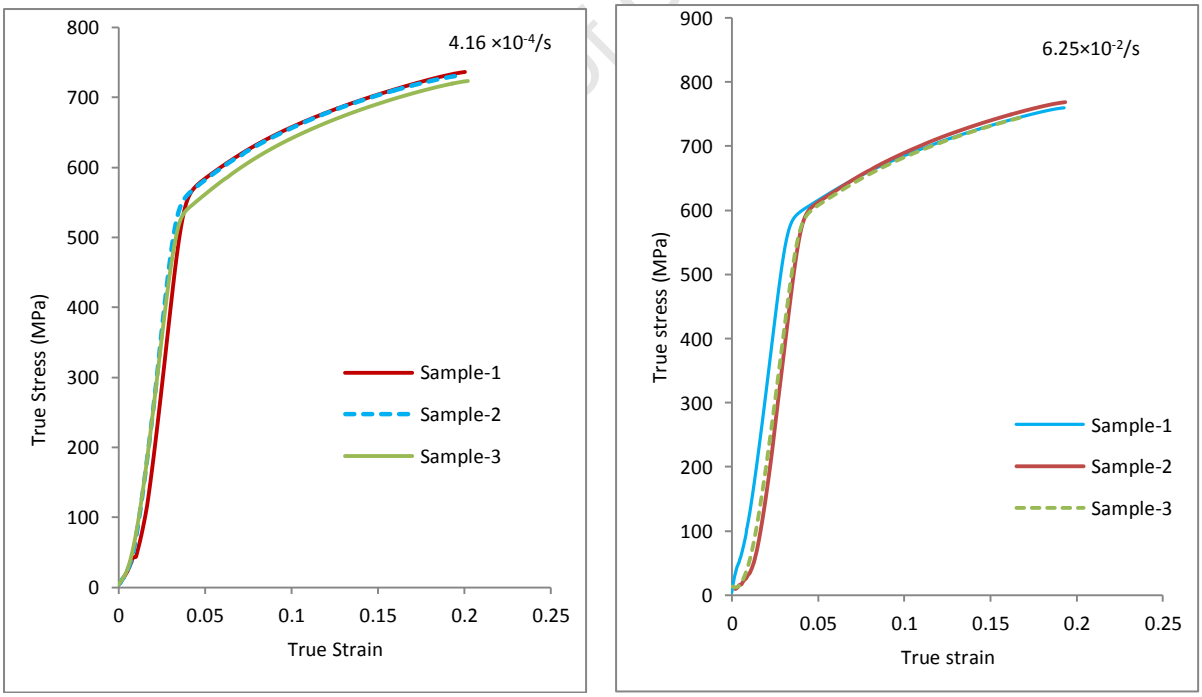

Figure 3-3: True stress versus true strain curves of Domex 550MC at various strain rates

Table 3-5: Mechanical properties of Domex 700MC (Rolling Direction)

Sample No.	Strain rate/s	Yield Strength (True) (MPa)	Mean Average Yield Strength (MPa)	U.T.S (MPa)	Mean Average U.T.S (MPa)	Elongation %
A-001-RD	4.16×10^{-4}	790	793±1	1000	1000	22
B-001-RD	4.16×10^{-4}	790		1000		21
C-001-RD	4.16×10^{-4}	800		1000		20.4
D-050-RD	2.083×10^{-2}	770	790±1	975	985	21
E-050-RD	2.083×10^{-2}	800		990		20.2
F-050-RD	2.083×10^{-2}	800		990		20
G-100-RD	4.166×10^{-2}	800	787±1	990	980	20.4
H-100-RD	4.166×10^{-2}	800		990		20
I-100-RD	4.166×10^{-2}	760		960		20.6
J-150-RD	6.25×10^{-2}	800	800±1	1000	1000	19
K-150-RD	6.25×10^{-2}	800		1000		20
L-150-RD	6.25×10^{-2}	800		1000		20

Table 3-6: Mechanical properties of Domex 700MC (Transverse Direction)

Sample No	Strain rate/s	Yield Strength (True) (MPa)	Mean Average Yield Strength (MPa)	U.T.S (MPa)	Mean Average U.T.S (MPa)	Elongation %
A-001-TD	4.16×10^{-4}	800	800.3±1	1010	1023	20
B-001-TD	4.16×10^{-4}	800		1060		21.6
C-001-TD	4.16×10^{-4}	810		1000		20
D-050-TD	2.083×10^{-2}	820	813±1	1000	987	21.2
E-050-TD	2.083×10^{-2}	810		960		21.4
F-050-TD	2.083×10^{-2}	810		1000		20.8
G-100-TD	4.166×10^{-2}	800	787±1	990	980	20.8
H-100-TD	4.166×10^{-2}	800		990		20.8
I-100-TD	4.166×10^{-2}	760		960		20
J-150-TD	6.25×10^{-2}	800	800±1	1000	1000	21.4
K-150-TD	6.25×10^{-2}	800		1000		21
L-150-TD	6.25×10^{-2}	800		1000		21.2

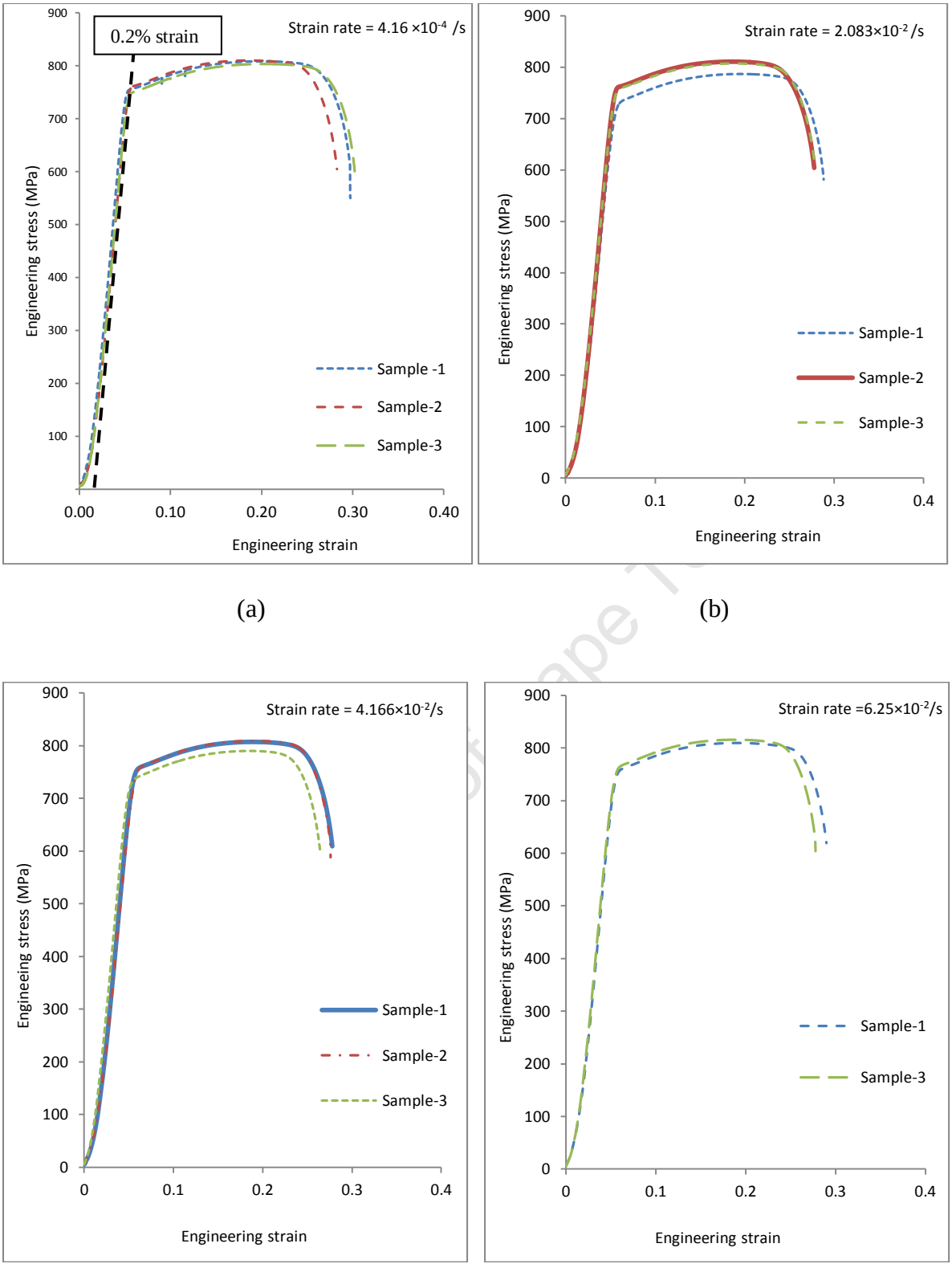

Figure 3-4: Engineering stress versus engineering strain curves of Domex 700MC at various strain rates along the rolling direction

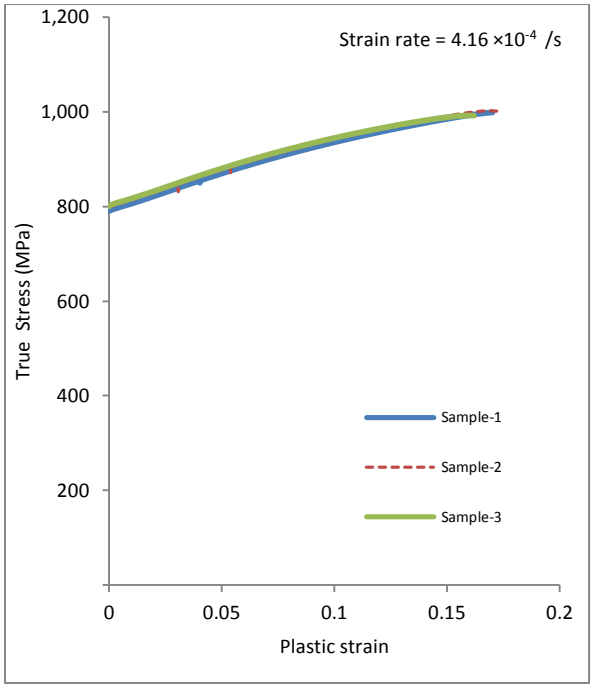

(a)

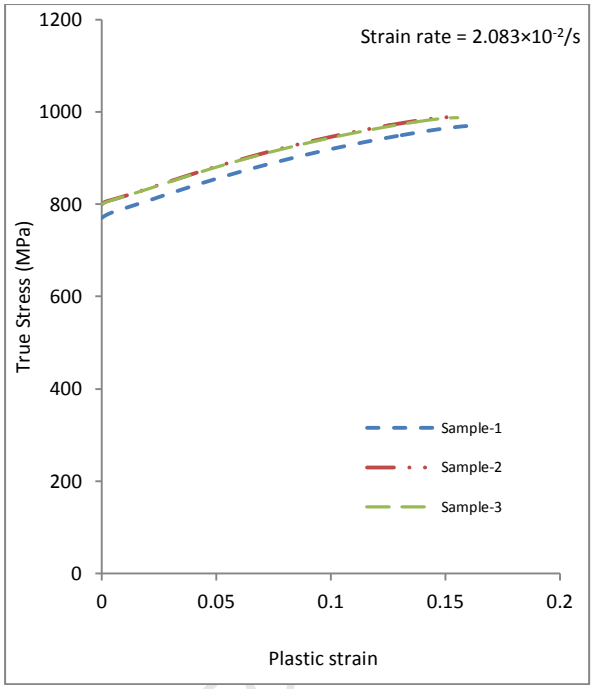

(b)

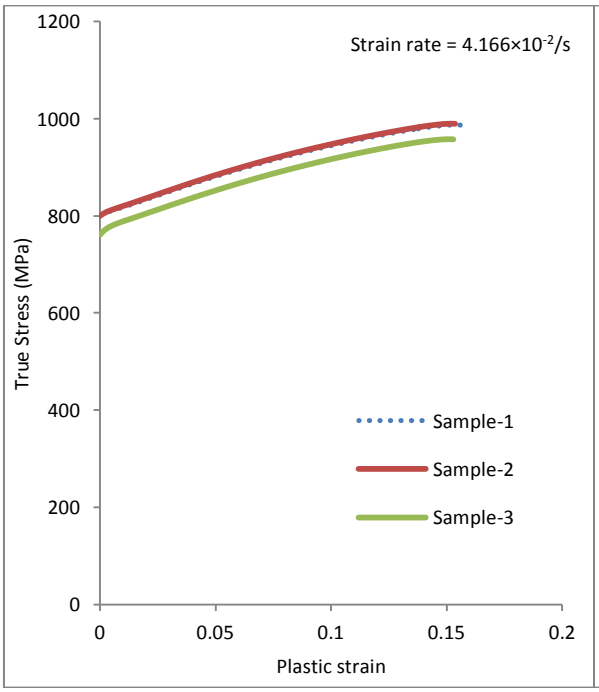

(d)

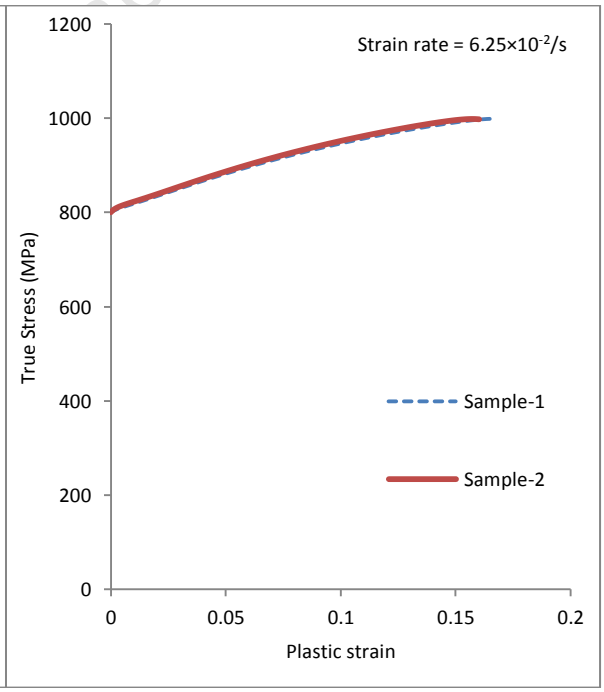

(c)

Figure 3-5: True stress versus true plastic strain curves of Domex 700MC at various strain rates along the rolling direction.

3.2 Fracture analysis of tensile samples

3.2.1 Influence of strain rate on failure of tensile specimens

Fracture under uniaxial tensile loading conditions should produce the formation of equiaxed dimples of different sizes depending on the strain rate. The cross sectional view of fractured surface of tensile sample tested at strain rate of 4.16 $\times 10^{-4}$/s is shown in Figure 3-6. The fractured surfaces of the tensile samples at different strain rates have a gray and fibrous appearance as shown in Figure 3-6a and b.

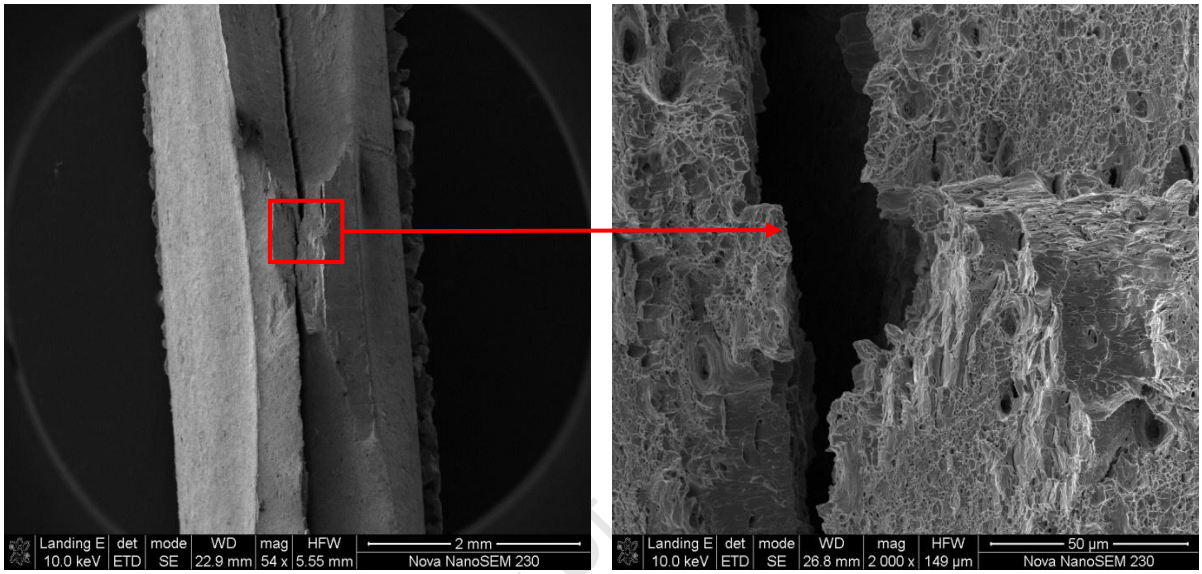

(a) Sectioned view of fractured tensile sample (b) Fractograph of tensile sample

Figure 3-6: Showing, (a) cross-sectional view and (b) fractograph of tensile samples

Fractographs of tensile samples at the different strain rates (4.16×10^{-4} to 6.25×10^{-2} s^{-1}) are given in Figure 3-7 a, b, c and d. The fractographs are showing equiaxed dimples of various sizes and quantities at different strain rates, as expected. Features of the dimple morphology were examined, in particular the distribution and quantity. The tensile samples obtained at ($4.16\times10^{-4}s^{-1}$) strain rates indicate the larger amounts of micro-voids and lower circular void diameters than at high strain rates ($6.25\times10^{-2}s^{-1}$).

The fractographic features of tensile samples tested at four different quasi-static strain rates will be used to compare with the blast tested fractured surfaces of plates at different charge masses in chapter 7.

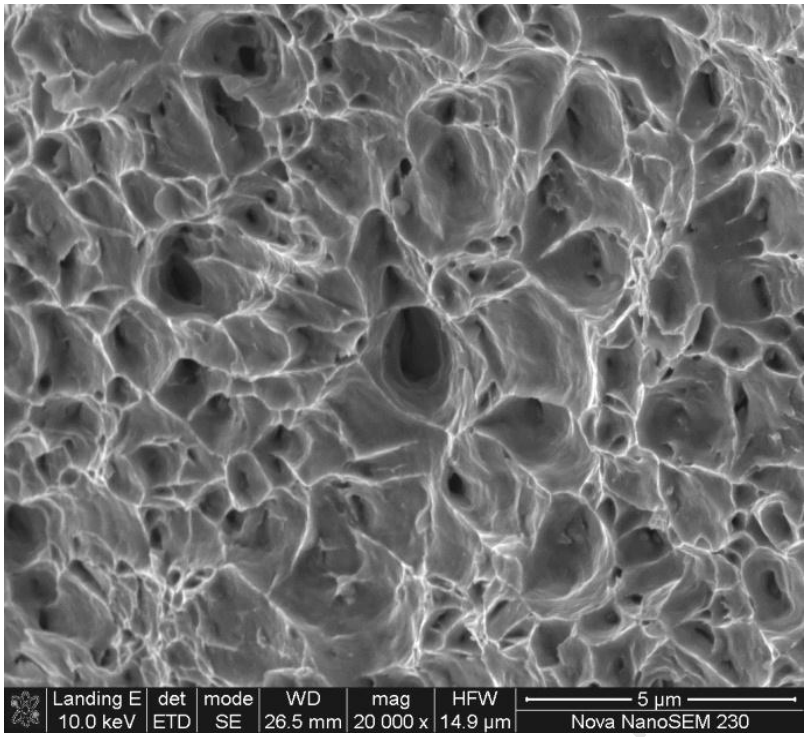

(a) 4.16×10^{-4} s^{-1}

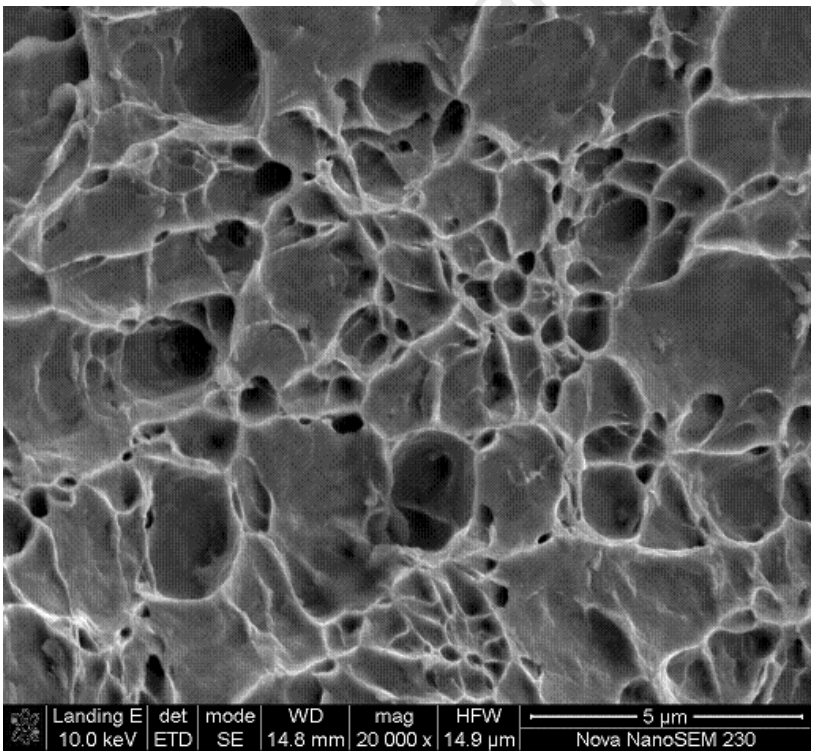

(b) $2.083 \times 10^{-2} s^{-1}$

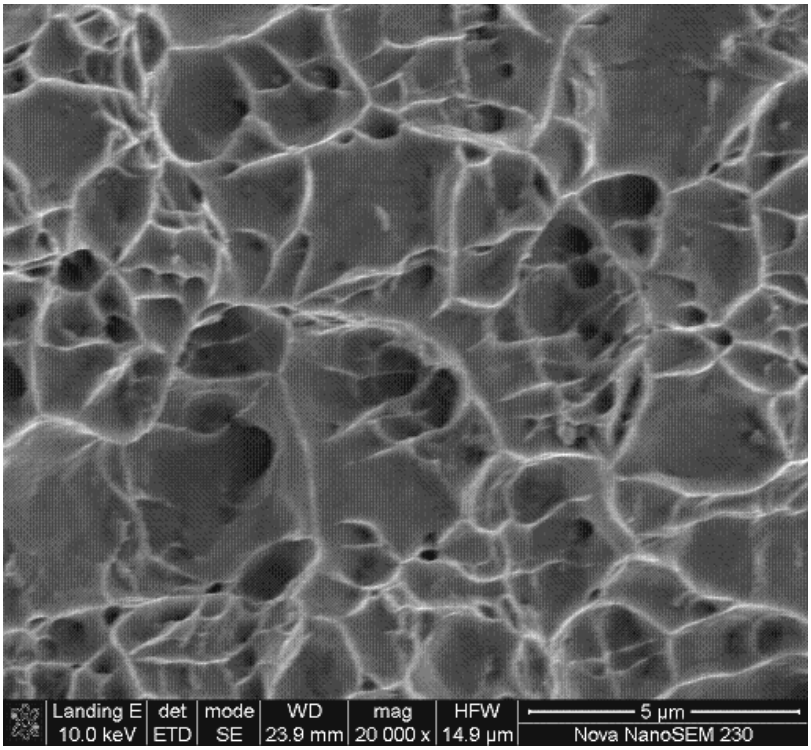

(c) 4.16 $\times 10^{-4}$ s^{-1}

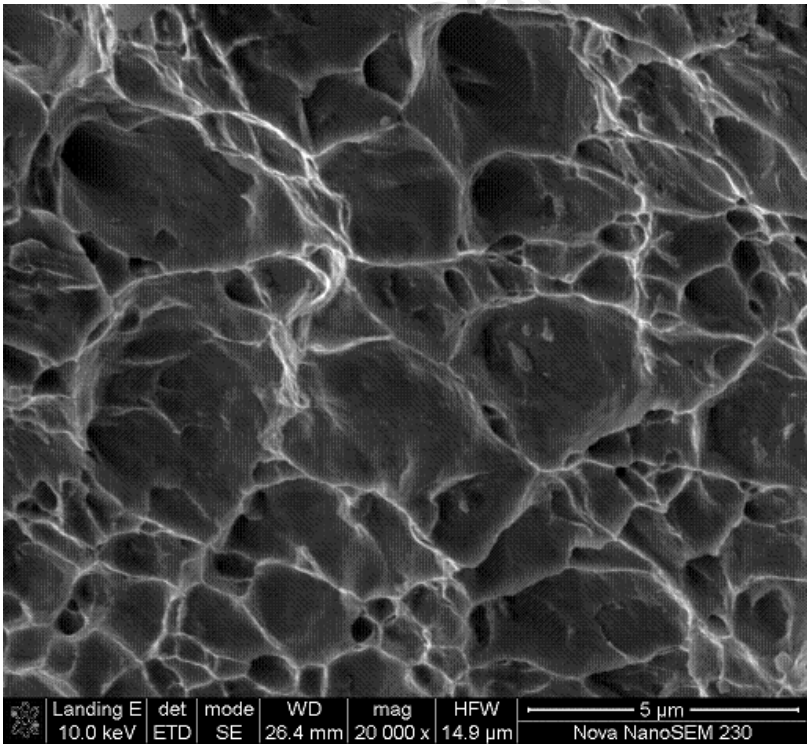

(d) $2.083 \times 10^{-2} s^{-1}$

Figure 3-7: Fractographs of tensile samples of Domex 700 MC steel at strain rates of (a) 4.16 $\times 10^{-4}$ s^{-1}, (b) 2.083×10^{-2} s^{-1}, (c) 4.16 $\times 10^{-4}$ s^{-1}, (d) 2.083×10^{-2} s^{-1} , showing equiaxed micro-voids of various sizes.

Chapter 4

4 Design of experiments

4.1 Constitutive relations

Deformation behaviour of metals over a wide range of strain rates and temperatures is important in metal forming, high-speed machining, high-velocity impact, penetration mechanics, explosive-metal interaction and other similar dynamic conditions. Mechanical properties of metals such as yield stress, ductility and strength are strongly dependent on applied strain-rate loadings and working temperatures. The characterization of the strain rate, temperature and work hardening dependence of mechanical behaviour of materials have attracted considerable attention for more than five decades [108]. There are different constitutive relations available in the literature used to model the mechanical response of structures subjected to blast loading and high velocity impact. An ideal plasticity model for metals should be able to describe the material properties such as strain-rate dependence, temperature dependence, strain and strain-rate history dependence, work hardening or strain-hardening behaviour (both isotropic and anisotropic hardening). Great progress has been made both experimentally and analytically and several constitutive models have been proposed based on experimental observations by von Karman [109] and Taylor [110].

Selection of a suitable constitutive relation that can consider various parameters like the stress strain behaviour of materials at larger strains, high strain rates, work hardening, loading history and temperature softening effects is very complex. A complete description that includes all these phenomena is however difficult to obtain from single model, as the model becomes more complex by increasing the number of parameters. The constitutive models vary from being purely empirical to highly theoretical. The empirical models are based on available experimental observations while the theoretical models are based on the microscopic nature of the material. In the current study, Cowper-Symonds and Johnson-Cook models were used for designing the blast loading experiments. The detail of these two models is given here and other widely used constitutive models like, Zerilli-Armstrong model, Bodner-Partom model, and Khan-Huang model and Zhao model are discussed in “Appendix D”.

4.1.1 Cowper-Symonds

Cowper-Symonds [111] suggested a strain rate dependent formulation for the numerical analysis of cantilever beams subjected to impact loading. The model describes strain rate sensitivity of metallic alloys to strain rate. The model was formulated by gathering test data of the dynamic lower yield stress of various materials at different strain rates. The relation between the dynamic stress σ and the strain rate of a particular material is given in Equation 4-1

$$\frac{\boldsymbol{\sigma}}{\boldsymbol{\sigma_0}} = \mathbf{1} + \left(\frac{\mathring{\boldsymbol{\varepsilon}}}{\mathbf{D}}\right)^{\frac{\mathbf{1}}{\mathbf{q}}} \qquad \text{4-1}$$

Where values for parameters D and q are called Cowper Symonds strain rate constants for the particular material, σ_o is the static yield stress and σ is the dynamic stress at the given strain rate ($\mathring{\varepsilon}$)

The value of constants D and q for annealed mild steel were suggested by Manjoine [112] as 40.4 s^{-1} and 5 respectively. These constants were derived from best curve fit of stress-strain data at strain rate up-to 100 s^{-1}. Recently Marais [113] and Abramowicz and Jones [114] published values of constants D and q for mild steel as 844 s^{-1}, 2.207 and 802 s^{-1}, 3.585 respectively. The Cowper-Symonds model does not consider temperature effects, it only accounts for the effects of strain rate and the strain hardening. Masui et al. [115] reported the effect of temperature on equivalent flow stress and on Young's modulus during the hot rolling process as indicated in Equations 4-2 and 4-3. In this model Young's modulus (E) decreases linearly for all T > 0, however the flow stress in unaffected for all T < 200˚C. This model was implemented successfully by Langdon et al.[116] and Chung Kim Yuen and Nurick [117] along with the Cowper-Symonds model.

$$\sigma = \begin{cases} \boldsymbol{\sigma_o} & \textbf{for } \mathbf{T} \leq \mathbf{200^{\circ}C} \\ \boldsymbol{\sigma_o}[\mathbf{1} - \mathbf{0.00178}(\boldsymbol{T} - \mathbf{200})] & \textbf{for } \mathbf{200^{\circ}C} < \boldsymbol{T} < \mathbf{700^{\circ}}\boldsymbol{C} \\ \boldsymbol{\sigma_o}[\mathbf{1} - \mathbf{0.133} - \mathbf{3.884} \times \mathbf{10^{-4}}(\boldsymbol{T} - \mathbf{700})] & \textbf{for } \mathbf{700^{\circ}C} \leq \mathbf{T} \leq \mathbf{1000^{\circ}C} \end{cases} \qquad \text{4-2}$$

$$E = \begin{cases} \mathbf{207} \times \mathbf{10^9} - (\mathbf{58.34} \times \mathbf{10^6})\boldsymbol{T} & \textbf{for } \mathbf{T} \leq \mathbf{600^{\circ}C} \\ \mathbf{3.1} \times \mathbf{10^5}(\mathbf{T} - \mathbf{1100})^2 + \mathbf{97} \times \mathbf{10^9} & \textbf{for } \mathbf{600^{\circ}C} < \boldsymbol{T} \leq \mathbf{1100^{\circ}}\boldsymbol{C} \end{cases} \qquad \text{4-3}$$

The Cowper-Symonds relation is an empirical equation which, nevertheless has proved to be valuable within a range of strain rates and is used extensively. It is not valid for a wide range of strains as the constants are determined for a specific strain value, as reported by Alves [118]. The constants determined at the yield strain are not suitable for high strains and large discrepancies can arise. An improvement to the Cowper-Symonds equation was proposed [118] to overcome this in the form of Equation 4-4.

$$\boldsymbol{\sigma_d} = \boldsymbol{\sigma_s} + \overline{\mathbf{m}}\dot{\boldsymbol{\varepsilon}}^{\overline{\mathbf{n}}} \qquad \text{4-4}$$

Where

$$\overline{\mathrm{m}} = \frac{\sigma}{\mathrm{C}^{\frac{1}{\mathrm{q}}}} \quad \text{and} \quad \overline{\mathrm{n}} = 1/\mathrm{q}$$

σ_d = dynamic stress, σ_s = static stress, C and q are constants. σ and $\dot{\varepsilon}$ are chosen freely from experimental data at a given strain and are kept constant. This modified equation can be used to calculate any stress by using constant $\overline{m}$ and $\overline{n}$. The strain hardening is strain rate independent i.e. an increase of strain rate shifts the entire curve up by the same amount for any strain.

4.1.2 Johnson-Cook (J-C) constitutive relation

Johnson and Cook [107] proposed an empirical model for materials subjected to large strains, high strain rates and high temperatures such as projectile impact. The model operates with variables that are available in most of the applicable computer codes. Due to its simplicity and the relative ease (in comparison to dislocation-mechanics-based models) of obtaining its constants, the Johnson-Cook material model has been very popular. The Johnson-Cook material model takes the form of a product of dependencies. The material behaviour is a function of the multiplicative effects of the strain, strain rate and temperature. There is no representation of thermal or strain rate history effects. The von Mises equivalent flow stress can be expressed as given in Equation 4-5[107].

$$\boldsymbol{\sigma} = [\boldsymbol{A} + \boldsymbol{B}\mathcal{E}^{\boldsymbol{n}}]\left[\mathbf{1} + \boldsymbol{C}\boldsymbol{\ell}\boldsymbol{n}\frac{\mathring{\varepsilon}}{\mathring{\boldsymbol{\varepsilon}}_{\mathbf{0}}}\right][\mathbf{1} - \boldsymbol{T}^{*\boldsymbol{m}}] \qquad 4\text{-}5$$

Where

$$\boldsymbol{T}^{*} = \frac{\mathbf{T} - \boldsymbol{T}_{\boldsymbol{ref}}}{\boldsymbol{T}_{\boldsymbol{melt}} - \boldsymbol{T}_{\boldsymbol{ref}}} \qquad 4\text{-}6$$

T^* is the homologous temperature, T is the absolute temperature, ε is the equivalent plastic strain, $\mathring{\varepsilon}$ is the equivalent plastic strain rate, ε_0 is the reference strain rate (often taken as 1 s^{-1}). T_{ref} is the reference temperature (taken as room temperature) and T_{melt} is the melting temperature of the material. The homologous temperature is zero for temperatures less than the reference temperature and equal to one for temperatures above the melting temperature. For temperatures above the melting temperature the flow stress is zero and there is no resistance to flow. The model operates with five material constants *A*, *B*, *C*, *n* and *m*. The first bracket in the model represents the strain hardening, the second term describes the strain-rate sensitivity and the third bracket represents the temperature softening in the Equation 4-5 and Equation 4-6 for obtaining the homologous temperature.

It was shown by Liang and Khan [108] that the Johnson-Cook [107] material model is appropriate for most work hardening metals. It fails to predict sequential loading experiments such as strain rate 'jump' tests. It was also shown to be inappropriate for metals whose work hardening rate, $d\sigma/d\epsilon$ decreases with increasing strain rate (such as Tantalum). The multiplicative form of the temperature dependence was deemed to be appropriate for most metals [108]. It has been observed that many ductile metals exhibit a sudden increase in strength at strain rates above a transition point in the range 10^3 s^{-1} - 10^4 s^{-1}[108]. The effect of strain rate on material strength is not a linear function of the natural log as the Johnson-Cook material model suggests. It is for this reason that some revised versions of the Johnson-Cook model having been presented. A slightly modified form of the Johnson-Cook equation was presented by Holmquist and Johnson [119] in order to better represent the effect of strain rate and the Equation is 4-7 is modified form.

$$\boldsymbol{\sigma} = [\boldsymbol{A} + \boldsymbol{B}\mathcal{E}^{\boldsymbol{n}}]\ \left(\frac{\mathring{\boldsymbol{\varepsilon}}}{\mathring{\boldsymbol{\varepsilon}}_{\mathbf{0}}}\right)^{\boldsymbol{C}}[\mathbf{1} - \boldsymbol{T}^{*\boldsymbol{m}}] \qquad 4\text{-}7$$

Rule and Jones [120] also presented a revised version which essentially includes additional coefficients to more accurately represent the effects of strain rate. This revision gives more accurate results for high strain rate applications such as the Taylor test. The form of the equation is given in Equation 4-8.

$$\boldsymbol{\sigma} = [\boldsymbol{A} + \boldsymbol{B}\mathcal{E}^{\boldsymbol{n}}]\left[\mathbf{1} + \boldsymbol{C}\boldsymbol{\ell}\boldsymbol{n}\frac{\dot{\varepsilon}}{\dot{\varepsilon}_0} + \boldsymbol{C}\mathbf{1}\left(\frac{\mathbf{1}}{\boldsymbol{C}\mathbf{2}-\boldsymbol{\ell}\boldsymbol{n}\frac{\dot{\varepsilon}}{\dot{\varepsilon}_0}} - \frac{\mathbf{1}}{\boldsymbol{C}\mathbf{2}}\right)\right][\mathbf{1} - \boldsymbol{T}^{*\boldsymbol{m}}] \qquad 4\text{-}8$$

Where C_1 and C_2 are additional material coefficients

4.1.3 Determination of J-C parameters

The J-C parameters for the Domex 550MC and Domex 700MC were determined from the quasi-static tensile data, given in Chapter 3. An offset of 0.2% strain is plotted on the engineering stress-strain diagrams of Domex 550 MC (Figure 3-2) and Domex 700 MC (Figure 3-4a) at strain rate 4.16×10^{-4}/s for the determination of constant "A". The yield stress corresponding to 0.2% offset strain was considered as constant "A" for both the materials. The strain hardening constants "B" and "n" of Domex 550 MC and Domex 700 MC were determined from graphs of log (plastic stress) versus log (plastic strain) in the plastic region of the quasi-static data. The graph of log (plastic stress) versus log (plastic strain) of both the steel at strain rate of 4.16×10^{-4} /s are shown in Figure 4-1a and b respectively. The strain rate sensitivity parameter "C" was taken from Autodyn library [97] used for steel AISI 4340 and the value of m "1" was chosen. The J-C parameters determined directly from the data are summarized in Table 4-1.

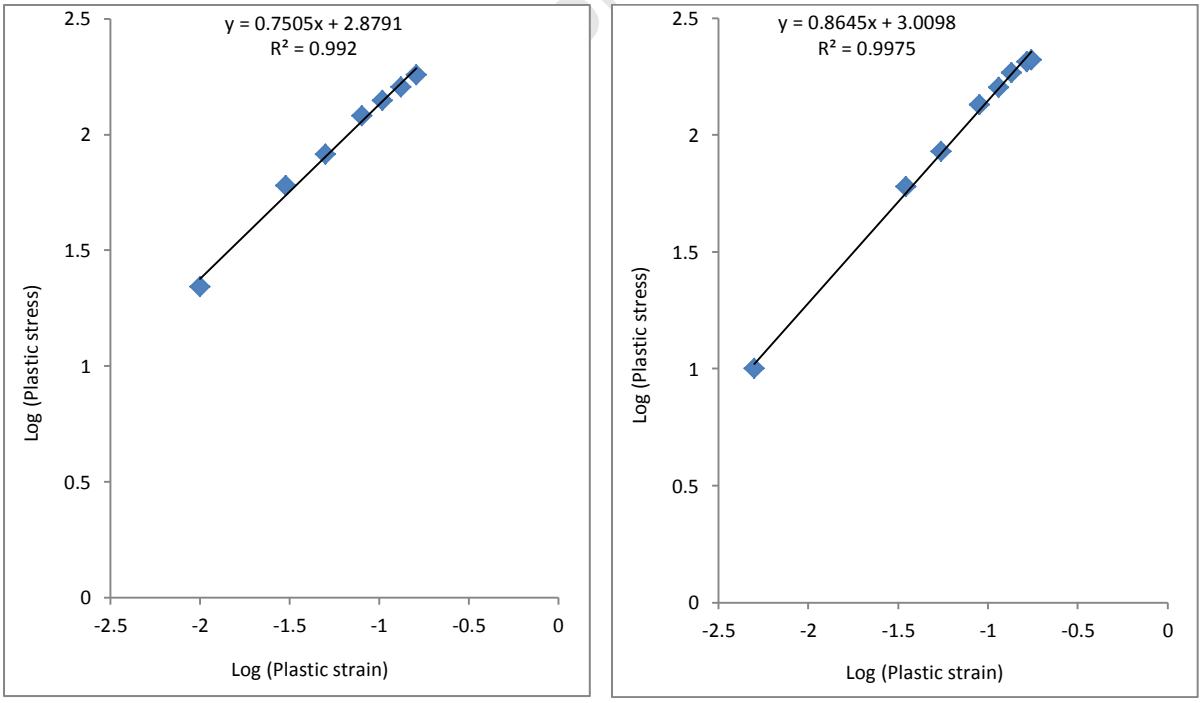

(a) Constant "B" and "n" for Domex 550MC (b) Constant "B" and "n" for Domex700MC

Figure 4-1: Plots of log (true plastic stress) versus log (true plastic strain) for the determination of Johnson-Cook constants "B" and "n".

4.2 Finite Element Modelling (FEM)

Simulations of blast loading of Domex 550MC and Domex 700MC plates were performed using the finite element code ABAQUS/Explicit [75] before starting the experimental program. ABAQUS/Explicit offers a finite element capability that provides non linear dynamic analysis for a variety of solid and structural elements using an explicit time integration scheme. The explicit procedure uses the central difference operator to integrate through time by using small time increments with the use of lumped element mass matrices.

The purpose of this simulation was to determine parameters such as charge mass ranges and plate thickness for the experiments. To reduce computational cost, axi-symmetric modelling was applied for the simulation of localized blast loading of single plates. The plate was discretized using reduced integration continuum elements with hourglass control. The size of the element was 200 μm over the charge radius and 400 μm for the remaining plate area. Both the clamps considered as rigid bodies and hence described as analytical rigid surfaces. A frictional contact was prescribed between the respective upper and lower plate faces and corresponding clamp surfaces. The friction coefficient for the clamps and surfaces was assumed to be $\mu = 0.9$ during the analysis and the friction coefficient between the surfaces of the layered plates was assumed to be $\mu = 0.3$. The variation in quasi-static material properties with strain was defined in a piecewise manner. The Cowper-Symonds and Johnson-Cook constitutive relations were used for modeling the blast loading experiments. The material input parameters used for simulating the Domex 550 MC and Domex 700 MC steel plates are given in Table 4-1. The values of D and q for Domex 550 MC and Domex 700MC were taken from references [112] and [133] respectively.

Table 4-1: Input data used for ABAQUS simulations

Description	Domex 550MC	Domex 700MC
Plate radius (mm)	100, 150	100
Plate thickness (mm)	4 and 6	4, 6 and 8
Density (Kg/m^3)	7850	7850
$\dot{\varepsilon_0}$ (per second) = (D)	40.4	3110
q	5	2.23
Poisson's Ratio (ν)	0.33	0.33
Young's Modulus (E)	210 GPa	210 GPa
Failure strain (%)	20	26
Specific heat (J/kg-K)	452	452
Loading time (μs)	2.2 (a = 16.5mm)	2.66 (a=20mm)
A (MPa)	560	790
B (MPa)	757	1023
n	0.75	0.8645
C	0.014	0.014
m	1	1

4.2.1 Modelling the blast

The response of circular plates subjected to localized blast loading has been studied theoretically and numerically using ABAQUS/Explicit [45;46;60;70;128;129]. Balden and Nurick[76] modeled the localized explosive blast on a circular plate using the hydro-dynamic code AUTODYN 2D. Hydro-dynamic codes are better suited to model the explosive interaction with structures than general Finite Element codes because of its possibility to combine the use of Eulerian and Lagrangian mesh. The AUTODYN model consists of two Eulerian spaces, representing air and explosive, interacting with a Lagrangian mesh occupied by the deformable mild steel plate. The air media is assumed to behave as an ideal gas and hence only one equation of state is specified. The explosive behaviour was modelled using the Jones-Wilkins-Lee equation of state for PE4 explosive material as defined in the AUTODYN material library. The response of the mild steel plate was simulated using a shock equation of state and Johnson Cook strength model. The pressure on the mild steel plate was recorded along the plate radius. It was found that the maximum pressure at discrete points along the plate radius is consistent with Bimha [129] who assumed a similar blast pressure history profile.

The exact nature of pressure wave due the blast load is very complex. Grobbelaar and Nurick [130] used computational techniques to model the explosive by using the Jones-Wilkins-Lee equation of state to simulate the pressure wave. The detonation, subsequent expansion of the plastic explosive and interaction of the explosive with the structure was investigated. Four load/plate diameter ratios were considered and the trends predicted exhibited satisfactory correlation with the experimental results.

Bimha et al. [128;129] carried out numerical studies on the circular plates subjected to localized blast loading. Various ratios of charge to plate radius $\left(\frac{a}{R}\right)$ ranging from 0.15 to 0.6 with at various impulses were considered. For localised loading conditions, Bimha [129] approximated the blast load as a pressure load as function of radial distance from the centre of the explosive as shown in Equations 4-10. The pressure generated using uniform rectangular loading on the entire surface area can be estimated by the equation.

$$\mathbf{P} = \frac{\mathbf{I}}{\mathbf{A.t}} \qquad 4\text{-}9$$

Where I, is the blast impulse, A is the loaded area and t is the duration of the blast.

$$I = \tau \int_0^R P\,(r)\,dA \qquad 4\text{-}10$$

Equation 4-10 can be written as

$$\mathbf{I = \tau \int_0^a P_0\,dA + \tau \int_a^R P_0 e^{-k(r-a)}\,dA} \qquad 4\text{-}11$$

That becomes

$$\mathbf{I = \tau \int_0^a 2\pi r P_0 dr + \tau \int_a^R 2\pi r P_0 e^{-k(r-a)} dr} \qquad 4\text{-}12$$

Where dA =2πrdr in Equation 4-12

After integration

$$\mathbf{I = \pi \tau P_0 \left[a^2 + 2 \left\{ \left(\frac{a}{k} + \frac{1}{k^2} \right) - \left(\frac{R}{k} + \frac{1}{k^2} \right) e^{k(a-r)} \right\} \right]} \qquad 4\text{-}13$$

P_0 = constant for $r \leq a$ 4-14

And

$$\mathbf{P(r) = P_0 e^{-k(r-a)}} \quad \text{for} \quad a \leq r \leq R \qquad 4\text{-}15$$

If the explosive is spread all over the target plate then a= R and the result will be

$$\mathbf{I = PA\tau} \qquad 4\text{-}16$$

A= area = π a^2 and $I = \pi \tau P_0 a^2$

Where "I" is the impulse, "τ" is the loading time duration and "P(r)" is a pressure distribution function and "k" is exponential decay constant. The loading time duration "τ" can be calculated by the Equation 4-17

$$\mathbf{\tau = \frac{a}{v_b}} \qquad 4\text{-}17$$

V_b is the burn velocity of the explosive and "a" is the radius of the explosive material. It was assumed that the duration of loading is equal to the approximate explosive burn time. The imparted pressure is related to the impulse by the following equation

$$\mathbf{I = 2\pi \int_{t_0}^{t_{blast}} \int_{r_0}^{R} P(r,t) r.\,dr.\,dt} \qquad 4\text{-}18$$

$$\mathbf{P(r) = P_o} \quad \text{for} \quad \mathbf{0 \le r \le r_b} \quad \text{and} \quad \mathbf{0 \le t \le t_{blast}} \qquad 4\text{-}19$$

$$\mathbf{P(r) = P_0 e^{-K(r-rb)}} \qquad 4\text{-}20$$

For $r_b \le r \le r_p$ and $0 \le t \le t_{blast}$

Where I is the measured blast impulse, P(r,t) is the axi-symmetrical blast pressure as a function of radius (r) and time (t) and P_o : peak pressure, r : radial distance from explosive center; t : time; k : decay constant; t_{Blast} : duration of blast.

The method of calculating exponential decay constant was derived by Bimha [129] by using the experimental results of Radford [131] as given in Equation 4-21.

$$\mathbf{k = 130 - 261\left(\frac{a}{R}\right) + 948\left(\frac{a}{R}\right)^2} \qquad 4\text{-}21$$

The method is applicable for the following range

$$0.15 < \left(\frac{a}{R}\right) < 0.6$$

Various pressure pulse can be applied for the modelling the blast response. Farrow et al. [71] used both a triangular and a rectangular pressure pulse to predict plate deflections, deformation shapes, residual strains and dynamic yield stress of a circular plate subjected to uniformly distributed explosive loading using the ABAQUS/Explicit finite element code. The rectangular pulse gave results, which corresponded more favourably with the experiment compared to the triangular approximation because of either the difference in pressure peaks or the duration of applied load. In the current studies, the rectangular pressure pulse is used for modelling the localized blast loads.

The pressure profile is applied for duration equal to the burn time (τ) of the explosive PE4. The burn time was calculated as the charge radius divided by the detonation velocity of explosive. The charge radius 16.5mm and 20mm was selected for Domex 550MC and Domex 700MC plates respectively. The burn time 2.2 and 2.66 microseconds was calculated for diameters 33mm and 40mm by using 7500 ms^{-1} explosive burn velocity. The pressure load is applied using a FORTRAN coded VDLOAD user subroutine in ABAQUS/Explicit.

The pressure is assumed to be uniform from the centre of the plate to the edge of the explosive after which an exponential decay of the load is considered up to the plate radius as suggested by Bimha [129] and used pressure profile shown in Figure 4-2.

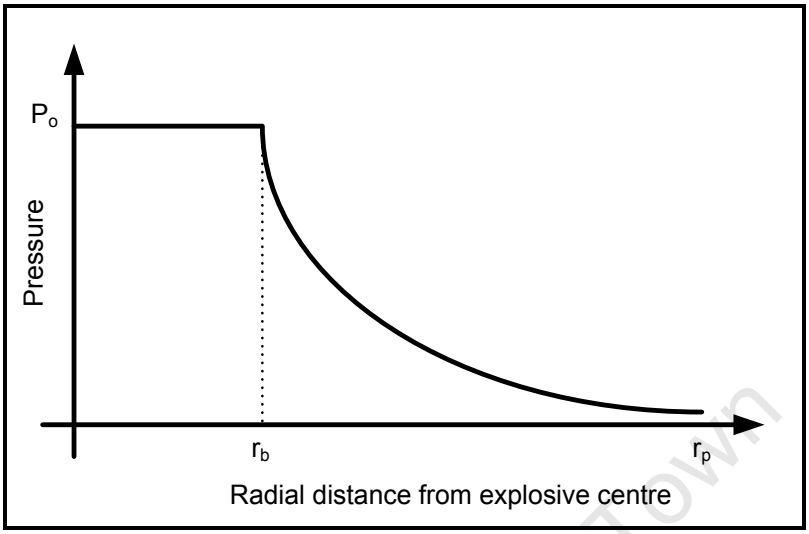

Figure 4-2 : Spatial distribution of idealized pressure loading used in FE simulations [129]

The sizes of the plates, charge diameter and the amount of the explosive needed for the series of experiments were approximated by using the simulation results. The effective mass of the explosive was calculated by using the Kennedy [132] method. According to Kennedy [132], the lateral edges of the explosive have to be subtracted from the total mass of explosive in order to estimate the mass of explosive that will drive a metal plate to its maximum velocity.

Table 4-2 is used to get suitable charge heights with respect to charge diameter that can give effective mass of the explosive. For simulations, two sizes of plates were considered, 200mm and 300mm in diameter and various thicknesses. The charge diameters of 20mm, 33mm, 40mm and 50mm were used in numerical simulations. Table 4-2 indicates the relationship between effective charge heights and the charge masses in regards to various charge diameters.

For the charge diameter of 20mm, the maximum effective charge height is 17mm. This corresponds to a charge mass of 8.7g. The further increase in mass will increase the height but not contribute effectively toward the impulse transfer to the plate due to side losses. This charge mass can give an impulse of 16 to 18 Ns that is insufficient for a test series.

Table 4-2: Effective charge mass and height with respective diameters

Charge diameter (mm)	20	25	30	33	35	40	45	50
Effective charge height (mm)	17.3	21.7	26.0	28.6	30.3	34.6	39.0	43.3
Charge height (mm)	Charge weights (g)							
16	8.2	12.8	18.4	22.3	25.1	32.8	41.5	51.2
17	***8.7***	13.6	19.6	23.7	26.7	34.8	44.1	54.4
18	9.2	14.4	20.7	25.1	28.2	36.9	46.7	57.6
21	10.8	16.8	24.2	29.3	32.9	43.0	54.4	67.2
22	11.3	***17.6***	25.3	30.7	34.5	45.1	57.0	70.4
23.0	11.8	18.4	26.5	32.1	36.1	47.1	59.6	***73.6***
25.0	12.8	20.0	28.8	34.9	39.2	51.2	64.8	80.0
26.0	13.3	20.8	***30.0***	36.2	40.8	53.3	67.4	83.2
27.0	13.8	21.6	31.1	37.6	42.3	55.3	70.0	86.4
29.0	14.9	23.2	33.4	***40.4***	45.5	59.4	***75.2***	92.8
30.0	15.4	24.0	34.6	41.8	***47.0***	61.4	77.8	96.0
31.0	15.9	24.8	35.7	43.2	48.6	63.5	80.3	99.2
34.0	17.4	27.2	39.2	47.4	53.3	***69.6***	88.1	108.8

4.3 Theoretical prediction

The Domex 550MC and Domex 700MC single plates of various thicknesses were considered for numerical analysis of experimental design. The estimated impulse values, charge diameters and plate sizes are given in Table 4-3. The ABAQUS/explicit input files used in simulations for both materials are given in “Appendix C”.

Table 4-3: Considered plate and charge diameters at impulses for simulations

Plate diameter (mm)	300	200
Charge diameter (mm)	(30, 50)mm	(20, 33)mm
Plate thickness (mm)	4, 6, 8	4, 6, 8
Impulse (Ns)	15, 30, 45, 60, 75, 90, 100 and 125	15, 30, 45, 60, 75, 90, 100 and 125

4.3.1 Simulation results of 4mm thick single plates (Domex 550 MC)

4.3.1.1 Single 4mm thick plates (R =100mm, a= 16.5mm)

The input parameters used to run the numerical model are given in Table 4-1. The finite element simulation results of 4mm thick single plates are given in Table 4-4. A graph of displacement versus impulse is given in Figure 4-3, whereas linear increase in midpoint displacement with increasing impulse was noted. No thinning was found at an impulse of 45Ns as indicated in Figure 4-4. Thinning in the plates along with the permanent plastic deformation occurred at an impulse of 60Ns and 75Ns as shown in Figure 4-5 and Figure 4-6 respectively. The plate was failed with a cap diameter of 40mm at an impulse of 90Ns as indicated in Figure 4-7.

The model was also run without considering the strain rate sensitivity of the material. In this case the 4mm thick single plates subjected to localized load diameter of 20mm and 33mm was failed at 30Ns with a cap diameter of 44mm and 50mm as shown in Figure 4-8 and Figure 4-9 respectively.

The simulations show that various levels of damage and failure could be achieved in the 4mm thick plates, in this configuration, for the impulse range achievable in the BISRU laboratory.

The finite element simulation results of the 4mm thick single of 200mm diameter subjected to explosive load diameter of 20mm are given in “Appendix E”.

Table 4-4: Midpoint displacement predictions from simulations of 4mm thick single plates subjected to localized blast loading (R = 100mm, a = 16.5mm)

Impulse (Ns)	Maximum midpoint displacement(mm)
15	10
20.3	14
22	15
30	21
35.3	25
42.1	29
45	31
54.1	38
60	42
75	50 (necking)
90	Capping failure

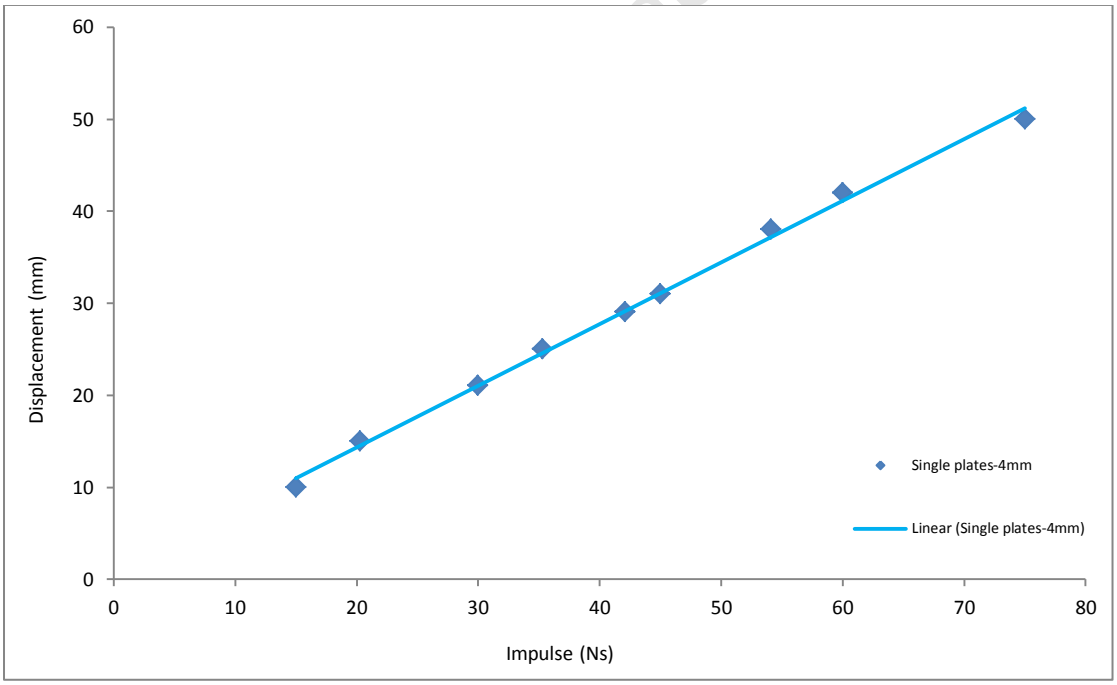

Figure 4-3: Graph of predicted midpoint displacement versus impulse of 4mm thick single plates (R=100, a=16.5mm)

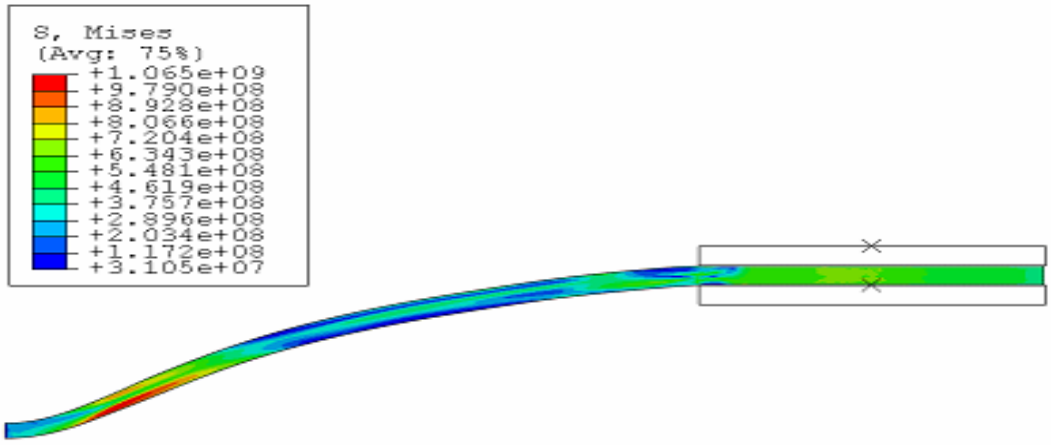

Figure 4-4: FE predictions of 4mm thick plate of Domex 550MC subjected to an impulse of 45Ns (R=100, a = 16.5mm)

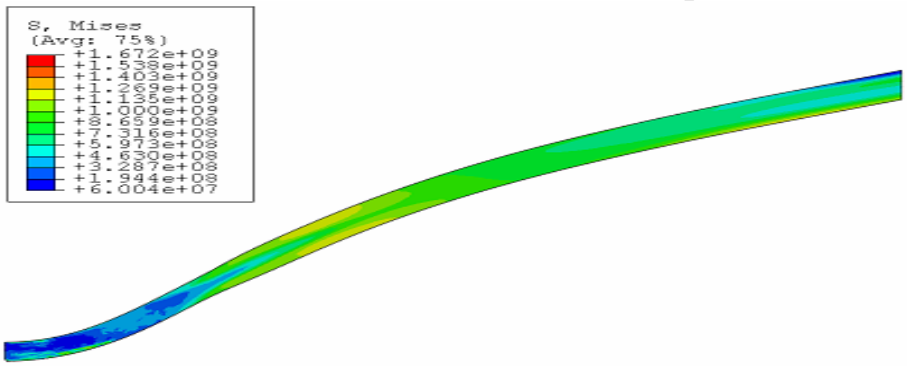

Figure 4-5: FE predictions of 4mm thick plate of Domex 550MC subjected to an impulse of 60Ns (R=100, a = 16.5mm)

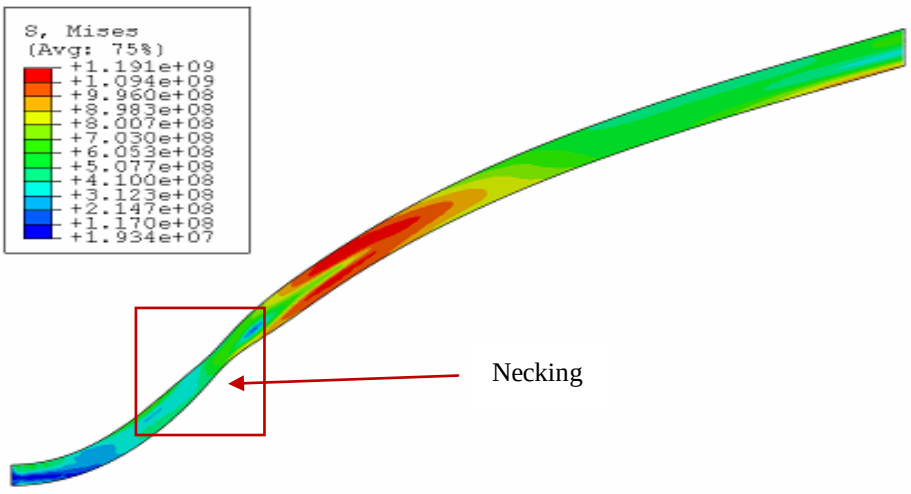

Figure 4-6: FE predictions of 4mm thick plate of Domex 550MC subjected to an impulse of 75Ns (R=100, a = 16.5mm)

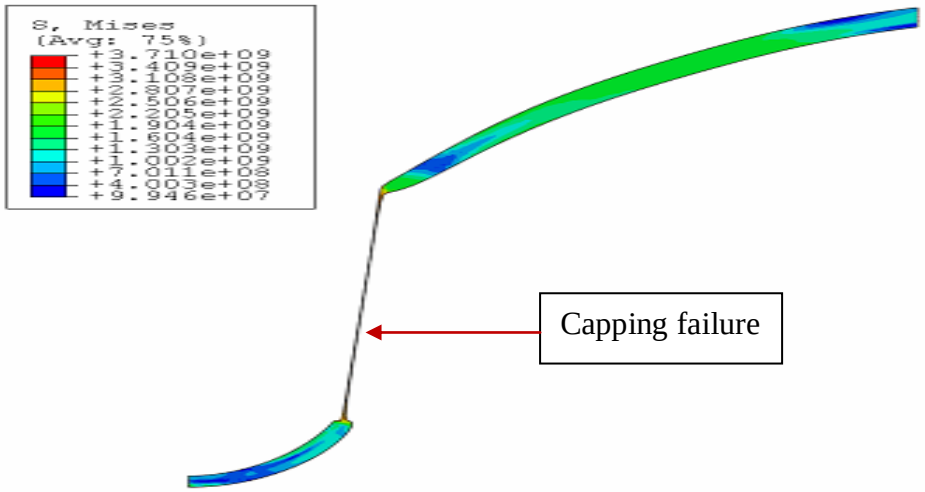

Figure 4-7: FE predictions of 4mm thick plate of Domex 550MC subjected to an impulse of 90Ns (R=100, a = 16.5mm)

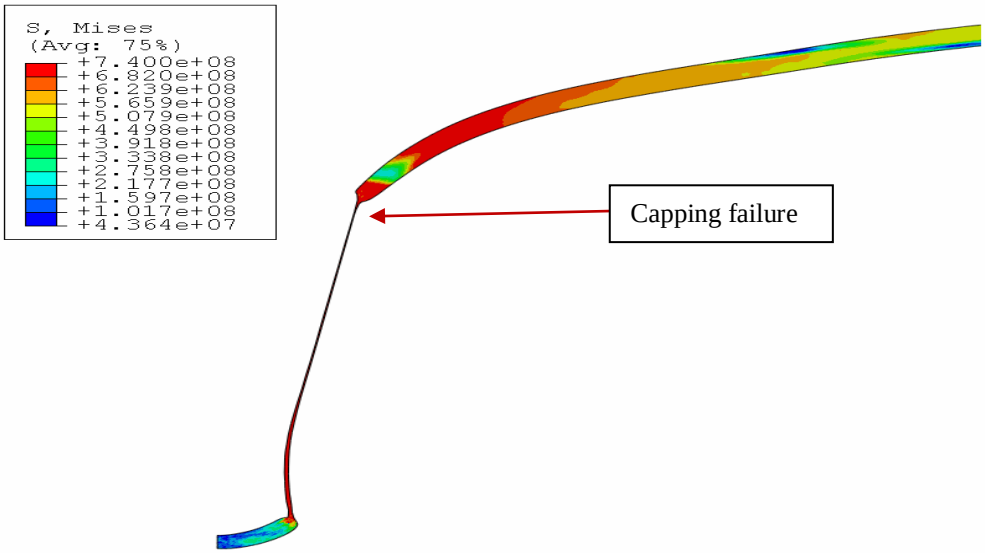

Figure 4-8: FE predictions of 4mm thick plate of Domex 550MC subjected to an impulse of 30Ns (a=10mm), without considering strain rate sensitivity

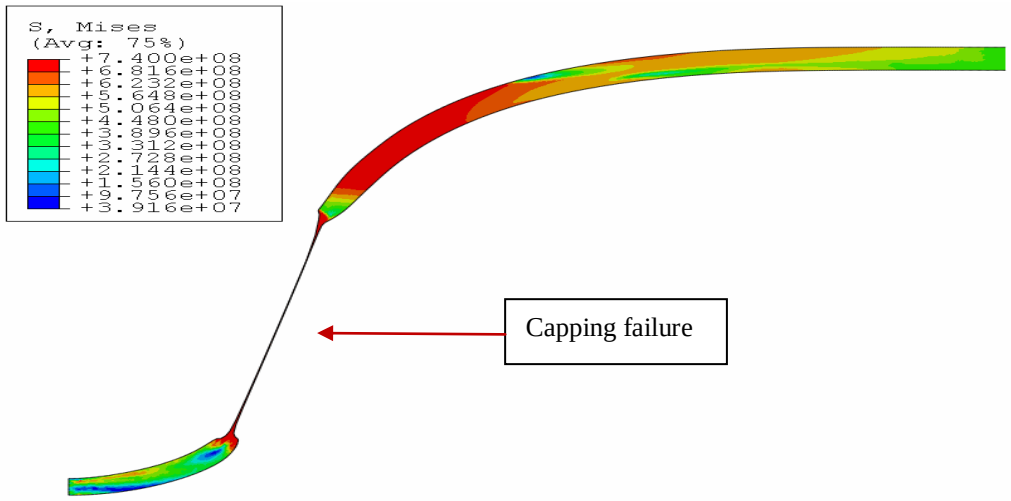

Figure 4-9: FE predictions of 4mm thick plate of Domex 550MC subjected to an impulse of 30Ns (a =16.5mm), without considering strain rate sensitivity

4.3.1.2 Single 4mm thick plates (R= 150mm, a=15mm, a= 25mm)

Target plates of 300mm diameter were subjected to the explosive load diameters of 30mm and 50mm. The simulation results of 300mm diameter plates of 4mm thick single subjected to localized blast load diameter of 30mm and 50mm are shown in Table 4-5. The single plates subjected to blast load diameter of 30mm were capped at an impulse of 100Ns. The plates subjected to a load diameter of 50mm did not cap up to 125Ns impulse.

Table 4-5: Midpoint displacement predictions from simulations of 4mm thick single plates subjected to localized blast loading (plate diameter = 300mm)

Impulse (Ns)	Maximum midpoint displacement (mm)	
	a= 15mm	a = 25mm
15	12	10
30	21	16
45	30	24
60	41 Necking	31
75	50 Necking	38
100	Cap Ø=37mm	50

Further details of simulation of 4mm thick single plates of diameter 300 mm subjected to 30mm and 50mm charge diameter are given in “Appendix E”.

4.3.2 Theoretical predictions of 6mm thick plates (Domex 550 MC)

The 6mm thick single plates were subjected to central charge diameter of 30mm and 50mm. The simulation results at two charge diameters are shown in Table 4-6. Thinning initiated at an impulse of 75Ns at a charge diameter of 30mm. Necking was observed at an impulse of 100Ns and 125Ns. At a charge diameter of 50mm, necking started at an impulse of 125Ns.

The details of 300mm diameter plates of thickness 6mm subjected to charge diameter of 30mm and 50mm are given in "Appendix E".

Table 4-6: Midpoint displacement predictions from simulations of 6mm thick single plates subjected to localized blast loading (plate diameter = 300mm)

Impulse (Ns)	Maximum midpoint displacements (mm)	
	a= 15mm	a = 25mm
15	7	6.5
30	14	13
45	21	19
60	27	24
75	34 Thinning	29
100	45 Necking	34 Thinning
125	59 Necking	43 Necking

4.3.3 Theoretical predictions of Domex 700 MC steel plates

The Domex 700MC plates of a diameter of 200mm and thickness 4mm, 6mm and 8mm were subjected to localized blast loading at a charge diameter of 40mm for all the plates. The analysis was run for the impulses from 20Ns to 140 Ns. The J-C material model was used for the simulations and material flow stress was considered as mentioned in Equation 4-5. For considering the strain rate sensitivity of the material, the 4043 steel parameters were considered and taken from the ABAQUS material library. The simulation results (obtained by using 4043 steel parameter) of 4mm, 6mm and 8mm thick plates are given in Table 4-7.

Table 4-7: Midpoint displacement prediction from simulations of single plates of different thickness, using J-C parameters (Domex 700MC)

Impulse (Ns)	Plate thickness 4mm	Plate thickness 6mm	Plate thickness 8mm
	Maximum deflections (mm)	Maximum deflections (mm)	Maximum deflections (mm)
20	13	8	---
38	27	12	---
45	34	20	12
57	40	27	17
65	42	30	20
75	Failed	36 (necking)	24
85		41 (necking)	28
100		Failed	34
110			37 (necking)
120			43 (necking)
130			Failed

4.3.4 Predictions of 4mm thick single plates (Domex 700MC)

Domex 700MC single plates of 4mm thickness subjected to charge diameter of 40mm were deformed plastically up to an impulse of 65Ns. The midpoint deflection increased with increasing the impulse as indicated in Table 4-7. At an impulse of 75Ns, the plate was failed as depicted in Figure 4-10.

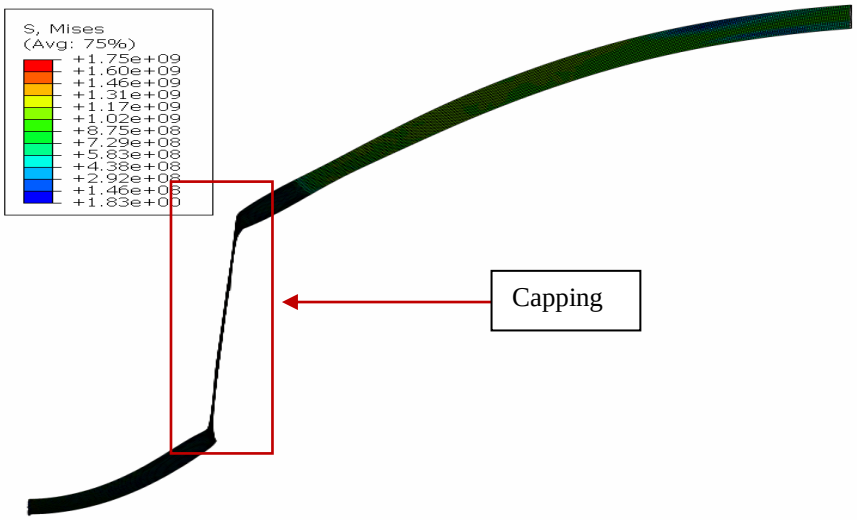

Figure 4-10: FE predictions of 4mm thick single plate of Domex 700MC subjected to an impulse of 75 Ns (charge diameter = 20mm)

4.3.5 Predictions of 6mm thick single plates (Domex 700MC)

Domex 700MC single plates of 6mm thickness subjected to charge diameter of 40mm were deformed plastically up to an impulse of 65Ns. Decrease in thickness was observed in the plates subjected to an impulse of 75Ns and at 85Ns as indicated in Figure 4-11 and Figure 4-12. This configuration was failed at an impulse of 100Ns as shown in Figure 4-13. The simulations indicate that experiments in the BISRU laboratory could produce a range of failures in 6mm thick configurations for the charge masses permitted.

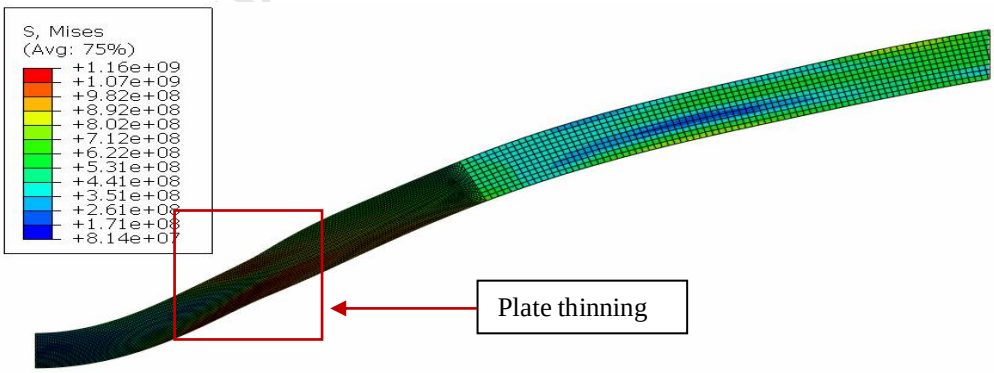

Figure 4-11: FE predictions of 6mm thick plate of Domex 700MC subjected to an impulse of 75 Ns (charge diameter = 20mm)

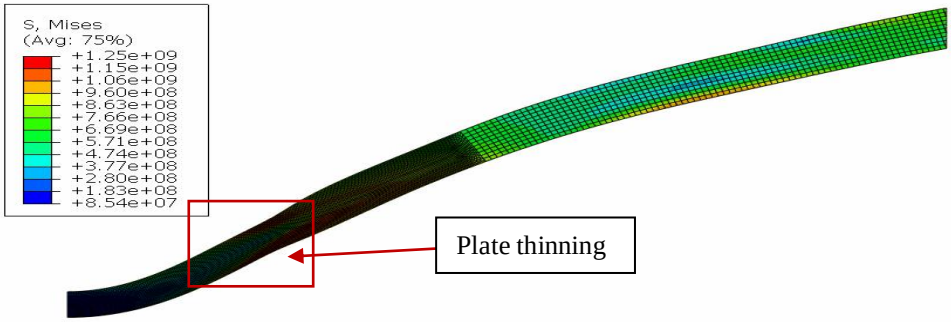

Figure 4-12: FE predictions of 6mm thick plate of Domex 700MC subjected to an impulse of 85 Ns (charge diameter = 20mm)

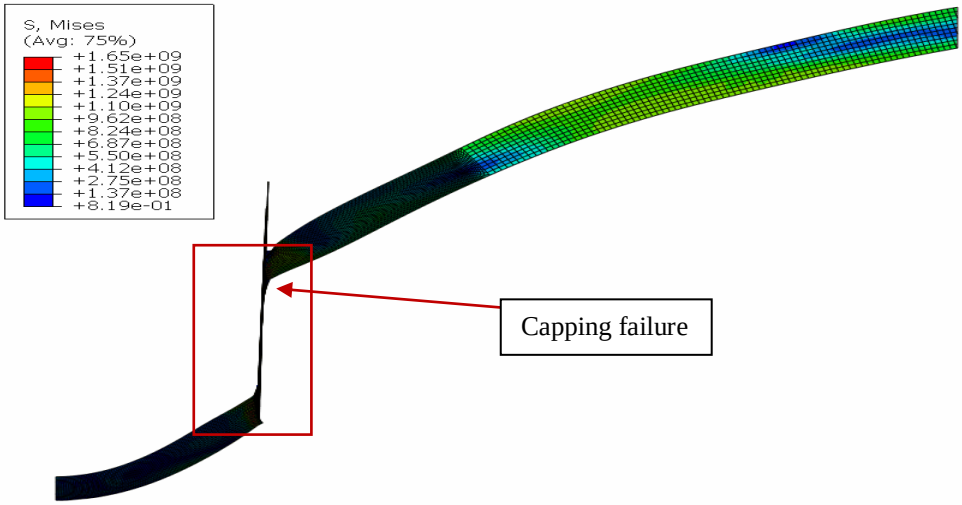

Figure 4-13: FE predictions of 6mm thick plate of Domex 700MC subjected to an impulse of 100 Ns (charge diameter = 20mm)

The details of predictions of 8mm thick single plates are given in "Appendix E"."

The plates of Domex700 were also analyzed using Cowper-Symonds model. The variation in material hardening was defined in a piecewise manner and strain rate sensitivity was considered using Cowper-Symonds relationship. The values of strain rate constants (D and q) were used, proposed by Balden [133]. The simulated results of 4mm, 6mm and 8mm thick single plates are given in Table 4-8. The simulated results by using Cowper-Symonds relationship are different from the results obtained from the J-C model. Lower deformations for all the thicknesses and charge masses were obtained by using Cowper-Symonds relationship as compared to J-C model.

Further details of simulation results of 4mm, 6mm and 8mm thickness by using Cowper-Symonds relationship are given in "Appendix E".

Table 4-8: Midpoint displacement predictions from simulations of single plates of different thicknesses, using Cowper-Symonds relations (Domex 700MC)

Impulse (Ns)	Maximum theoretical deflections (mm)		
	Plate thickness 4mm	Plate thickness 6mm	Plate thickness 8mm
20	12	6	---
38	26	15	---
45	28	18	12
57	35	23	16
65	39	26	18
75	45	30	21
85	51 (necking)	34	24
100		39	28
110		43	31
120		46	33
130		50	36
140		53	38

4.3.6 Summary

The axi-symmetric finite element model of Domex 550MC and Domex 700MC plates were developed for the simulation of the Mode I failure (Large inelastic deformation). The sizes of the target plates and the respective explosive charge diameters for the blast loading experiments were approximated with the help of simulated results.

On the basis of the numerical results of Domex 550MC steel, plates and charge diameters of 200mm and 33mm are selected. The plates of diameter of 200mm were torn before 75Ns as per the simulation results.

The Domex 700MC steel is comparatively a stronger than Domex 550MC, the higher charge masses were needed for plate tearing. According to the simulation results, 120 to 140 (Ns) impulse is needed to tear the plates of 6mm thickness. The plates and charge diameters of 200mm and 40mm were selected respectively for Domex 700MC steel. With this charge diameter, the use of 70g charge mass is possible that can participate effectively towards the transfer of impulse.

The requirement of charge masses of explosive PE4 to tear the plates of 300mm diameter is greater than the specified limits of blast chamber. The plate of 8mm thickness also needs higher charge masses to tear the test plates; these charge masses are greater than the safe limit of present available facility.

Chapter 5

5 Experimental results and observations

In this chapter, the results of blast experiments of various configurations based on the total thickness of 4mm and 6mm are presented. For the 4mm thick configuration, two materials Domex 550MC and Domex 700MC having different yield strength are considered. For 6mm configuration, Domex 700MC plates are studied in various combinations as shown in Figure 5-1.

Two configurations of 4mm thickness, namely 4mm thick single and double (2+2)mm for Domex 550MC and Domex 700MC are considered. Four configurations of 6mm thickness namely 6mm thick single, double (3+3)mm, (4+2)mm and triple (2+2+2)mm are studied for Domex 700MC subjected to localized blast loading experiments.

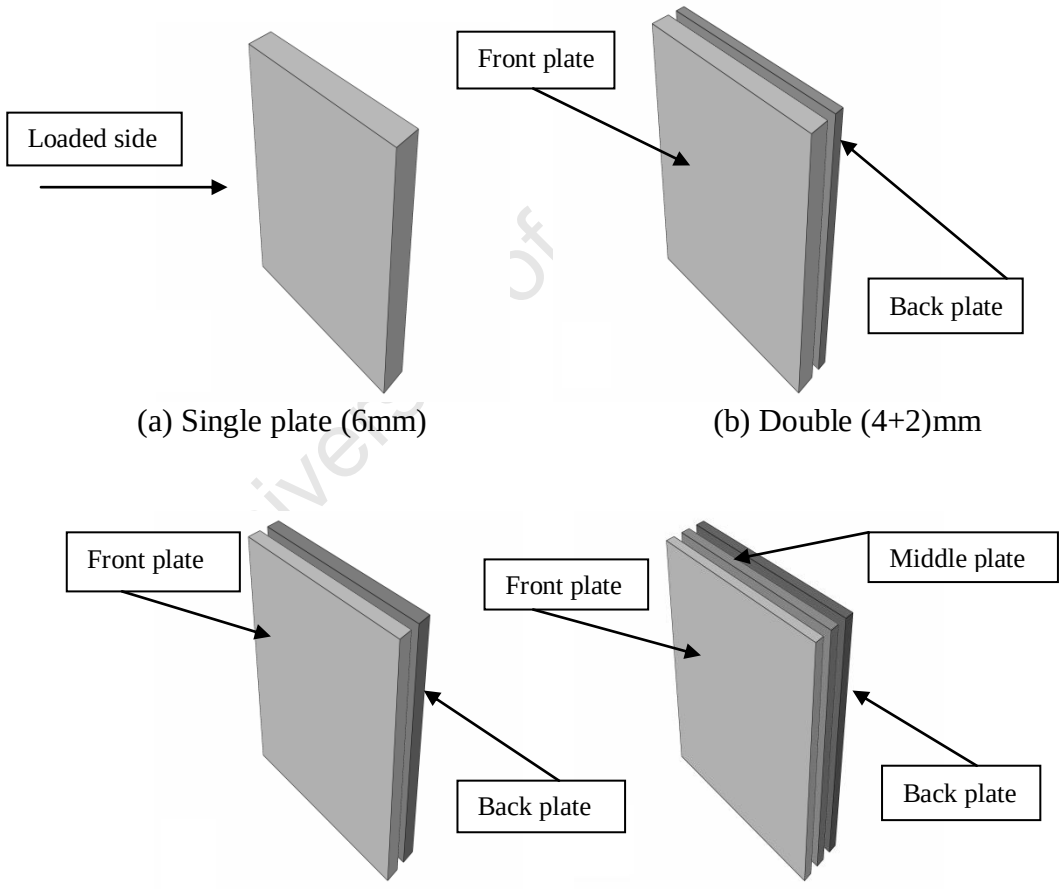

(a) Single plate (6mm) (b) Double (4+2)mm

(a) Double (3+3)mm (b) Triple (2+2+2)mm

Figure 5-1: Various configurations of 6mm thick plates

5.1 Testing methods

The ballistic pendulum shown in Figure 5-2 was used to measure the impulse imparted to the target plate. This pendulum is consisted of a steel I-beam hanging on four spring steel cables by means of adjustable screws. Counter-weights were used to balance the mass of the test rig attached to the front side of the pendulum to ensure that the tension in each of the spring steel remains equal. A pen is attached at the back side of the pendulum to record the oscillation amplitude on tracing paper. The pendulum oscillations can be related directly to the impulse generated by the explosive and transmitted to the attached test plates.

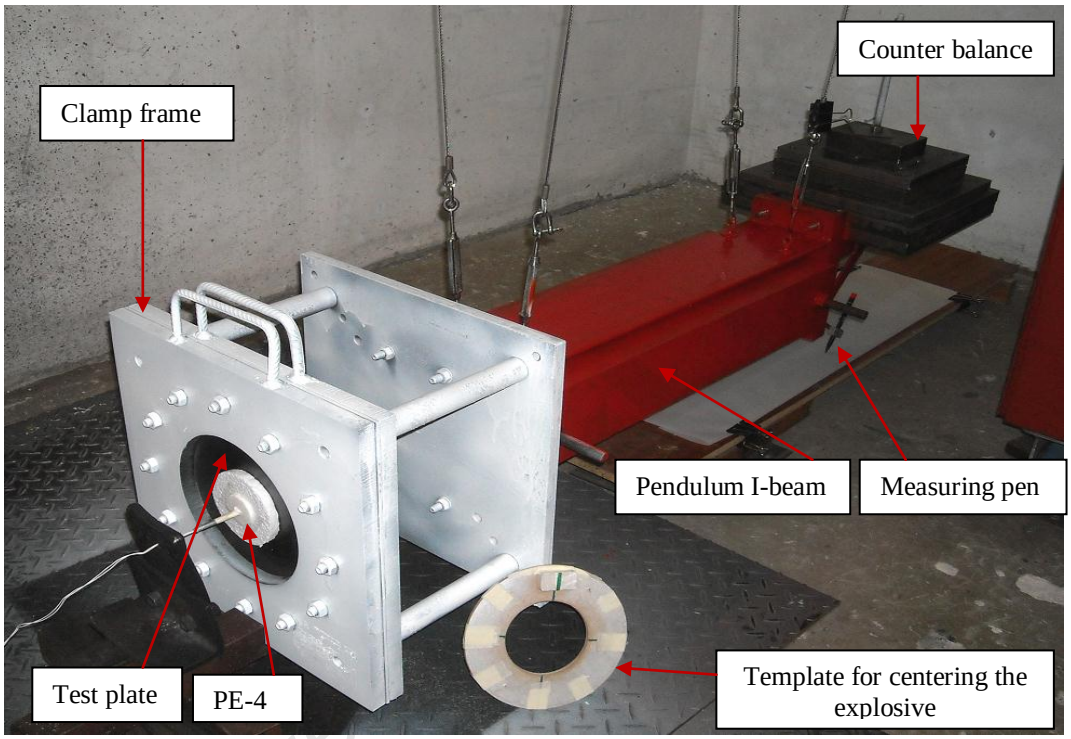

Figure 5-2: Photograph of test plate attached to ballistic pendulum

5.1.1 Pendulum set-up for blast testing

Prior to the test, the pendulum was adjusted and levelled to get repeatable and accurate results. The components (test plates, clamp frames etc) of the front portion of the ballistic pendulum are all weighed so that the counter-masses at the rear of the pendulum can be determined. The main component (I-beam) of the pendulum is also weighed for the determination of the total mass of the pendulum. The distance between the centre of gravity of the front components and the front of the pendulum is approximated and used to position the counter-masses at the rear of the pendulum. A spirit-level is used in conjunction with the adjustable screws on the pendulum to ensure the pendulum is horizontal and balanced.

The target plates of 400 by 400 mm square were bolted between the two 20mm thick annular steel clamps with circular diameter of 200mm. Drawings of the test plates and annular clamps are shown in Figure 5-3. The annular clamps act as a rigid boundary and help in fixing the plate to the pendulum. The whole clamped assembly was mounted to the front of the

pendulum. The existing pendulum as used in previous blast loading experiments (for example [33;34]), was utilized to investigate the response of multi-layered and single plates subjected to localized blast loading. A photograph of the pendulum and attached target plates along with the counter masses is shown in Figure 5-2.

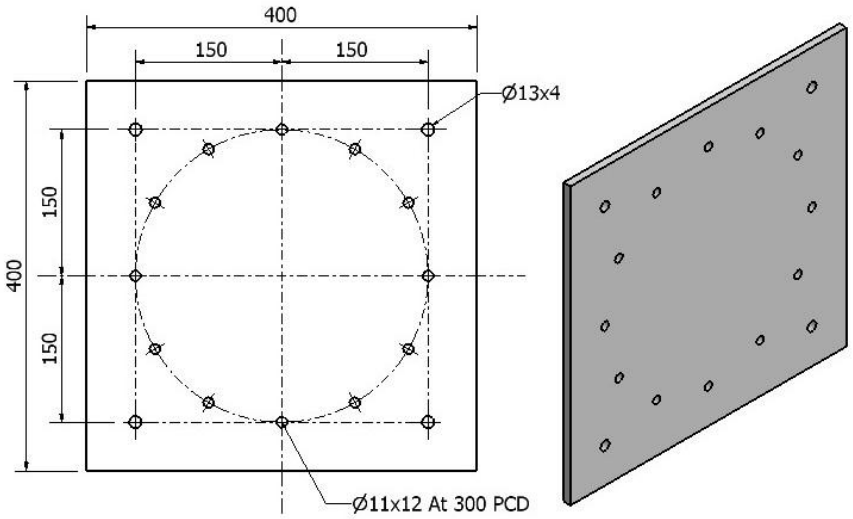

(a) Drawing of the test plate

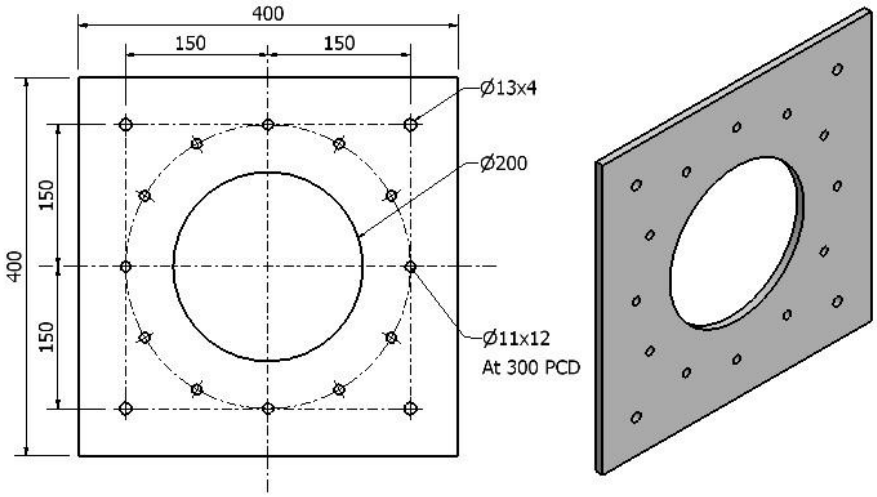

(b) Drawing of the clamps

Figure 5-3: Drawings of test plate and annular steel clamps

The explosive in the form of disk (33mm or 40mm diameter) was spread onto a 12mm thick polystyrene foam pad and centrally positioned by using templates. A leader of 1g explosive was attached to the middle of the explosive disc. The approximate burn speed of plastic explosive (PE-4) is 7500m/s and a density of 1.6 g/cm^3[37]. The explosive mass was varied by increasing the height for higher impulsive loads. The explosive disc mounted onto a piece of polystyrene foam, which acts as a constant stand-off distance and also prevented spallation at close stand-off distances.

The position of the explosive relative to the plate being tested is crucial for symmetric loading and subsequent deformation and failure. Two templates were used in the current set of experiments to ensure that localized blast loading should be at midpoint of test plate. The explosive is first positioned at the centre on polystyrene using a first template. The second template is used to centre the polystyrene having explosive attached on one side in the clamping frame. A mark placed in the centre of the explosive during moulding into the first template is used to place the detonator in the middle of the explosive.

The impulses imparted on the target plates were calculated by using the theory established and used for many years [134], given in "Appendix A". In the post test examination, plate responses were noted for the deformation profile, large inelastic deformation, tearing and capping for each applied impulse.

5.2 Experimental results and observations of Domex 550 MC

5.2.1 Single plates of 4mm configuration

Table 5-1 shows the results from the blast tests of 4mm thick single plates, for various charge masses. The single plates deformed up to the charge mass of 23.5g and started tearing at a charge mass of 30g. Complete tearing of the plates was observed at charge mass of 37.5g. Midpoint deflection of the plate increases with the increase of charge mass as shown in Figure 5-4. In Figure 5-4, plates are stacked in the order of increasing impulse from bottom to top. It is very clear in the photograph that the midpoint deflection is increasing at each step, moving from bottom to top. At 30g charge mass, a crack of length 22mm was developed at a diameter of 22mm. Thickness contraction (that is thinning) at a diameter of 22mm was observed to initiate at 23.5g and increased to a contraction of 1.5mm at 30g, as shown in photograph Figure 5-4. On further increasing impulse, capping failure occurred as demonstrated in the top plate in Figure 5-4. The diameter of the torn cap was 20 to 22mm, which is less than charge diameter (of 33mm).

Table 5-1: Results of 4mm thick single plate subjected to localized blast loading, charge diameter 33mm (Domex 550MC)

Test No*	Charge mass (g)	Impulse (Ns)	Permanent midpoint deflection (mm)	Impulse/deformation Ns/mm
SA041209SA	7 + 1 = 8	22	10.36	2.1
SA041209SB	15 + 1 = 16	38.1	17.85	2.1
SA041209SC	22.5 + 1 = 23.5	45.4	24.44	1.9
SA081209SD	29+1= 30	57.7	29.47 Partial tearing	2.0
SA151209SE	36.5 + 1=37.5	63.4	Cap Ø = 20 - 22mm	

* SA (name of author), 6 digits " 041209" (represents date), S (configuration "single"), A-E (Serial No.)

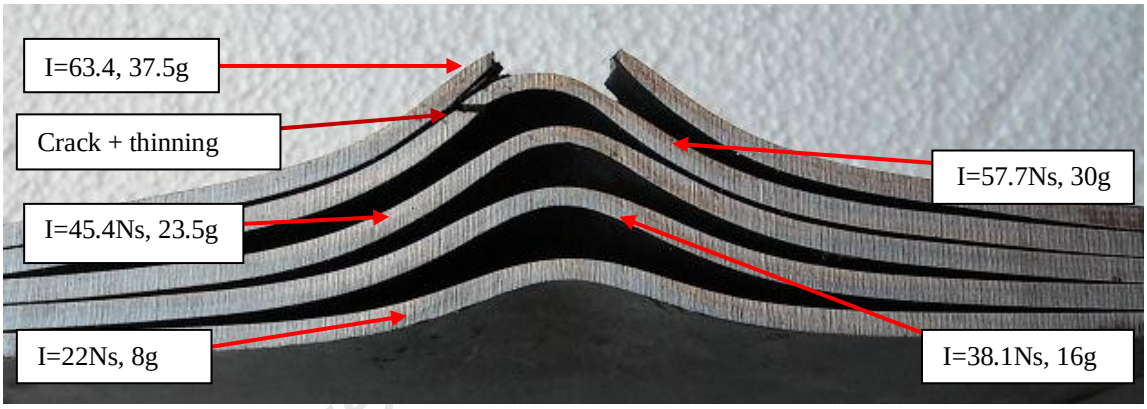

Figure 5-4: Photograph of the cross-sectional view of 4mm thick single plates at (8g, 16g, 23.5g, 30g and 37.5 g), showing deformation and tearing in order of increasing a charge mass, from bottom to top)

5.2.2 Double (2+2)mm plates of 4mm configuration

Table 5-2 shows the results of experiments on the double plates (2+2)mm of 4mm thick configuration, tested at various charge masses. In this configuration, the front and back plates deformed up to the charge mass of 16g and soon after the tearing initiated on front plate (exposed to explosive) at a charge mass of 23.5g as indicated in Figure 5-5.

In the Figure 5-5, the double plates are stacked in the order of increasing impulse from bottom to top. In third set of double plates from the bottom tested at 23.5g, the front plate was capped at a diameter of 25mm whereas minor cracking was developed in back plate, the set is not considered to be failed. Both the plates were capped at a charge mass of 30g. At 30g, cap of the front plate was still attached and the back plate cap was removed. This set of double plates cannot be considered for protection. The impulse obtained at 30g charge mass is a

threshold impulse of double plate configurations. At a charge mass of 37.5g, both the plates were capped with comparatively larger cap diameter than cap diameter at a charge mass of 30g. The diameter of caps torn away at charge mass of 37.5g was 28.5mm for front plate and 29.5mm of the back plate.

Table 5-2: Results of double (2+2)mm plates subjected to localized blast loading, charge diameter 33mm (Domex 550MC)

Test No*	Charge mass (g)	Impulse (Ns)	Permanent midpoint deflection of front plate (mm)	Permanent midpoint deflection of back plate (mm)	Impulse/Deformation Ns/mm (front plate)
SA071209DG	7+1= 8	20.2	12.28	12.82	1.6
SA071209DH	15+1=16	36.1	21.81	22.5	1.7
SA071209DI	22.5+1= 23.5	45.6	27.95	28.65	1.6
SA151209DJ	29+1=30	59.9	30.5 partial tearing	Cap	2.0
SA151209DK	36.5+1=37.5	61	Cap Ø = 28.5	Cap Ø = 29.5	

* SA (name of author), 6 digits "071209" (represents date), D (configuration "double"), G-K (Serial No.)

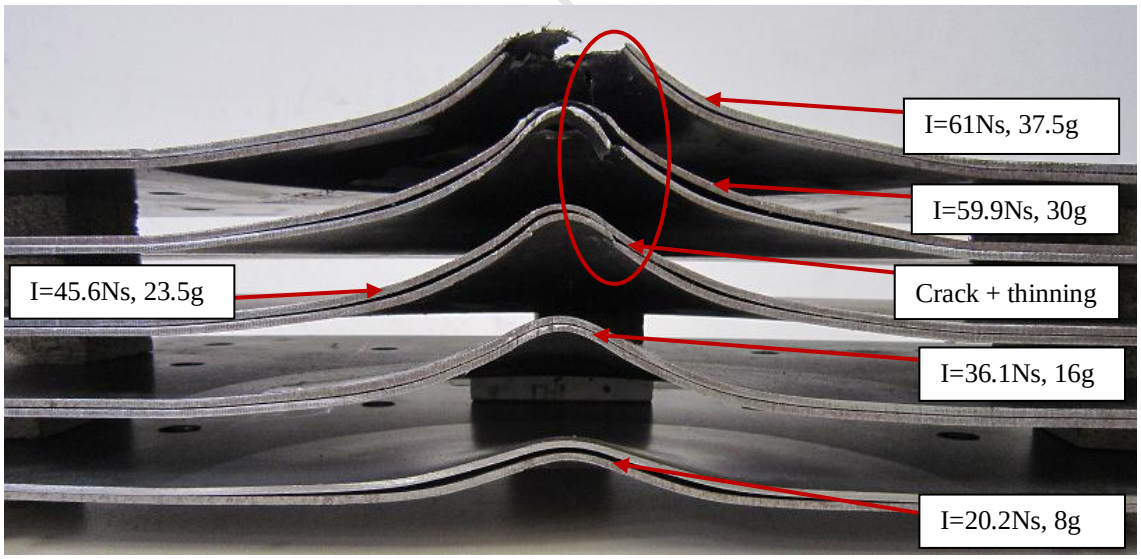

Figure 5-5: Photograph of the cross-sectional view of double (2+2)mm plates at (8g, 16g, 23g.5g, 30g and 37.5g), showing deformation and tearing in order of increasing charge mass from bottom to top)

5.3 Experimental results and observations of Domex 700MC plates

5.3.1 Single plates of 4mm configuration

Table 5-3 shows the results of the 4mm thick single plates of Domex 700MC, tested at various charge masses. The single plates deformed up to the charge mass of 27g, with a maximum midpoint deflection of 27.47mm.

Necking was observed at a diameter of 25mm on plates subjected to a charge mass of 33g as indicated in Figure 5-6. At a charge mass of 38g, the plate was cracked from the neck at a diameter of 25mm. The plate was capped at a charge mass of 44g as shown in Figure 5-6.

Figure 5-6 shows a photograph of the tested plates at various impulses. The midpoint deflection increased with increasing impulse, as indicated in Figure 5-8 from bottom to top.

Table 5-3: Results of 4mm thick single plate (Domex 700MC) subjected to localized blast loading, charge diameter 40mm

Test No*	Charge mass (g)	Charge height (mm)	Impulse (Ns)	Midpoint deflection (mm)	Deflection thickness ratio	Impulse / Mass
D700Th4-SA	9+1=10	4.97	22.5	11.30	2.83	2.25
D700Th4-SB	17+1=18	8.92	41.1	20.12	5.03	2.28
D700Th4-SC	21+1=22	10.94	45.6	24.10	6.03	2.07
D700Th4-SD	26+1=27	13.43	56.9	27.47	6.87	2.11
D700Th4-SE	32+1=33	16.41	68.8	31.40	7.85	2.09
D700Th4-SF	37+1=38	18.9	81.7	39.93 cracking	9.98	2.15
D700Th4-SG	43+1=44	21.88	85.6	Cap Ø=26mm	--	1.95

* D (Domex), Th4 (sheet thickness in mm), S (configuration “single”), A-G (Serial No.)

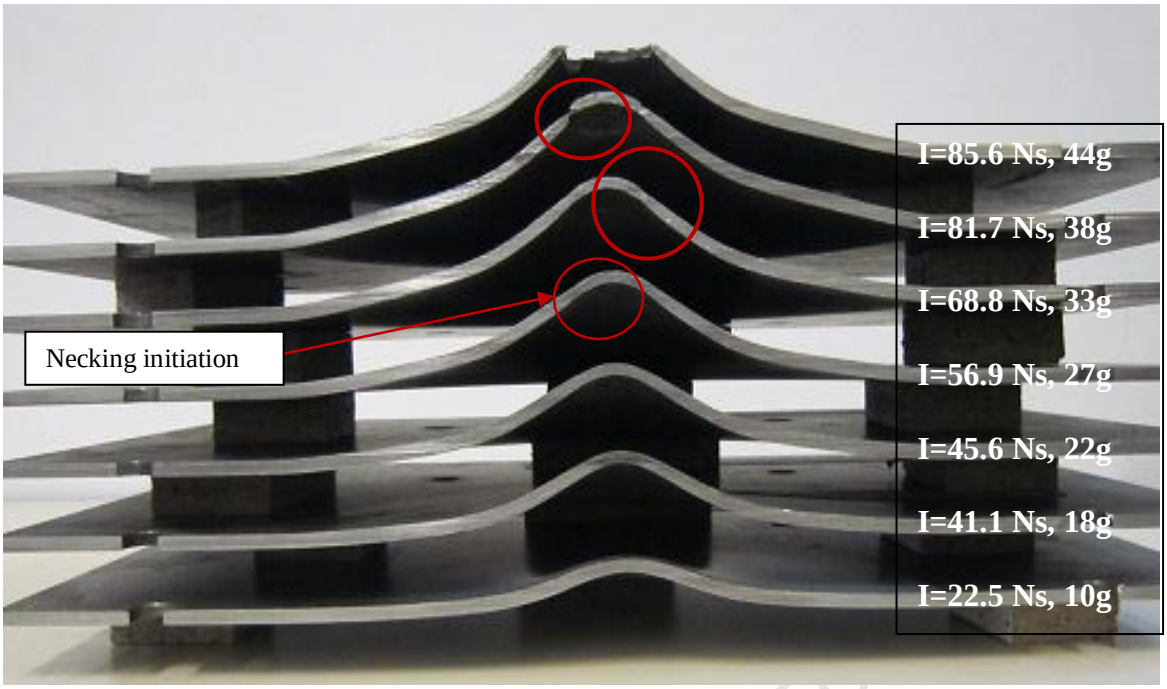

Figure 5-6: Photograph of the cross-sectional view of single 4mm thick single plates at (10g, 18g, 22g, 27g, 33g, 38g and 44g), showing deformation and tearing in order of increasing charge masses from bottom to top)

5.3.2 Double (2+2)mm plates of 4mm configuration

Table 5-4 shows the results of the double (2+2)mm plates of 4mm configuration, tested at various charge masses. The double plates exhibited plastic deformation up to charge mass of 18g, with necking exhibited at higher masses. Necking in the front plate initiated at a central diameter of 26mm in a plate tested at 22g as shown in Figure 5-7a. At a charge mass of 27g, the front plate was capped, as shown in Figure 5-7b and the torn cap remained attached whereas the neck was formed in back plate at a diameter of 26mm.

Both plates were capped at a charge mass of 33g, with front and back plate cap diameters of 28mm and 30mm respectively, as depicted in Figure 5-8. The cross-sectional view of blast tested double plates at increasing charge masses, from bottom to top, is shown in Figure 5-8, indicated deformation, tearing and capping failure at respective charge masses.

Table 5-4: Results of double (2+2)mm plates subjected to localized blast loading (Domex 700MC), charge diameter 40mm

Test No*	Charge mass (g)	Charge height (mm)	Impulse (Ns)	Midpoint deflection (mm)	Deflection thickness ratio	Impulse / Mass
D700Th2+2-DA	10	4.97	21.7	12.92	3.23	2.17
D700Th2+2-DB	18	8.92	35.4	21.42	5.36	1.97
D700Th2+2-DC	22	10.94	43.8	25.65	6.41	1.99
D700Th2+2-DD	27	13.43	52.8	29.10	7.28	1.95
D700Th2+2-DE	33	16.41	63.7	Capped	--	1.93

* D (Domex), Th2+2 (sheet thickness in mm), D (configuration "double"), A-E (Serial No.)

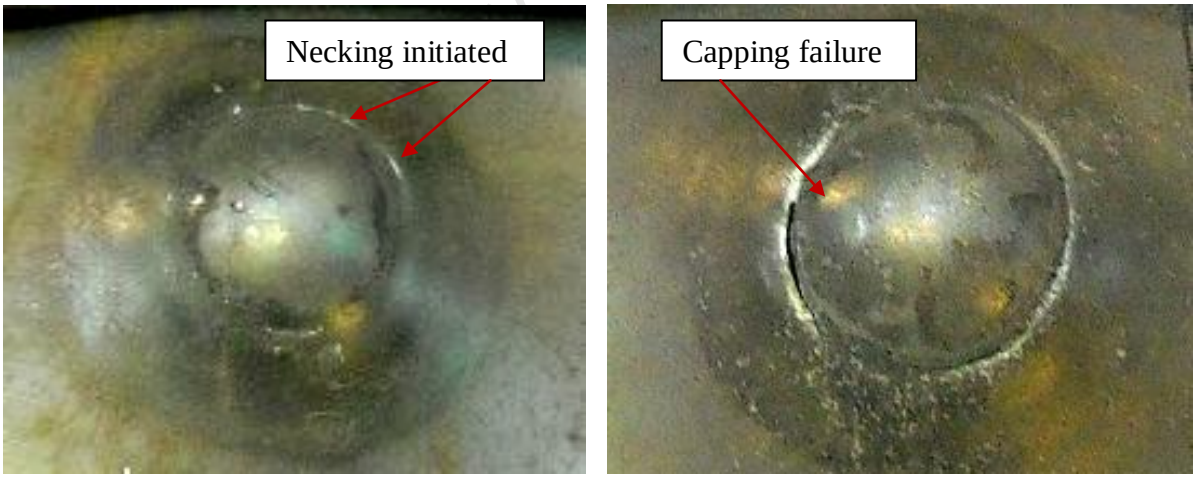

(a) Charge mass 22g (b) Charge mass 27g

Figure 5-7: Photographs to show necking initiation (a) and capping failure of front plate (b)

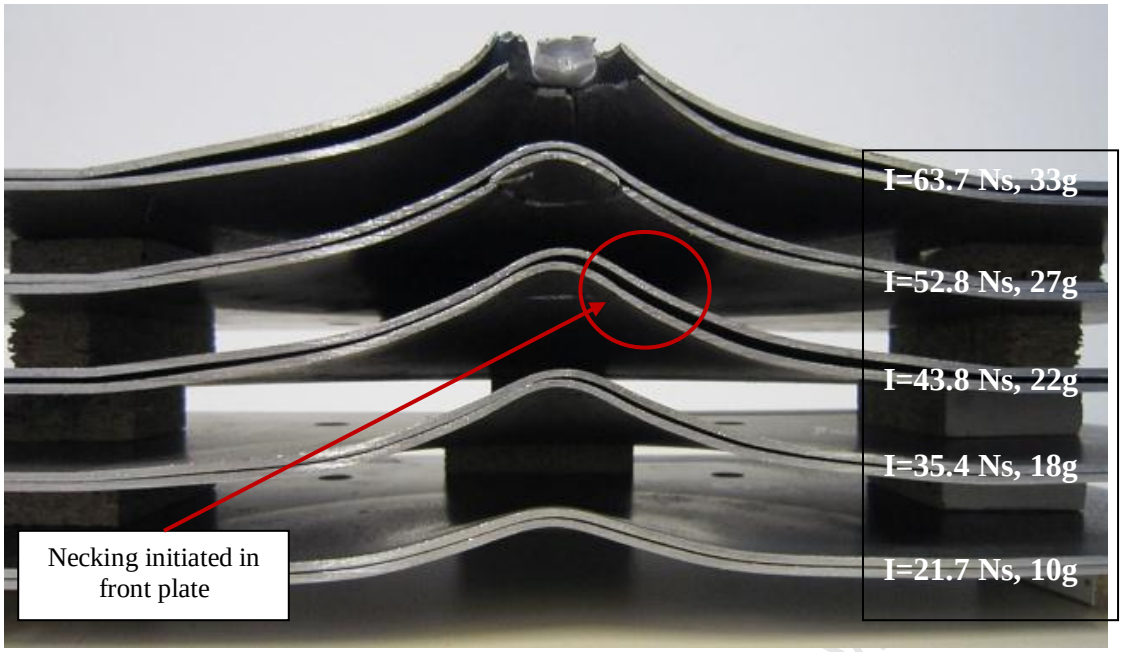

Figure 5-8: Photograph of the cross-sectional view of double (2+2)mm plates at (10g, 18g, 22g, 27g and 33g), showing deformation and tearing in order of increasing charge mass from bottom to top)

5.3.3 Single plates of 6mm configuration

Table 5-5 shows the result of testing the 6mm thick single Domex 700MC plates, at various charge masses. An increase in midpoint deflection has been observed in plates with the increase in charge mass. The plates permanently deformed up to a charge mass of 50g. The maximum midpoint deflection without necking or tearing was 23mm. On further increasing the impulse, necking started in the plates. At a charge mass of 62g, the plate was capped at diameter of 40mm.

A cross-sectional photograph of all the tested plates is shown in Figure 5-9 to demonstrate the deformation and tearing of plates with increasing charge mass, from bottom to top.

Table 5-5: Results of 6mm thick single plates subjected to localized blast loading, charge diameter 40mm (Domex 700MC)

Test No*	Charge mass (g)	Charge height (mm)	Impulse (Ns)	Midpoint deflection (mm)	Deflection thickness ratio	Impulse / Mass
D700Th6-SA	18	8.92	38.3	10.36	1.73	2.13
D700Th6-SB	22	10.94	45.4	12.9	2.15	2.06
D700Th6-SC	27	13.43	54.3	14.76	2.46	2.01
D700Th6-SD	33	16.41	67.1	16.82	2.80	2.03
D700Th6-SG	50	24.86	94.5	23	3.83	1.89
D700Th6-SH	56	27.85	103.5	25.03 cracked	4.17	1.85
D700Th6-SI	59	29.34	109.8	31.88 cracked	5.31	1.86
D700Th6-SJ	62	30.84	108	Capped	--	1.74

* D (Domex), Th6 (sheet thickness in mm), S (configuration “Single”), A-J (Serial No.)

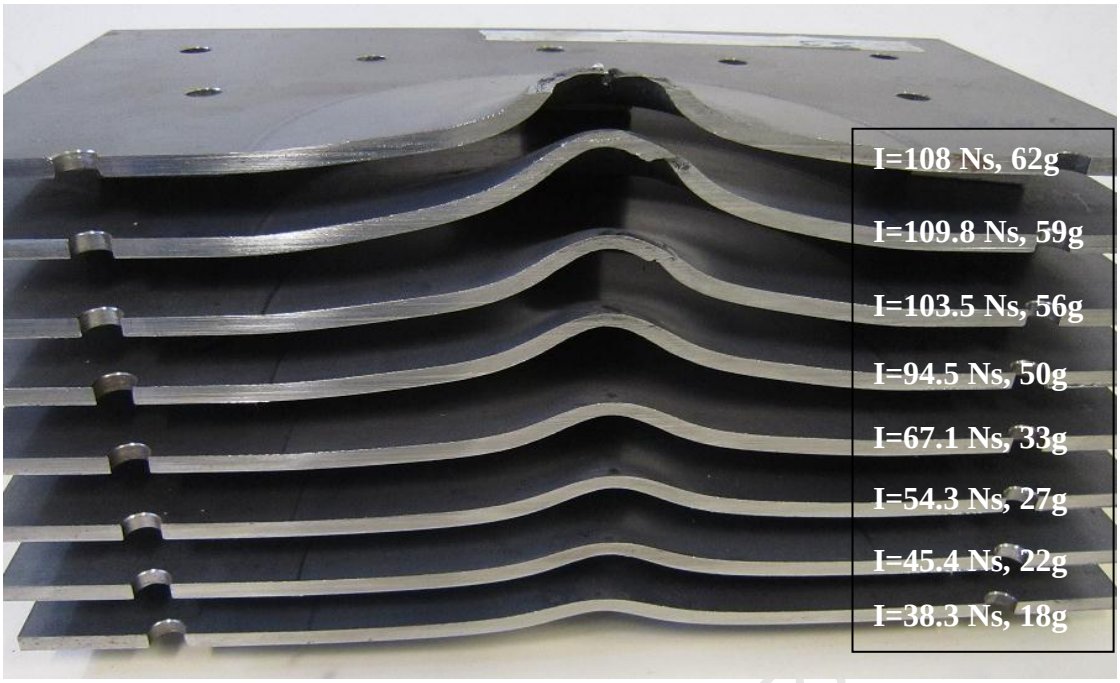

Figure 5-9: Photograph of the cross-sectional view of 6mm thick single plates, showing deformation and tearing in order of increasing charge masses (18g, 22g, 27g, 33g, 50g, 56g, 59g and 62g, from bottom to top)

5.3.4 Double (3+3)mm plates of 6mm configuration

Table 5-6 shows the results of double (3+3)mm thick plates, tested at various charge masses. The back plate midpoint deflections were considered in case of double plate configurations. The double (3+3)mm plates permanently deformed up to a charge mass of 56g. A circular ring of 51-52mm diameter appeared on the rear face of the back plates at a charge mass of 50g, 56g, 62g and 68g as indicated in Figure 5-10 and Figure 5-12b.

An annular ring of outer diameter of 52mm, with a forged shiny surface, was noted in back side of all the front plates tested at 59g, 62g and 68g charge masses. This shiny annular surface may be due to the friction or sliding of plates with each other during blast loading. This shiny forged or stamped surface on the back face of the front plate is shown in Figure 5-11.

Minor necking started to appear in front plates at a diameter of 23mm in the plates tested at a charge mass of 56g. Visible necking and reduction in thickness was observed in the front plate at diameter of 24mm tested at a charge mass of 62g. A small crack of length 6 to 8mm was developed in a front plate whereas the back plate did not crack.

At a charge mass of 68g, a 22mm long crack developed at the diameter of 25mm in front plate whereas the back plate was able to withstand the higher load without cracking. Photographs of the front and the back plates tested at 68g are shown in Figure 5-12.

The double (3+3)mm configuration provides better protection than the single 6mm single plate. Up to charge mass of 68g, this configuration is still capable of providing protection, as no capping failure was observed during the blast experiments.

A photograph of a cross-sectional view of a set of plates tested at increasing impulses is shown in Figure 5-13, indicated the increase in midpoint deflection with increasing the charge mass, from bottom to top.

Table 5-6: Results of double (3+3)mm plates subjected to localized blast loading, charge diameter 40mm (Domex 700MC)

Test No*	Charge mass (g)	Charge height (mm)	Impulse (Ns)	Midpoint deflection of back plates (mm)	Deflection thickness ratio	Impulse/ Mass
D700Th3+3-DA	18	8.92	39	11.55	1.93	2.16
D700Th3+3-DB	22	10.94	42.3	13.97	2.33	1.92
D700Th3+3-DC	27	13.43	54.1	16.24	2.71	2.00
D700Th3+3-DD	33	16.41	62.1	18.65	3.11	1.88
D700Th3+3-DG	50	24.86	91	23.81	3.94	1.82
D700Th3+3-DH	56	27.85	105	25.72	4.29	1.87
D700Th3+3-DJ	62	30.84	108.7	27.19	4.53	1.75
D700Th3+3-DK	68	33.82	114.6	28.48	4.75	1.68

* D (Domex), Th3+3 (sheet thickness in mm), D (configuration “double”), A-K (Serial No.)

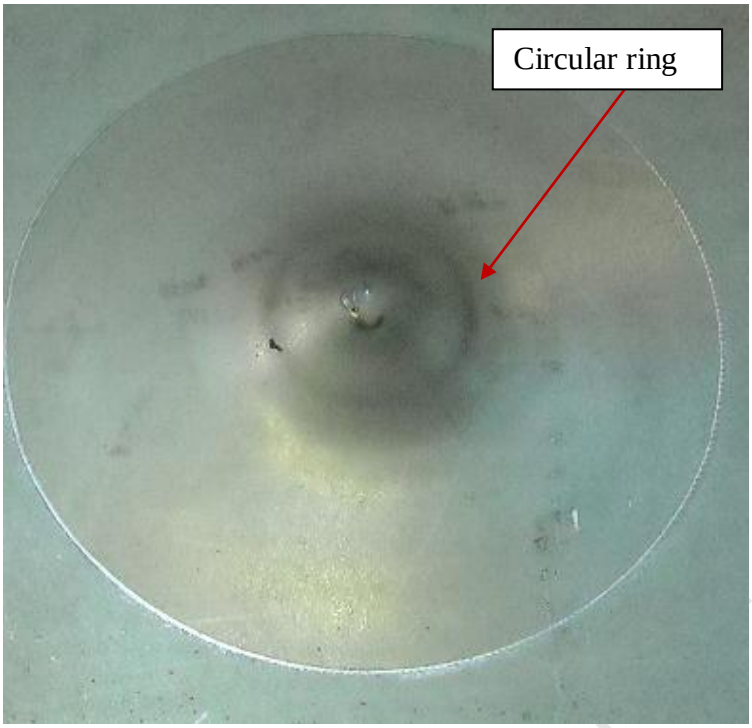

Figure 5-10: Photograph shows a circular ring of diameter 23mm in back plate (m=56g)

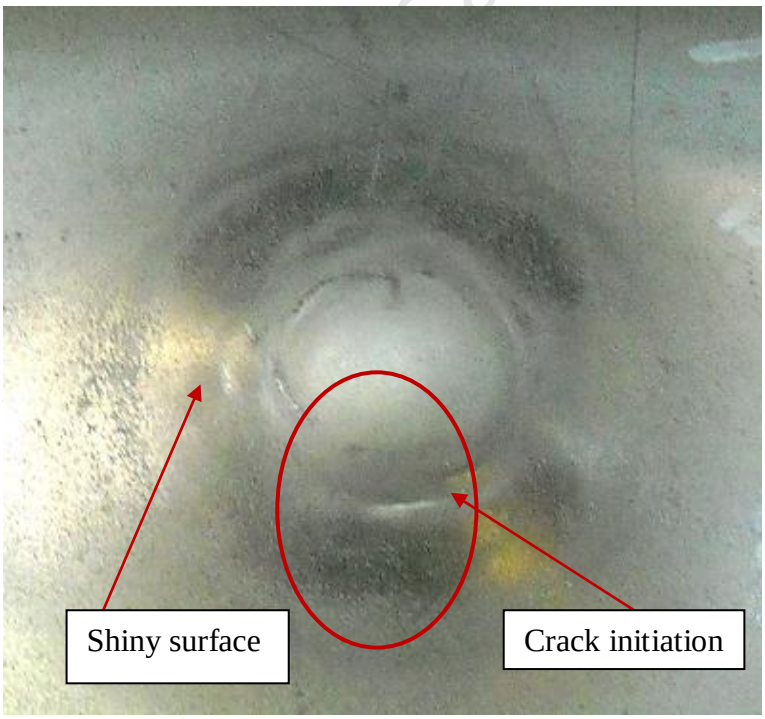

Figure 5-11: Photograph shows a crack initiation in front plate (m=62g)

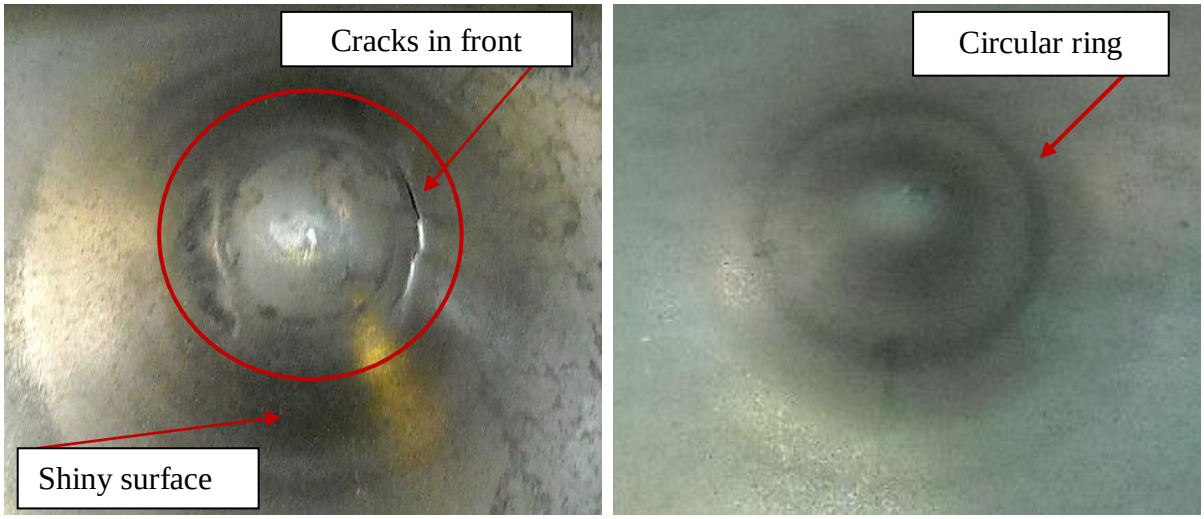

(a) Front plate (b) Back plate

Figure 5-12: Photographs show a cracks in front plate (a) at a diameter of 25mm and a circular ring (b) (m= 68g)

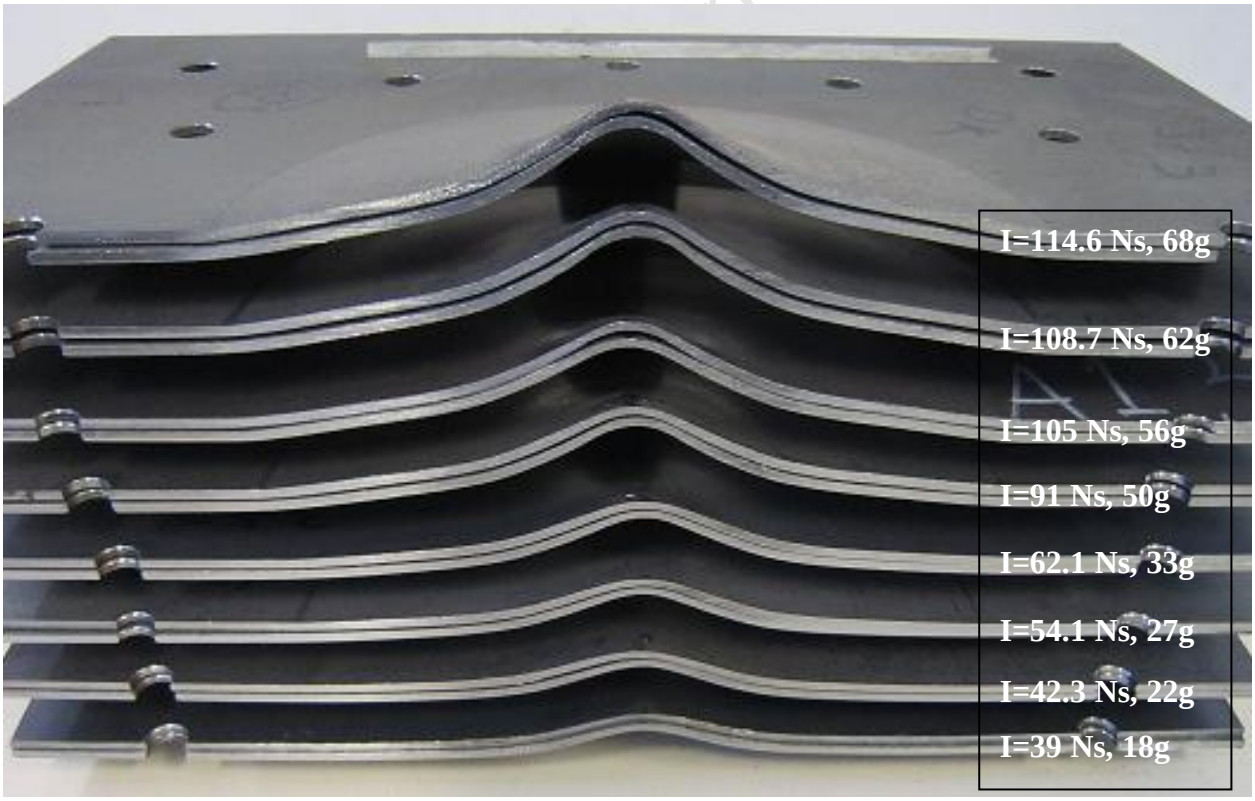

Figure 5-13: Photograph of the cross-sectional view of double (3+3)mm plates, showing deformation and tearing in order of increasing charge masses (18g, 22g, 27g, 33g, 50g, 56g, 59g and 62g, from bottom to top)

5.3.5 Double (4+2)mm plates of 6mm configuration

Table 5-7 shows the results of double (4+2)mm plates of 6mm configuration, tested at various charge masses. In this configuration, the 4mm thick plates exposed to the blast were named as front plates and 2mm thick plates are the back plates. The double (4+2)mm plates plastically deformed up to a charge mass of 56g without any crack. The midpoint deflections in both plates increased with increasing in impulse. In Table 5-7, the back plate midpoint deflections are given, as these are more important for protection purposes. The deflections were very similar, as illustrated in Figure 5-17.

Table 5-7: Results of double (4+2) mm plates subjected to localized blast loading, charge diameter 40mm (Domex 700MC)

Test No*	Charge mass (g)	Charge height (mm)	Impulse (Ns)	Midpoint deflection of back plates (mm)	Deflection thickness ratio	Impulse/ Mass
D700Th4+2-DA	18	8.92	37.3	12.96	2.16	2.07
D700Th4+2-DB	22	10.94	46.3	15.2	2.53	2.10
D700Th4+2-DC	27	13.43	55.8	16.94	2.82	2.07
D700Th4+2-DD	33	16.41	66.1	20.41	3.4	2.0
D700Th4+2-DE	38	18.9	72.7	22.55	3.76	1.91
D700Th4+2-DF	44	21.88	85.5	25.34	4.22	1.94
D700Th4+2-DG	50	24.86	92.8	27.78	4.63	1.86
D700Th4+2-DH	56	27.85	105.9	28.32	4.72	1.89
D700Th4+2-DI	62	30.86	113.9	30.98 Cracked	5.16	1.84
D700Th4+2-DJ	68	33.82	116.6	29.74 Cracked	4.96	1.71
D700Th4+2-DK	74	36.8	126.7	31.01 Cracked	5.17	1.71

* D (Domex), Th4+2 (sheet thickness in mm), D (configuration “double”), A-K (Serial No.)

At a charge mass of 62g, tearing initiated in both front (4mm) and back (2mm) plates. Both plates were cracked at a central diameter of 25mm as shown in Figure 5-14.

Partial tearing occurred in front plate and 75% of the diameter was cracked whereas the back plate crack was 50% of the diameter. The crack was greater in front plates than back plates. A shiny annular ring (with inner diameter 55mm and 66mm outer diameter) starts to form at the back side of all the front plates tested at charge masses 62g, 68g and 72g as shown in Figure 5-14, Figure 5-15 and Figure 5-16 respectively.

At a charge mass of 68g, a 10mm long crack was developed at a diameter of 29mm in the front and back plates. Both plates were cracked in a similar way but with cracks forming on opposite side to each other, indicated in Figure 5-15. At a charge mass of 74g, a minor crack was developed at a diameter of 19mm in both plates as shown in Figure 5-16.

Capping failure was not observed at any charge mass up to 74g in (4+2)mm configuration. The plastic deformation of the back plates is greater than the deformation of the front plates. The deformation profiles of the back and front plates were different as shown in Figure 5-17.

A cross-sectional view of double (4+2)mm plates at increasing impulses is indicated in Figure 5-17, showing deformation, and tearing in order of increasing charge masses, from bottom to top.

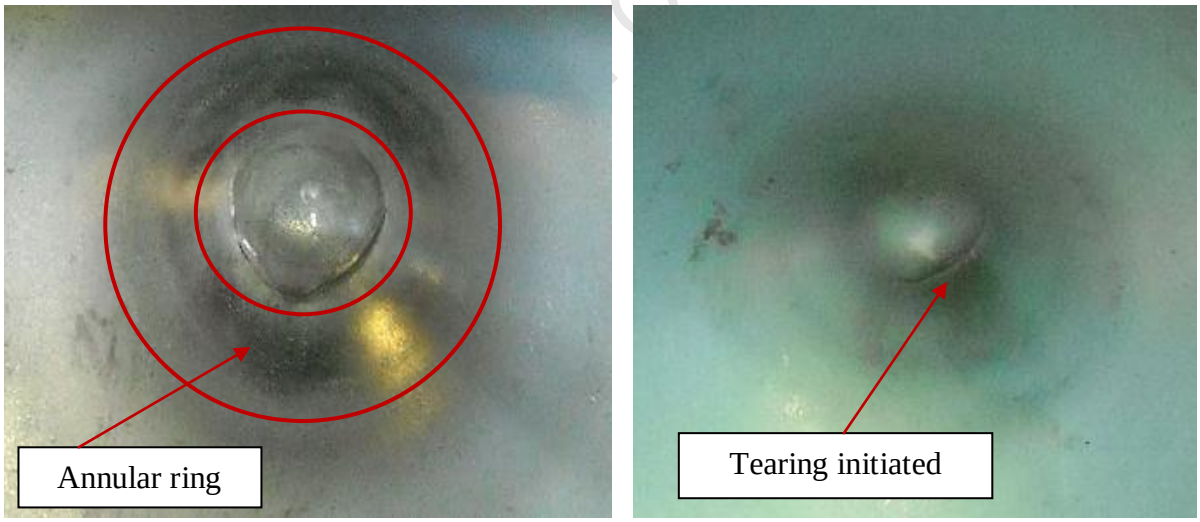

(a) Front plate (b) Back plate

Figure 5-14: Photograph shows a front (a) and back (b) plates tested at charge mass of 62g

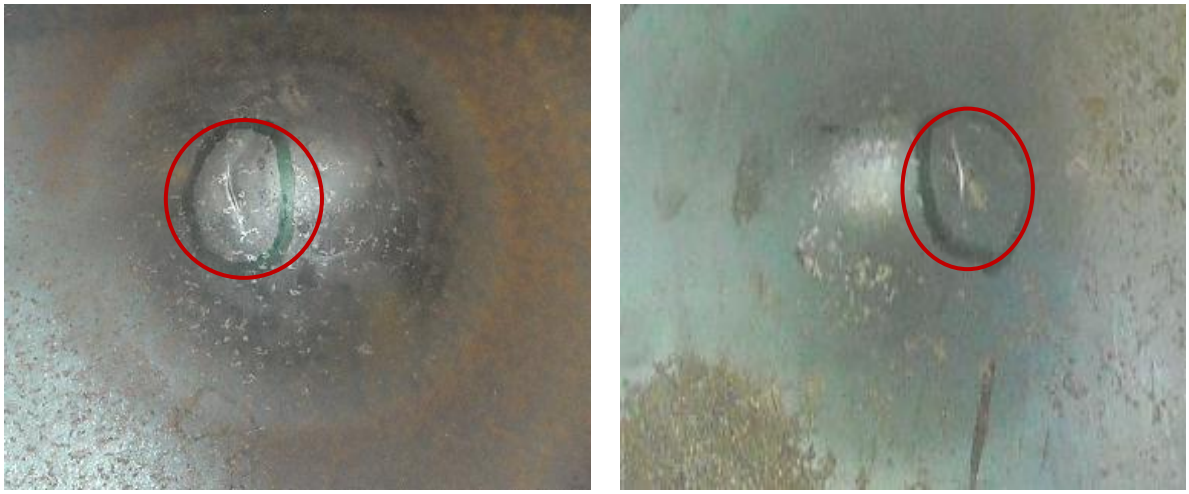

(a) Front plate (b) Back plate

Figure 5-15: Photograph shows a cracks in front (a) and back (b) plates (m=68g)

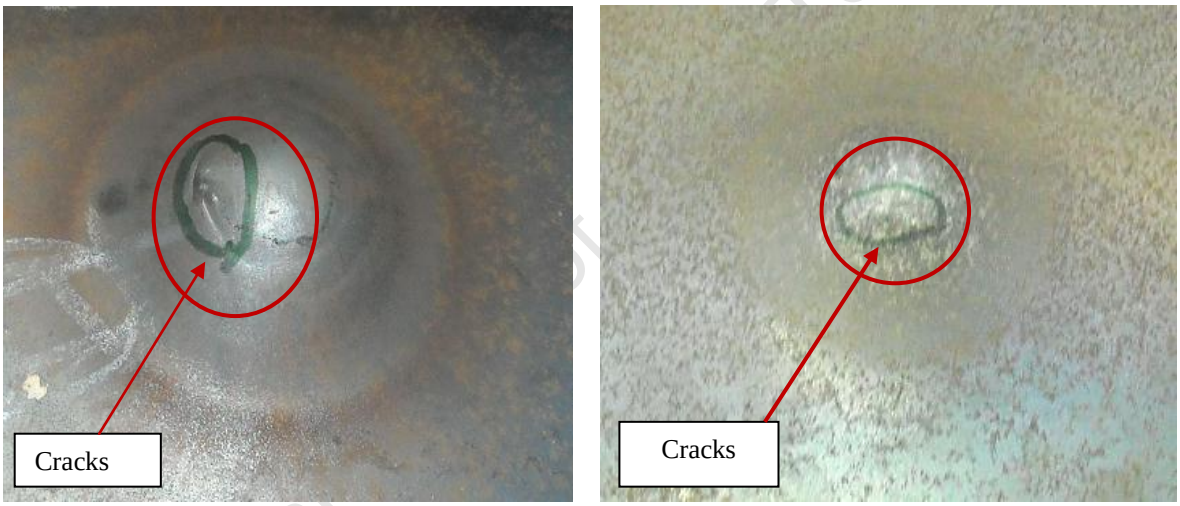

(a) Front plate (b) Back plate

Figure 5-16: Photographs show a cracks in front (a) and back (b) plates (m= 74g)

Figure 5-17: Photograph of cross-sectional view of double (4+2)mm configuration, showing deformation and tearing in order of increasing charge masses (18g, 22g, 27g, 33g, 50g, 56g, 59g, 62g and 74g, from bottom to top)

5.3.6 Triple plates (2+2+2)mm of 6mm configuration

Table 5-8 shows the results of triple (2+2+2)mm plates of 6mm configuration, tested at various charge masses. The triple plates plastically deformed up to a charge mass of 38g. Midpoint deflections in all plates (front, middle and back) increased with the increase in impulse, and were very similar in magnitude for all three plates.

Triple plate configurations exhibited tearing at a charge mass of 44g. At a charge mass of 44g, a 31mm long crack in front plate at central diameter of 30mm was developed with a small opening as shown in Figure 5-18. Middle and back plates did not show any cracks. On increasing to a charge mass of 50g, the front plate capped (cap diameter of 30mm), as indicated in Figure 5-19a. Minor cracks developed in the middle plate at a diameter of 29mm, with an annular shiny ring on back side as shown in Figure 5-19b.

At a charge mass of 56g, the front and the back plates were capped whereas the middle plate did not crack. The cap diameter of the front plate was 30mm and back plate failed in petalling fashion.

At a charge mass 62g, triple plates showed similar trend with failure of front and back plate with no cracks evident in the middle plate. The cap diameters were 30mm and 34mm for front and back plates respectively.

A photograph of a cross-sectional view of triple plates tested at various charge masses is shown in Figure 5-20, indicating deformation and tearing in order of increasing charge masses, from bottom to top.

Table 5-8: Results of triple (2+2+2)mm plates subjected to localized blast loading, charge diameter 40mm (Domex 700MC)

Test No*	Charge mass (g)	Charge height (mm)	Impulse (Ns)	Midpoint deflection of back plates (mm)	Deflection thickness ratio	Impulse/ Mass
D700Th2+2+2-TA	18	8.92	37.6	12.56	2.09	2.09
D700Th2+2+2-TB	22	10.94	48	14.54	2.42	2.18
D700Th2+2+2-TC	27	13.43	56.2	18.4	3.07	2.08
D700Th2+2+2-TD	33	16.41	69	20.2	3.37	2.09
D700Th2+2+2-TE	38	18.9	77.3	22.28	3.71	2.03
D700Th2+2+2-TF	44	21.88	83.6	24.45	4.08	1.90
D700Th2+2+2-TG	50	24.86	91	27.92	4.65	1.82
D700Th2+2+2-TH	56	27.85	106	26.5 **Middle plate	4.42	1.89
D700Th2+2+2-TI	62	30.86	112.4	29.45 **Middle plate	4.91	1.81

* D (Domex), Th2+2+2 (sheet thickness in mm), T (configuration “Triple”), A-H (Serial No.)
* Middle plate deflection is reported because the back plate is capped.

Figure 5-18: Photograph shows a front plate failure at a diameter 38mm (m = 44g)

(a) Front plate (b) Middle plate

Figure 5-19: Photographs show a middle plate failure (a) and annular shiny ring in back plates (b) at a charge mass of 50g

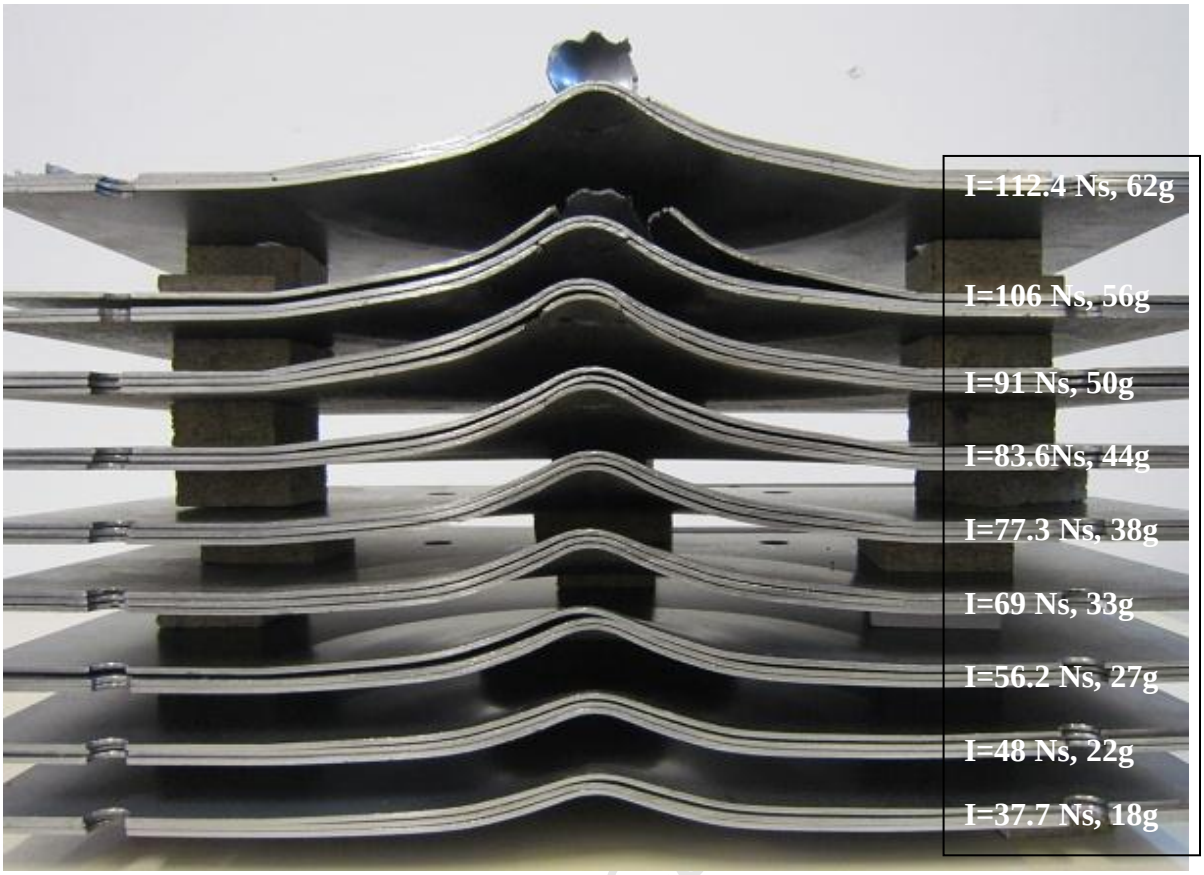

Figure 5-20: Photograph of the cross-sectional view of triple (2+2+2)mm configuration, showing deformation and tearing in order of increasing charge masses (18g, 22g, 27g, 33g, 50g, 56g, 59g, 62g and 74g, from bottom to top)

5.4 Summary

5.4.1 Configurations of 4mm thickness

Domex 550 MC single plates of 4mm thickness exhibited initiation of cracking at a charge mass of 30g, providing protection up to a charge mass of 23.5g. The double plate (2+2)mm of Domex 550 MC provided protection at 16g, and the plates exhibited cracking at a charge mass of 23.5g. Comparison of both configurations (single and double) indicated that a single plate gave a better protection than double plates.

Domex 700MC single plates of 4mm thickness start to crack at a charge mass of 38g. The double(2+2)mm plate of Domex 700MC were capped at a charge mass of 33g. Comparison both configurations (single and double) of 4mm thick Domex 700MC plates indicated that single plates showed a better protection than double plates.

For both materials, Domex 550MC and Domex700MC, the single plates performed better than double plates for 4mm configurations.

5.4.2 Configurations of 6mm thickness

The 6mm thick single plates started cracking at a charge mass of 56g. These plates were capped at a charge mass of 62g. The cap had a flat and shiny appearance like brittle fracture. This configuration can safely be used up to charge mass of 50g (without cracking and loss of containment).

In double plates of configuration (3+3)mm, the front plate exhibited cracking at a charge mass of 62g and the back plate did not show cracking. Minor cracks appeared in a front plate tested at a charge mass of 68g whereas the back plate did not show cracking. The plates of this configuration were not capped up to charge mass of 68g. This configuration can still withstand further blast loads.

In plates of double (4+2)mm configuration, cracking was initiated at a charge mass of 62g in both front and back plates. The plates of this configuration were not capped up to 74g charge mass. The back plate was torn up to 30% of the diameter of the neck.

In triple plate configuration, the front plate started tearing at a charge mass of 44g. At a charge mass of 56g, the front and the back plates were capped.

Comparison of four above configurations of Domex 700MC plate indicates that the double (3+3)mm and (4+2)mm plates give better protection than single (6mm) and triple (2+2+2)mm plate.

Chapter 6

6 Analysis of deformed plates (Mode I)

In this chapter the analysis of Domex 550MC and Domex 700MC plates of 4mm and 6mm thick configurations is given. The analysis of deformed plates contains displacement versus impulse graphs and deformation profiles of the plates tested at various charge masses. The deformations were compared with each other. The micro-structures of the plates before and after blast testing are studied.

6.1 Single plates of 4mm thickness (Domex 550MC)

Midpoint deflections of 4mm thick single plates at increasing impulses are shown in Figure 6-1. The midpoint deflection increases with increasing impulse (charge mass). Deformations in the blast tested plates from boundary to midpoint were measured at 10 mm intervals of radial distances for all the experiment to compare the deformation profiles of both the set of experiments (single and double plates). The deformation profiles of Mode I failure of all the single plates tested at different charge masses/impulses is shown Figure 6-2. At lower impulse (22 Ns), the plate deformation started 35mm away from the boundary and up to the midpoint as indicated in Figure 6-2. At higher impulses, plates deformed from boundary to midpoint with greater plastic deformation at the central point of the plates as depicted in Figure 6-2 for a charge mass of 23.5g.

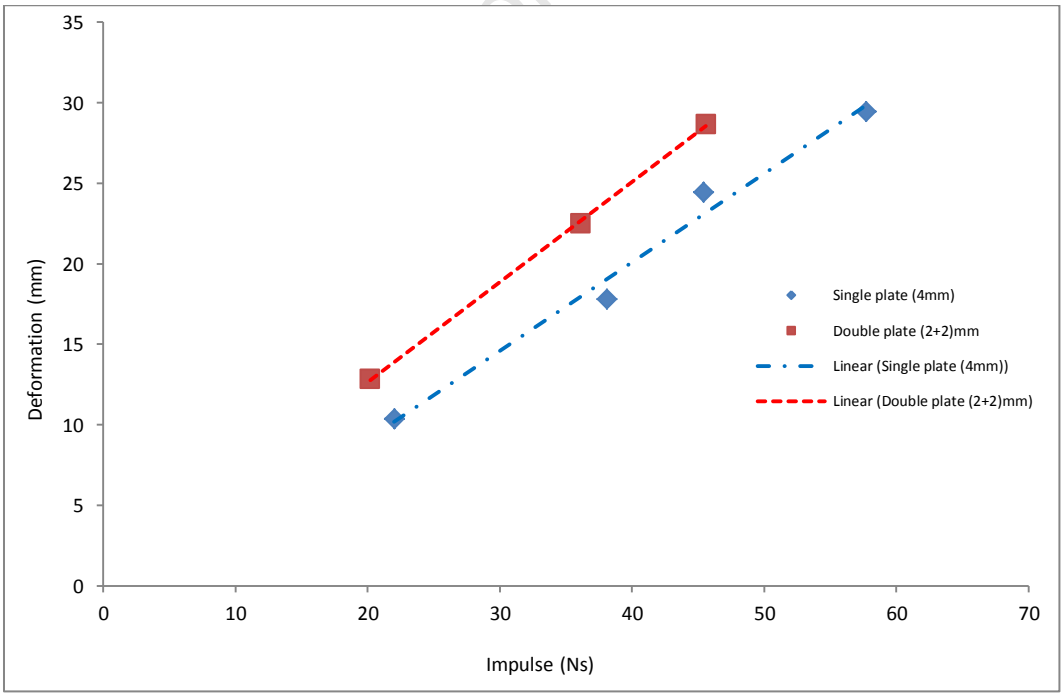

Figure 6-1: Graph to show the experimental displacements versus impulse of blast loaded 4mm thick single and double (2+2)mm plates (Domex 550MC)

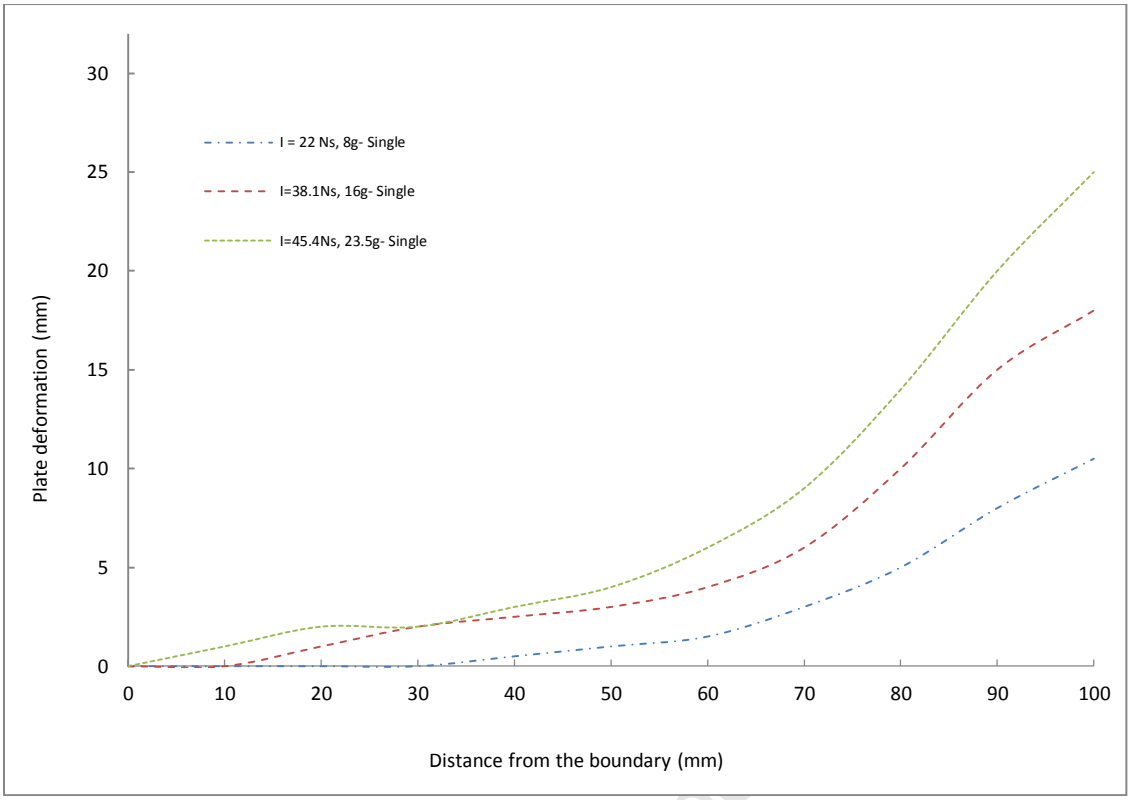

Figure 6-2: Deformation profiles of 4mm thick single plates (Domex 550MC)

6.2 Double (2+2)mm plates (Domex 550MC)

Permanent midpoint deflections of double plates are higher than the single plates at equal charge masses as shown in Figure 6-1. The deformation profiles of layered plates at various charge masses/impulses up to Mode I failure is shown Figure 6-3. Displacement due to the plastic deformation in layered plates was found to be less localized at all charge masses, compared to single plates. The displacements of the back plates are used for the construction of the deformation profiles. The deformation profiles of front and back plates are different depending on imparted impulse and discussed in Chapter 8.

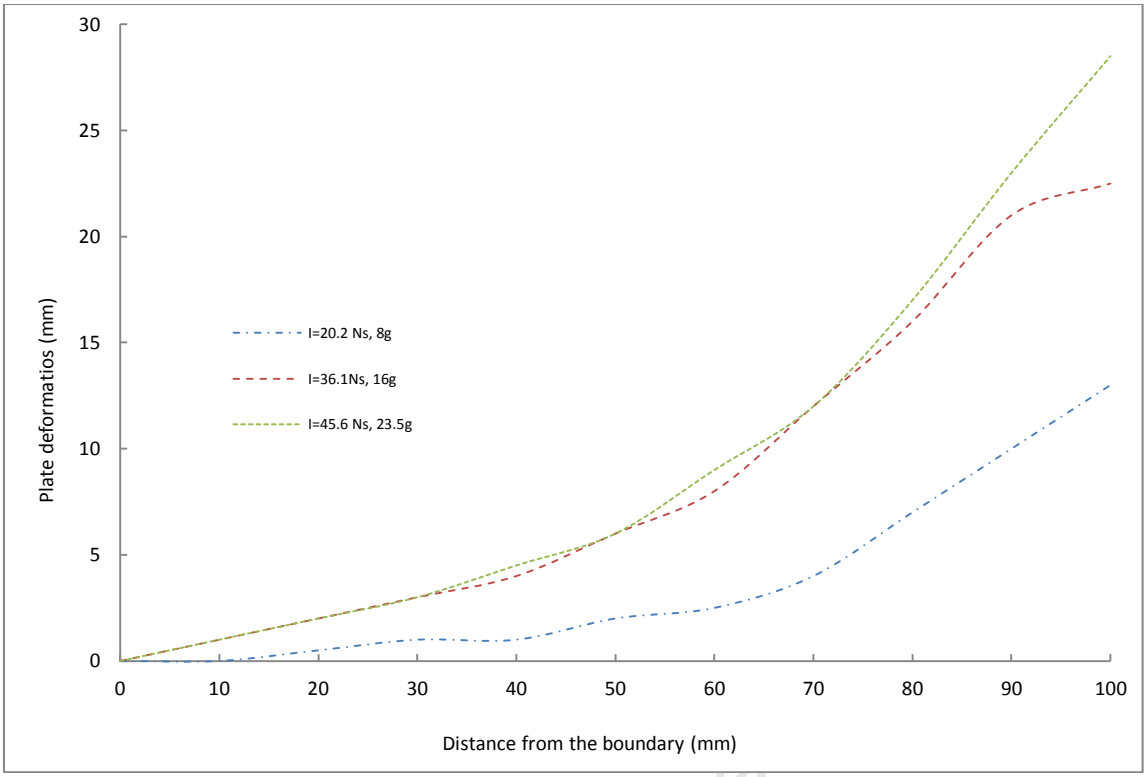

Figure 6-3: Deformation profiles of double (2+2)mm plates at increasing impulses (Domex 550MC)

6.3 Single plates of 4mm thickness (Domex 700MC)

Linear increase in midpoint deflections with the increase in charge mass was found in 4mm thick single plates of Domex 700MC. Increases in midpoint deflection with increasing impulses of single and double plates are shown in Figure 6-4. After blast testing, the deformations in all the plates from boundary to midpoint were measured at 5 mm intervals of radial distances for all the experiment of Domex 700MC steel to compare the deformation profile of both the set of experiments (single and double plates). The deformation profiles of all the 4mm thick single plates (up to Mode I failure) are shown in Figure 6-5. The plate deformations from boundary to midpoint increase with the increase in charge mass.

6.4 Double (2+2)mm plates (Domex 7000MC)

Permanent midpoint deflections of double (2+2)mm plates are higher than the single plates at equal charge masses as shown in Figure 6-4. The deformation profiles of layered plates at various charge masses/impulses up to Mode I failure are shown Figure 6-6. Displacement due to the plastic deformation in layered plates was found to be less localized at all charge masses, compared to single plates. The displacements of the back plates are used for the construction of the deformation profiles.

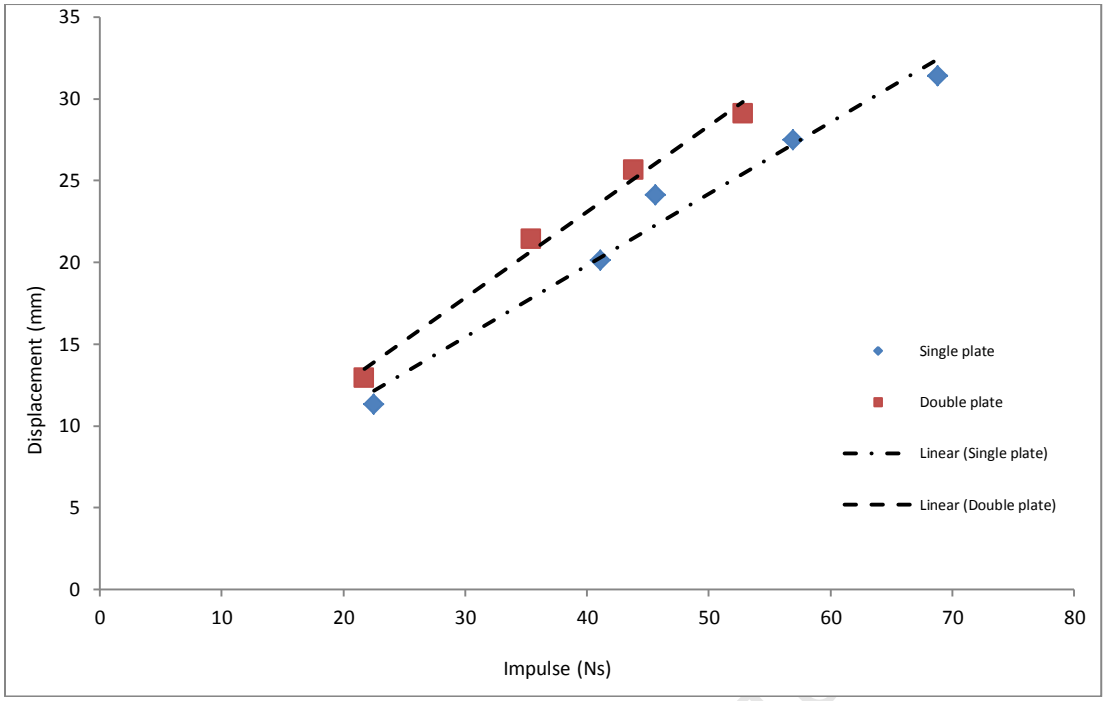

Figure 6-4: Graph to show the displacement versus impulse of blast loaded 4mm thick single and double (2+2)mm plates (Domex 700MC)

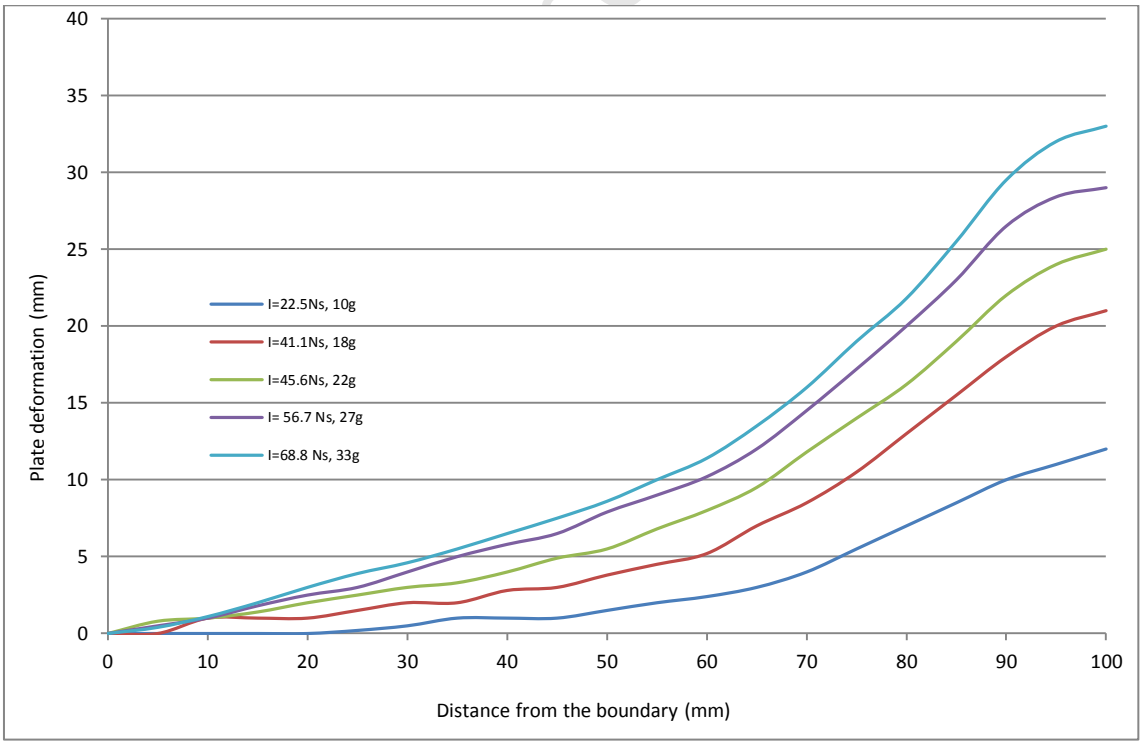

Figure 6-5: Deformation profiles (Mode I) of blast loaded 4mm thick single plates (Domex 700MC)

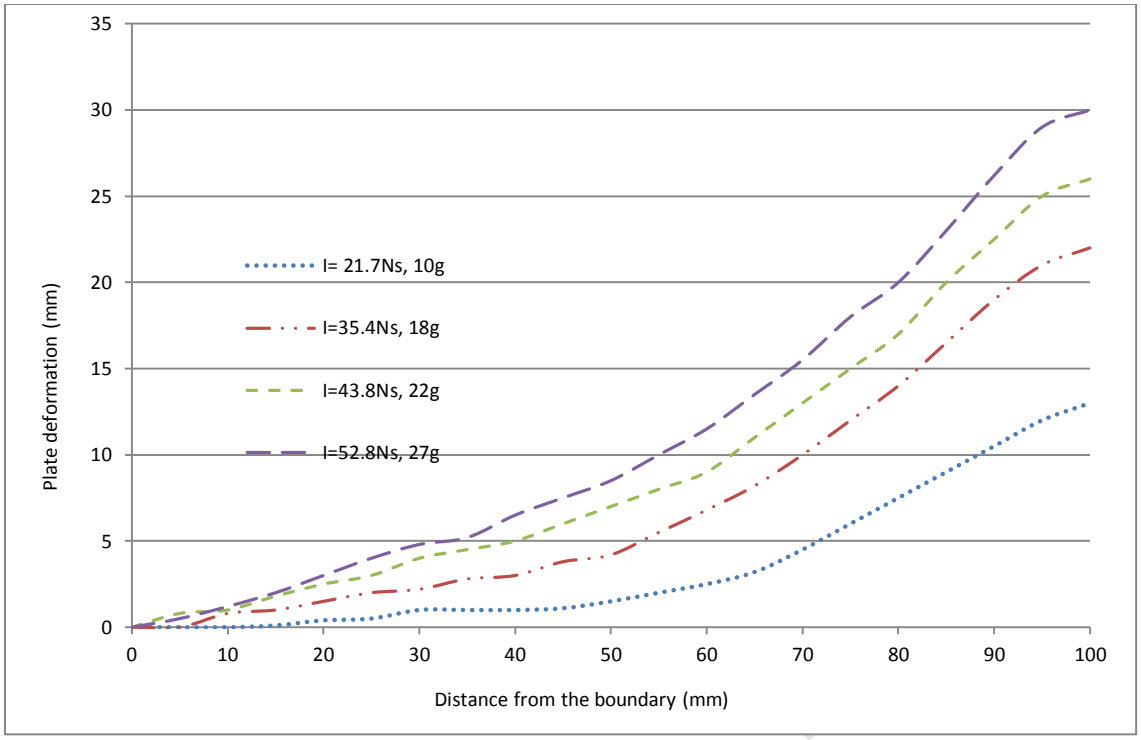

Figure 6-6: Deformation profiles (Mode I) of blast loaded double (2+2)mm plates (Domex 700MC)

6.5 Single plates of 6mm thickness

Midpoint deflections of 6mm thick single plates at increasing impulses up to Mode I failure are shown in Figure 6-7. The midpoint deflection increases by increasing the impulse/ charge mass.

Deformations in the blast tested plates from boundary to midpoint were measured at 5 mm intervals of radial distances. The deformation profiles of all the 6mm thick single plates for Mode I failure, tested at different charge masses/impulses are shown in Figure 6-8. Up to charge mass of 56g and an impulse of 103.5Ns, plates deformed by large inelastic response (Failure Mode I) and showed an inner dome at the middle of the plate over a global dome as indicated in Figure 6-9 and Figure 6-10. The deformation profiles in Figure 6-8, up to a charge mass of 56g are showing higher midpoint deflection and contribution of plastic deformation in midpoint deflection measurements, also indicated by the formation of an inner dome.

Chung Kim Yuen and Nurick [45] reported global and inner domes in built-in plates subjected to localized blast loading. In 6mm thick single plates the inner dome was not visible.

Reduction in thickness at midpoint (Mode Itc), less than the charge diameter was noted up to a charge mass of 50g. Thinning in the central area of mild steel plates subjected to localized blast loading was also reported by Nurick and Radford [33]. On further increasing the charge mass, necking started at a diameter of 40mm to 42mm.

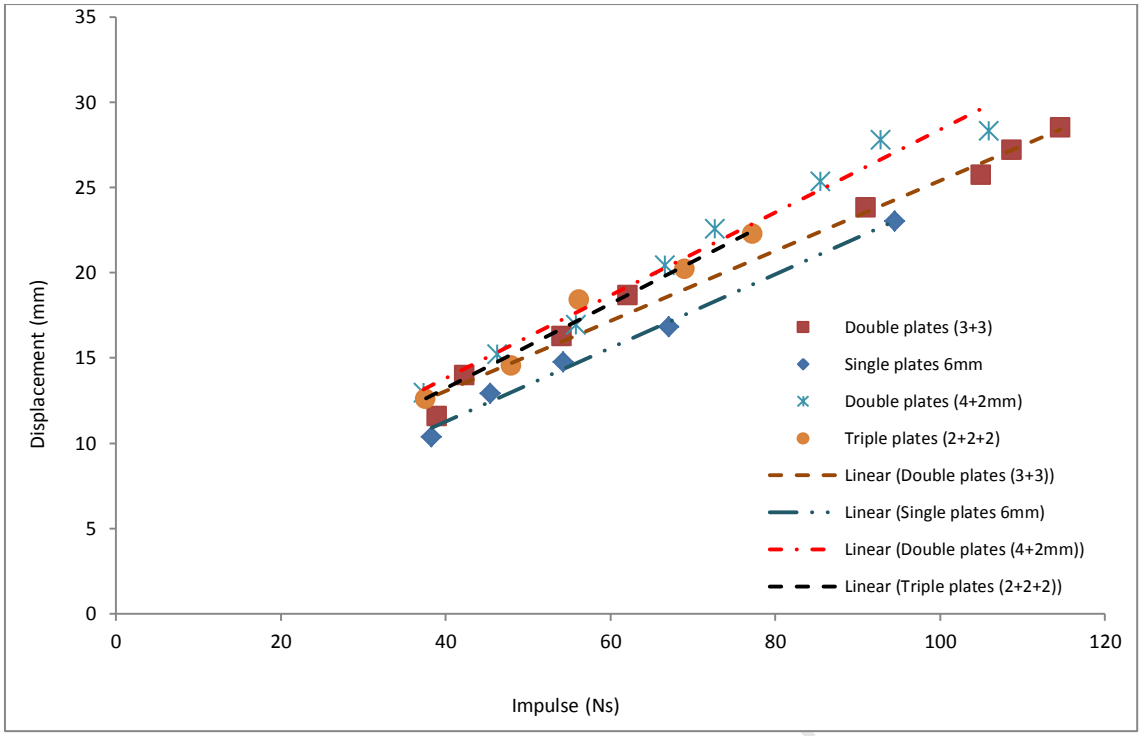

Figure 6-7: Graph to show the experimental displacement versus impulse of 6mm thick single, double(3+3)mm, double (4+2)mm and triple (2+2+2)mm plates (Domex 700MC)

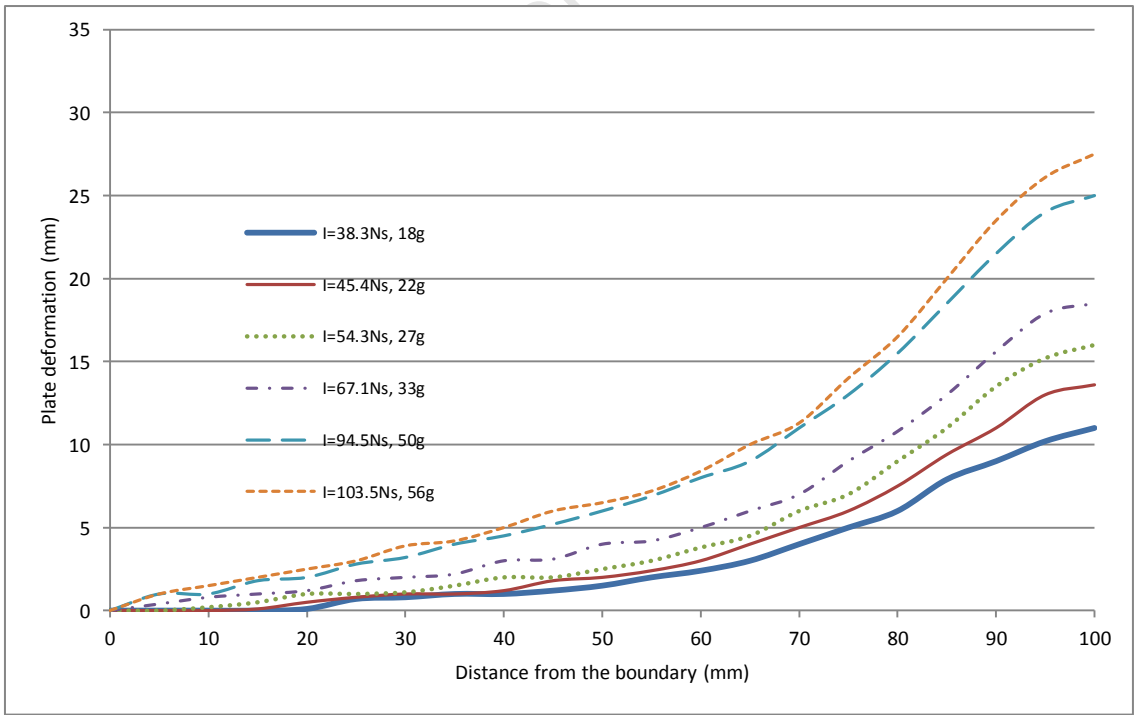

Figure 6-8: Graph to show the deformation profiles of blast loaded 6 mm thick single plates (Domex 700MC)

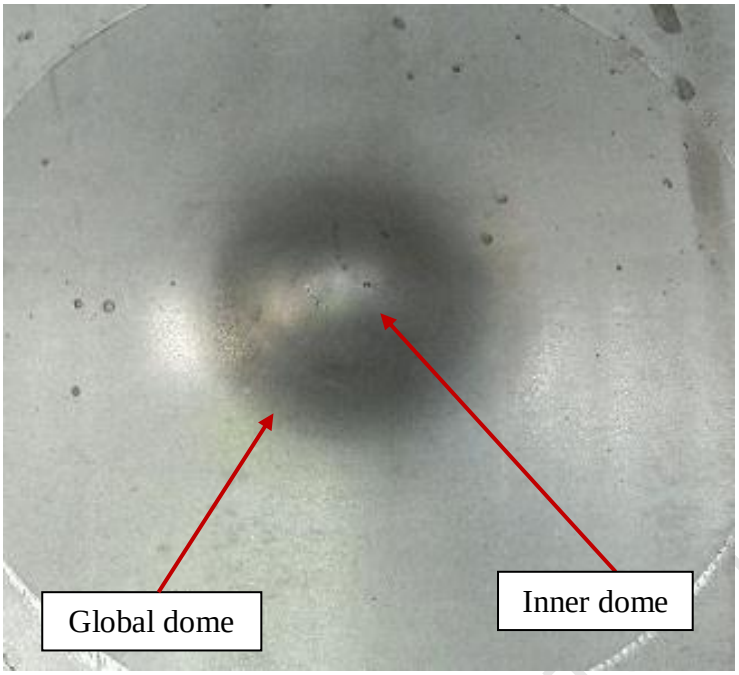

Figure 6-9: Photographs of 6mm thick single plate tested at a charge mass of 50g (57.7 Ns), showing inner and global domes

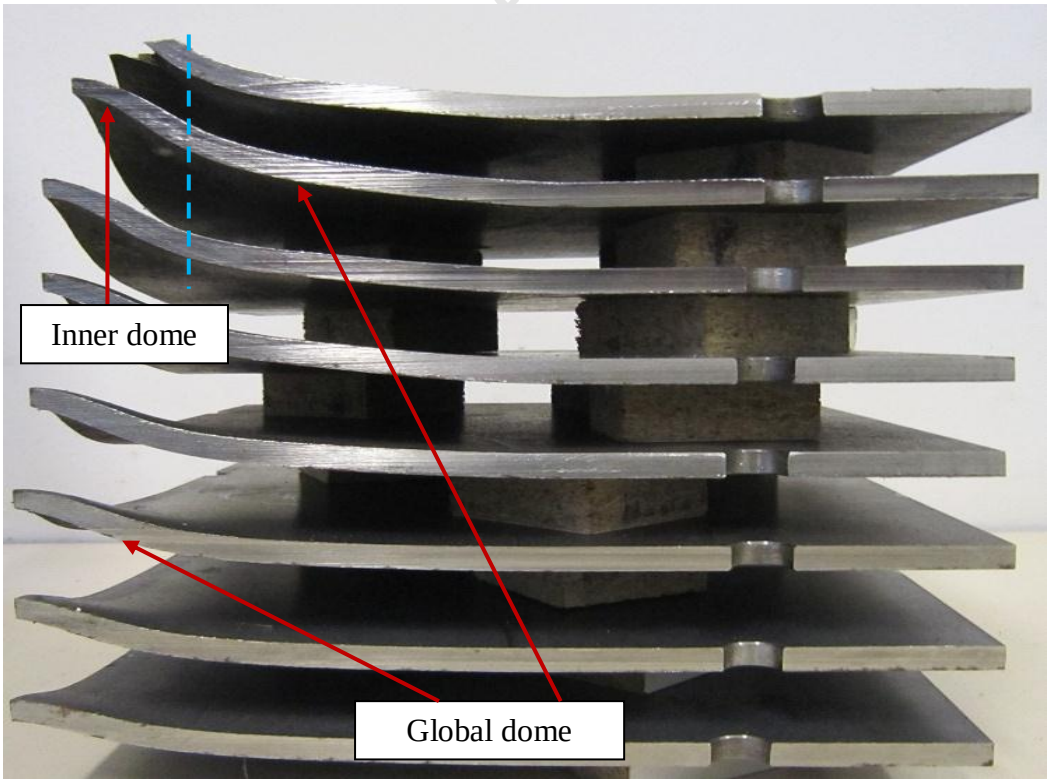

Figure 6-10: Photograph of the sectioned 6mm thick single plates show a formation of inner dome superimposed in a larger uniform global dome

6.6 Double (3+3)mm plates (Domex 700MC)

Permanent midpoint deflections of double (3+3)mm plates are greater than the 6mm thick single plates for equal charge masses. The increase in midpoint deflection with impulse is shown in Figure 6-7. The double (3+3)mm plate did not fail at any charge mass up to a charge mass of 68g, with the maximum permanent midpoint deflection of 28.48mm. At a charge mass of 62g, a small crack was observed in the front plate.

The deformation profiles of layered plates at various charge masses are shown Figure 6-11. The back plate deflections were used for the construction of deformation profiles. The magnitude of the deformation increased with the increase in charge mass. The profiles are indistinguishable at a charge mass of 56g and 62g, due to the similarity of the impulse.

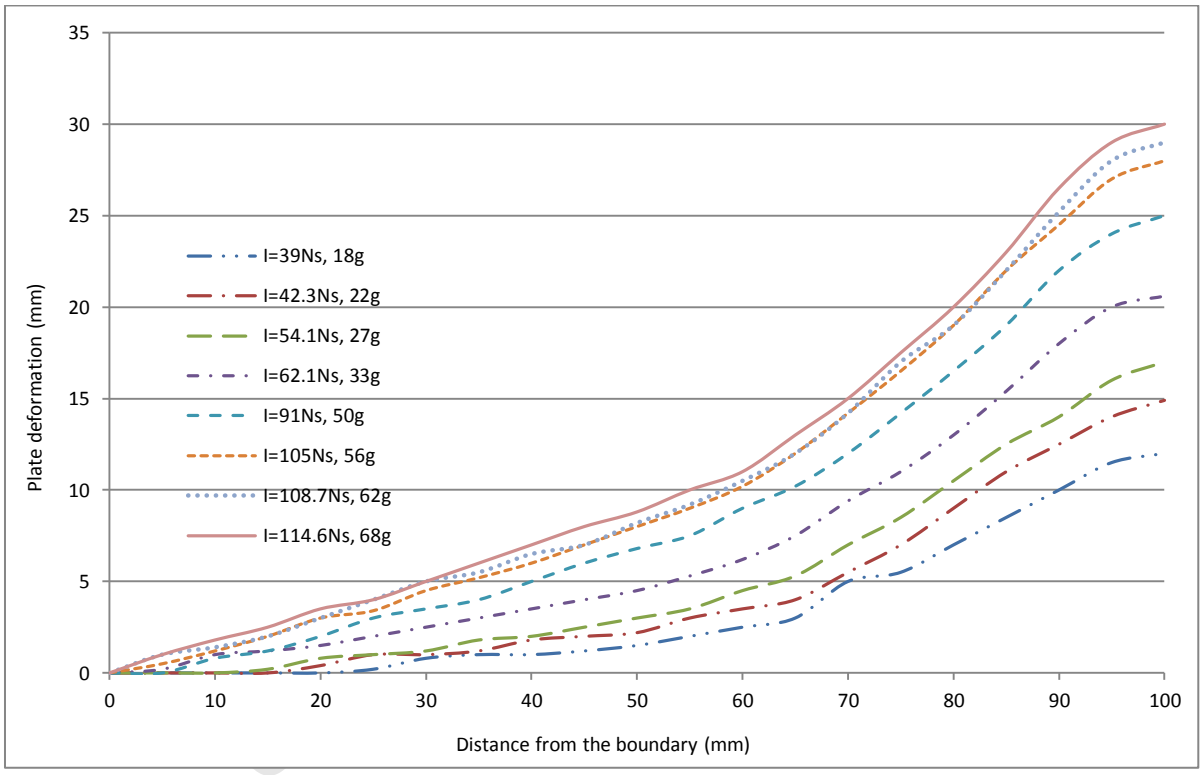

Figure 6-11: Deformation profiles of double (3+3)mm plates at increasing impulses (Domex 700MC)

6.7 Double (4+2)mm plate (Domex 700MC)

The increase in midpoint deflection in double (4+2)mm plates with the increase in impulse is shown in Figure 6-7. The double (4+2)mm plate did not fail by capping at any charge mass up to 74g. After the charge mass of 56g, minor cracks in front and back plates at a charge mass of 62g, 68g and 74g were observed.

The deformation profiles of double (4+2)mm layered plates at various charge masses are shown Figure 6-12. The deformation from the boundary to midpoint increased gradually with the increase in charge mass. Initially, a greater increase in midpoint deflection was noted up

to a charge mass of 50g. On further increase in charge mass, the difference in deflections from boundary to midpoint is not significant.

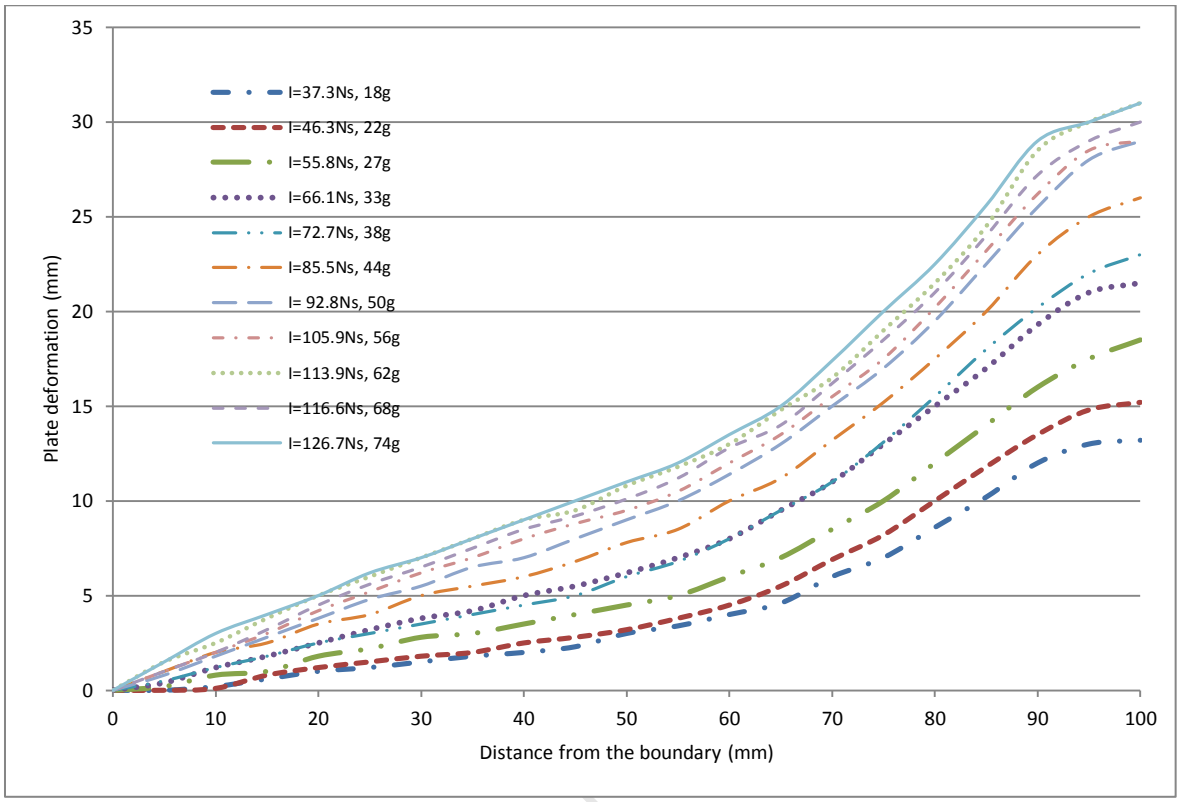

Figure 6-12: Deformation profiles of double (4+2)mm plates at increasing charge masses/impulses (Domex 700MC)

6.8 Triple (2+2+2)mm plates (Domex 700MC)

The increase in midpoint deflection in triple (2+2+2)mm plates with the increase in impulse is shown in Figure 6-7. The triple (2+2+2)mm plates started cracking at a charge mass of 44g.

The deformation profiles of triple (2+2+2)mm plates at various charge masses are shown Figure 6-13. The deformation from the boundary to midpoint increased gradually with the increase in charge mass up to 50g. On further increase in charge mass, the plates started cracking.

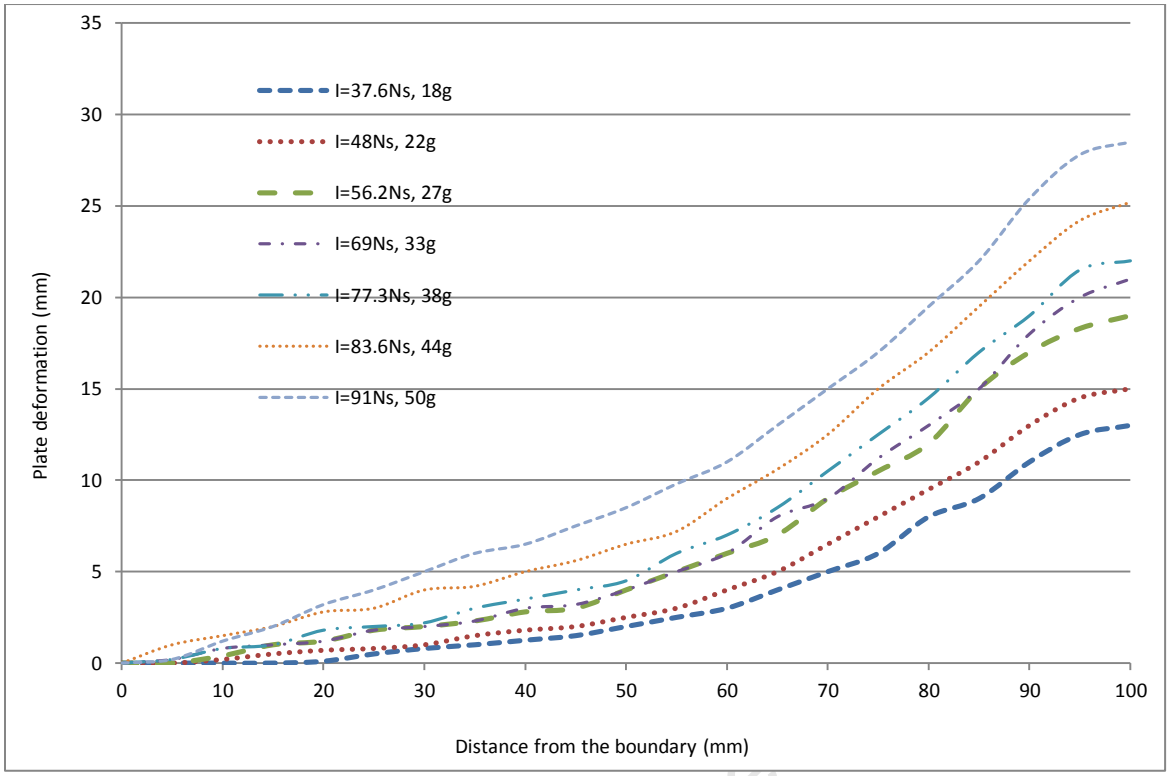

Figure 6-13: Deformation profile (Mode I) of triple (2+2+2)mm plates at increasing impulses (Domex 700MC)

6.9 Metallurgical Analysis

This part considers the metallographic study of as-received material and the micro-structural changes after blast testing. In blast loading experiments, the strain rates can be high as the order of $10^7 s^{-1}$. The presence of localized shear bands due to adiabatic heating have been reported in material deformed at high strain rates by many authors [95]. The purpose of this metallographic study was to investigate the effect of adiabatic heating due to blast loading of Domex 550MC and Domex 700MC steel plates over the charge diameter. The effect of the blast loading on the grain size variations of the microstructure of Domex 550MC was studied at various impulses.

A metallographic study of single and double layered plates of Domex 550MC and single, double and triple layered target plates of Domex 700MC was carried out before and after the blast tests for selected portions of deformed and torn regions. All the plates were used in the as-received condition for blast tests. The samples for microscopy before and after blast testing were carefully obtained from the area of interest by using coolant to avoid heating during sampling. Highly deformed and torn regions of all the plates after blast testing were considered for metallographic study. The samples were mounted and mechanically polished, adopting standard metallographic techniques. In order to reveal different phases, polished samples were etched in a 2% nital solution for approximately 20 seconds.

The detailed metallographic observations of Domex 550MC and Domex 700MC steel plates are given below

6.9.1 Micro-structural study of Domex 550MC plates

The microstructures of virgin 4mm and 2mm thick plates (as-received) of Domex 550MC are shown in Figure 6-14a and Figure 6-15a respectively. These microstructures consist of equiaxed fine grains of ferrite and a minute quantity of pearlite at the grain boundaries.

The microstructures of the single and double plates subjected to various impulses are shown in Figure 6-14 (b, c, d) and Figure 6-15 (b, c, d) and are composed of deformed grains of ferrite. These deformed grains are due to plastic deformation during blast loading at a range of impulses. The effect of the blast loading on the grain size of the microstructure was also studied at various impulses. The grain size was measured by using optical microscope, along the deformation direction towards the centre of plate to study the effect of increasing impulses on microstructures. The increase in elongation of deformed grains was found to increase as the charge mass increases.

The average grain size of 4mm and 2mm thick steel plates after blast loading at different impulses is shown in Table 6-1 and Table 6-2 respectively. The average grain sizes of as-received 4mm and 2mm thick plate were 7.5 and 4 microns correspondingly. The grain sizes of both the plates increased with increasing charge mass as indicated in Table 6-1 and Table 6-2. Midpoint deflection thickness ratio versus normalized grain size graph indicates the initial increase in grain size of 2mm thick plate is greater than of 4mm thick plate, as approaching to capping failure, final grain size seems similar in both plates depicted in Figure 6-16. Increase in grain size in the 4mm thick plates exhibited a linear trend with increasing impulse, as shown in Figure 6-17. In case of 2mm thick plates, the initial increase in grain size is greater than in 4mm thick plates and starting grain size is also smaller than the 4mm thick plate, whereas at higher impulses, increase in grain size becomes linear with the impulse as shown in Figure 6-17.

The metallographic investigations of the single and double blast tested torn plates was also carried out. In these plates, torn regions near the crater peripheries are considered. The microstructures of the torn plates due to localized blast loading near the crater peripheries of single and double plates are shown in Figure 6-14d and Figure 6-15d. All the microstructures composed of a ferritic phase and elongated grains. The presence of martensitic microstructure around the torn region of blast tested plates is not revealed in micro-structural study, demonstrating that the temperature of the plates at all charge masses remained below transformation temperatures.

(a) As-received

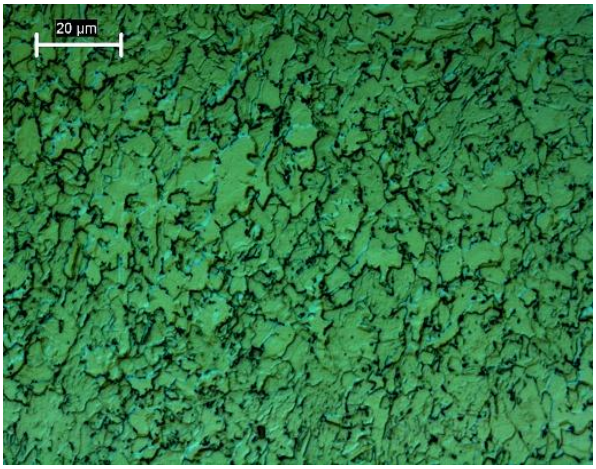

(b) Microstructure at 22 Ns (8g)

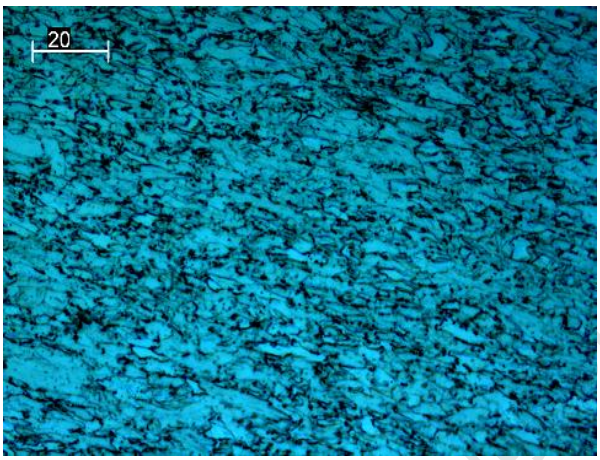

(c) Microstructure at 45.4 Ns (23.5g)

(d) Microstructure at 63.4 Ns (37.5g)

Figure 6-14: Microstructures of 4mm thick plate (Domex 550MC) at various impulses, etched in 2% nital.

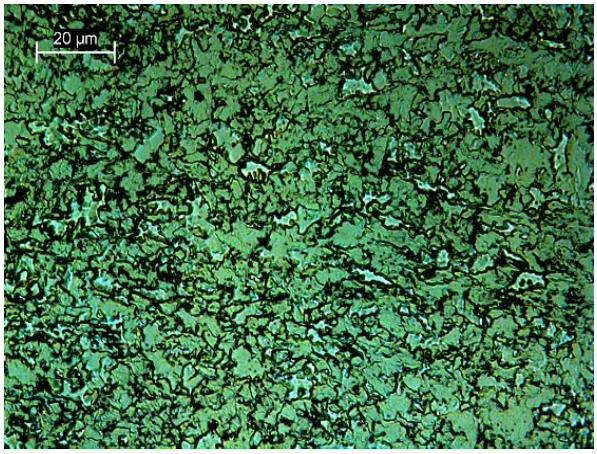

(a) As-received

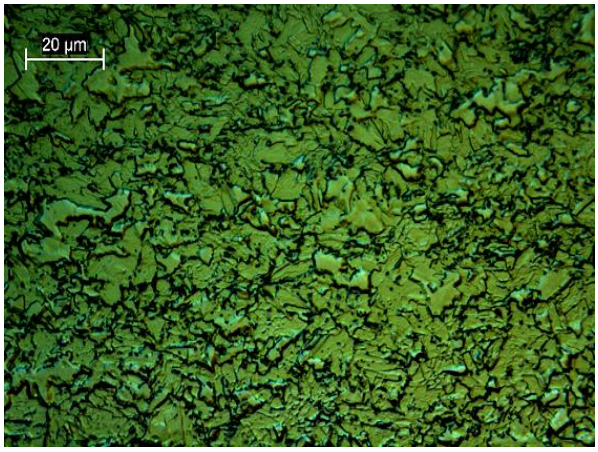

(b) Microstructure at 20.2 Ns (8g)

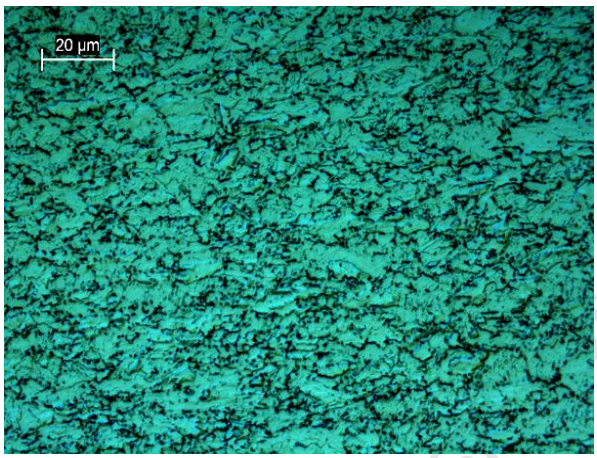

(c) Microstructure at 45.6 Ns (23.5g)

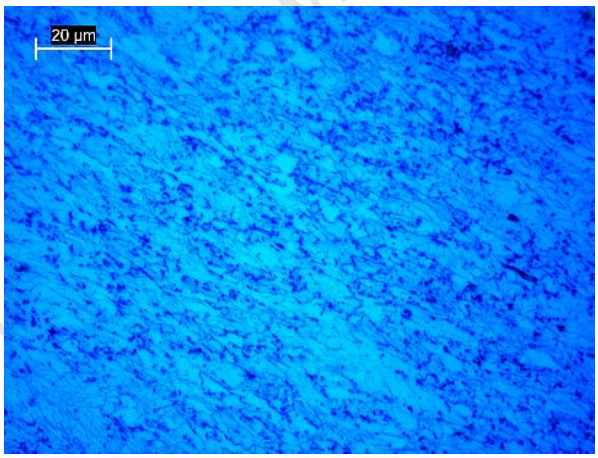

(d) Microstructure at 61 Ns (37.5g)

Figure 6-15: Microstructures of 2mm thick plate (Domex 550MC) at various impulses, etched in 2% nital

Table 6-1: Grain sizes of 4mm thick single plate (Domex 550MC) towards the midpoint at different charge masses

Charge mass (g)	Mean average grain size (micron)	Standard Deviation	Maximum grain size (microns)	Minimum grain size (microns)	Normalized grain size
As-received	7.5	1.88	12	4	1
7 + 1 = 8	9	2.2	25	6	1.24
15 + 1 = 16	11	3.36	21	7	1.48
22.5 + 1 = 23.5	12	3.8	22	7	1.6
29+1= 30	13	4.5	24	5	1.7
36.5 + 1=37.5	14.2	4.5	23	8	1.9

Table 6-2: Grain sizes of 2mm plate (Domex 550MC) towards the midpoint of plates at different charge masses

Charge mass (g)	Grain size (micron)	Standard deviation	Maximum grain size (microns)	Minimum grain size (micron)	Normalized grain size
As-received	4	1.6	11	3	1
7 + 1 = 8	10	2.46	16	6	2.4
15 + 1 = 16	---	---	---	---	----
22.5 + 1 = 23.5	13.3	3.6	21	6	3.17
29+1= 30	14.3	3.9	23	8	3.4
36.5 + 1=37.5	15.1	4.1	23	8	3.5

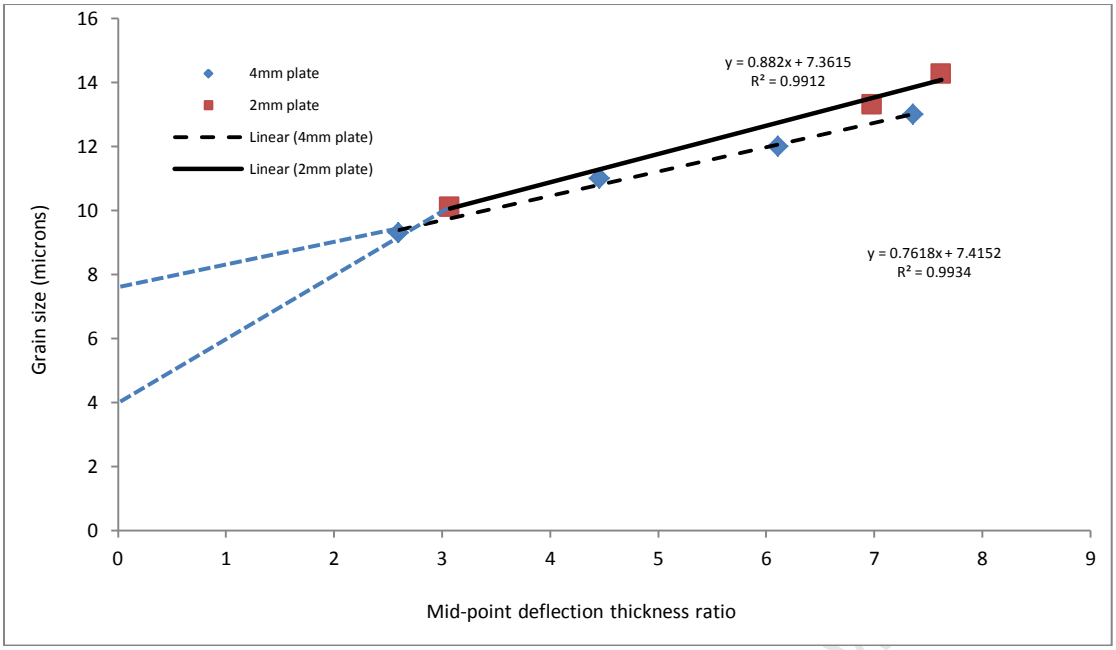

Figure 6-16: Graph to show the midpoint deflection thickness ratio versus grain size of 4mm and 2mm thick plates (Domex 550MC)

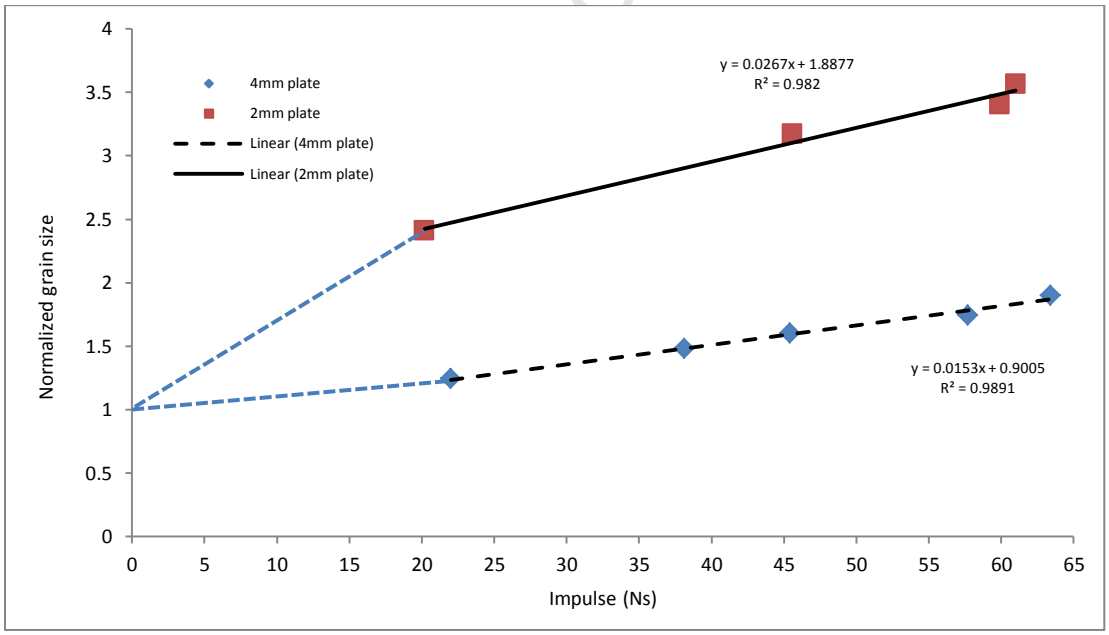

Figure 6-17: Graph to show the effect of impulse on the grain size of 4mm and 2mm thick plates (Domex 550MC)

6.9.2 Micro-structural study of Domex 700MC plates

A metallographic study of single 6mm thick, double (3+3)mm, (4+2)mm and triple (2+2+2)mm layered target plates was carried out before and after the blast tests for selected portions of deformed and torn regions.

The microstructure of virgin (as-received) steel plates in both the directions is shown in Figure 6-18a and b and consisted of equiaxed fine grains of ferrite. The average grain size of the virgin material is 4 microns. The focus of the micro-structural study on Domex 700MC was the fractography, as grain size elongation has been reported already for Domex 550MC and was not the focus of the thesis.

The highly deformed grains of the plate tested at 33g charge mass are shown in Figure 6-19. This image shows strong shear localization that occurred during localized blast loading. Shear localization in torn regions of 4mm thick plate tested at 33g charge mass at different magnifications is also shown in Figure B-1, Figure B-2 and Figure B-3 in "Appendix B".

Figure 6-20a and b are showing microstructures of the torn regions of 4mm thick single steel plate tested at 38g. The width of the localized regions can be approximated from 15 to 40 microns from SEM images shown in Figure 6-20a and b. The microstructures are unaffected further away from these localized narrow zones.

Figure 6-21 and Figure 6-22 show the inter-granular and trans-granular fracture path in the micro-structure of 4mm and 6mm single steel plates of Domex 700MC, tested at 38g and 56g charge masses respectively. The mode of failure during the blast loading was mostly inter-granular and in some samples mixed mode of failure was found as indicated in Figure B-4 and Figure B-5 "Appendix B".

Figure 6-23 shows microstructure of the torn regions of 6mm thick single steel plates. The width of the localized deformed regions in 6mm single plates can be approximated from 6 to 15 microns from SEM images in Figure 6-23. The deformed zone in 6mm torn plate was found to be narrower than in the 4mm thick plates. The microstructures are unaffected further away from these localized narrow zones and the effect of shearing decreased gradually moving away from the crack as shown in Figure B-6 of "Appendix B".

The carbon content of the considered alloy steels is 0.12 % as indicated (by the line A- Á) in Iron –Iron carbide phase diagram shown in Figure 2-23. At this composition, the Domex 550MC and Domex 700MC contain 87.17% ferrite and 12.8% of pearlite at room temperature with a lamellar aspect. The material transforms from (ferrite + pearlite) to austenite at 723 ^{o}C. The temperature of complete transformation of (ferrite + pearlite) to austenite varies approximately from 723 to 890^{o}C for Domex 550MC and Domex 700MC. Rapid cooling of a material from austenite region results in a martensitic microstructure whereas slow cooling results the microstructure composed of ferrite and pearlite.

In high strain rate deformations like in localized blast loadings and projectile impact, the temperatures of the material can increase up to austenitic region in micro-seconds followed by quenching by the surrounding bulk material. A rise in temperature up to 762°C in the torn region was also reported by Langdon et al. [61] and Wiehahn et al. [59] during the adiabatic analysis of locally loaded mild steel plates by using ABAQUS/ Explicit version 5.8.

The microstructures of Domex 550MC and Domex 700MC blast tested plates at all the charge masses showed ferrite + pearlite and deformed regions of localized bands. The presence of deformed zones in the microstructure demonstrates that the temperature of the Domex plates at all charge masses remained below transformation temperatures. Previous study on adiabatic shear localization by Bai and Dodd [95] and Raftenberg and Krause [93] indicated that these shear bands may either consist of deformed material or transformed material depending on the temperature of local area due to adiabatic heating. Deformation bands are regarded as zones of intense plastic shear whereas transformation bands are zones of intense shear in which a phase transformation has occurred. The dendritic microstructure results in iron alloys, solidified from molten state and the rapid cooling from austenite results in a martensitic microstructure. The presence of martensitic or the dendritic microstructure around the torn region of blast tested plates is not revealed in the current study.

The current study on the locally blast loaded plates did not reveal any transformed region as reported by Raftenberg and Krause [93] as a result of heat generated during tearing. This means that the temperature of torn regions of blast tested plates due to adiabatic heating did not reach up to the phase transformation temperature or melting point of material in current experiments.

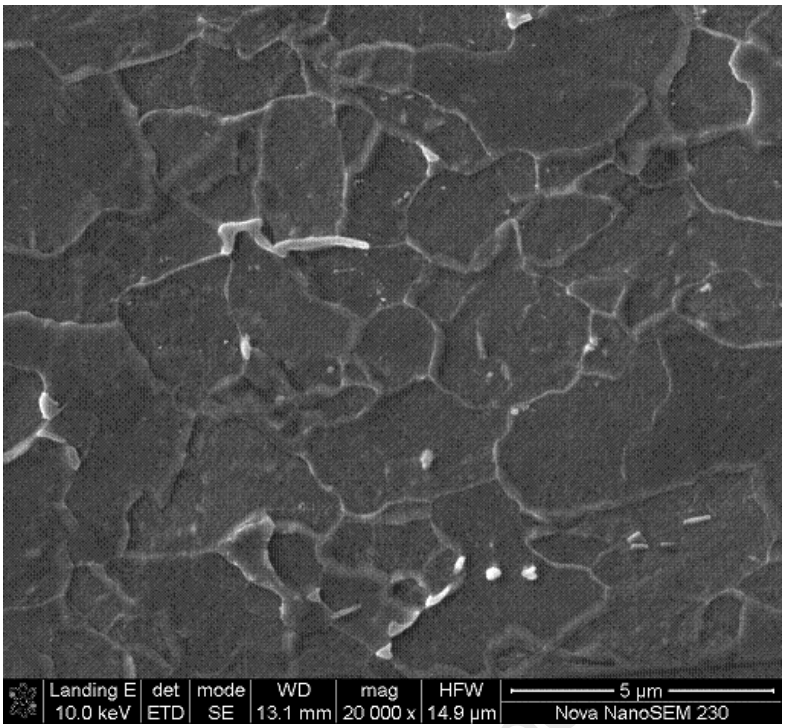

(a) Micro structure (along the rolling direction)

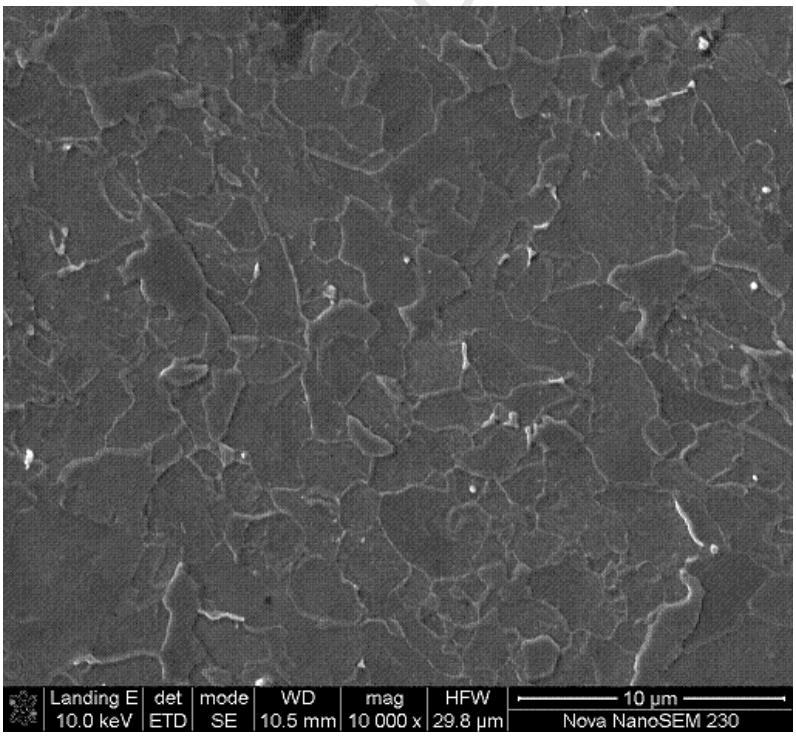

(b) Micro-structure (across the rolling direction)

Figure 6-18: Microstructures of Domex 700MC steel plates, etched in 2% nital

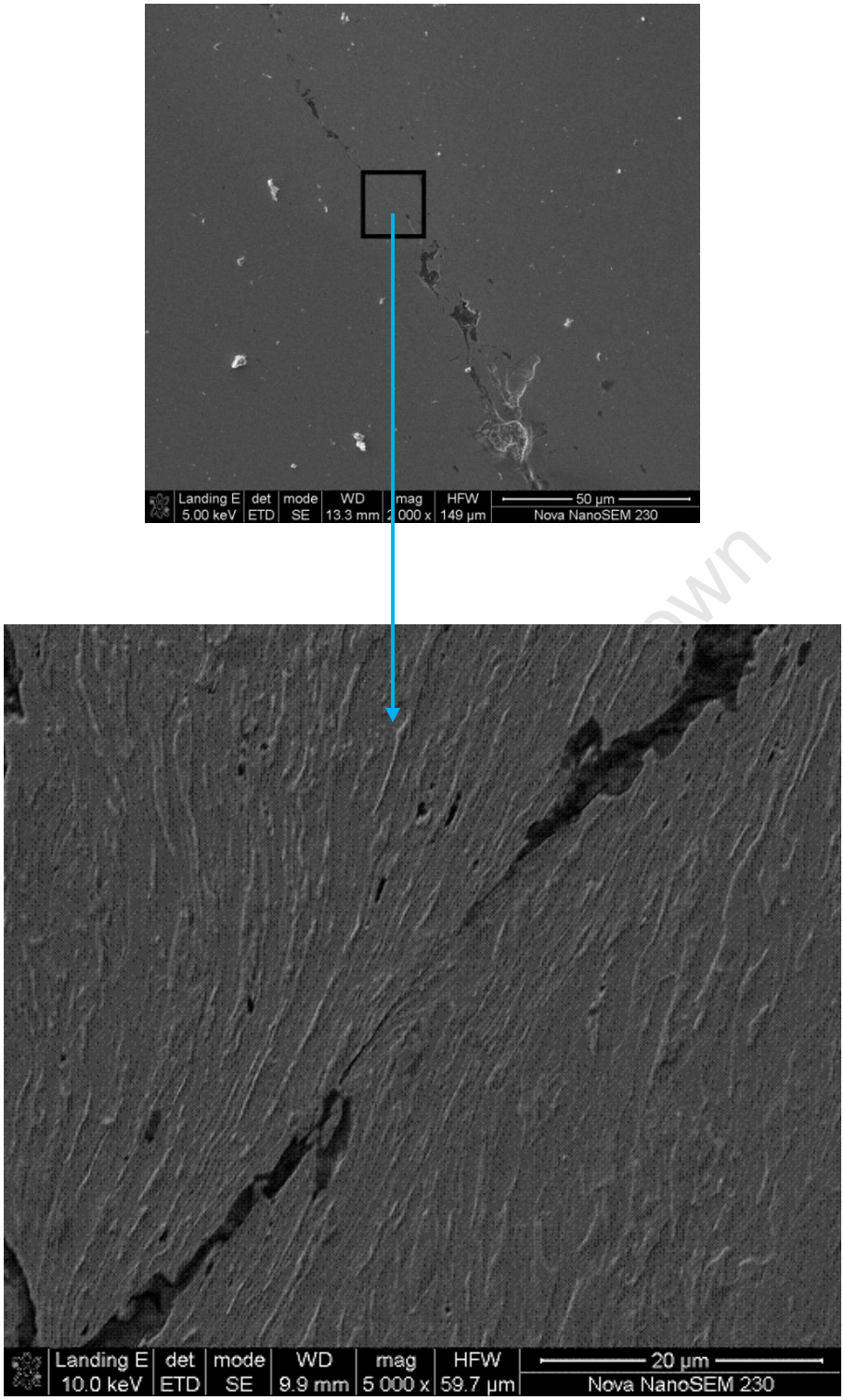

Figure 6-19: Microstructures of 4mm thick single plates of Domex 700MC (m=33g, I=68.8 Ns), etched in 2% nital

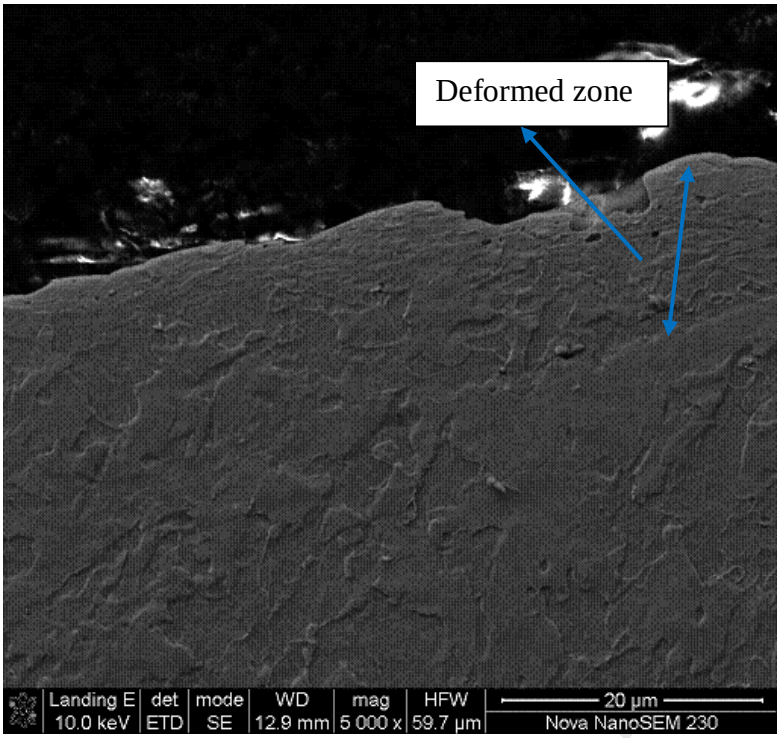

(a)

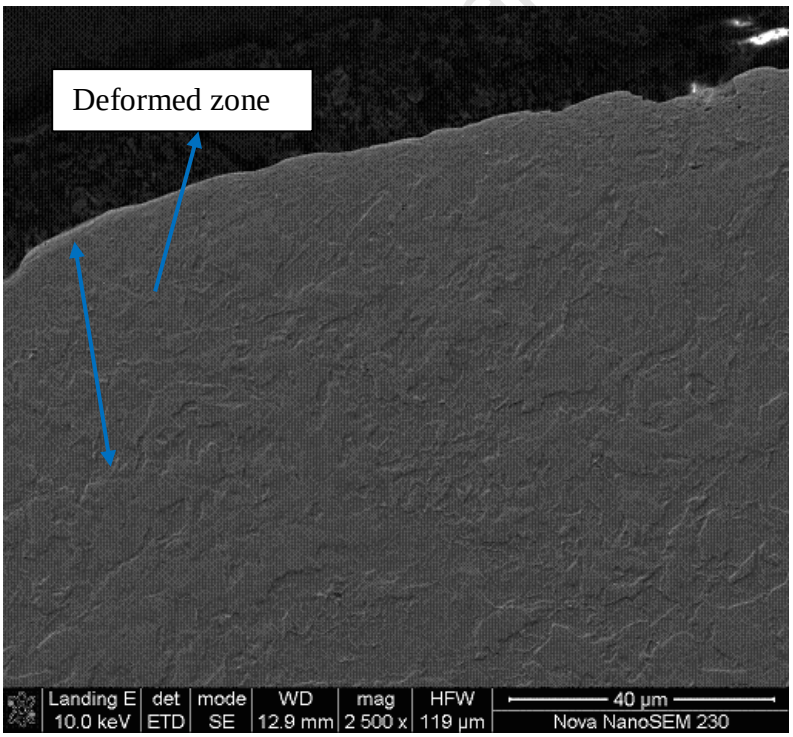

(b)

Figure 6-20: Microstructures of 4mm thick single plates of Domex 700MC (m=38g, I=81.7 Ns), showing effected zone after blast test, etched in 2% nital

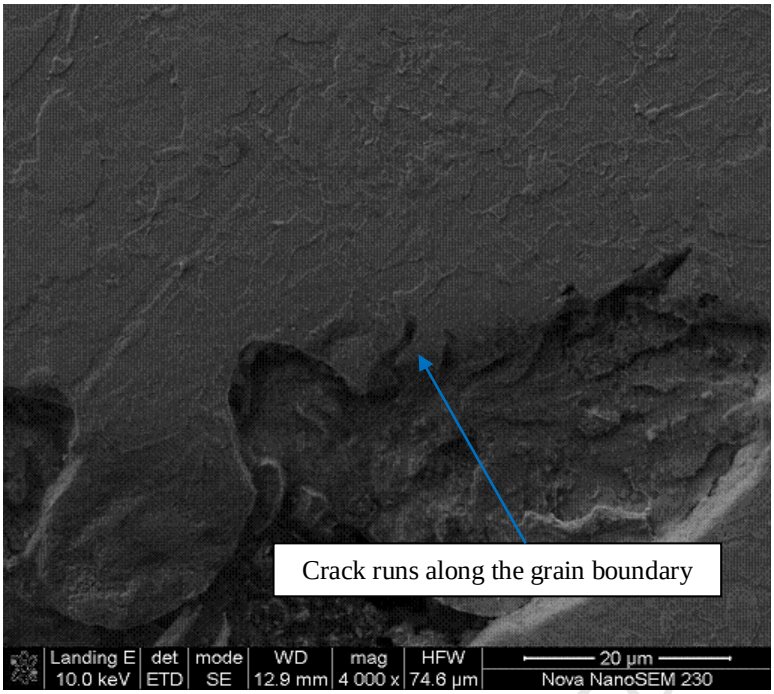

Figure 6-21: Microstructures of 4mm thick single plates of Domex 700MC (m=38g, I=81.7 Ns), shows inter-granular and trans-granular fracture

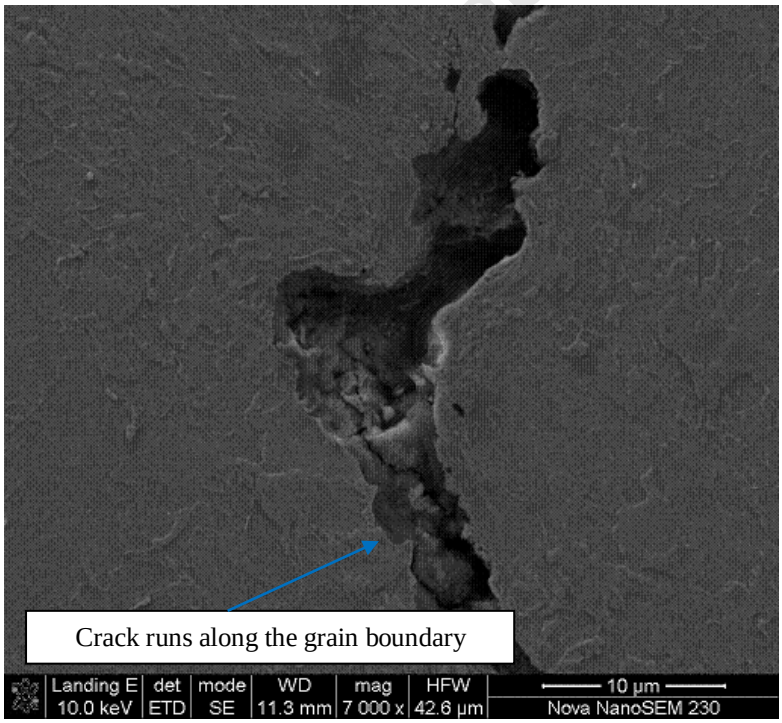

Figure 6-22: Microstructures of 6mm thick single plates of Domex 700MC (m=56g, I=103.5Ns), shows inter-granular and trans-granular fracture

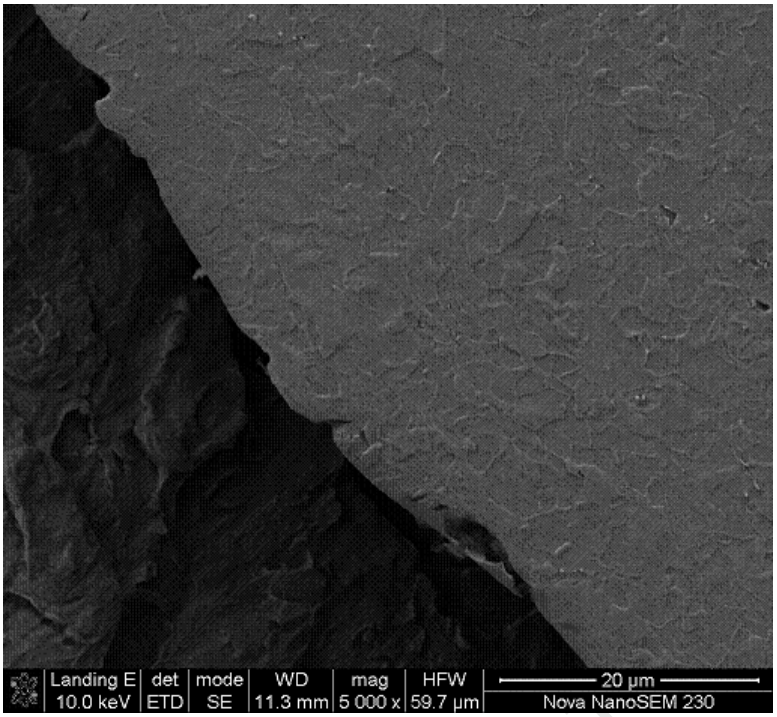

(a)

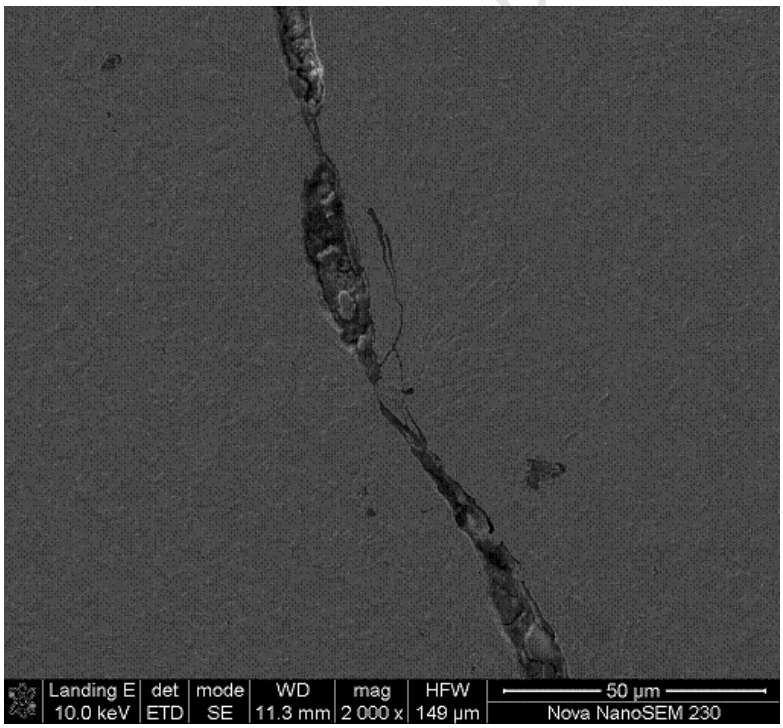

(b)

Figure 6-23: Microstructures of 6mm thick plates of Domex 700MC (m=56g, I=103.5Ns), etched in 2% nital

6.10 Summary

Experimental study of 4mm configurations of Domex 550MC and Domex 700MC plates subjected to localized blast loads was carried out. It was noted that midpoint deflection of the layered plates is greater than the single plates for equal charge masses for both the materials. The plastic deformations in the plates as a result of blast loads are less localized up to the boundary in double layered plates. The deformations are more concentrated in the central region in the single plates.

The comparison of all the configurations of 6mm thickness, namely 6mm single, double (3+3)mm, double (4+2)mm and triple (2+2+2)mm indicates that the plastic deformations of (4+2)mm configuration at all charge masses is greater than the other three configurations. The single 6mm thick plate configurations deformed less than the other configurations.

The microstructures of Domex 550MC and Domex 700MC blast tested plates composed of ferrite + pearlite and deformed regions of localized bands. Grain size increases with the increase of impulse (Domex 550MC). Deformation zone is narrower in 6mm thick plates compared to 4mm thick plates of Domex 700MC. Inter-granular and mixed mode of failure were exhibited by blast loaded plates.

Chapter 7

7 Analysis of fractured plates (Mode II)

This chapter is composed of two parts. The first part presents the macro observations on the plates, failed in Mode II. The second part deals with the fractography of selected torn plates of Domex 700MC. Two configurations of 4mm thickness (4mm single and double 2+2mm) and the four configurations of 6mm thickness (6mm single, double (3+3)mm, (4+2)mm and triple (2+2+2)mm were considered.

The fractographic features of the blast tested plates at different charge masses were compared with fractured surfaces of the tensile samples tested at three different quasi-static strain rates given in Chapter 3.

7.1 Analysis of 4mm thick single torn plates (Domex 550MC)

Partial tearing of 4mm thick single plates started at a charge mass of 30g over a charge diameter (33mm) as shown in Figure 7-1. Capping failure was observed at a charge mass of 44g as indicated in Figure 7-2. The diameter of the cap was 26mm (that is 7mm less than charge diameter). In case of mild steel circular plates subjected to localized blast loads, the diameter of the cap was equal to the charge diameter, previously reported by Nurick and Radford [33] and Wierzbicki and Nurick [46].

Figure 7-1: Photographs of 4mm thick single plate (m=30g, I=57.7 Ns), show a partial tearing

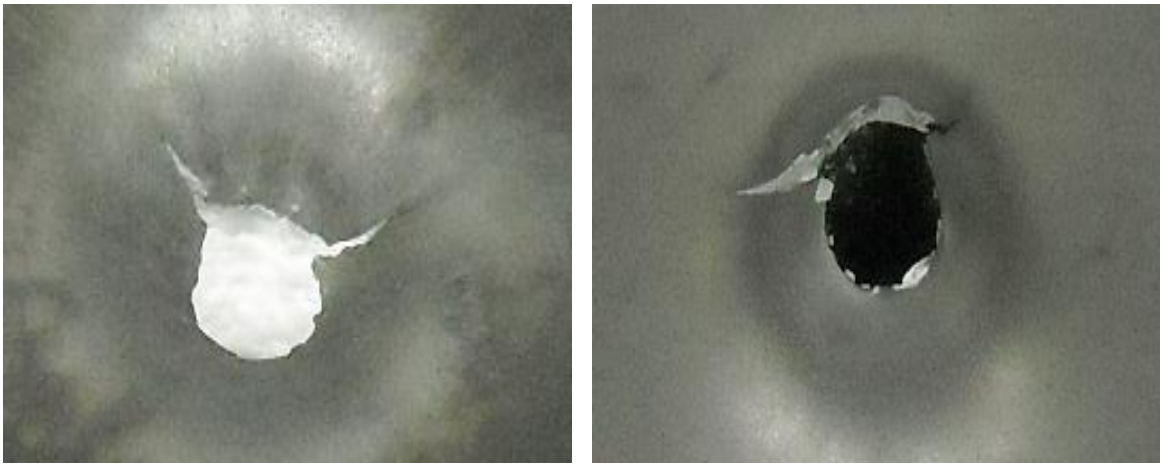

(a) Front face (b) Back face

Figure 7-2: Photographs of 4mm thick single plate (m= 37.5g, I=63.4 Ns), showing capping failure

The deformation profiles of the torn plates (tested at charge masses of 30g and 37.5g) are shown Figure 7-3. The 30g test plate was plotted up to crack location whereas the the profile of the plate tested at 37.5g was drawn up to the cap diameter. The profiles are very similar to each other, but significantly different to the Mode I profiles shown in Figure 6-2.

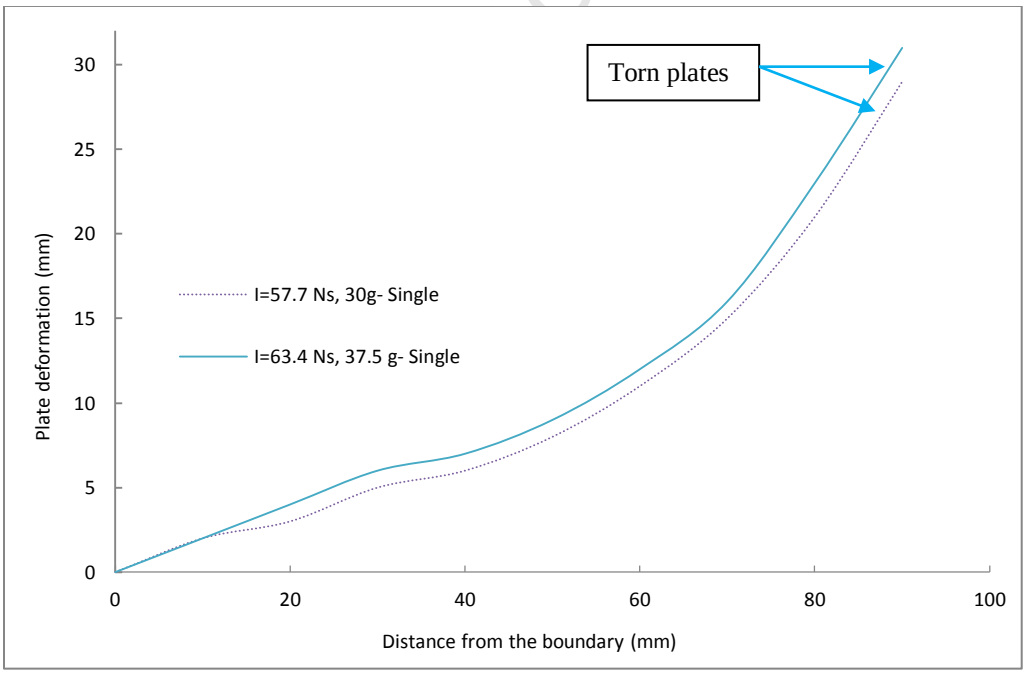

Figure 7-3: Deformation profiles of 4mm thick single torn plates (Domex 550MC)

The response of the plate tested at a charge mass of 30g can be considered as a transition mode from failure Mode I to Mode II. The response of all the configurations can be classified as pre-threshold impulse and post-thereshold impulse behaviours, since the responses are different in each group. The transition between the failure Modes-I and Mode-II was defined

as Mode II* by Langdon et al. [35]. The impulse at which Mode II* occurs is the threshold impulse.

7.2 Analysis of double (2+2)mm torn plates (Domex 550MC)

Partial tearing of double (2+2)mm plates started at a charge mass of 23.5g in the back plates, but without the front plate being torn, as depected in Figure 7-4. At a charge mass of 30g, the back plate was fully capped and the partial tearing occurred in front plate as indicated in Figure 7-5. The front and the back plates were capped at a charge mass of 37.5g as shown in Figure 7-6b and c. The cap diameters of front and back plates were 28.5mm and 29.5mm respectively and also can be partly seen in Figure 5-5. The cap diameters are 4mm to 5mm less than the charge diameter.

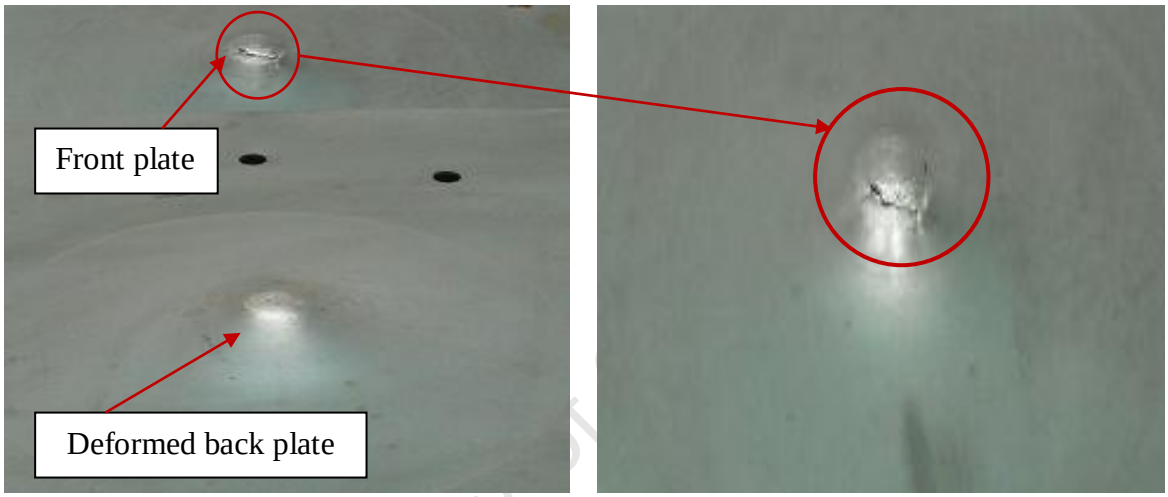

Figure 7-4: Photographs of double (2+2)mm plates (m=23.5g, I= 45.6Ns), showing partial tearing in the front plate and deformation in the back plate

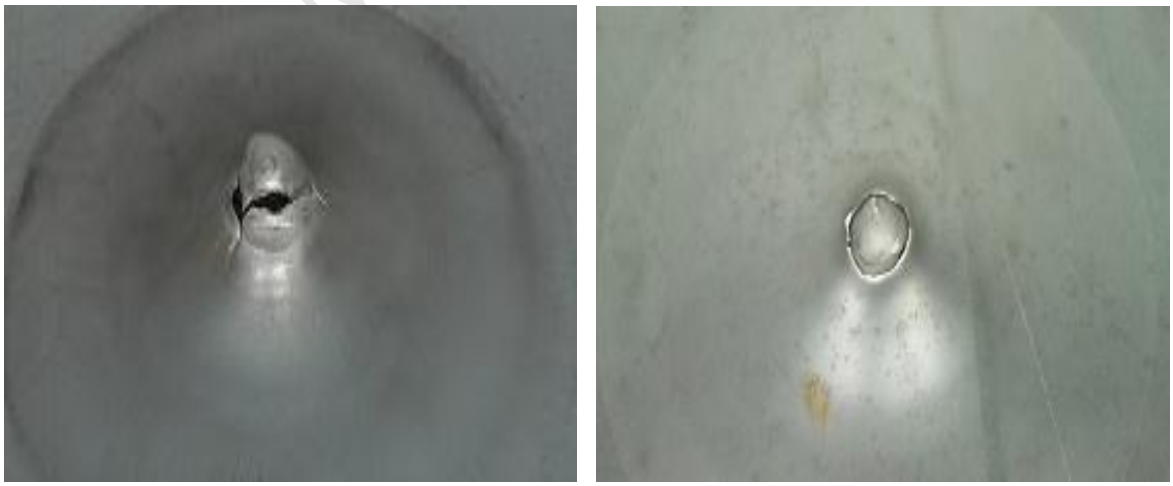

Front plate Back plate

Figure 7-5: Photographs of double (2+2)mm plates (m=30g, I= 59.9 Ns), showing partial tearing of front plate and capping failure of back plate

(a)

(b) Front plate

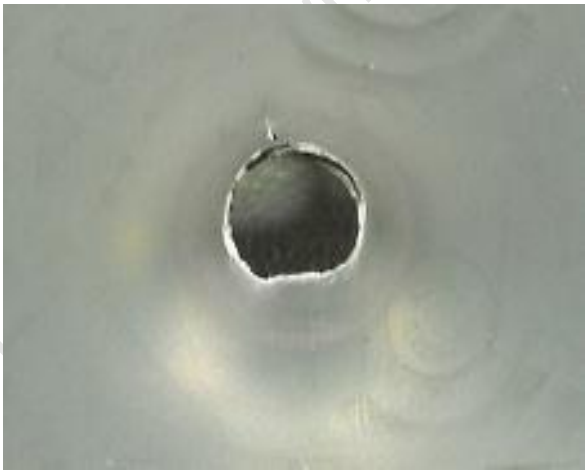

(c) Back plate

Figure 7-6: Photographs of double (2+2)mm plates (m=37.5g, I=61Ns), showing capping failure of front and back plates

The deformation profiles of the back plates of double (2+2)mm configuration at a charge mass of 30g and 37.5g are shown Figure 7-7. Both profiles up to 60mm distance from the boundary are nearly identical. The plastic deformation at a point of failure in a plate tested at higher charge mass (37.5g) showed less failure deformation than the plates tested at lower charge mass (30g).

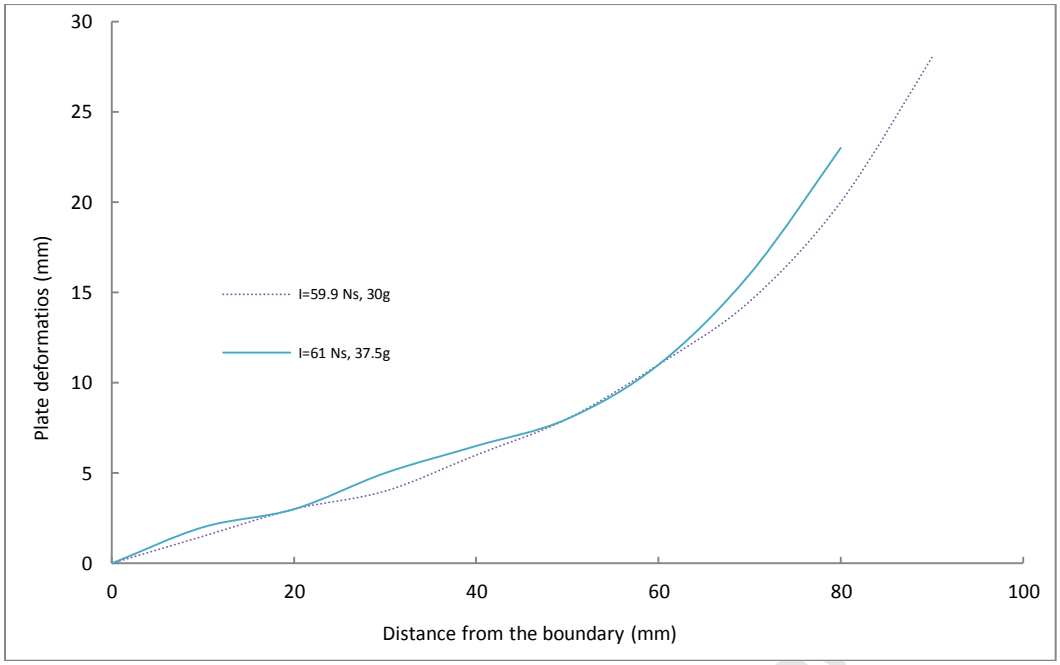

Figure 7-7: Deformation profiles of double (2+2)mm plates at increasing impulses (Domex 550MC)

7.3 Analysis of 4mm thick single torn plates (Domex 700MC)

Partial tearing/cracking of plates occurred at a charge mass of 38g, the plate was cracked at a central diameter of 25mm as shown in Figure 7-8. The thickness of the plate at a point of inflection was reduced from 4mm to 2.5mm. At a charge mass of 44g the plate was capped with a cap diameter of 26mm. The cap diameter was 14mm less than the charge diameter (40mm). The fractured plate appearance is shiny and bright as indicated in shown in Figure 7-9.

The deformation profiles of the torn plates tested at a charge mass of 38g and 44g are shown in Figure 7-10. Both profiles show same behavior up to a failure of plate tested at a charge mass of 44g. The failure deformation of the plate tested at a charge mass of 38g is higher than the plate tested at 44g indicating the change in failure mode from ductile to brittle by increasing charge mass.

Figure 7-8: Photograph of 4mm thick single plate (m=38g, I=81.7Ns), shows tearing at neck

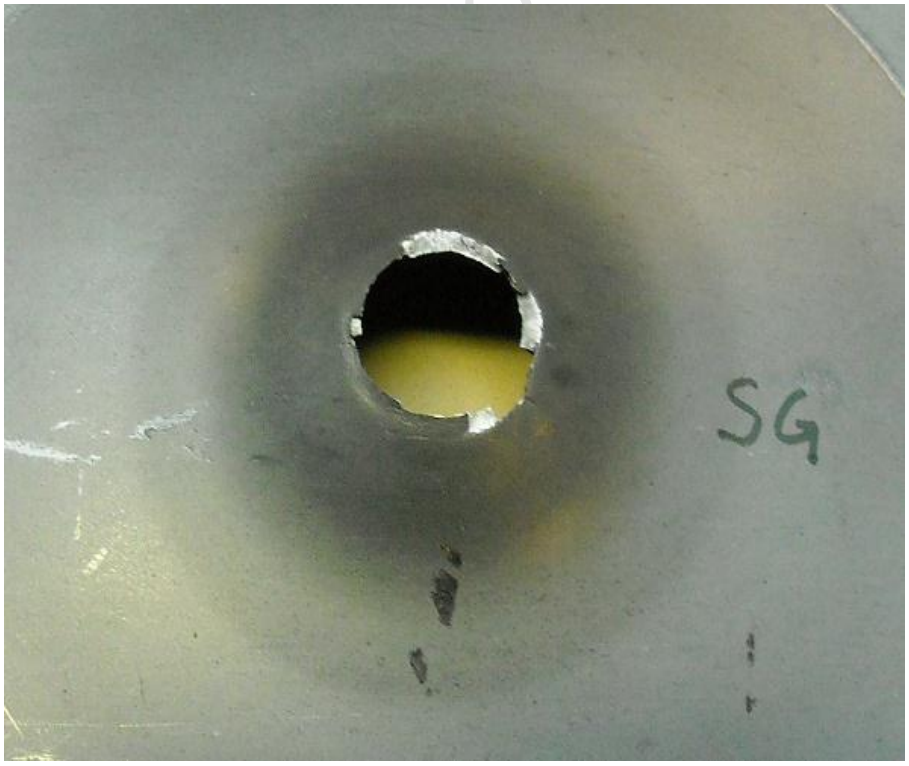

Figure 7-9: Photograph of 4mm thick single plate (m=44g, I=85.6Ns), shows capping failure

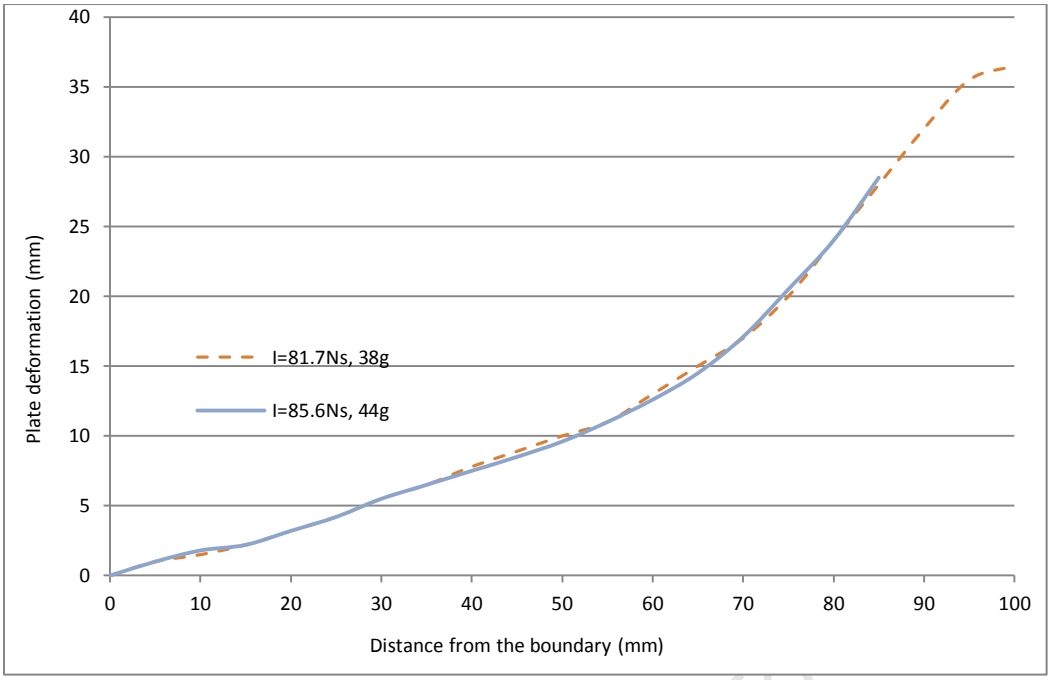

Figure 7-10: Deformation profiles of 4mm thick single torn plates (Domex 700MC)

7.4 Analysis of double (2+2)mm torn plates (Domex 700MC)

The double (2+2)mm plates of Domex 700MC started cracking at a charge mass of 27g. The front plate was capped, as shown in Figure 7-11 and the torn cap remained attached due to the presence of the back plate. A neck formed in back plate at a diameter of 26mm.

At a charge mass of 33g, both plates were capped, with front and back plate cap diameters of 28mm and 30mm respectively, as depicted in Figure: 7-12. The cap diameter was 10mm to 12mm less than the charge diameter (40mm).

The deformation profiles of torn double (2+2)mm plates tested at a charge mass of 27g and 33g are shown in Figure 7-13. The deformation profile of front plate tested at charge mass of 33g runs similar to the profile of 27g charge mass plates up to point of failure. The front and back plate deformation profiles tested at a charge mass of 33g are different from each other. The overall deformation of the back plate is greater than front plate as depected in Figure 7-13. The overall deformation from boundary to point of fracture is greater in case of back plate as the front plate cracked.

For mild steel target plates, the cap and the charge diameteres were equal as reported by Nurick and Radford [33] and Wierzbicki and Nurick [46]. The diameters of the torn caps were 7mm and 14mm less than charge diameter for Domex 550MC and Domex 700MC respectively. Decrease of cap diameter with the increase in strength of the target plates indicates the increase of localization of blast load towards midpoint.

Figure 7-11: Capping failure of front plate (m=27g)

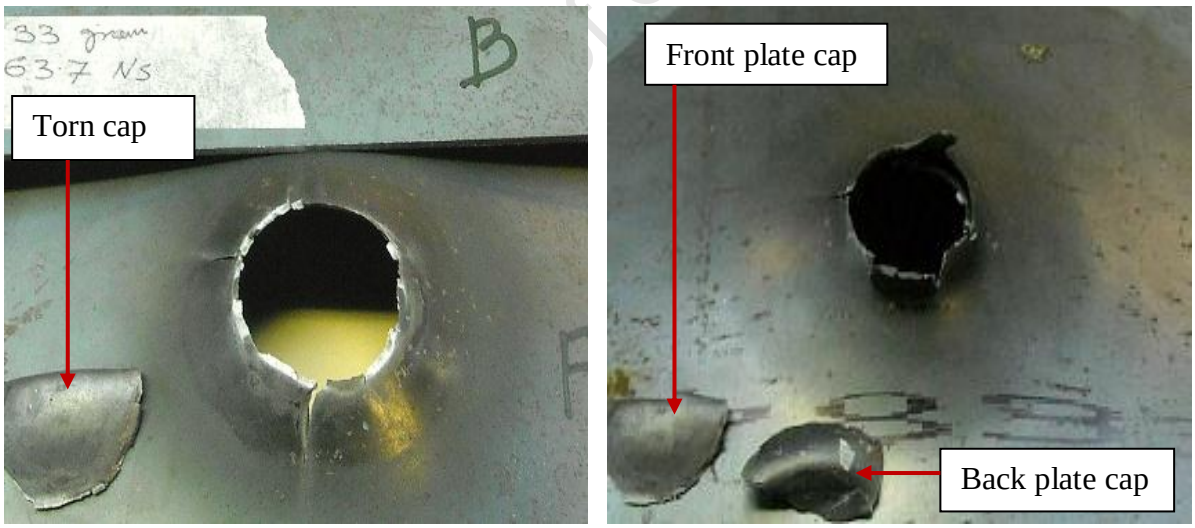

(a) Front plate (b) Back plate

Figure: 7-12: Photographs of double (2+2mm) plates (m=33g, I = 63.7 Ns), (a) front plate, (b) back plate

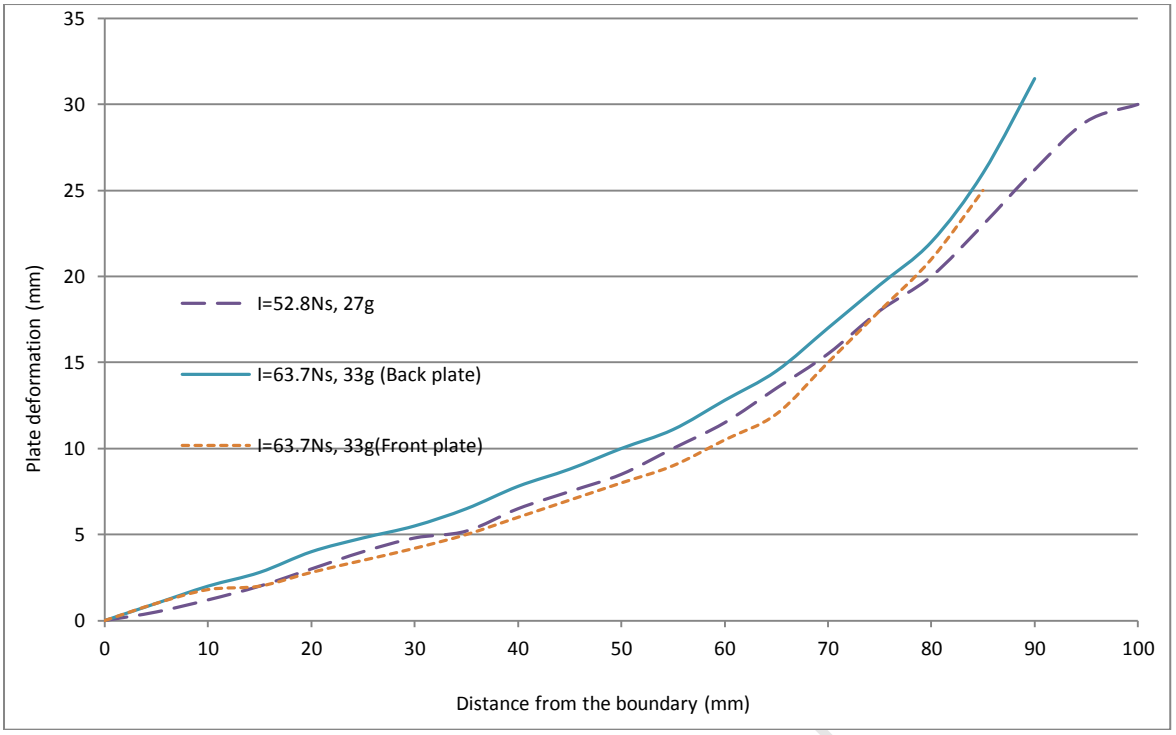

Figure 7-13: Deformation profiles of blast loaded double (2+2)mm plates (Domex 700MC)

7.5 Analysis of 6mm thick single plates (Domex 700MC)

The 6mm thick single plates started necking at a charge mass of 56g over a central diameter of 40mm to 42mm. A 35mm long crack was formed at one side of the neck diameter as indicated in Figure 7-14, known as partial tearing (Mode II*c).

On increasing the charge mass up to 59g, 110mm long cracks formed at an angle of 45° towards rolling direction. The crack had a visible opening of 8mm wide at a diameter of 41mm as indicated in Figure 7-15. The plate fractured surface shows the bright shiny appearance. Mode IIc (complete tearing) was noted at a charge mass of 62g (108 Ns) as indicated in Figure 7-16. The plate was capped at diameter of 40mm tested at a charge mass of 62g. The diameter of hole created as a result of the removal of fragments from the central portion of the plates was equal to the charge diameter (40mm). The cap has a flat and shiny appearance like brittle fracture, as shown in Figure 7-16.

The deformation profiles of torn plates of 6mm thickness, tested at a charge mass of 56g, 59g and 62g are shown in Figure 7-17. The plastic deformation from boundary to fracture point in a plate tested at a charge mass of 59g is greater than the plate tested at 62g. At a charge mass of 59g, most of the energy is consumed in plastic deformation whereas at 62g the energy is also absorbed in capping failure.

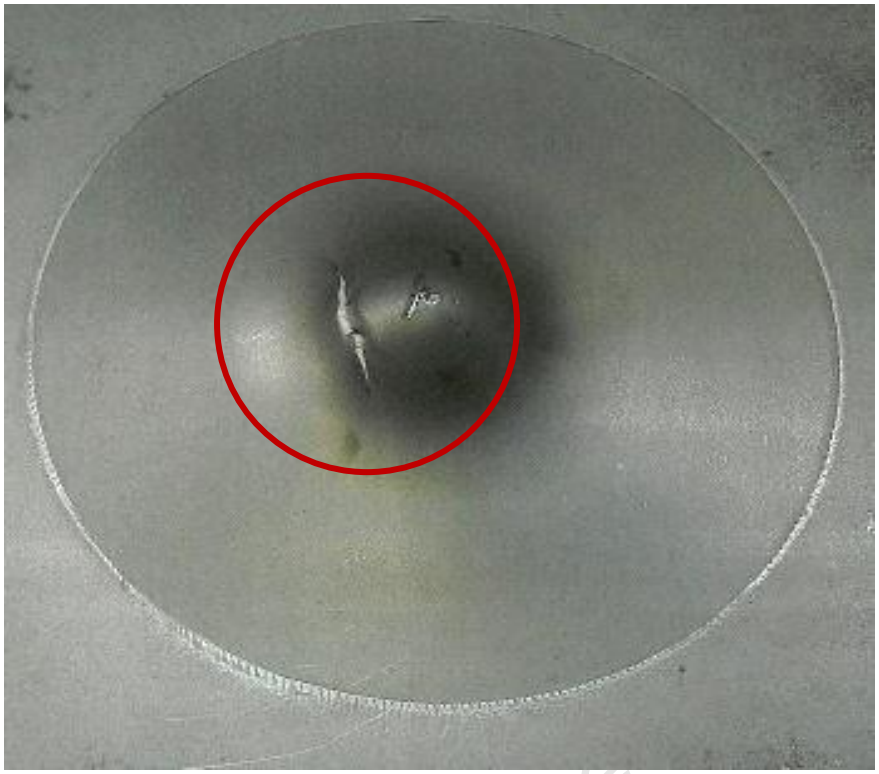

Figure 7-14: Photograph of 6mm thick single plate (m=56g), shows failure Mode II*c

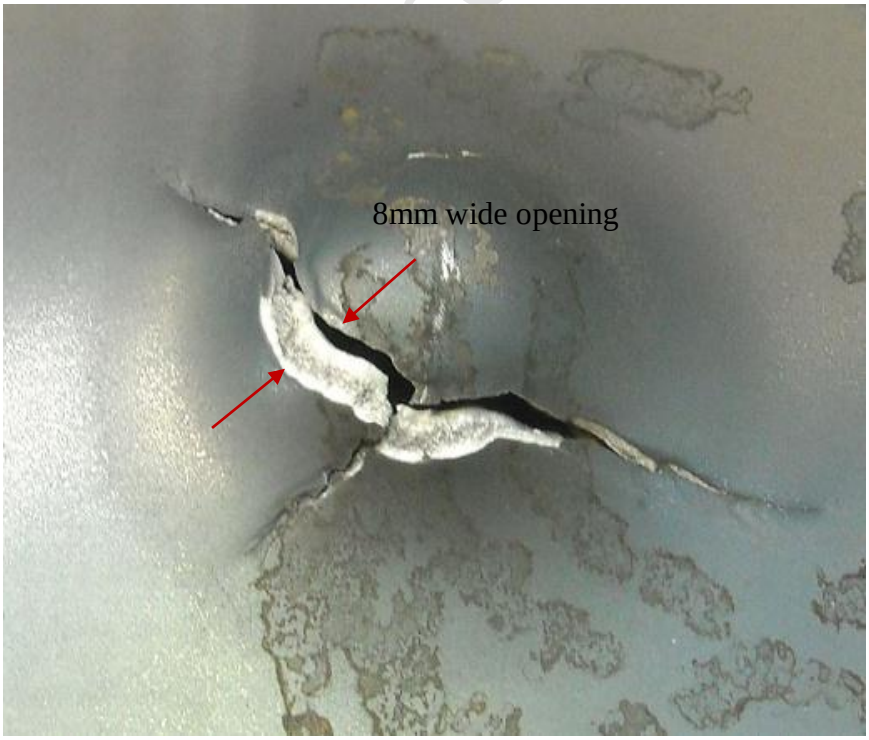

Figure 7-15: Photograph of 6mm thick single plate (m= 59g), shows tearing

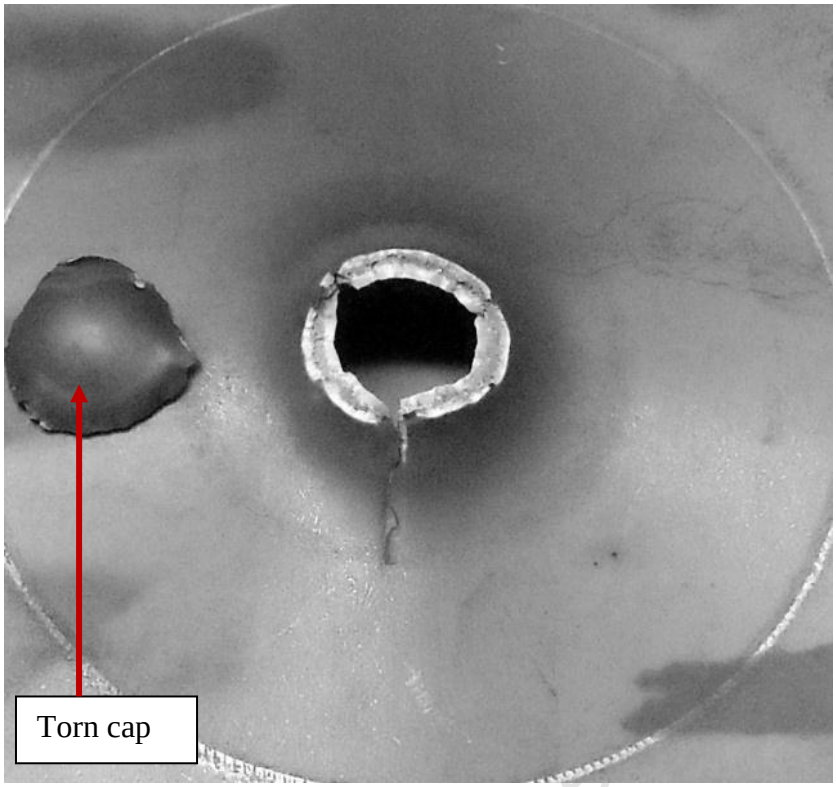

Figure 7-16: Photograph of 6mm thick single plate (m= 62g), shows capping failure

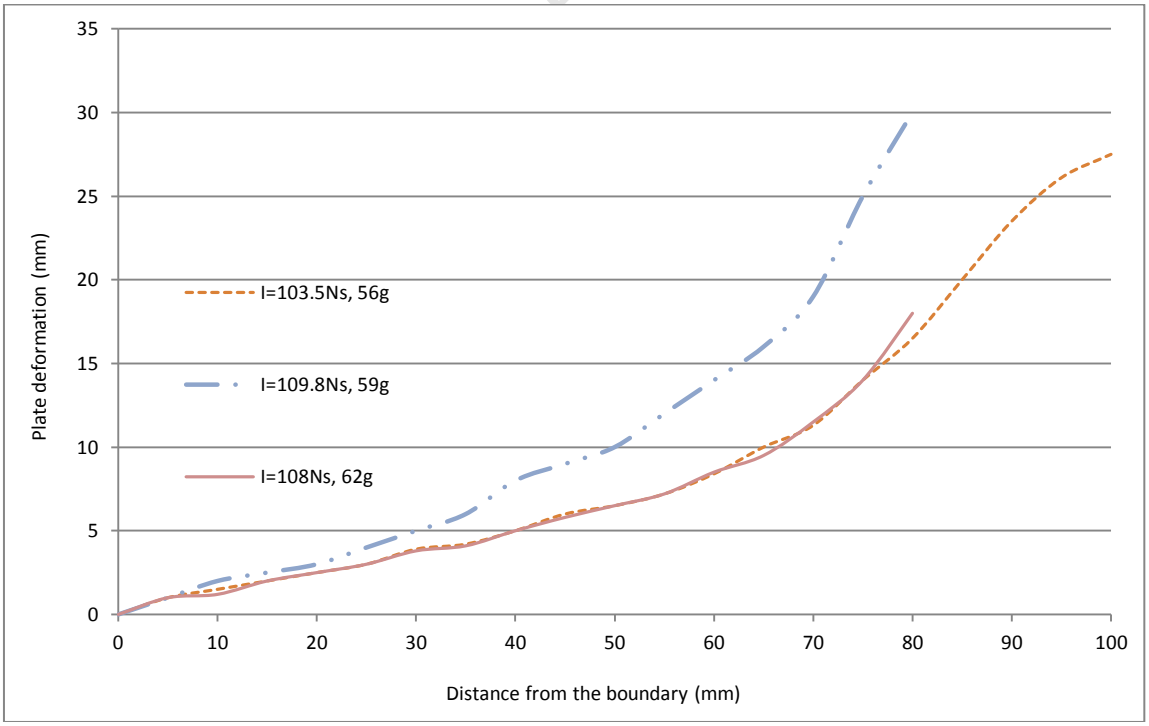

Figure 7-17: Graph to show the deformation profiles of 6 mm thick single plates (Domex 700MC)

7.6 Analysis of double (3+3)mm plates (Domex 700MC)

The back plates of double (3+3)mm configuration did not fail at any charge mass up to 68g, The maximum midpoint deflection of the back plate was 28.48mm at a charge mass of 68g. At a charge mass of 62g, small crack was observed in the front plate. A visible crack in the front plate was developed at a charge mass of 68g.

7.7 Analysis of double (4+2)mm torn plates (Domex 700MC)

The double (4+2)mm plate did not fail by capping at any charge mass (up to 74g). After the charge mass of 56g, minor cracks were observed in front and back plates tested at a charge masses of 62g, 68g and 74g as indicated in Figure 5-17. In this configuration, the back plate deformation is greater than the front plate deformation at all charge masses. The difference in deformation in both plates is visible in Figure 5-17. This difference in plastic deformation may be attributed due to greater elastic recovery in the thicker plates.

7.8 Analysis of triple (2+2+2)mm plate (Domex 700MC)

The triple (2+2+2)mm plates started cracking at a charge mass of 44g. The triple plate configuration was considered failed if partial tearing or complete tearing occurred in the back plate.

Above 50g charge mass, the plates started cracking. Front and back plates failed or capped in different manners. The torn back plates tested at a charge mass of 56g and 62g are shown in Figure 7-18. The capping failure of front plates are typical of locally blast loaded plate response, whereas the back plate failures are not.

The deformation profiles of fractured back plate of triple (2+2+2)mm configuration at a charge mass of 56g and 62g are shown Figure 7-19. At both charge masses the profiles are similar.

The back plates of double or triple configurations were not loaded directly by a charge mass. The back plates were loaded by the front plate fragments for double configurations. In case of triple plate configuration the back plates were loaded by the front and middle plates fragments. The shape of the cap from the front plates at various charge masses is approximately circular and and had a diameter between 29 and 31mm.

(a) Charge mass 56g (b) Charge mass 62g

Figure 7-18: Capping failure of back plates of triple (2+2+2)mm configuration at (a) 56g and (b) 62g charge mass (Domex 700MC)

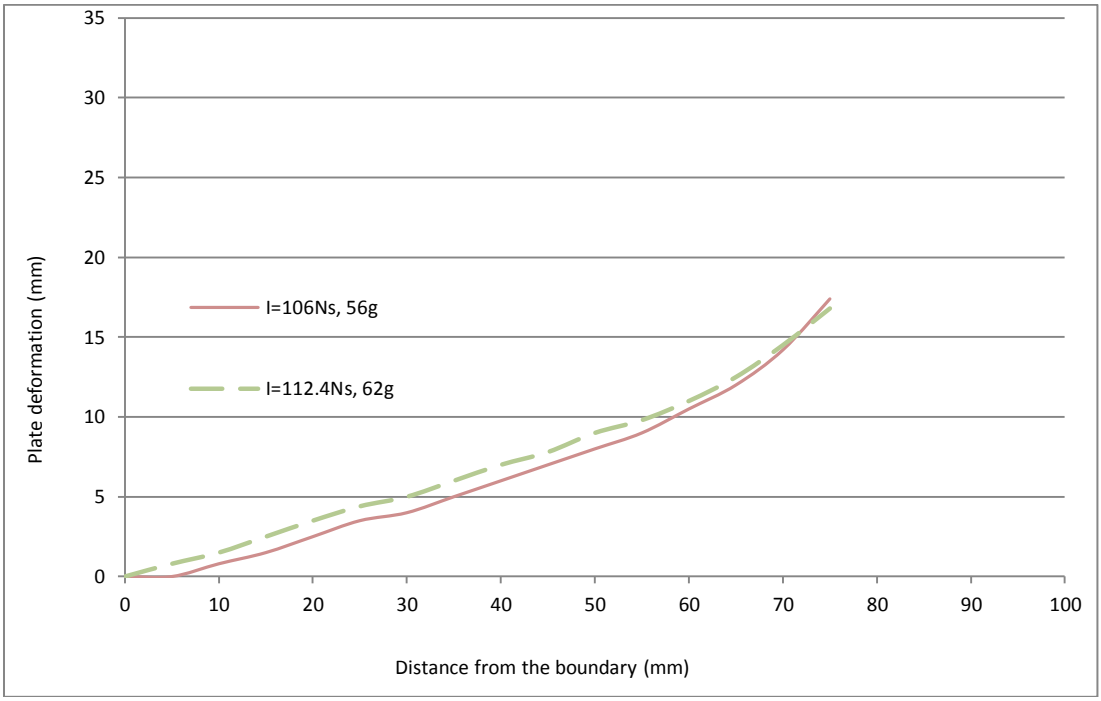

Figure 7-19: Deformation profile of triple (2+2+2)mm plates at a charge mass of 59g and 62g (Domex 700MC)

7.9 Fractography of blast tested torn plates (Domex 700MC)

The failure analysis of fractured Domex 700 MC plates at various charge masses was carried out. Samples from the fractured plates were carefully obtained for fractography and cleaned ultrasonically. The fractured tensile samples reported in chapter 3 were used as a reference to

compare the dimple morphology of the blast tested fractured surfaces. Fractographs of the tensile samples tested at four different strain rates favourable for ductile fracture at room temperature are given in Chapter 3 and Figure B-7 of "Appendix B". Dimple morphology observed in all the fractured surfaces exhibited different densities of micro-voids initiated at the inclusions/second phase particles. A typical example of the dimple appearance at inclusion sites is shown in Figure 7-20.

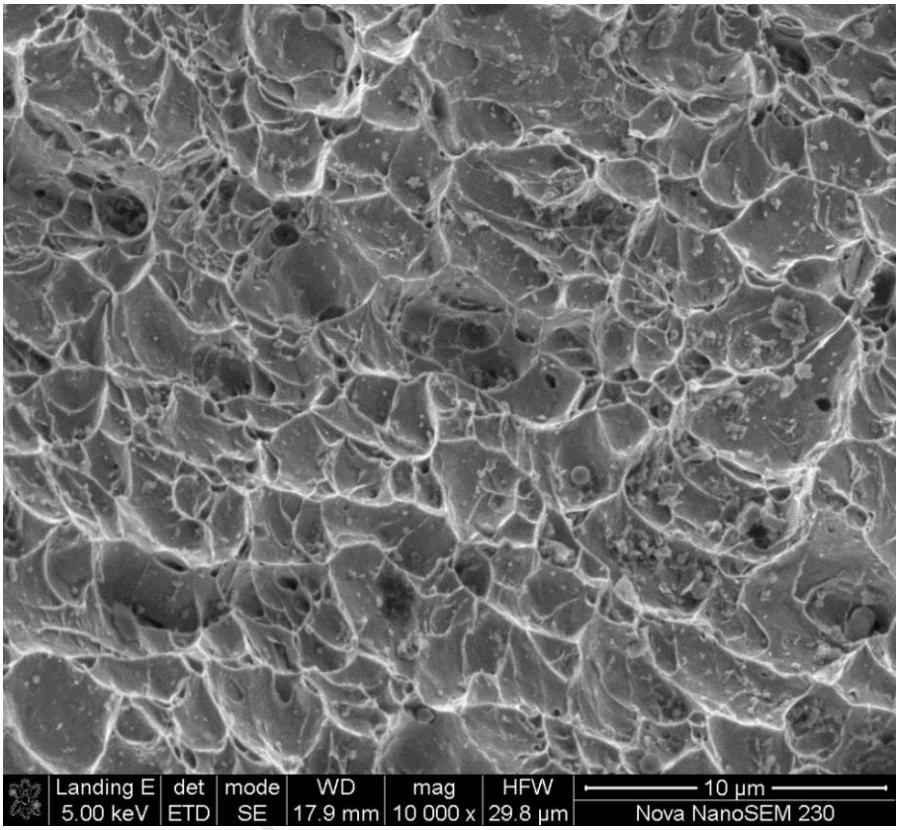

Figure 7-20 : Typical dimple morphology, with micro-voids evident around the inclusions, for blast loaded plates

The fracture surfaces of the 2mm and 6mm thick plates are different in appearance. The fractured surfaces of double (2+2)mm and triple (2+2+2)mm showed a dull appearance, opposite to the appearance of 6mm fractured surface (shiny and bright). Stereo-photographs of double and triple fractured plates are shown in Figure: 7-21a and b, indicated a ductile nature of fracture.

The fracture surfaces of double, triple and single plates show various zones in fractograph. Figure 7-22a and b show two distinct zones in the one side of the fractured surface of 6mm thick plate tested at 62g of explosive: the inner flat fibrous zone where the fracture begins and the outer shear lip zone where the fracture terminates. The fibrous zone is a region of slow crack growth at the fracture origin that is usually at or close to tensile axis [81].

The fractured surfaces of 6mm thick single plates show two types of surface appearances, one side shows (flat and featureless surface) as depicted in Figure 7-22a and (Figure B-13 and Figure B-14 of the "Appendix B"). The other side shows a shiny surface appearance as shown in Figure 7-23.

It is to be noted that stereo-photographs, shown in Figure 7-23 were taken few weeks after the blast testing, some areas of the fractured surface are affected by corrosion attack.

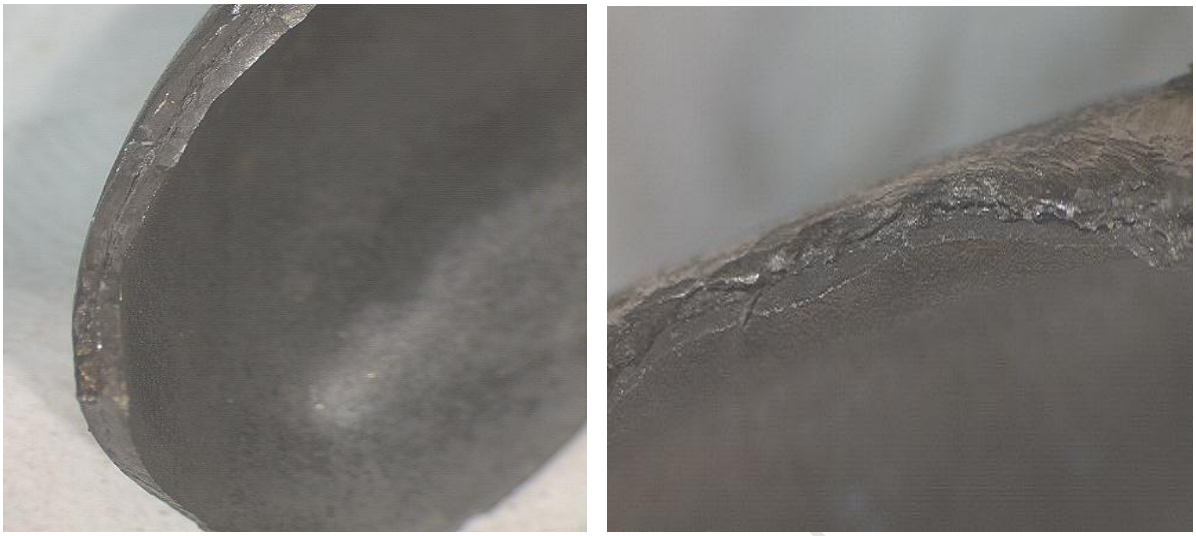

(a) Double (2+2)mm (b) Triple (2+2+2)mm

Figure: 7-21 Stereo-photograph of torn caps of double (2+2)mm and triple (2+2+2)mm plates, showing dull appearance

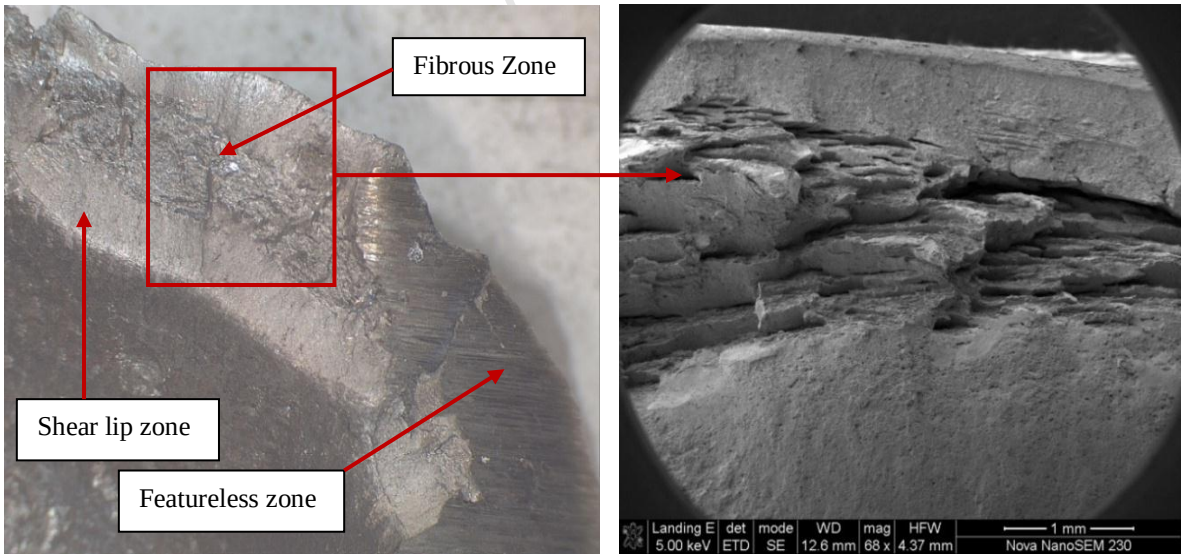

(a) (b)

Figure 7-22: Photographs to show the fractured surface zones of 6 mm thick single plates (m=62g, I=108 Ns)

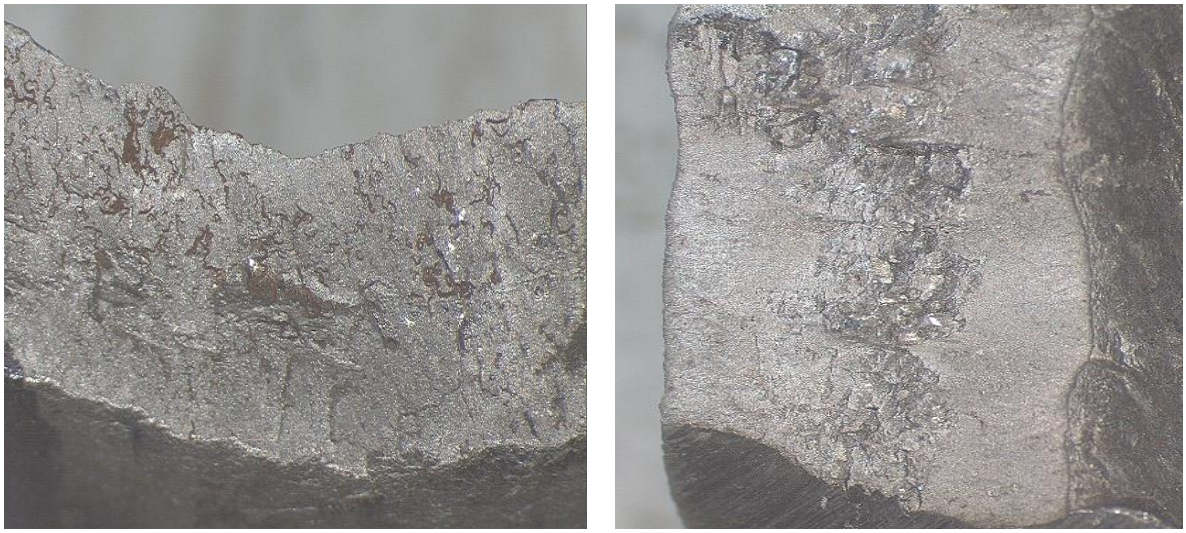

Figure 7-23: Stereo-photographs of torn cap of 6mm thick single plates, showing shiny appearance, an indication of brittle fracture

7.9.1 Fracture analysis of 4mm thick single plates

There were two plates available for fractography (tested at 38g and 44g). The SEM fractographs of the plates fractured at 38g and 44g charge masses are shown in Figure 7-24 and Figure 7-25 respectively. Both fractographs show dimples in various concentrations.

A close comparison of fractographs of the sample in Figure 7-24 and Figure 7-25 show a larger quantity of dimples at 38g. The dimples were also larger in diameter at the higher charge mass (44g). Fractographs at 44g also exhibited a small amount of river patterns, associated with micro-voids as depicted in Figure 7-25 (and Figure B-8 of "Appendix B"). The river patterns indicate that the fracture is not completely ductile, but has some brittle qualities.

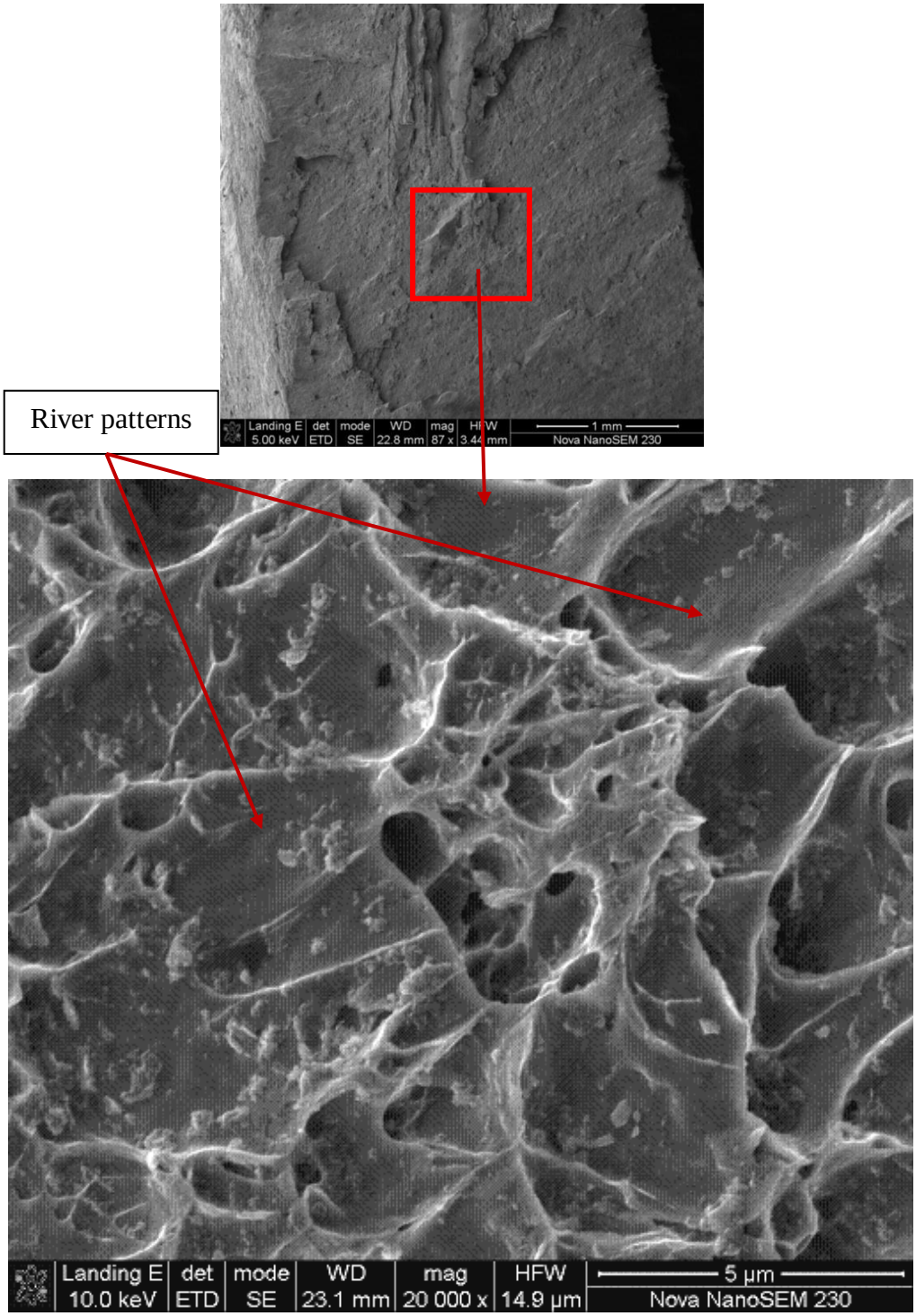

Figure 7-24: Fractograph of 4 mm thick single plates after blast testing at a charge mass of 38g, (I=81.7 Ns), shows micro-voids

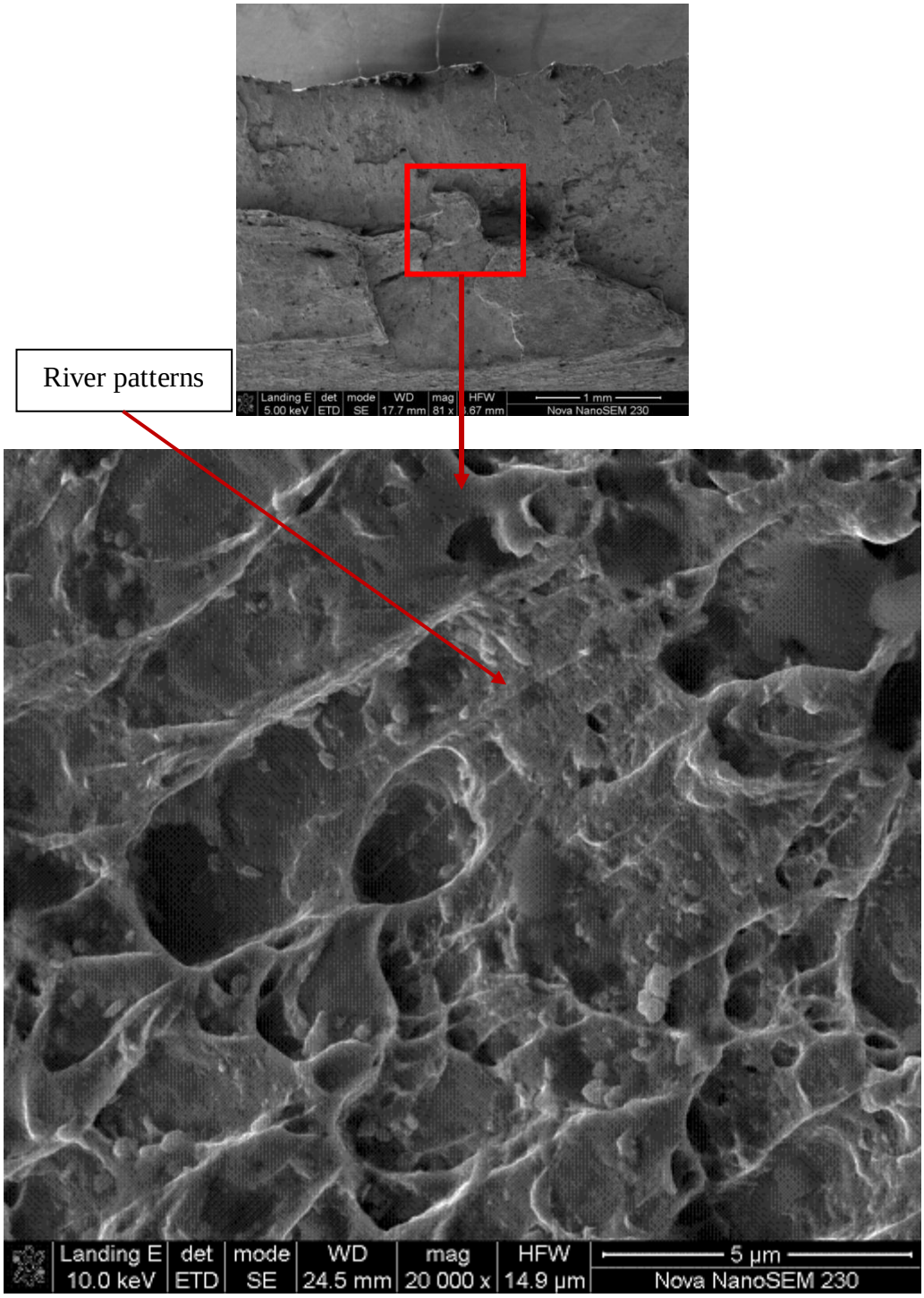

Figure 7-25: Fractograph of 4mm thick single plates after blast testing at a charge mass of 44g, (I=85.6 Ns), show micro-voids along with river patterns

7.9.2 Fracture analysis of double (2+2)mm plates

The front and the back plate of this configuration were capped at the charge mass of 33g. The samples from both fractured plates were obtained for fractography. The fractographs of front and the back plate tested at 33g are shown in Figure 7-26 and Figure 7-27 respectively. Both samples show dimple morphology, showing that the fracture is ductile in nature. The size and

the shape of the dimples in the front and back plate are different. The fractograph of the front plate exhibited equiaxed dimples as shown in Figure 7-26 and these dimples are larger in diameter than the dimples in back plate as indicated in Figure 7-27. The back plate fractograph shows the elongated dimples that are smaller in diameter. The interested reader may also refer to Figure B-9 in "Appendix B".

Dimple morphology is influenced by the loading condition [81]. The equiaxed dimples are obtained during uniaxial loading whereas the elongated dimples are achieved in shear loading. Dimple shapes are governed by the state of stress within the material as the micro-voids form and coalesce. Fracture surfaces that result from shear loading conditions exhibit elongated dimples. Dimple orientation varies with stress orientation and dimple shape is a function of stress orientation, shear stress develops elongated or parabolic shaped dimples [81].

The comparison of front and back plate fractographs indicated that the state of stress and the forces applied due to localized blast loading over charge diameters were different in nature for front and back plates. The state of stress changes in layered plates. The front plate experienced a uniaxial load whereas the back plate experienced a shear stress or load.

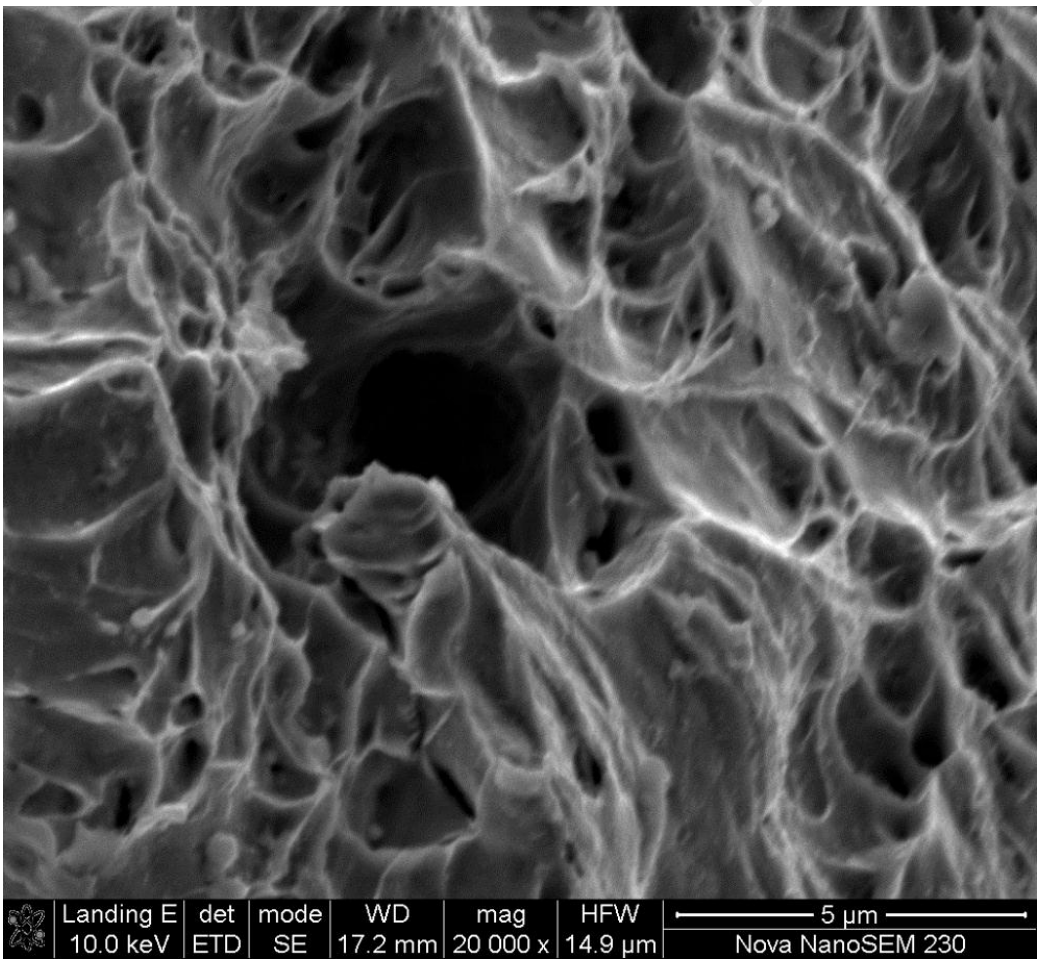

Figure 7-26: Fractograph of front plate tested at a charge mass of 33g, (I=63.7 Ns), shows equiaxed dimples (uniaxial tensile failure)

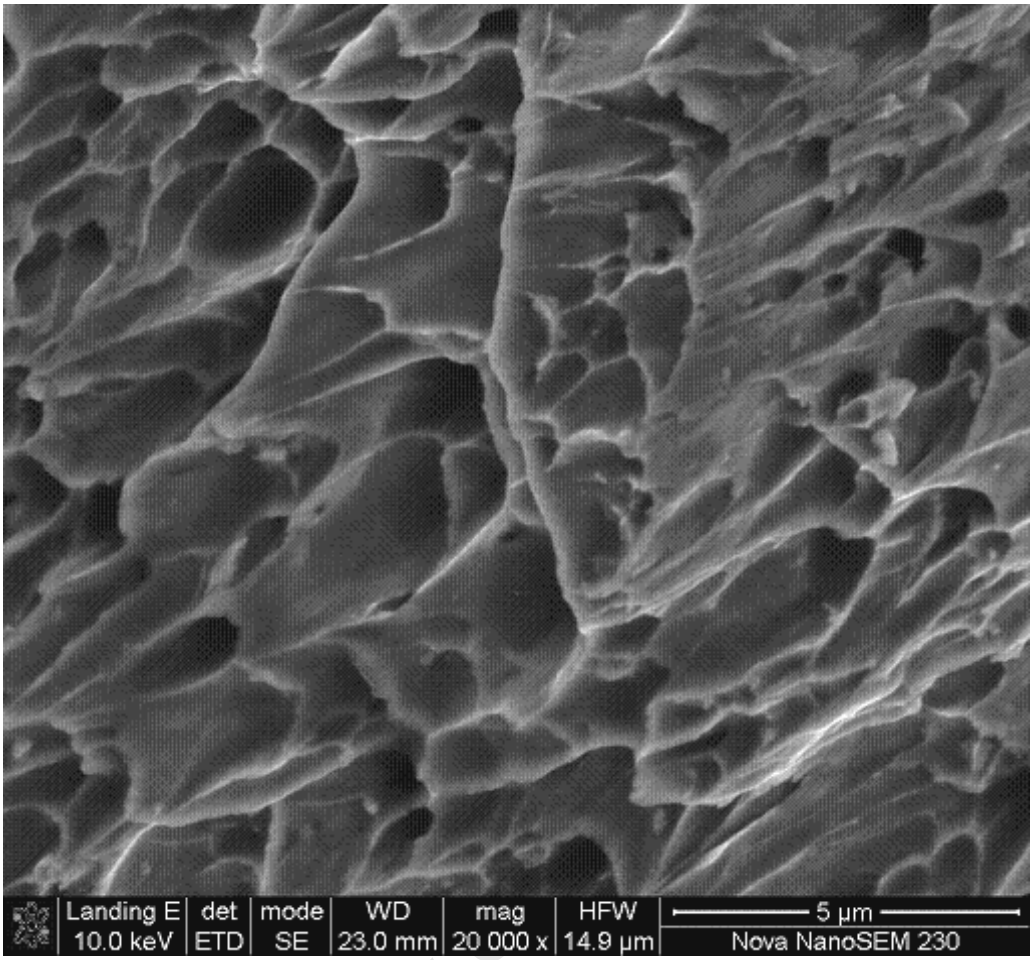

Figure 7-27: Fractograph of back plate tested at a charge mass of 33g, (I=63.7 Ns), shows elongated dimples (shear component to failure)

The front plates are loaded directly by the blast wave, these plates exhibited a uniaxial load and fractographs of front plates show equiaxed dimple morphologies as depicted in (Figure B-9a of "Appendix B"). The back plates do not have any direct contact with the blast wave. The torn back plates are loaded by the high velocity fragments generated due to the tearing of first plates as a result of blast load. These high velocity fragments cause a non-uniform load on back plates, as revealed by fractured surface dimple morphology as indicated in (Figure B-9b of "Appendix B").

The higher quantity of small size dimples in the back plate fractograph indicating the application of high strain rates on the front plates compare to back plate.

7.9.3 Fracture analysis 6mm thick single plates (Domex 700MC)

There were two plates in 6mm configuration tested at 59g and 62g charge mass available for the fractography. The failure analysis of these plates was conducted on SEM and the fractographs at similar magnifications are shown in Figure 7-28 and Figure 7-29. Both the fractographs show the dimple morphology with different concentrations of micro-voids. The

quantity of micro-voids is greater in a sample tested at a charge mass of 59g. The equiaxed dimples of different sizes are visible in the fractograph shown in Figure 7-28. In Figure 7-29, a few larger dimples are visible. Comparison of both fractographs shows that the diameter of dimples is larger at higher charge mass 62g. The fractograph of the plate tested at a charge mass of 62g contains river patters along with a few micro-voids. River patterns generally appear in materials which failed in a brittle mode [81].

The greater failure deformation of the plate tested at 59g is shown in the deformation profiles in Figure 7-17, also indicating the brittle nature of fracture at higher charge mass. The river patterns along with scarcity of micro-voids in the fractograph are also shown in (Figure B-10, Figure B-11 and Figure B-12 of "Appendix B"); indicate the brittle nature of fracture.

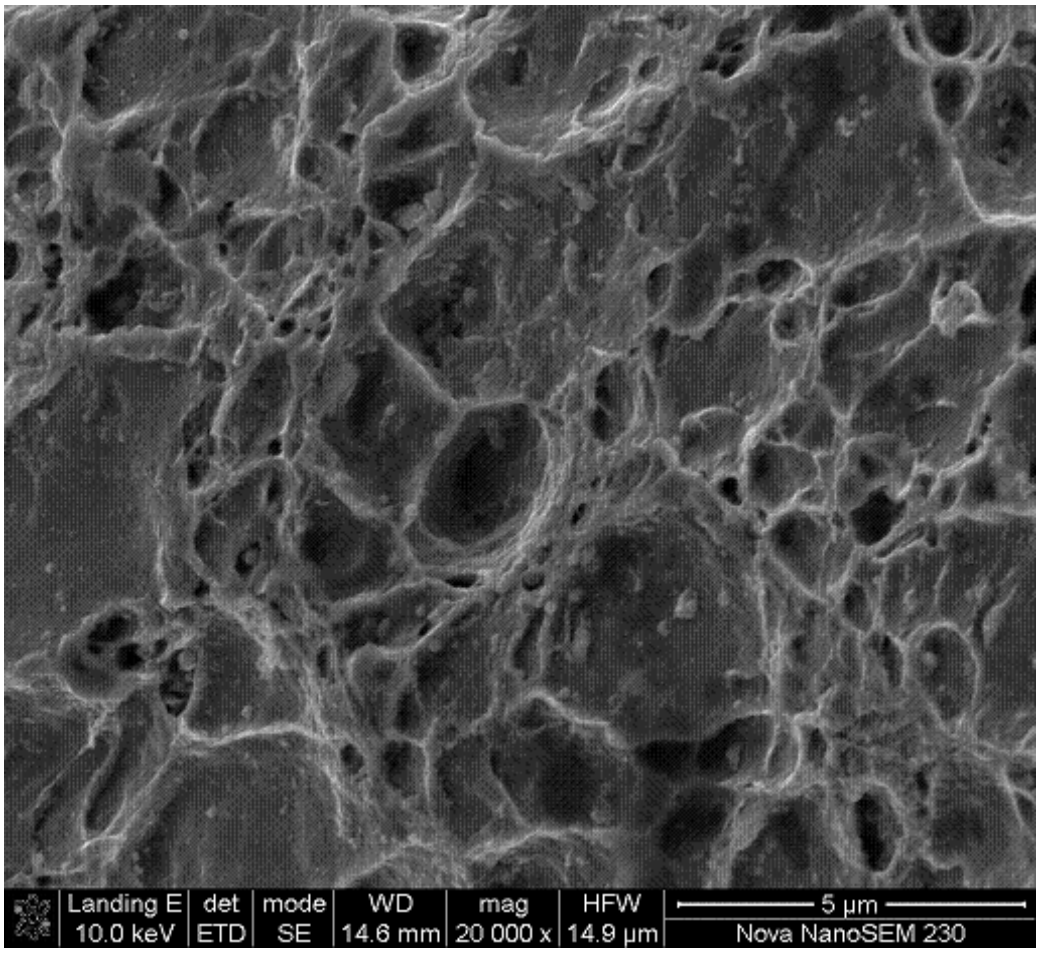

Figure 7-28: Fractograph of 6 mm thick single plates after blast testing at a charge mass of 59g, (impulse=109.8 Ns) (No river patterns)

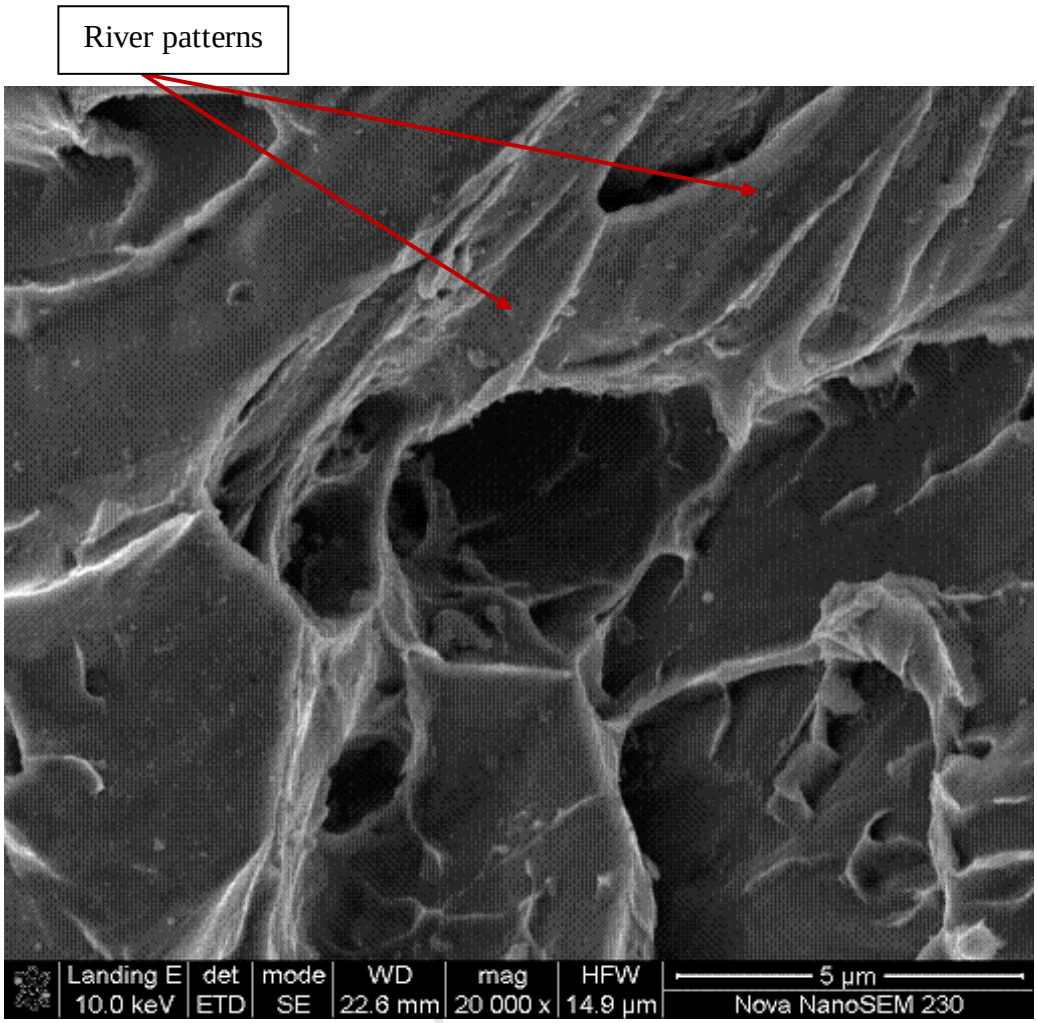

Figure 7-29: Fractograph of 6 mm thick single plate, after blast testing at a charge mass of 62g, (I=108 Ns), shows dimples and river patterns

7.9.4 Fracture analysis of triple (2+2+2)mm torn plates (Domex 700MC)

The samples of triple plate configuration tested at charge masses of 50g, 56g, and 62g were examined using fractography. The front plate fractograph of the blast tested torn plate at a charge mass of 50g shows equiaxed microvoids of different sizes as indicated in Figure 7-30.

For a charge mass of 56g the front and back plates were capped. The fractographs of the torn plates are shown in Figure 7-31, Figure 7-32 and Figure 7-33. Two zones in the fractured surface of the front plate, tested at 56g are shown in Figure 7-31. The inner zone is a flat fibrous where the fracture initiates and the outer zone where the fracture terminates. Two similar zones were also seen in 6mm thick torn plates indicated in Figure 7-22. The fibrous zone is a region of slow crack growth at the fracture origin that is usually at or close to tensile axis [81].

The fractographs of the front plate tested at 56g shows equiaxed dimples as shown in Figure 7-32. The back plate fractograph exhibited slightly elongated dimples as shown in Figure 7-33 and in Figure B-15 “Appendix B”.

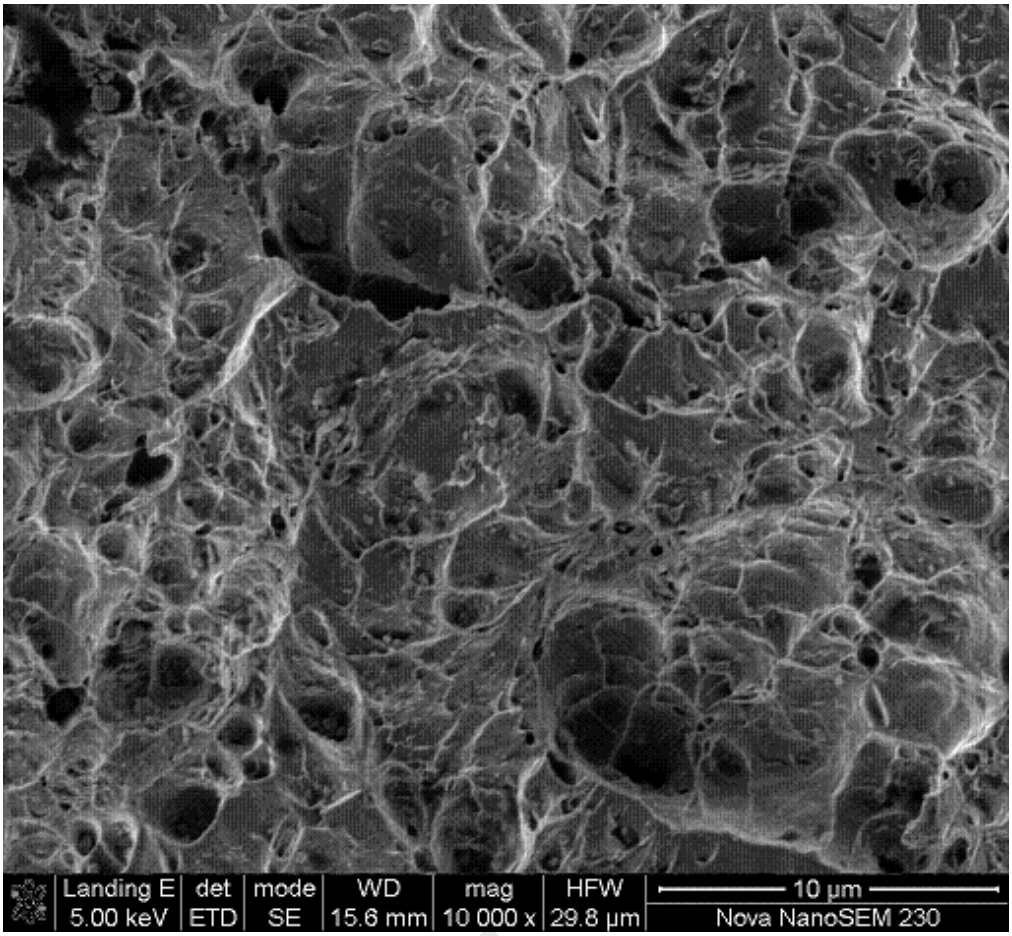

Figure 7-30: Fractograph of front plate tested a at charge mass of 50g, (impulse=91Ns)

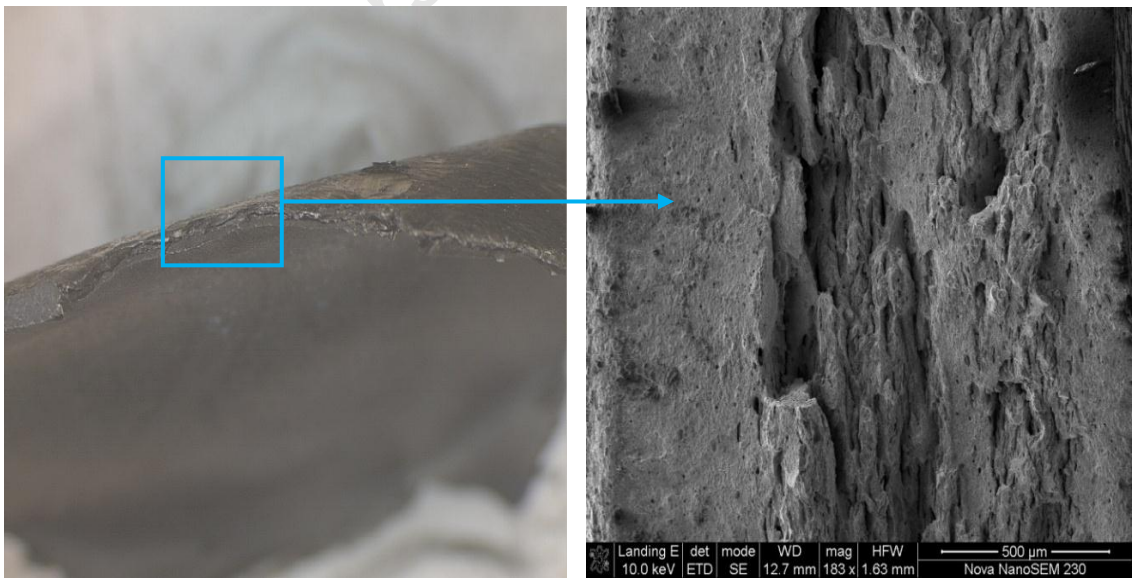

Figure 7-31: Fractographs of a front plate (2+2+2 = 6mm) after blast testing at a charge mass of 56g, impulse=106 Ns

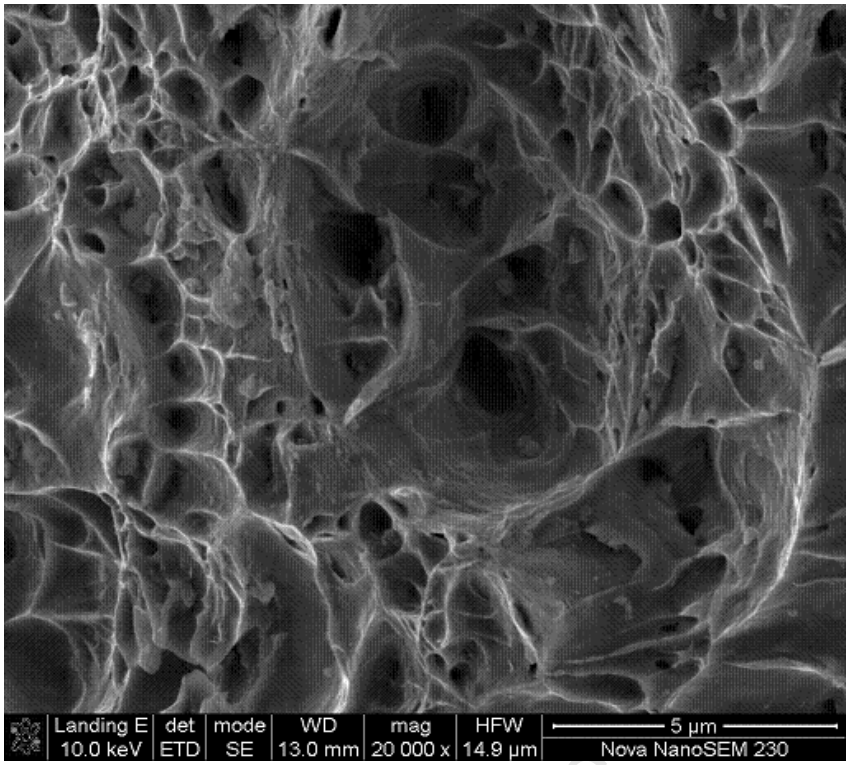

Figure 7-32: Fractograph of the front plate (2+2+2)mm after blast testing at a charge mass of 56g, (I=106 Ns)

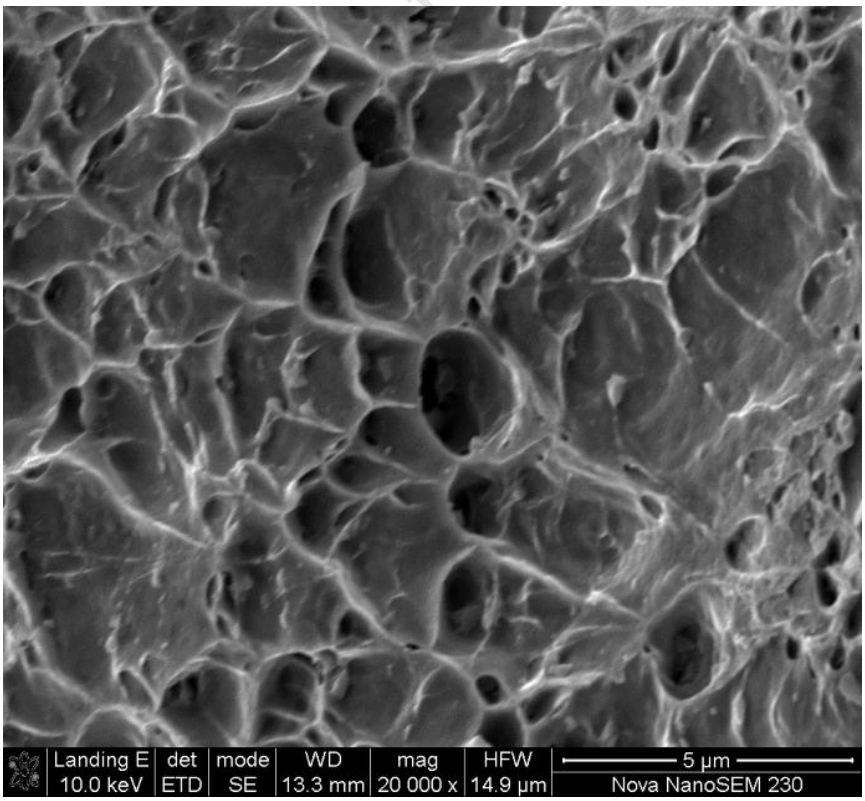

Figure 7-33: Fractograph of the back plate (2+2+2)mm after blast testing at a charge mass of 56g, (I=106 Ns)

At a charge mass of 62g, the front and back plates were capped and the middle plate was not. The fractographs of front and the back plates tested at 62g are shown in Figure 7-34 and Figure 7-35. The front and the back plate fractographs display different dimple morphologies. As the front plate shows equiaxed dimples whereas the back plate shows the elongated dimples indicating the application of different loading conditions. This phenomenon is also demonstrated in Figure B-16 of the "Appendix B". The same dimple morphology was also seen in case of 4mm double layered plates indicated in Figure 7-26 and Figure 7-27.

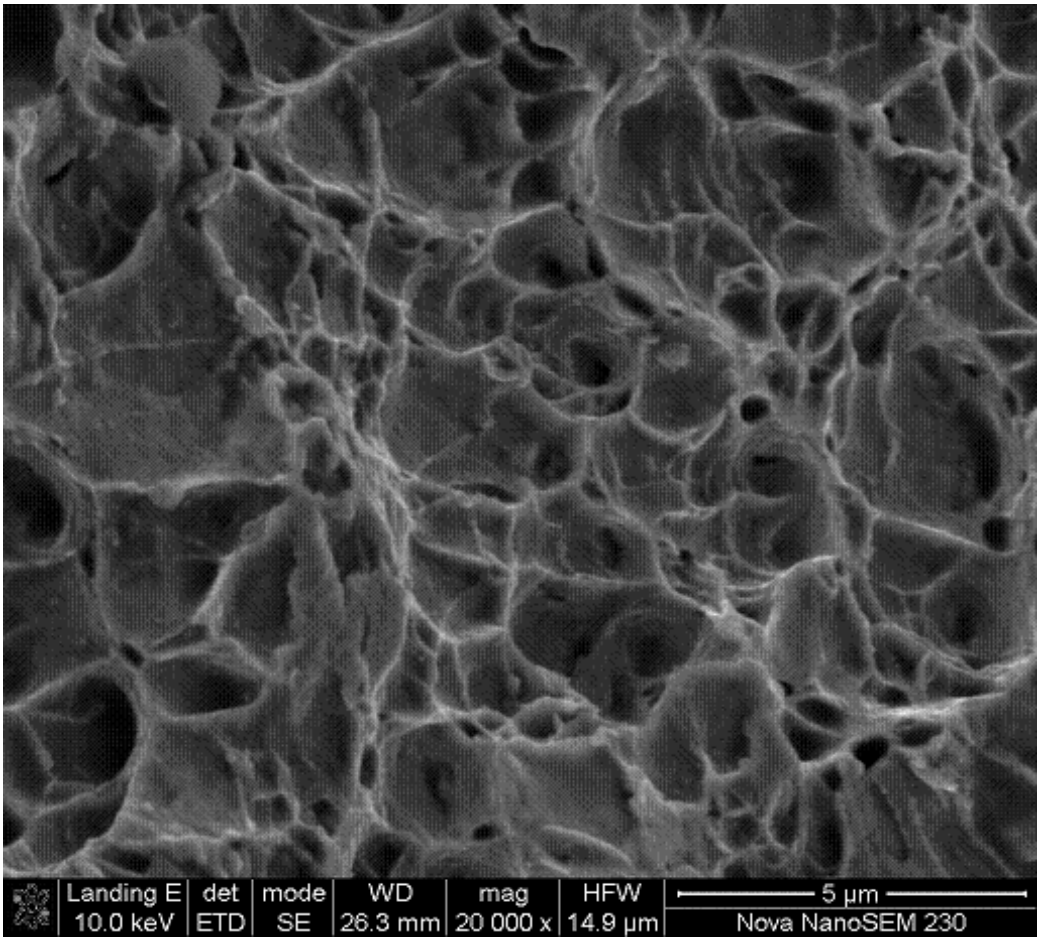

Figure 7-34: Fractograph of front plate of (2+2+2)mm configuration after blast testing at a charge mass of 62g, (I=112.4 Ns), shows equiaxed dimples

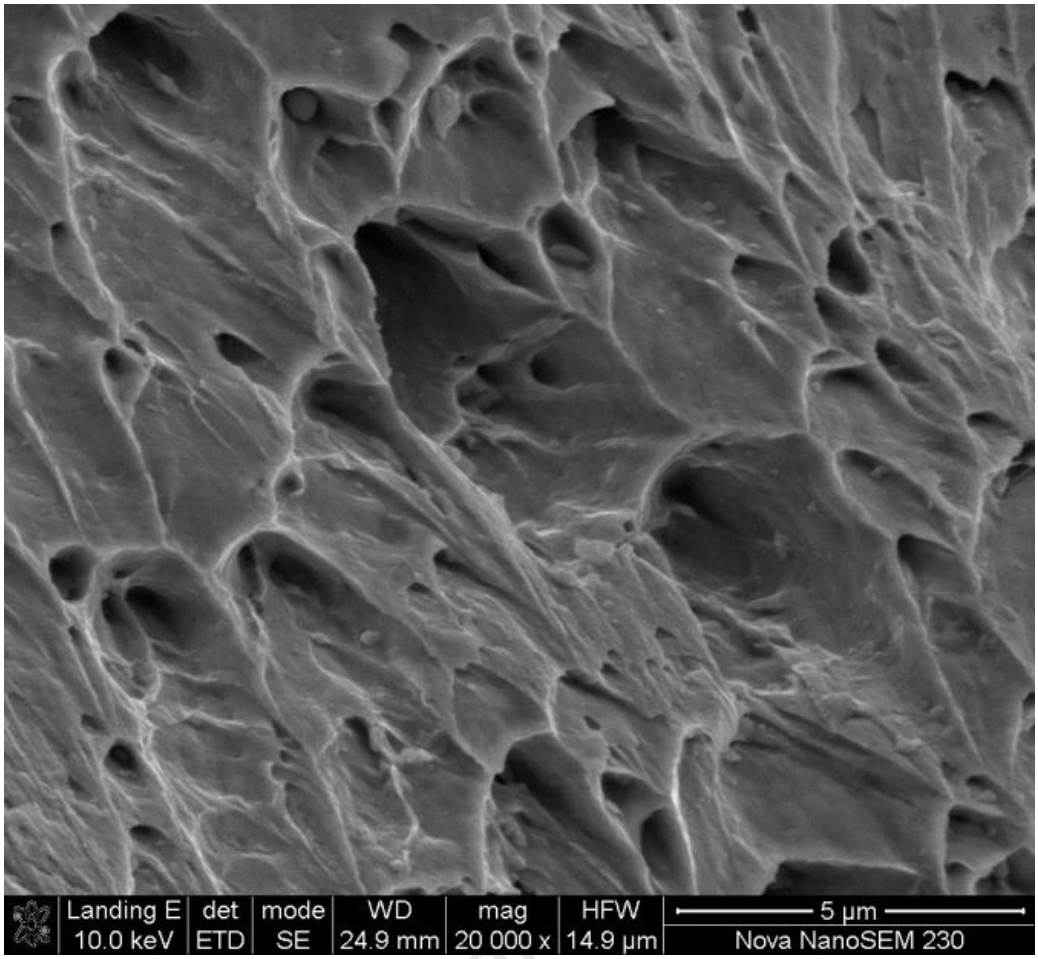

Figure 7-35: Fractograph of back plate of tripe (2+2+2)mm configuration after blast testing at a charge mass of 62g, (I=112.4 Ns), shows elongated dimples

At a charge mass of 68g, the front plate capped and a minor crack developed in the middle plate. The back plate did not rupture. The front plate fractured surface is shown in Figure 7-36. Various sizes of equiaxed dimple morphology are evident, and are also shown in Figure B-17 of the "Appendix B" at lower magnification.

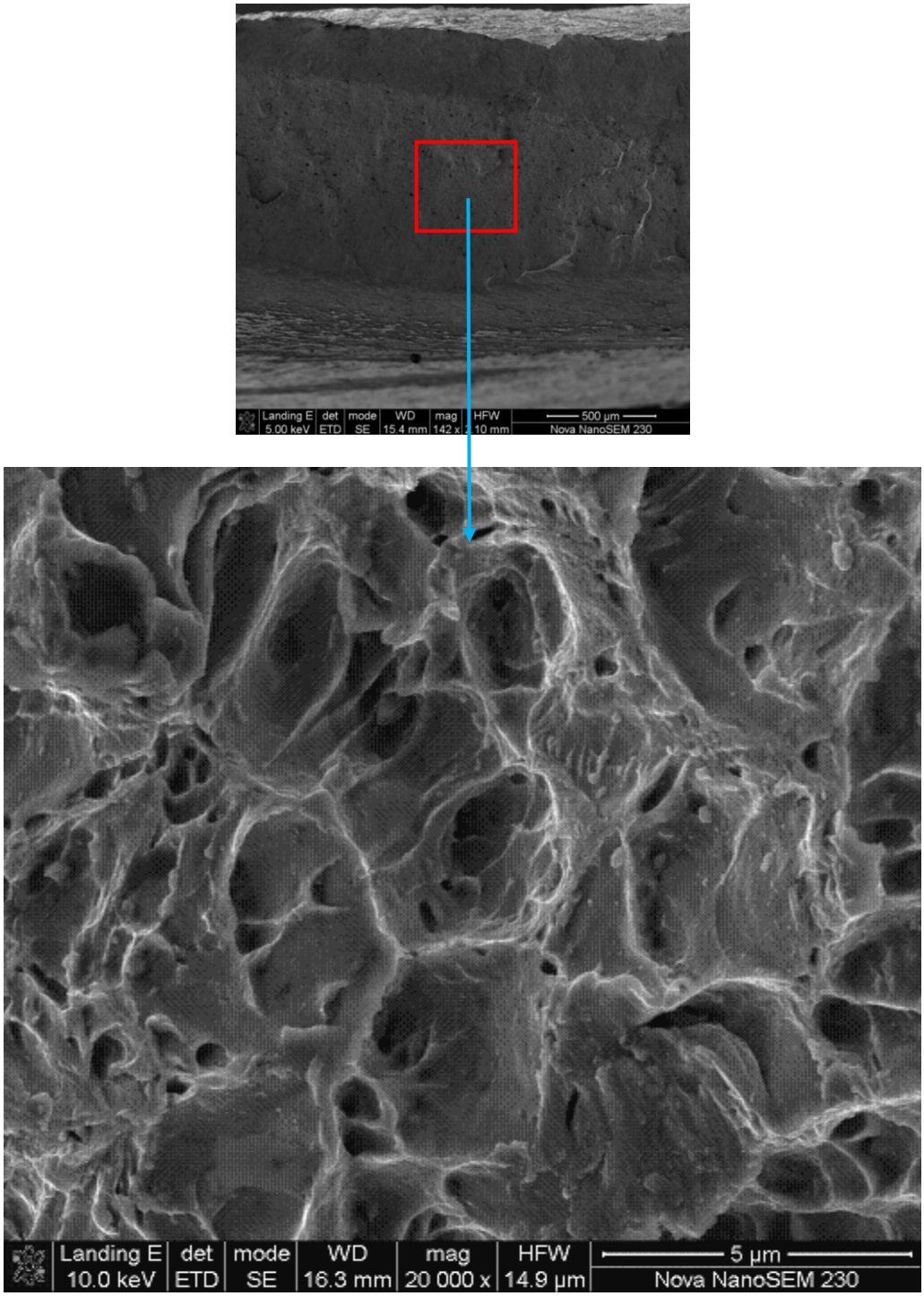

Figure 7-36: Fractographs of front plate of triple (2+2+2)mm plate configuration after blast testing at charge mass of 68g, (I=126.1Ns.)

7.9.5 Fracture analysis of double (3+3)mm and double (4+2)mm plates

The double layered plates (3+3)mm and (4+2)mm of 6mm configuration provided better protection than single and triple layered plates. These plates showed minor cracks at charge masses of 68g and 74g as shown in Figure 7-37. These plates were not considered for fractography due to the unavailability of the samples.

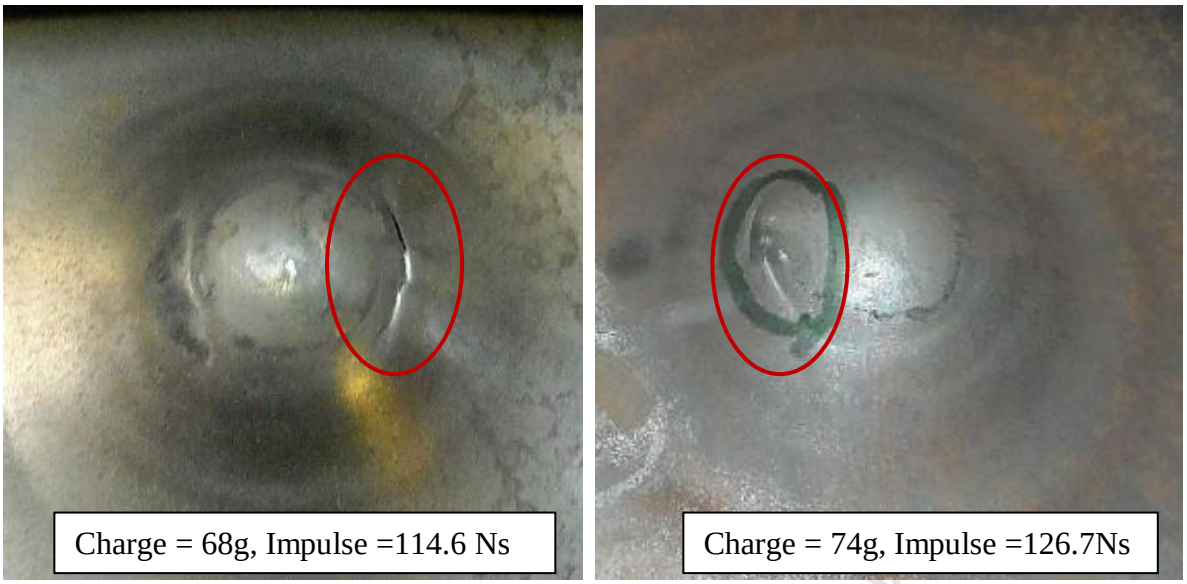

(a) Back plate of (3+3)mm configuration (b) Back plate of (4+2)mm configuration

Figure 7-37: Photographs to show minor cracks in back plates of (3+3)mm and (4+2)mm configurations

Chapter 8

8 Discussion

This chapter discusses the results from blast tests on the 4mm and 6mm thick configurations of Domex 550MC and Domex 700MC plates. Single and layered plate configurations with the same nominal thickness are compared in terms of midpoint displacement, deformation profiles, failure modes, impulse to failure and dimple morphology. The experimental results are used to evaluate the protection level offered by each thickness to find the best combination.

8.1 Relationship between impulse and charge mass

All the target plates of 6mm thick configuration were tested at equal charge masses ranging from 18g to 68g as indicated in Table 8-1. The impulse imparted to the plates of various configurations is very consistent for a given charge mass, with the exception of the 68g, where the variation in impulse is approximately 10%. A graph of impulse versus charge mass is shown in Figure 8-1. There is a linear trend if increasing impulse with increasing charge mass, as observed by Nurick and Marten [16, 17]. The relationship is approximately {Impulse (Ns) =2(charge mass)g}.

Table 8-1: Relationship between impulse and charge mass of 6mm thick configurations

Charge mass (g)	Impulse (Ns)				
	Single 6mm	Double (3+3)mm	Double (4+2)mm	Triple (2+2+2)mm	Mean average (Ns)
18	38.3	39	37.3	37.6	38 ± 1
22	45.4	42.3	46.3	48	45 ± 3
27	54.3	54.1	55.8	56.2	55 ± 1
33	67.1	62.1	66.1	69	66 ± 3
38	--	--	72.7	77.3	75 ± 2
44	--	--	85.5	83.6	84.5 ± 1
50	94.5	91	92.8	91	92.± 1
56	103.5	105	105.9	106	105 ± 1
62	109.8	108.7	113.9	112.4	111 ±3
68	108	114.6	116.6	126.14	116 ± 9

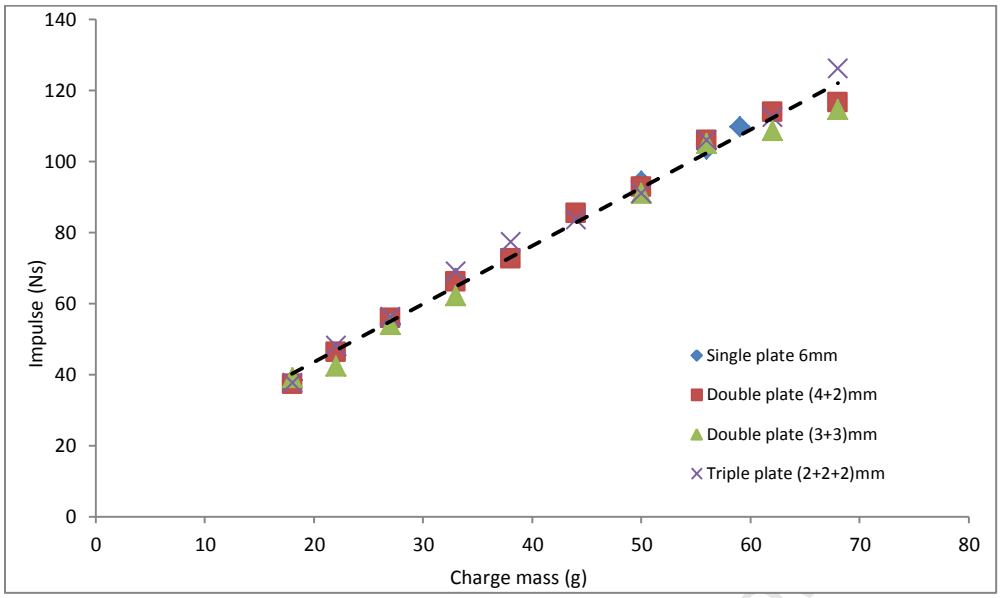

Figure 8-1: Graph to show the impulse versus charge mass of 6mm thick single, double {(3+3, 4+2)}mm and triple (2+2+2)mm plates

8.2 Comparison of 4mm thick single and double plates of Domex 550MC

In general, the deformation in double(2+2)mm plates is greater than the deformation in 4mm thick single plates at all charge masses. A comparison of midpoint deflections of 4mm thick single and double(2+2)mm plates at equal charge masses is shown in Figure 6-1.

The transition between Mode-I and Mode-II failure was defined as Mode II* by Langdon et al. [35]. The impulse at which Mode II* occurs is the threshold impulse. The deformation profiles were grouped according to pre and post threshold impulse, Different profiles were observed after tearing than prior to this failure as shown in Figure 8-2 and Figure 8-3. Prior to the threshold impulse, double layered plates showed greater deformations at equal charge masses, as indicated in Figure 8-2 (a, b and c). At the threshold impulse, the deformation behaviour of both configurations is similar as shown in Figure 8-2d. After the threshold impulse, the trend of deformation profiles starts changing, here the single plates started to deform more than layered plates after threshold impulse as depicted in Figure 8-3.

Failure Mode I (large inelastic response) and Mode Itc (large inelastic response with thinning in central area) responses were noted for both configurations as impulse increased from 20 Ns to 45 Ns. The reduction in thicknesses of both plate configurations were found at the central portion of the plates over the diameter smaller than charge diameter. Reduction in thickness was more prominent in 4mm thick single plates than in the double plates. At lower impulses, no significant reduction in thickness was observed. At the impulses 36Ns to 45Ns, a 1.3 mm total reduction in thickness in single and double plates was found. Thinning in the central area of mild steel plates subjected to localized blast loading was also reported by Nurick and Radford [33].

At 23.5g charge mass, the single plates did not exhibit tearing whereas the double plates exhibited higher midpoint deflections of the back plate and partial tearing of the front plate. Further increase in impulse at a charge mass of 30g led to partial tearing (Mode II*c) in the central area of the single plate. The double plates exihibited capping failure at 30g charge mass whereas the single plates showed the partial tearing. In the case of double plates, a cap was torn away from the back plate whereas the front plate was partially torn at a charge mass of 30g.

Mode IIc (complete tearing) was noted in 4mm thick single and double plates at an impulse of 57 Ns. The diameter of the hole in the single plate was 20 to 22mm whereas in the double plates, it was larger between 28.5mm and 29.5mm. The shape of holes in double plates was rounded whereas single plate was torn in a petalling fashion as indicated in Figure 7-6 and Figure 7-2.

The single 4mm thick Domex 550MC outperformed the double plate counterpart, both in terms of larger midpoint displacements for a given charge mass and higher threshold impulse.

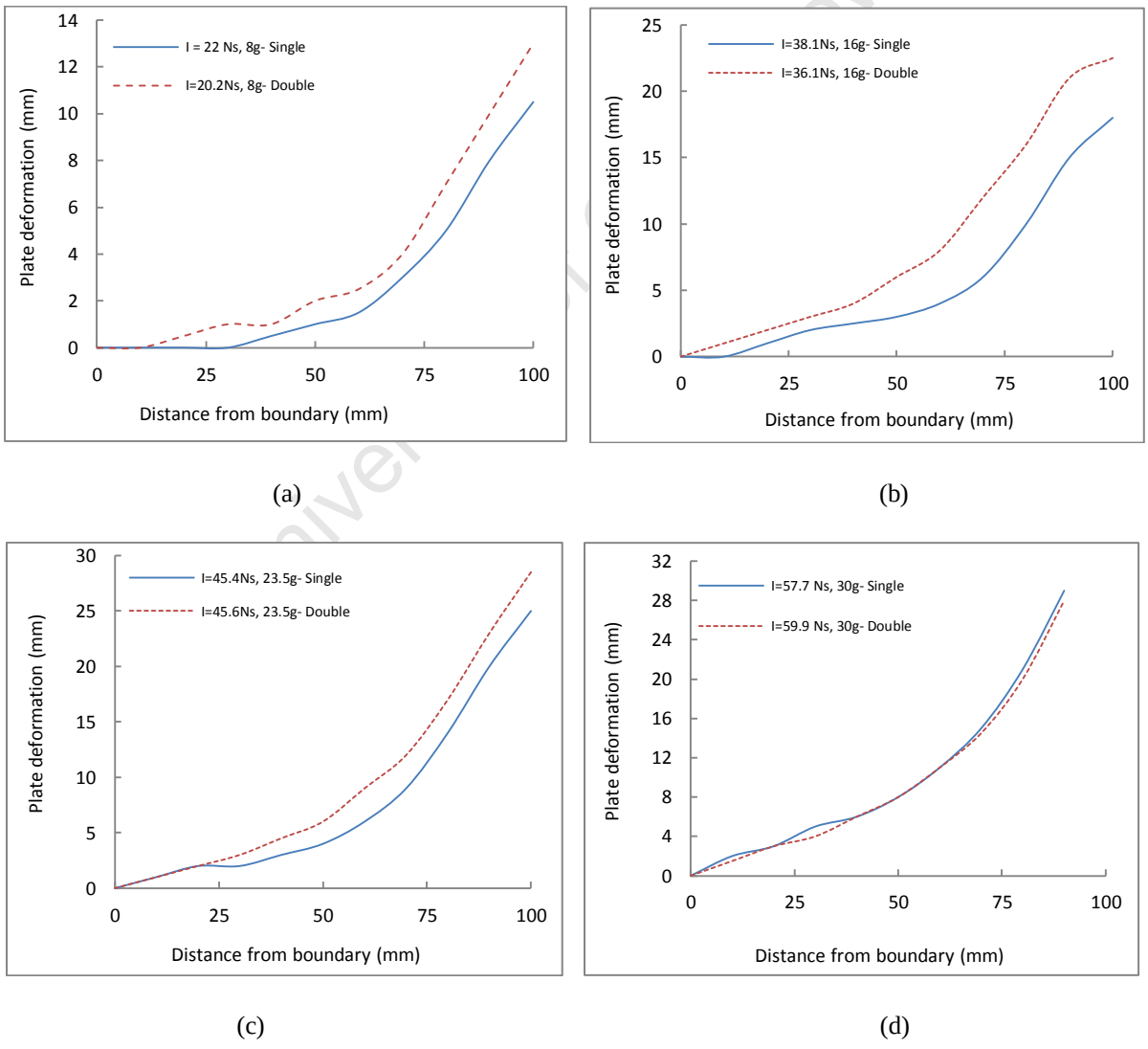

Figure 8-2: Comparison of deformation profiles of 4mm single and double (2+2)mm plates at (a) 8g, (b) 16g, (c) 23.5g and (d) 30g of explosive charge

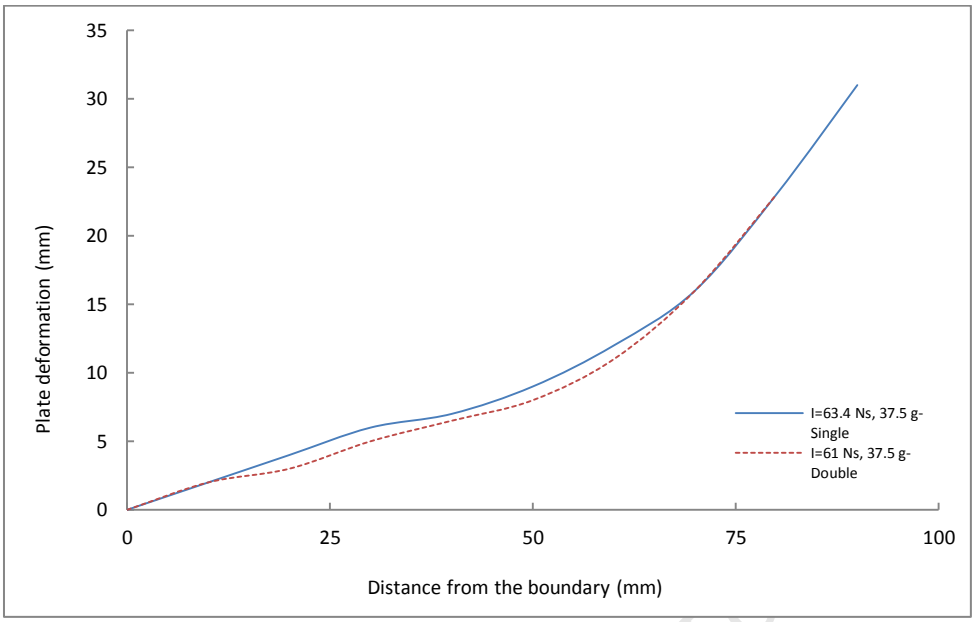

Figure 8-3: Comparison of deformation profiles of 4mm thick single and double (2+2)mm plates at 37.5g, indicating the change in deformation trend of single plate (post threshold impulse)

8.2.1 Comparison between experimental and predicted results

Plate deformations were simulated using ABAQUS/Explicit for 4mm thick single plates of Domex 550MC, and were compared with experimental midpoint deflections after the blast tests for the Mode I failures. Table 8-2 shows experimental and predicted deformations of 4mm thick single plates at increasing charge masses.

Comparison of experimental and predicted midpoint deflections of 4mm thick single plates are shown in Figure 8-4. The experimental results showed a lower midpoint deflections than the predicted deformations.

Table 8-2: Experimental and predicted deformations of 4mm thick single plates of Domex 550MC

Charge mass (g)	Midpoint deflection of 4mm thick single plates	
	Predicted (mm)	Experimental (mm)
8	15	10.3
16	25	17.85
23.5	29	24.44
30	38	29.47

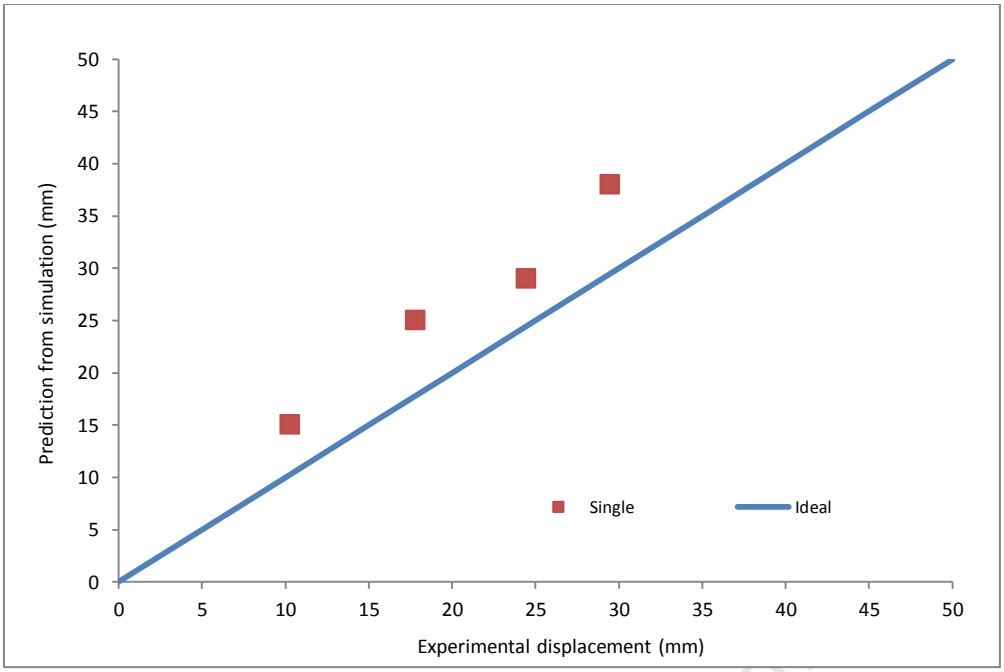

Figure 8-4: Experimental midpoint displacements versus predicted midpoint displacements for 4mm thick single and double (2+2)mm plates (Domex 550MC)

8.3 Comparison of 4mm thick single and double (2+2)mm plates (Domex 700MC)

The comparison of deformation profiles of 4mm thick single and double plates at equal charge masses are given in Figure 8-5 and Figure 8-6. There is a change in the shape of the deformed profile once Mode II initiates. At all charge masses, the deformation in double plates is greater than in the single plates. The difference is most evident at low charge masses. At the threshold impulse, the deformation profiles are almost identical as indicated in Figure 8-7a and b. After threshold impulse, 4mm thick single plates showed larger midpoint deflections than double plates as demonstrated in Figure 8-8 because the cap size is smaller in the single plates. This behaviour was also noted during the comparison of 4mm configurations of Domex 550MC plates.

A summary of the response of 4mm thick single and double (2+2)mm plates is given in Table 8-3. The comparison of 4mm thick single and double plates of Domex 700MC show that the performance of single plates is better than the double plates when subjected to localized blast loading. For example, the double plate configuration completely perforated at a 33g charge mass (II_c) whereas the single plate exhibited Mode I failure only as shown in Table 8-3. The double plates fail at lower charge masses and impulses, reducing their protection level.

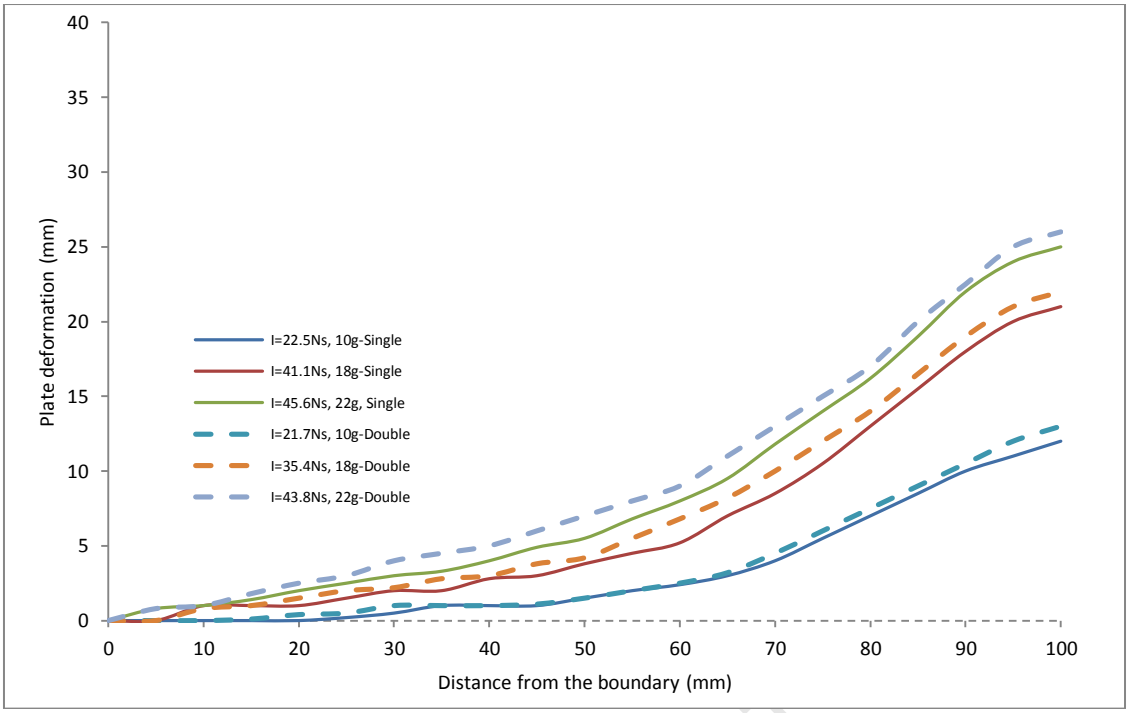

Figure 8-5: Comparison of deformation profiles of 4mm single and double (2+2)mm plates subjected to various charge masses (Domex 700MC)

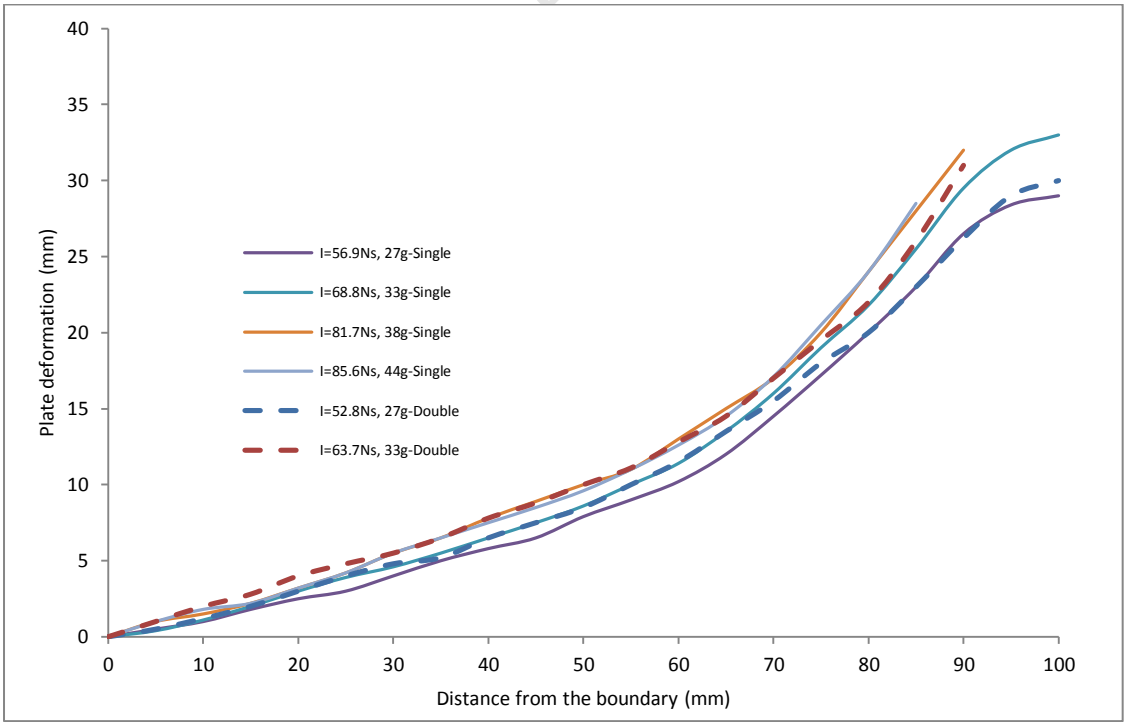

Figure 8-6: Comparison of deformation profiles of 4mm single and double (2+2)mm plates subjected to various charge masses (Domex 700MC)

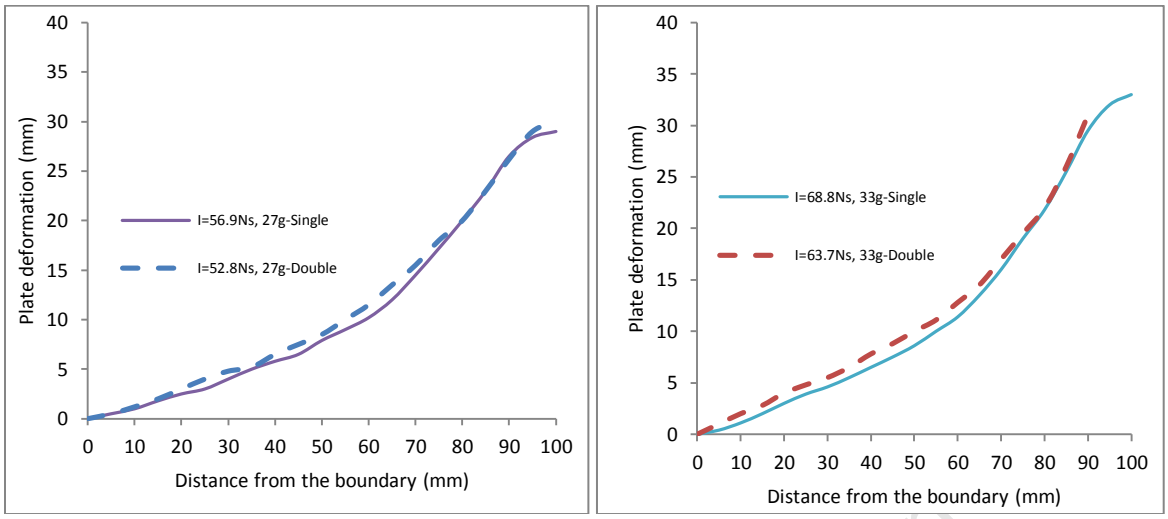

(a) (b)

Figure 8-7: Comparison of deformation profiles of 4mm single and double (2+2)mm plates at (a) 27g and (b) 33g of charge mass (Domex 700MC)

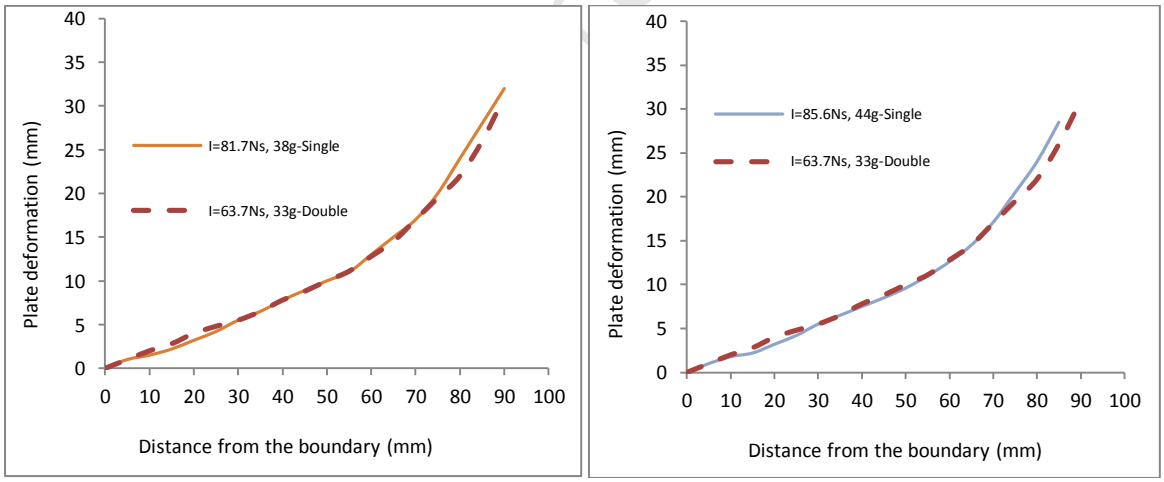

(a) (b)

Figure 8-8: Comparison of deformation profiles of 4mm single and double (2+2)mm plates at a charge mass of 33g and 44g (Domex 700MC)

Table 8-3: Summary of failure modes of 4mm configurations of Domex 700MC

Impulse Ns/ charge mass (g)	Failures modes 4mm thick single and double (2+2)mm plates		
	Single plate	Double plate	
		Front plate	Back plate
21-23/10	I	I	I
35-42/18	I	I	I
43-45/22	I	I	I
52-52/27	I	$II^{*}_{cp\ 90}$	I
52-68/33	I	II_c	II_c
81.7/38	$II^{*}_{cp\ 40}$	X	X
85.6/44	II_c (cap diameter = 26mm)	X	X

8.3.1 Non–dimensional analysis, comparing Domex 550MC and Domex 700MC

As the charge diameters of Domex 550MC and Domex 700MC were 33mm and 40mm respectively, non-dimensional impulse [17] was used to allow for comparison of blast-loaded plates of different load geometries and different yield strengths to be treated similarly. A graph of deflection-thickness ratio versus dimensionless impulse for Domex 550MC and Domex 700MC plates is shown in Figure 8-9. Once charge diameter and yield strength are accounted for, the data reduces to one data set in dimensionless form.

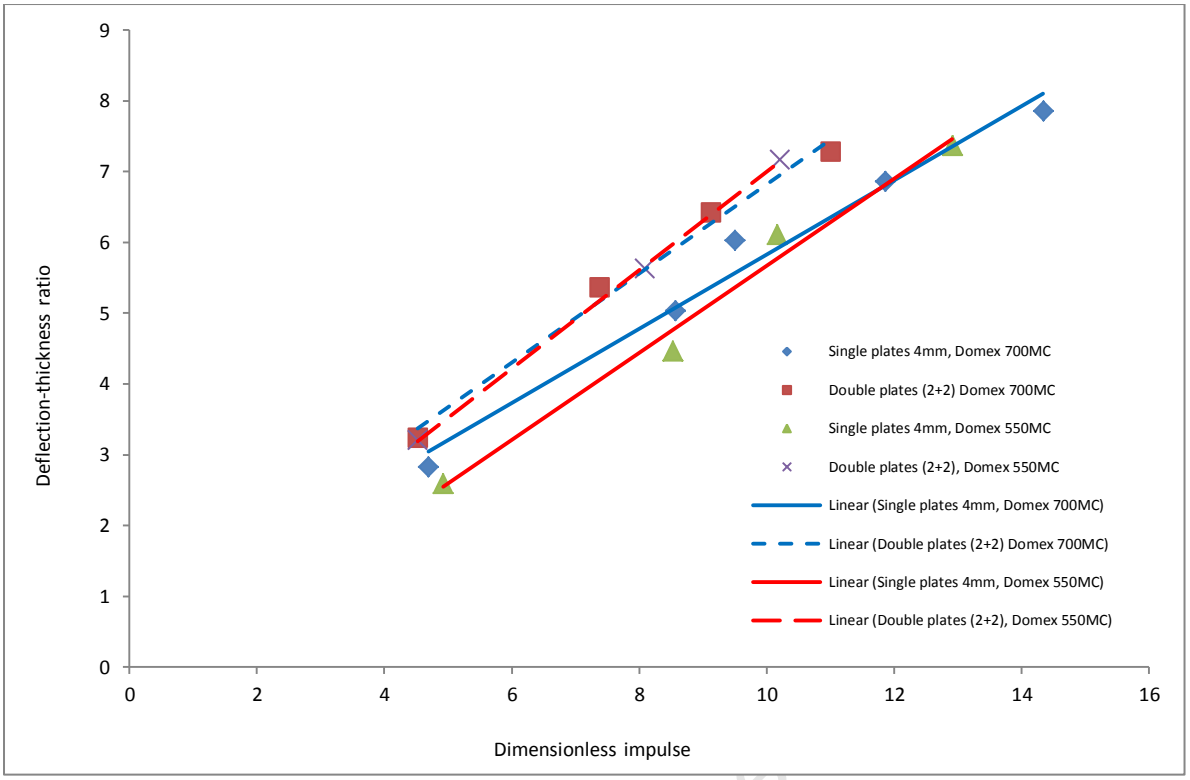

Figure 8-9: Graph to show deflection-thickness ratio versus dimensionless impulse of 4mm thick single and double (2+2)mm plates of Domex 700MC and Domex 550MC

8.3.2 Comparison of experimental and predicted deformations (Domex 700MC)

The single plates of Domex 700MC steel of 4mm, 6mm and 8mm thickness were simulated during the experimental design. The comparison of experimental displacements and the numerically predicted displacement of 4mm and 6mm thick single plates is shown in Figure 8-10. At lower charge masses, there is good correlation between the experimental and predicted deformations. At higher charge masses, the predicted deformations are greater than the experimentally obtained values.

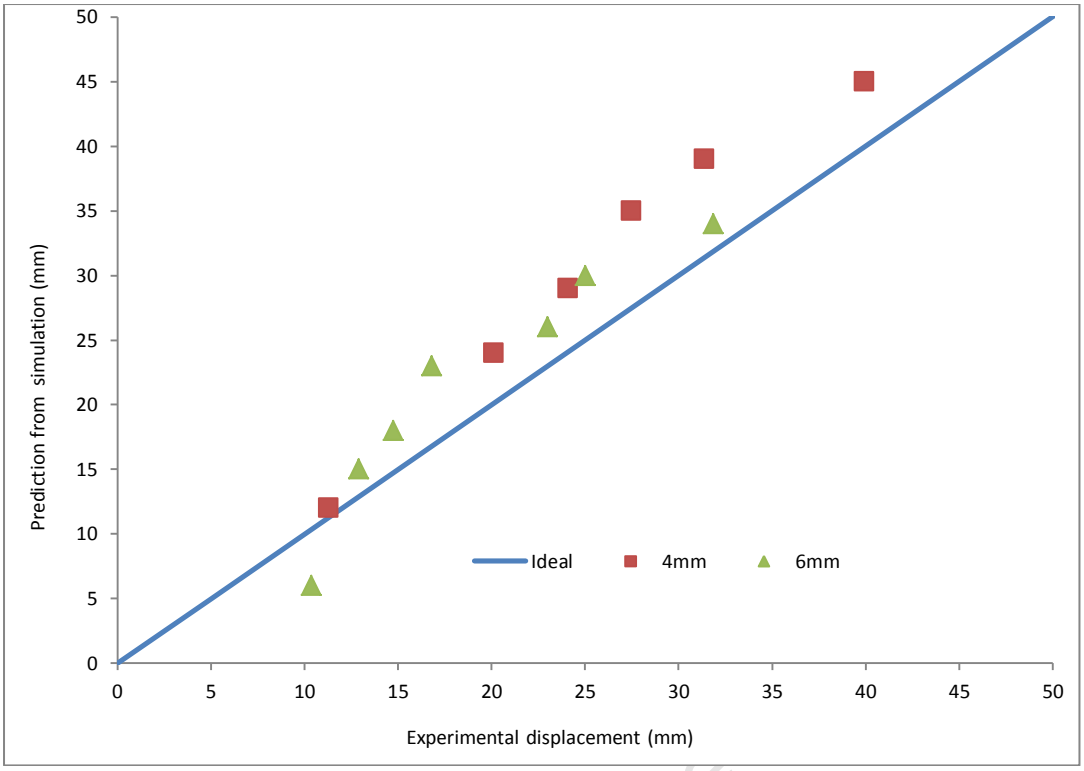

Figure 8-10: Graph to show the comparison of experimental versus theoretical deformations of 4mm and 6mm thick single plates of (Domex 700MC)

8.4 Comparison of 6mm thick configurations (Domex 700MC)

8.4.1 Comparison of midpoint deflections of 6mm thick single, double (3+3)mm, double (4+2)mm and triple (2+2+2)mm plates

The midpoint deflection versus impulse curves for the 4mm thick single and double (2+2)mm and the 6mm thick single, double (3+3)mm, double (4+2)mm and triple (2+2+2)mm plate configurations are shown in Figure 8-11.

The midpoint deflections of double (2+2)mm plates are grater than the 4mm thick single plates at equal charge mass. However, the double plates failed at lower charge mass than single plates as indicated in Figure 8-11. As expected, the thicker plate configuration outperformed the 4mm thick plate configurations, exhibiting lower displacements and higher tearing threshold impulses.

It is evident from Figure 8-11 that the 6mm thick single plates exhibited the lowest displacements. The double (4+2)mm configuration and triple (2+2+2)mm configuration had similar displacement and were the largest of the nominally 6mm thick configurations. It should also be noted that the difference in deflection response, is smaller, and consistent for the entire range of charge masses used herein.

Regarding the failure/cracking of plates at various charge masses, the triple plate configuration failed at the lowest impulse followed by 6mm thick single plates. The best performance was shown by the double plate configuration of (3+3)mm among the other three configurations.

The details of various failure modes along with the cracking percentage (cp) of all the configuration of 6mm thickness is given in Table 8-4. The cracking percentage was calculated from the entire circumference/point of inflection created before capping failure as shown in Figure 5-18 and Figure 5-19. As shown in Table 8-4, the front plates were cracked by 5 to 30 % at a charge mass of 62g and 68g for double (3+3)mm configuration whereas the back plate was not cracked. In a configuration (4+2)mm, the front plates cracked by 70 % and 15 % at a charge mass of 62g and 68g respectively and the back plates cracked by 30 %, and 5%.

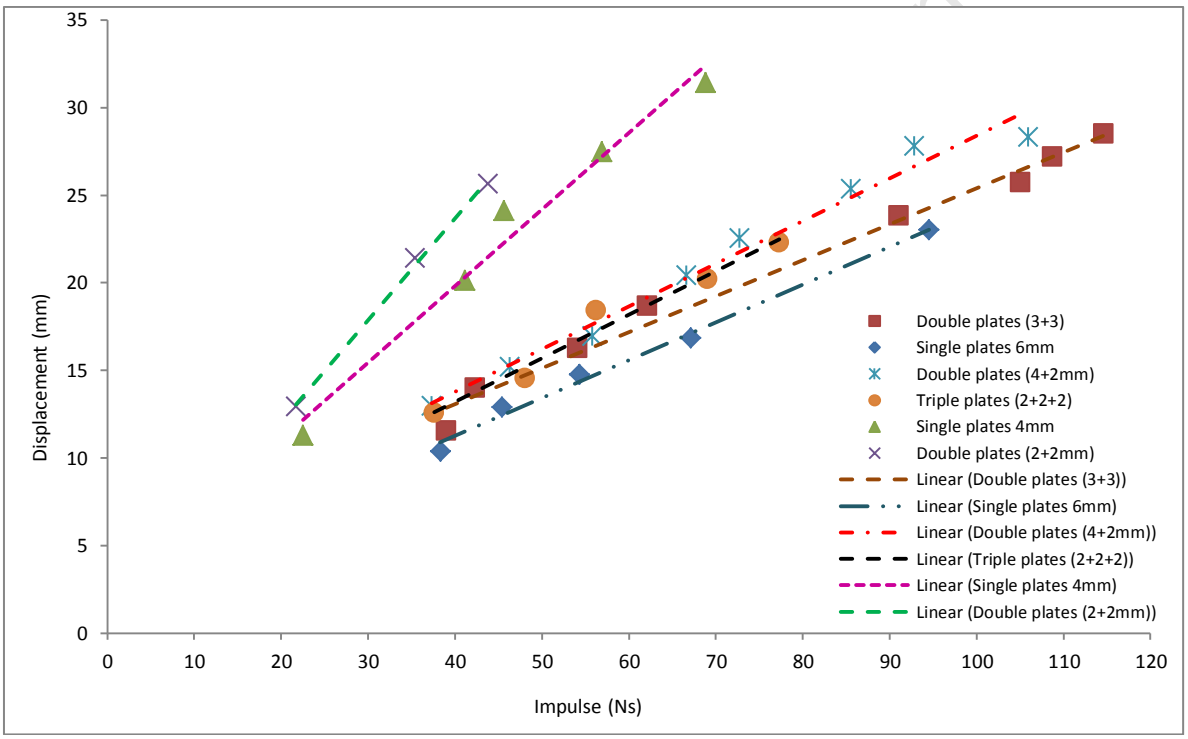

Figure 8-11: Graph to show the experimental displacement Vs impulse of single (6, 4)mm, double {(3+3), (4+2), (2+2)}mm and triple (2+2+2)mm plates (Domex 700MC)

Table 8-4: Summary of the failure modes of 6mm configurations (Domex 700MC)

Impulse Ns/ Charge (g)	Failures modes (Various configurations of 6mm thickness)							
	6mm Single	Double plate (3+3)mm		Double plate (4+2)mm		Triple plate (2+2+2)mm		
		Front	Back	Front	Back	Front	Middle	Back
37-40/18	I	I	I	I	I	I	I	I
42-48/22	I	I	I	I	I	I	I	I
53-56/27	I	I	I	I	I	I	I	I
62-69/33	I	I	I	I	I	I	I	I
72-77/38	x	x	x	I	I	I	I	I
83-85/44	x	x	x	I	I	$II^{*}_{cp\ 40}$	I	I
91-94/50	I	I	I	I	I	$II^{*}_{cp\ 90}$	$II^{*}_{cp\ 2}$	I
103-106/56	$II^{*}_{cp\ 40}$	I	I	I	I	$II^{*}_{cp\ 60}$	I	II_{c}
109.8/59	$II^{*}_{cp\ 60}$	x	x	x	x	x	x	x
108-112/62	II_{c}	$II^{*}_{cp\ 5}$	I	$II^{*}_{cp\ 70}$	II^{*}_{30}	$II^{*}_{cp\ 95}$	I	$II^{*}_{cp\ 90}$
114-126/68	x	$II^{*}_{cp\ 30}$	I	$II^{*}_{cp\ 15}$	II^{*}_{cp5}	$II^{*}_{cp\ 90}$	$II^{*}_{cp\ 5}$	I

8.4.2 Comparison of deformation profiles of 6mm thick configurations

The comparison of deformation profiles of 6mm thick single, double (3+3)mm, double (4+2)mm and triple (2+2+2)mm at a charge mass of 18g and 22g is shown in Figure 8-12.The deformation from boundary to midpoint in double (4+2)mm plate at both charge masses is greater than in other configurations. The 6mm thick single plates exhibited less deformation as compared to other three configurations. The deformations of double (3+3)mm and triple (2+2+2)mm plates are in between the 6mm thick single and double (4+2)mm plates. This indicates that the trend for midpoint displacement indicated in Figure 8-11 is evident at other positions in the profile as shown in Figure B-18 of "Appendix C".

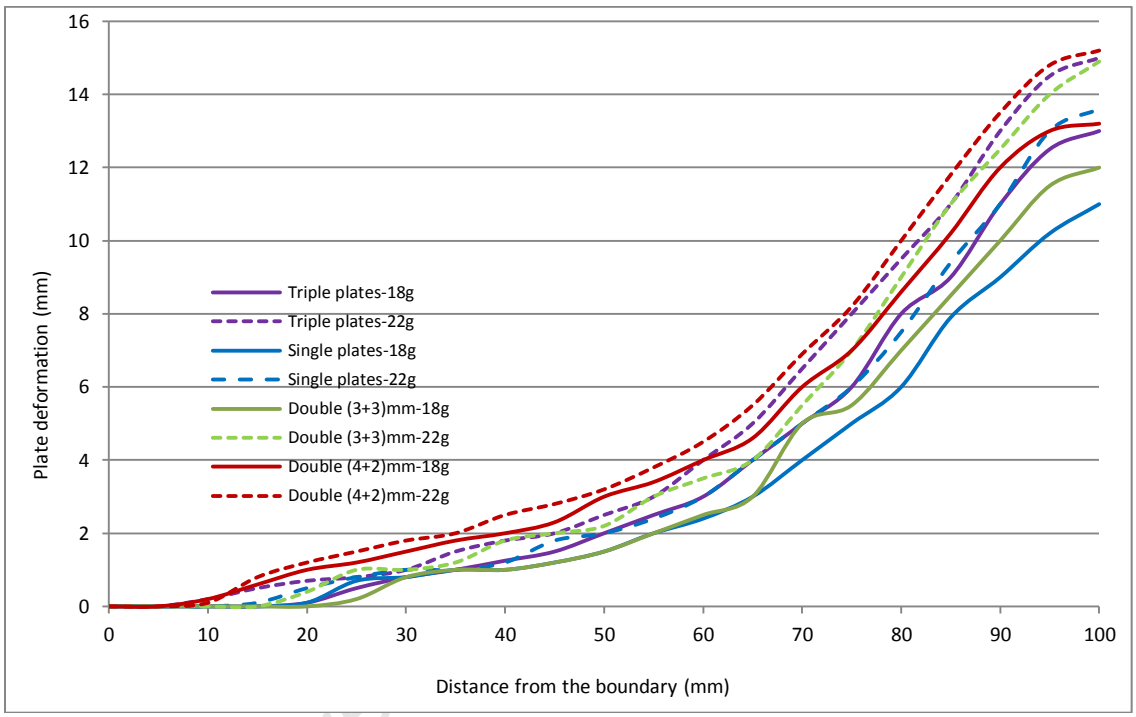

Figure 8-12: Comparison of deformation profiles of 6mm thick configurations at 18g and 22g charge masses

The deformation profiles at a charge mass of 50g and 56g are shown in Figure 8-13 and Figure 8-14 respectively. At a charge mass of 50g, all configurations exhibited two different trends. The 6mm thick single and double (3+3)mm plates exhibited equal deformation profiles and the deformations are lower than the other two configurations. The double (4+2)mm and triple (2+2+2)mm plates also exhibited similar behaviours and showed higher deformation than other two configurations. At all the charge masses, the deformations in triple (2+2+2)mm plates is greater than 6mm single plates up to a 50g charge mass.

At a charge mass of 56g, the back plate of triple (2+2+2)mm thick configuration failed. Up to failure point of triple plates, the deformation profiles of double (3+3)mm and triple (2+2+2)mm are similar.

Figure 8-15 shows the deformation profiles of 6mm configuration at a charge mass of 62g. At a charge mass of 62g, 6mm thick single and triple (2+2+2)mm plates failed and the triple plate deformations are greater than single plates. The deformation profiles of double (3+3)mm and triple (2+2+2)mm are similar up to the failure point of triple plate.

At a charge mass of 68g, the deformation profiles of back plate of double (3+3)mm and double (4+2)mm are shown in Figure 8-16. The deformations in double (4+2)mm plates are greater than in the double (3+3)mm plates. The back plate of double (4+2)mm configurations cracked at a charge mass of 68g.

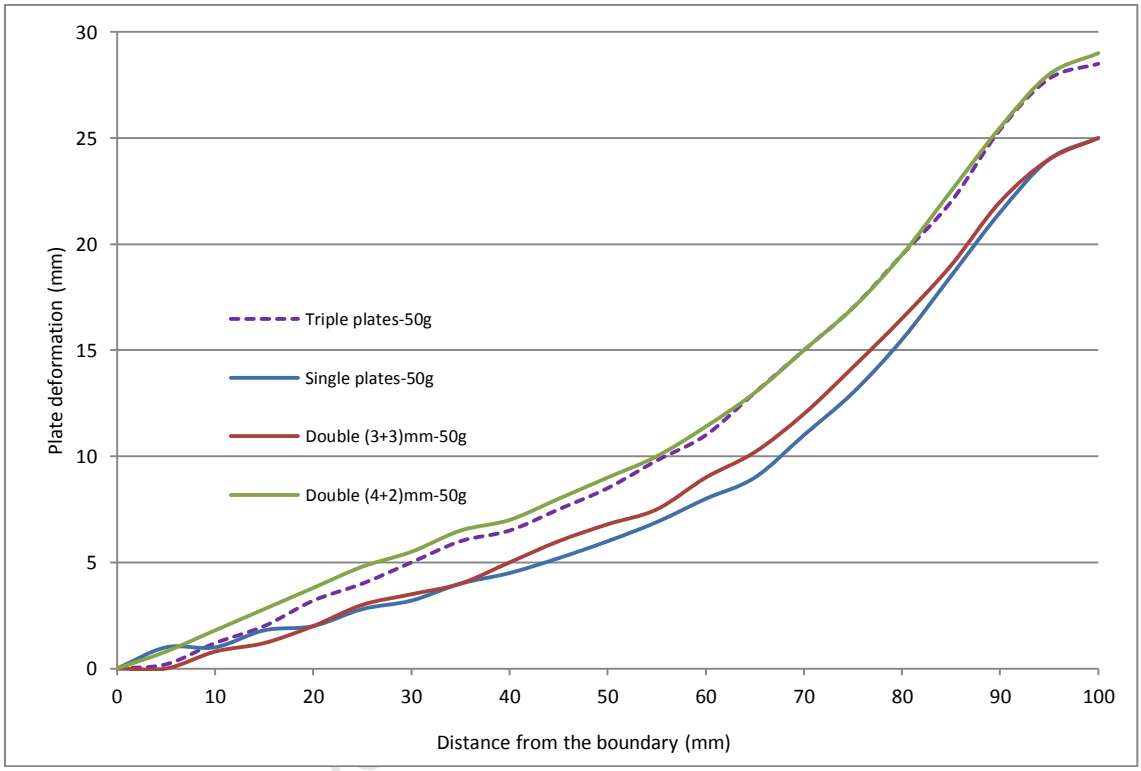

Figure 8-13: Comparison of deformation profiles of 6mm configurations at 50g of explosive charge mass

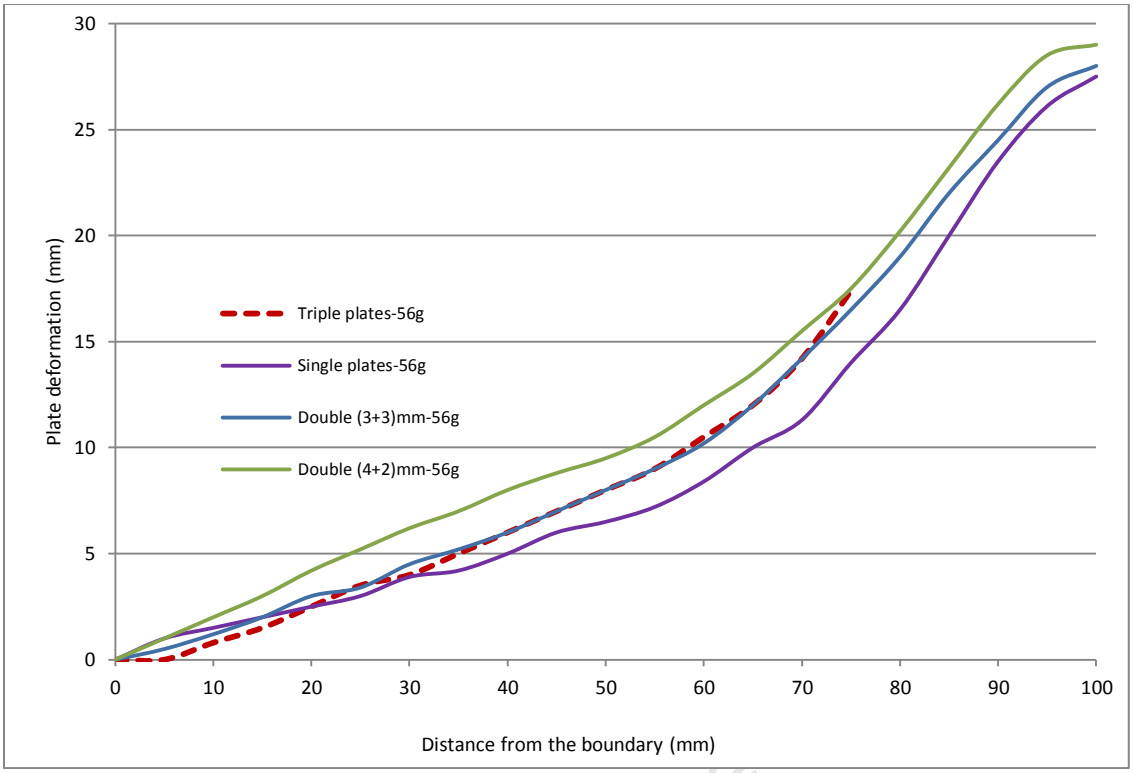

Figure 8-14: Comparison of deformation profiles of 6mm configurations at 56g charge mass

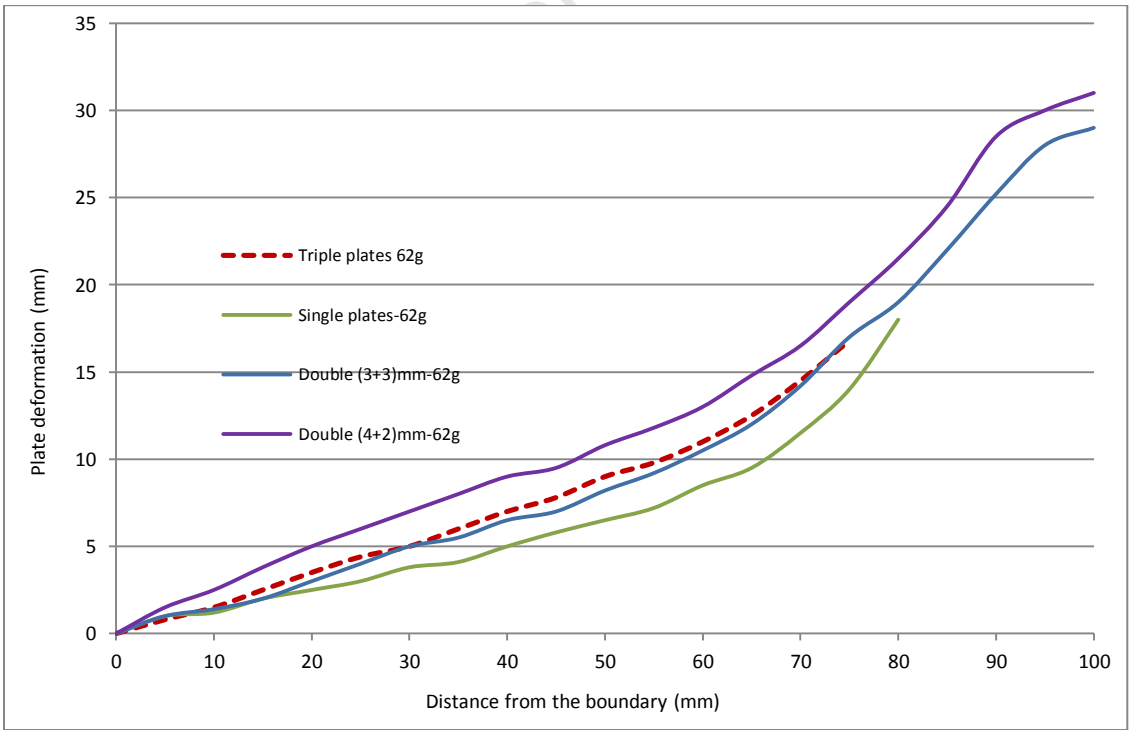

Figure 8-15: Comparison of deformation profiles of 6mm configurations at 62g charge mass

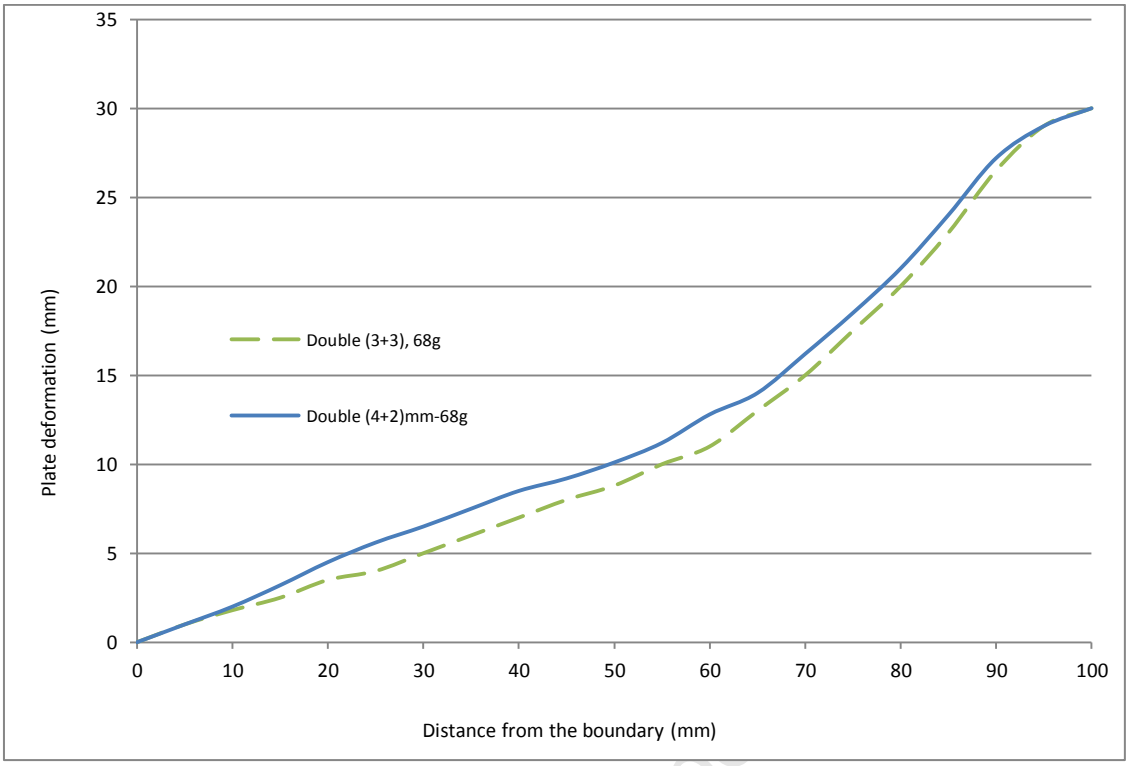

Figure 8-16: Comparison of deformation profiles of double (3+3)mm and double(4+2)mm at 68g charge mass

The comparison of 6mm thick single and triple (2+2+2)mm plates of Domex 700MC showed that the performance of 6mm thick single plates is better than the triple plates when subjected to localized blast loading.

The capping failure of all front plates of triple (2+2+2)mm configuration indicates the application of a uniform loading over a circular diameter during blast loading. The front plates capped radially with a cap diameter of 29 to 31mm that is 9mm to 10mm less than the charge diameter (40mm). The shape of the torn caps of all the front plates at various charge masses is circular as shown in Figure 8-17. The torn caps show a similarity of the applied load during blast loads.

The fragments of the back plates (of double and triple) are different in shape depending upon the charge mass. The back plates failure does not indicate uniform loading over a circular diameter. The back plates were not loaded directly by a charge mass but they were loaded by the front plates for double plate configurations and by the front and middle plates for the triple plate configurations.

The difference in failure mechanisms of the front and back plates was also observed during the fractography of the front and back plates, torn at various charge masses where the front plates showed equiaxed dimples (Figure 7-26 and Figure 7-34) and the back plates indicated elongated dimples (Figure 7-27 and Figure 7-35).

Charge mass 44 g

Charge mass 50 g

Charge mass 56g

Charge mass 62g

Charge mass 68g

Figure 8-17: Capping failure of front plates of triple (2+2+2)mm plate configuration at various charge masses (Domex 700MC)

The comparison of deformations of both the configurations 4mm and 6mm thickness of Domex 700MC plates was made by using the non-dimensional impulse [17]. Deflection-thickness ratio versus dimensionless impulse of 6mm configurations of Domex 700MC is shown in Figure 8-18 and deflection-thickness ratio versus dimensionless impulse of both 4mm and 6mm configuration is shown in Figure 8-19. The trend of performance did not change when converted to non-dimensional form.

The comparison of deflection-thickness ratios versus dimensionless impulse of both materials Domex 550MC and Domex 700MC in configurations of 4mm and 6mm thickness is shown in Figure 8-20. The 4mm thick single plates performed better than double (2+2)mm plates for both materials. The 4mm thick single plates of Domex 550MC and Domex 700MC failed at dimensionless impulse of 12 and 14 respectively whereas the double plates failed at dimensionless impulse of 9.5 and 11. For 6mm configurations, double plates performed better than single and triple plate configurations as the single plates failed at lower dimensionless impulse as indicated in Figure 8-20.

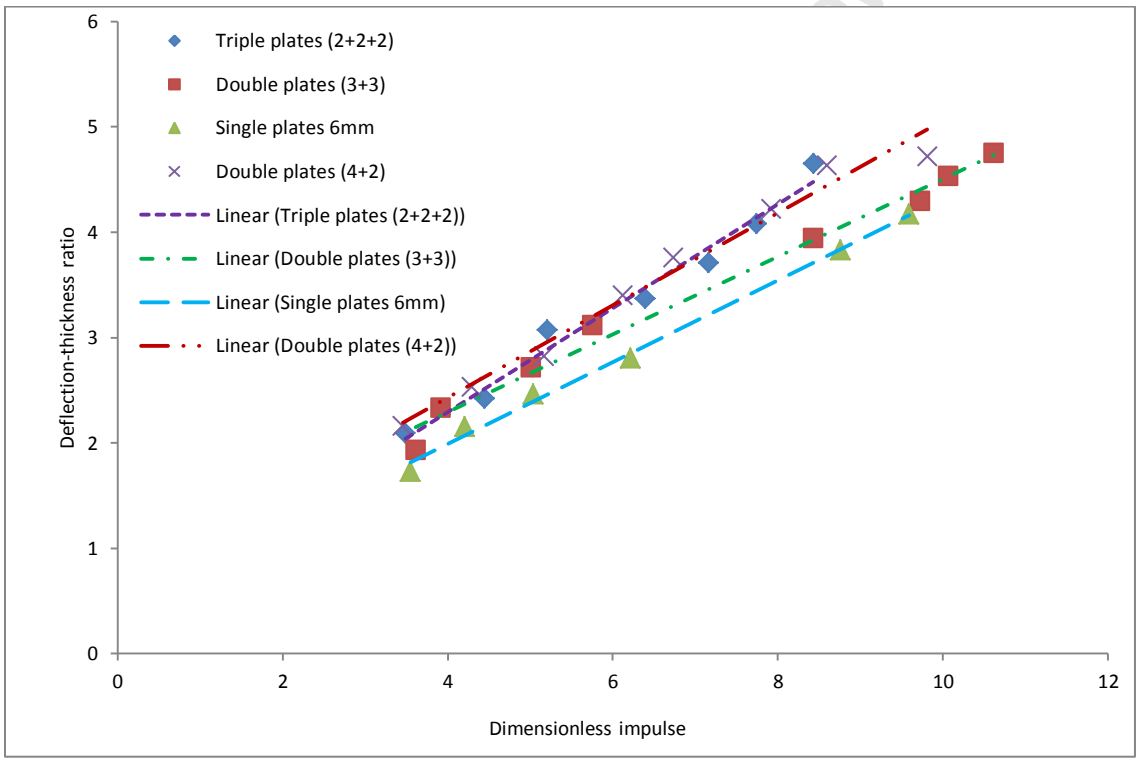

Figure 8-18: Comparison of deflection-thickness ratio versus dimensionless impulse of 6mm thick single, double (3+3)mm, (4+2)mm and triple (2+2+2)mm plates

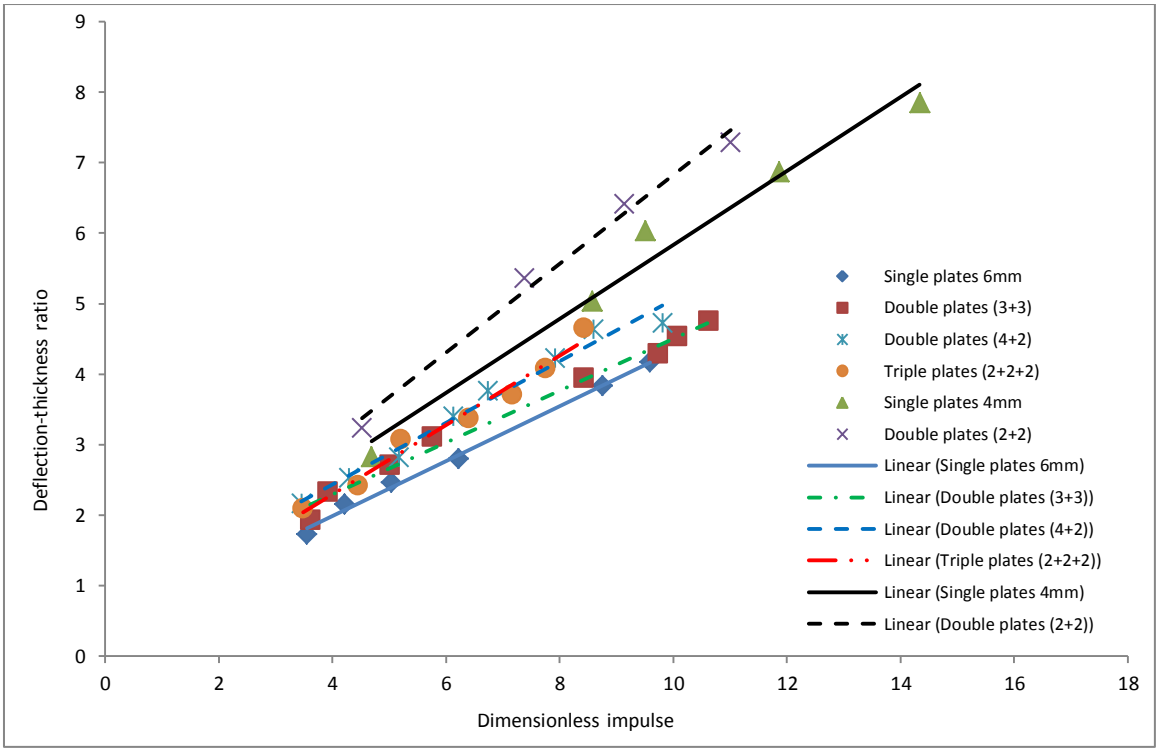

Figure 8-19: Graph to show deflection-thickness ratio versus dimensionless impulse of blast loaded 4mm and 6mm thick single plates (Domex 700MC)

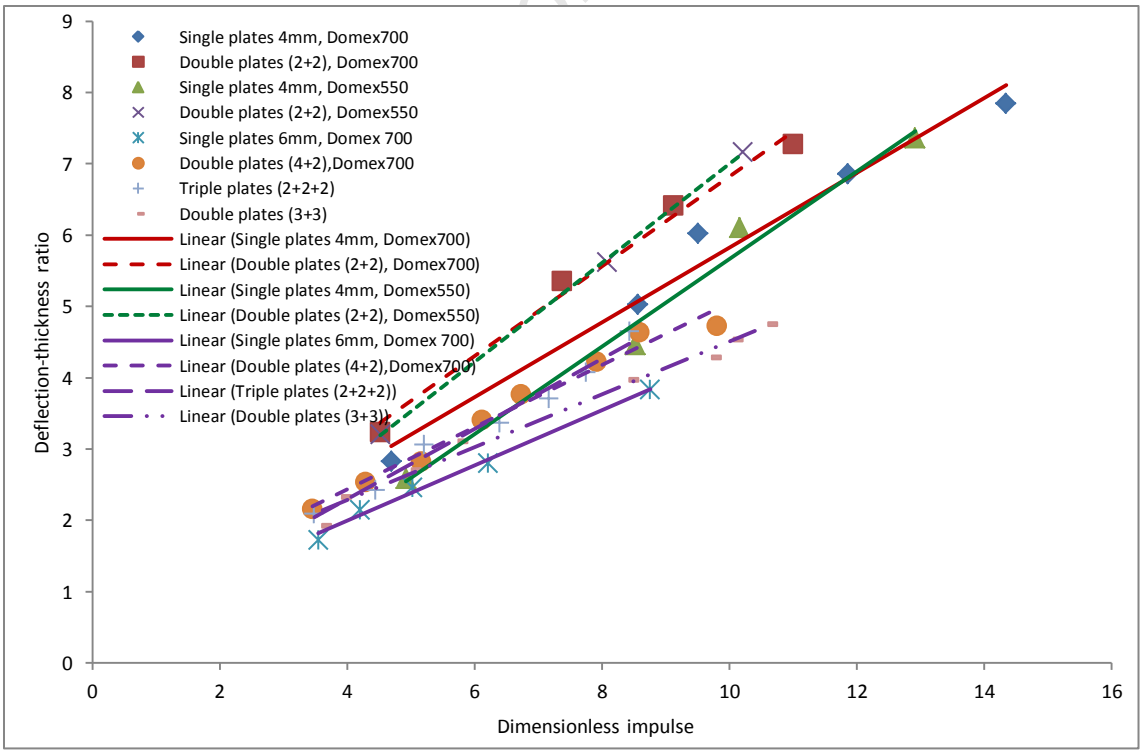

Figure 8-20: Deflection-thickness ratio versus dimensionless impulse of blast loaded 4mm and 6mm thick single plates of Domex 700MC and Domex 550MC

8.5 Effect of single, double and triple plates on dimple morphology

8.5.1 Quantity and size of dimples

It is observed that the dimple morphology is strongly affected by the charge mass/impulse. At higher charge masses, fewer dimples are present. It is assumed that the strain rate of test plates during blast loading increases with the increase of charge mass/impulse. This is also confirmed by FE simulations. The target plates were subjected to various impulses and the strain was measured over a charge diameter (40mm) at 50 microseconds. Increase in strain was found by increasing impulse as depicted in Table E-2 of "Appendix E". Fractography of the tensile sample at various strain rates (Chapter 3) indicated the higher quantity of dimples at low strain rates and larger diameters of the dimples at higher strain rates. Fractography of the torn plates at various charge masses also reflected the same trend of dimple morphologies.

Figure 8-21 shows the failure deformations of 4mm thick single plates tested at 33g, 38g and 44g charge mass. The plates deformed up to 33g and then started to tear. The deformation of cracked plate at 38g charge mass is 36.5mm whereas the deformation in case of 44g charge mass is 32mm that is less than the cracked plate at lower charge mass, hence showing less dimples at higher charge mass. Deformation profiles of plates tested at 38g and 44g charge mass are nearly of the same pattern up to the fracture, as the additional energy was used in the fracture of the plate tested at 44g, as deformation profiles at 38g and 44g are otherwise indistinguishable.

Comparison of fractured surfaces of 4mm thick single plates, tested at 38g and 44g indicated the presence of more dimples at lower charge mass. The size of dimples is larger in case the plates tested at higher charge mass as shown in Figure 7-24 and Figure 7-25.

The same trend can be seen in 6mm thick single plates tested at 59g and 62g. At 62g charge mass, the dimple size is bigger than obtained at 59g charge mass. In addition to this, river patterns are visible in the sample tested at 62g, discussed in section 7.9.3.

Dimple morphology can also related to the amount of plastic deformation at the point of fracture, higher the deflections at fracture (at lower charge mass) exhibit higher numbers of dimples. For the lower failure deformation (at higher charge mass), the fewer dimples are present and the size of dimples is larger.

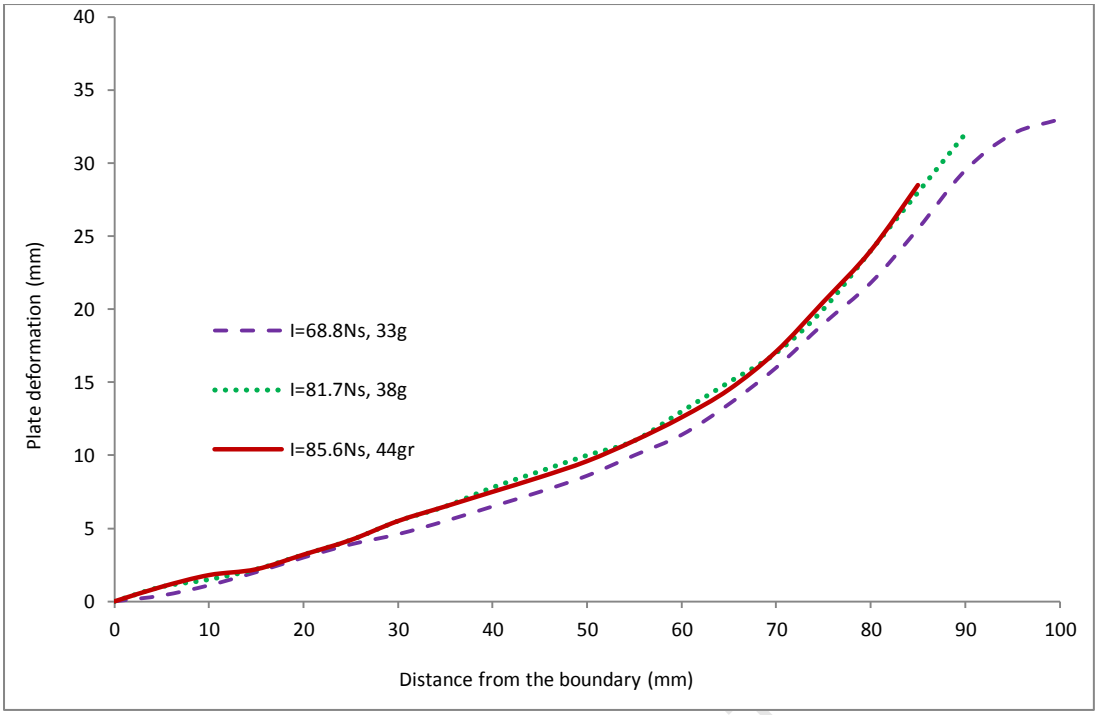

Figure 8-21: Deformation profiles of 4mm thick plates to show failure deflections at a charge mass of 33g, 38g and 44g

8.5.2 Influence of failure mode and deformation profile upon dimple morphology

Figure 8-22 shows the deformation profiles of 6mm thick single plates tested 56g, 59g and 62g charge mass. The 6mm thick single plates deformed up to 56g charge mass and then started to tear. At a charge mass of 59g, the plate was cracked over a charge diameter along with a failure deformation of 30mm. At a charge mass of 62g, the plate was capped with a failure deformation of 22mm. The plate tested at 62g shows lower deformation at the failure point and larger dimples compared to sample tested at 59g as indicated in Figure 8-23a and b.

The double layered plates of 4mm configuration tested at 33g also showed a larger amount of dimples at higher failure deformation as shown in Figure 7-26 (back plate fractograph) and Figure 7-27 (front plate fractograph). The deformation profiles of the front and back plate tested at 33g charge mass show a larger deformation of back plate as depicted in Figure 8-24.

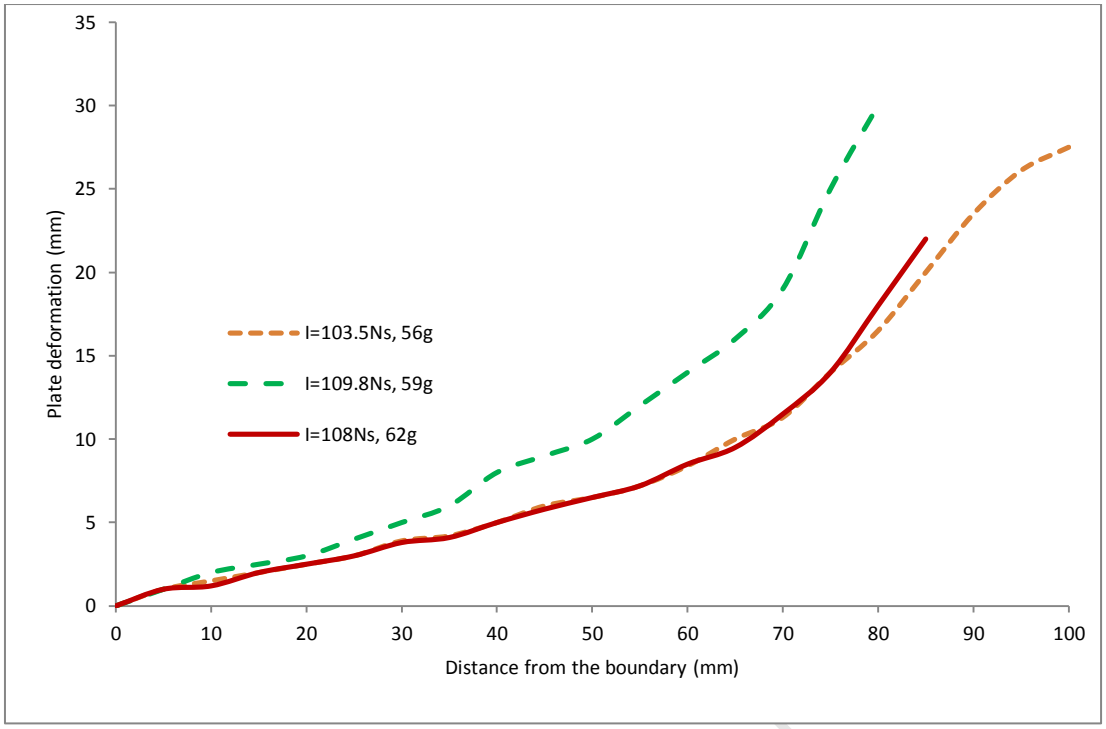

Figure 8-22: Deformation profiles of 6mm thick single plates to show failure deflections at a charge mass of 56g, 59g and 62g

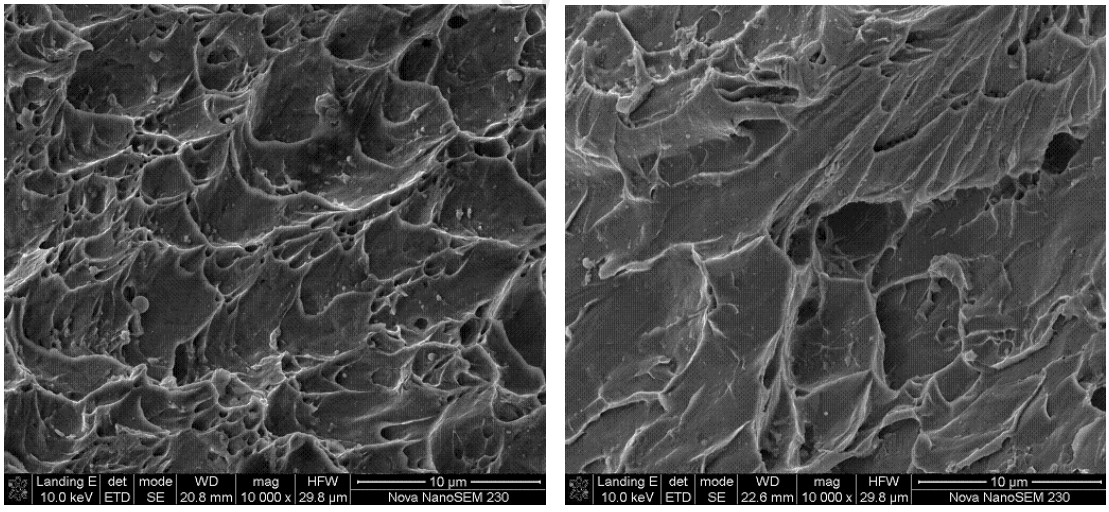

(a) Charge mass 59g (b) Charge mass 62g

Figure 8-23: Fractographs of 6 mm thick single plates of Domex 700 MC, after blast testing at (a) charge= 59g and (b) 62g

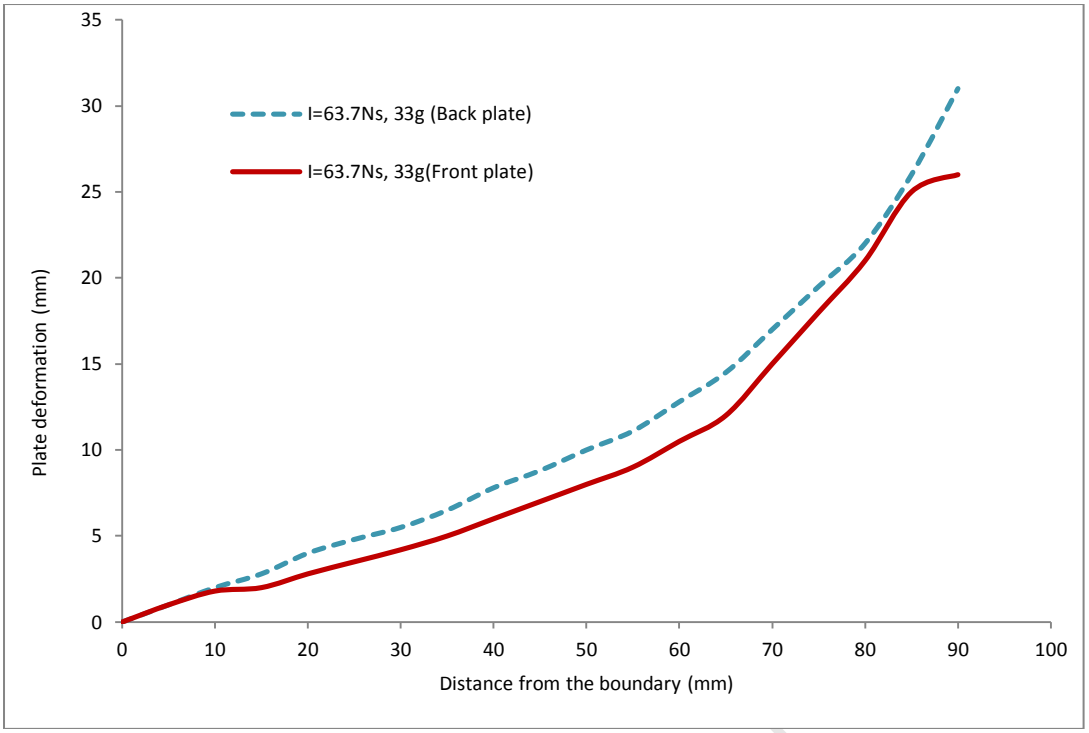

Figure 8-24: Deformation profiles of double (2+2)mm plates to show the amount of failure deformation of front and back plates tested at a charge mass of 33g

8.5.3 Change of dimple morphology

The metallographic observations of the 4mm and 6mm thick single torn plates indicate inter-granular and trans-granular failure paths in microstructures as shown in Figure 6-21, Figure 6-22 and Figure 6-23a and b. The majority of the dimples in fractographs of all configurations were initiated at inclusion sites.

In case of layered plates, double (2+2)mm plates in 4mm configuration and triple (2+2+2)mm plates in 6mm configuration exhibited different dimple morphology for front and back plates. The front fractured plates (exposed to explosive) generally exhibited equiaxed dimples (Figure 7-26 and Figure 7-34) whereas the back plates showed elongated dimples (Figure 7-27 and Figure 7-35. This means that the front plates experienced uniaxial loads and the back plates experienced shear load.

Generally, the ductile materials demonstrate large amounts of plastic deformation while brittle materials show little or no plastic deformation before fracture. The amount of deformation blast tested plates undergo before fracture, demonstrate that the material behaviour changes from ductile to more brittle as the charge mass increased in the single plates. Figure 8-25 shows a change in dimple morphology with the change in thickness of the target plates. The fractograph of the 2mm thick plates failed at a quasi-static strain rate shows large quantity of dimples of small size in diameters as indicated in Figure 8-25a. The fractographs of 2mm, 4mm and 6mm thickness failed as a result of localized blast loads show different dimple morphology in shape and quantity as indicated in Figure 8-25b, c and d.

The fractured surface of 2mm thick plates subjected to quasi-static strain rate and localized blast loading are showing equiaxed dimple morphology indicating the ductile nature of fracture. The fractured surface of 4mm thick single plate shows bigger microvoids along with appearance of river patterns, suggesting that the fracture was not completely ductile. The fractured surface of 6mm thick single plate contains river patters with a scarcity of microvoids, a more brittle failure mode.

Increase of thickness of target plates leads to the change in failure mode from ductile to a more brittle failure.

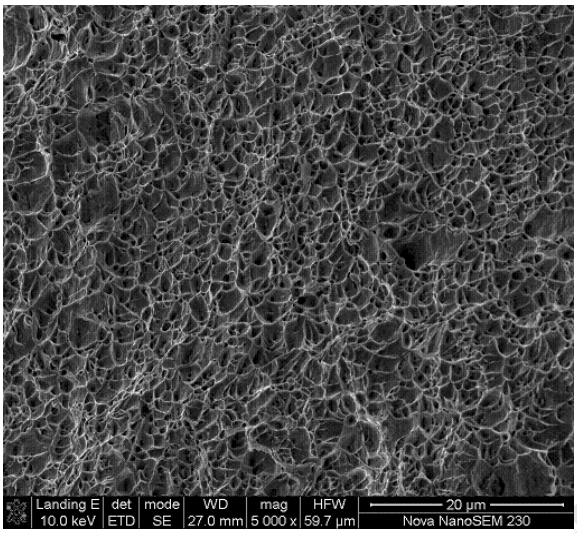

(a) 2mm thickness (uniaxial tension)

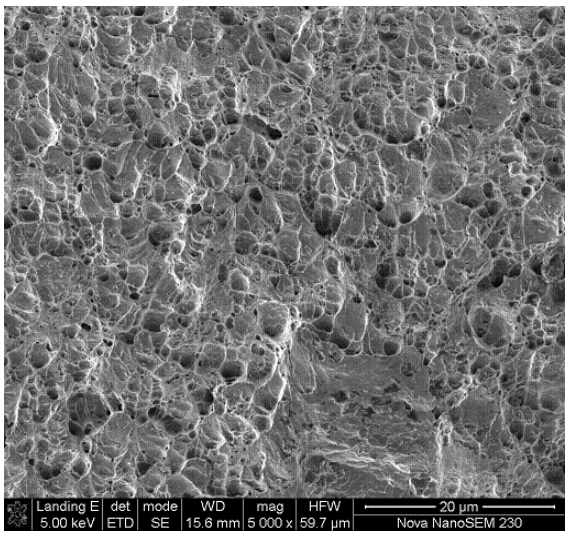

(b) 2mm thick front plate torn at 33g

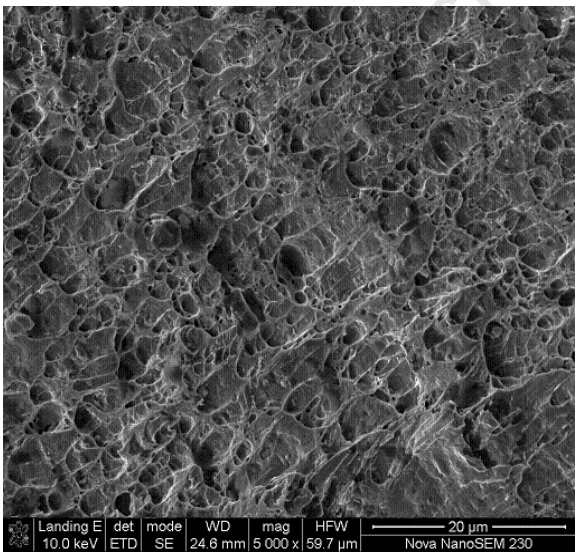

(c) 4mm thick plate torn at 44g

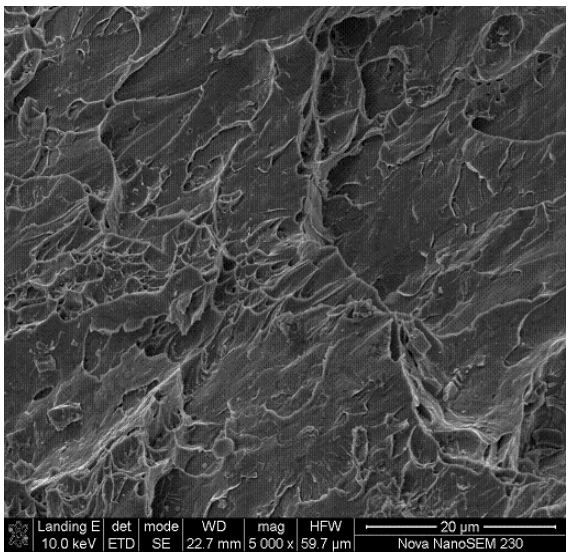

(d) 6mm thick plate torn at 62g

Figure 8-25: Fractographs of single plates of various thickness at failure points (a=quasi-static strain rate), (b, c, d = blast loaded fractured surfaces), showing change in dimple morphology with increasing thickness (Domex 700 MC)

Chapter 9

9 Conclusions and future work

9.1 Conclusions

For the 4mm configuration of Domex 550MC and Domex 700MC, double (2+2)mm plate deformations are greater than deformations of 4mm thick single plates at equal charge masses. The double (2+2)mm plates configuration failed at lower charge mass.

In localized blast loading experiments, the single plates of 4mm thickness for both materials provided better resistance than double (2+2)mm layered plates.

For 6mm configurations, the results are different. Here, the performance of double plates is better than single and triple plate configurations. The protection level of 6mm configurations decreases from No. 1 to No. 4 in the series given below, based on Table 8-4.

1. Double plate (3+3)mm
2. Double plate (4+2)mm
3. Single plate (6mm)
4. Triple plate (2+2+2)mm

The maximum protection is provided by double (3+3)mm followed by double (4+2)mm of 6mm configurations. The lowest protection level was observed in case of the triple plate configurations.

As expected, the midpoint deflections are greater for 4mm configurations than 6mm configurations before partial tearing initiated. In non-dimensional form, the responses for 4mm thick plates of Domex 550MC and Domex 700MC was indistinguishable.

Micro-structural study of the blast loaded plates revealed the deformed zones near the crater periphery. Strong shear localization was found during localized blast loading at the point of failure. These deformed zones are approximately 10-16 microns in width at each side of the crack, with the rest of area unaffected by the blast loading.

Fractography of the torn plates at various charge masses revealed the dimple morphology in all configurations is affected by the charge mass. The quantity of dimples decreases with increase in charge mass. The size of dimples increased with the increase in charge mass. The fractured surfaces of double and triple plates exhibited more “ductile failures” than the single plate failures. Higher quantities of micro-voids in layered torn plates indicate the ductile nature of fracture.

Fewer dimples were present in single plates compared to layered plates. The appearance of river patterns and scarcity of micro-voids in the 6mm thick single plates indicates a more

brittle nature of failure. The bright and featureless surface appearance in single plates, especially in 6mm thickness, is also an indication of the brittle fracture.

The modes of failure are different for single and layered plates as revealed by microvoid morphology. In layered plates, the front plates experiencing uniaxial load as their fractured surfaces are associated with the equiaxed dimple morphology. In layered plates, the back plates showed the elongated dimple morphology, indicating shear loading. It is to be noted that the back plates are not loaded directly by the charge mass.

The better performance of layered plates in the 6mm thick configuration is due to change in failure. Multi-layered plates exhibit failure modes that have more ductile characteristics than the single plates and hence absorb more energy prior to rupture. This trend was not observed in the 4mm thick configuration. Hence, multi-layered plates can exhibit improved performance over their equivalent mass counterparts if the overall configuration thickness is high enough to facilitate a difference in the ductile/brittle nature of the failure.

9.2 Future work

In the current study, plates of various configurations were subjected to localized blast loading up to point of failure. Once the plates were capped, they were not tested for increased blast loads that can give further higher strain rates. All the torn plates were associated with various amounts of plastic deformations that decreased with increasing a charge mass.

The increase in charge mass is supposed to increase the strain rate of deforming plates subjected to localized blast loads. Present blast testing facility does not have the arrangements that can measure the strain rates during blast loading. The arrangements should be made to measure the strain rates at each blast load to make comparison of microvoid morphology at each blast load. Currently, the measurement of strain rates of torn plates is not practical.

A series of the blast tests need to be performed on single plates of various thicknesses. The detailed experimental study of the plates subjected to localized blast loads from Mode II to Mode III (failure without permanent plastic deformations) or shear failure is needed to investigate the microvoid morphology at increasing charge masses/strain rates. The comparison of microvoid morphology among various thicknesses of single plates can give more insight into failure mechanisms and in designing of multi-layered armours.

Both configurations 4mm and 6mm exhibited different behaviours of protection, indicating the practical difficulties in deciding on the use of single or layered plates. Each configuration has its own protection level depending on the thickness. There is a need to extend the blast loading experiments to higher thickness to find out the critical thickness of single and layered plates that can provide better protection levels.

10 References

(1) Dawson-Howe K.M., William T.G. The detection of buried landmines using probing robots. Robotics and Autonomous Systems 23, 235-243. 1998.

(2) Anti-personnel Mines: An overview. International Committee of the Red Cross. 1996.

(3) US Department of State, Hidden Killers. The global landmine crisis. Report to Congress, Publication 10225. 1994.

(4) Ben-Dor G., Dubinsky A., Elperin T. Effect of air gaps on ballistic resistance of targets for conical impactors. Theoretical and Applied Fracture Mechanics 30, 243-249. 1998.

(5) Corran R.S.J., Shadbolt P.J., Ruiz C. Impact loading of plates-an experimental investigation. International Journal of Impact Engineering 1, 3-22. 1983.

(6) Dey S., Børvik T., Hopperstad O.S., Leinum J.R., Langseth M. The effect of target strength on the perforation of steel plates, using three different projectile nose shapes. International Journal of Impact Engineering 30, 1005-1038. 2004.

(7) Dey S., Børvik T., Teng X., Wierzbicki T., Hopperstad O.S. On the ballistic resistance of double-layered steel plates: an experimental and numerical investigation. International Journal of Solids and Structures 44, 6701-6723. 2007.

(8) Marom I., Bodner S.R. Projectile perforation of multilayered beams. International Journal of Mechanical Sciences 21, 489-504. 1979.

(9) Teng X., Wierzbicki T., Huang M. Ballistic resistance of double-layered armor plates. International Journal of Impact Engineering 35, 870-884. 2008.

(10) Teng X., Dey S., Børvik T., Werzbicki T. Protection performance of double-layered metal shields against projectile impact. Journal of Mechanics of Materials of Solids 2, 1307-1328. 2007.

(11) Woodward R.L., Cimpoeru S.J. A study of the perforation of aluminium laminate targets. International Journal of Impact Engineering 21, 117-131. 1998.

(12) Ben-Dor G., Dubinsky A., Elperin T. Effect of air gaps on ballistic resistance of ductile shields perforated by non-conical impactors. Journal of Mechanics of Materials and Structures 1, 279-299. 2006.

(13) Radin J., Goldsmith W. Normal projectile penetration and perforation of layered targets. International Journal of Impact Engineering 7, 229-259. 1988.

(14) Almohandes A.A., Abdel-Kader M.S., Eleiche A.M. Experimental investigation of the ballistic resistance of steel-fiberglass reinforced polyester laminated plates. Composites Part B Eng 27, 447-458. 1996.

(15) Zukas J.A. Impact effects in multi-layered plates. International Journal of Solids and Structures 38, 3321-3328. 2001.

(16) Nurick G.N., Martin J.B. Deformation of thin plates subjected to impulsive loading - a review. Part I: Theoretical considerations. International Journal of Impact Engineering 8, 159-169. 1989.

(17) Nurick G.N., Martin J.B. Deformation of thin plates subjected to impulsive loading - a review. Part II: Experimental Studies. International Journal of Impact Engineering 8, 171-186. 1989.

(18) Hogg P.J. Composites for Ballistic Applications. Department of Materials Queen Mary, University of London, UK . 2006.

(19) Baker W.E.: Explosions in Air. University of Texas, Austin, 1973.

(20) Marchand K.A., Alfawakhiri F. Blast and progressive collapse, Facts for steel buildings. American Institute of Steel Construction, Inc No. 2. 2004.

(21) Robertson N.J., Hayhurst C.J., Fairlie G.E. Numerical simulation of explosion phenomena, Twenty Years of Finite Element Analysis: Review and Future Prospects. International Journal of Computer Application in Technology 7, 316-329. 1994.

(22) Jacinto A.C, Ambrosini R.D., Danesi R.F. Experimental and computational analysis of plates under air blast loading. International Journal of Impact Engineering 25, 927-947. 2001.

(23) Cloete T.J., Nurick G.N., Palmer R.N. The deformation and shear failure of peripherally clamped centrally supported blast loaded circular plates. International Journal of Impact Engineering 32, 92-117. 2005.

(24) British Gas Research and Technology. The Steel Construction Institute, The effects of simplification of the explosion pressure-time history. Health and Safety Executive , 1-119. 1992.

(25) Young W.C., Budynas R.G.: Formulas for stress and strain, 7th edition. 2007.

(26) Kinney G.F., Graham K.J. Explosive shocks in air. 2nd edition. Berlin and New York Springer Verlag. 1985.

(27) Chipley M., Kaminskas M., Lyon W., Beshlin D., Hester M. Reference Manual to Mitigate Potential Terrorist Attacks Against Buildings, Risk Management Series, Federal Emergency Management Agency (FEMA 426). 2003.

(28) Zhu F., Lu G. A Review of Blast and Impact of Metallic and Sandwich Structures. Electronic Journal of Structural Engineering [special], 92-101. 2007.

(29) Formby S.A., Wharton R.K. Blast characteristics and TNT equivalence values for some commercial explosives detonated at ground level. Journal of Hazardous Materials 50, 183-198. 1996.

(30) Weckert S., Anderson C. A preliminary comparison between TNT and PE4 landmines. Defence Science and Technology Organisation,Weapons Systems Divisions, TN-0723. 2006.

(31) Hanssen A.G., Enstock L., Langseth M. Close-range blast loading of aluminium foam panels. International Journal of Impact Engineering 27, 593-618. 2002.

(32) Nurick G.N., Olson M.D., Fagnan J.R., Levin A. Deformation and tearing of blast-loaded stiffened square plates. International Journal of Impact Engineering 16, 273-291. 1995.

(33) Nurick G.N., Radford A.M. Deformation and tearing of clamped circular plates subjected to localised central blast loads. Recent Developments in Computational and Applied Mechanics: a volume in honour of John B.Martin, International Centre for Numerical Methods in Engineering, Barcelona, Spain , 276-301. 1997.

(34) Nurick G.N., Shave G.C. The deformation and tearing of thin square plates subjected to impulsive loads-An experimental study. International Journal of Impact Engineering 18, 99-116. 1996.

(35) Langdon G.S., Lemanski S.L., Nurick G.N., Simmons M.C., Cantwell W.J., Schleyer G.K. Behaviour of fibre-metal laminates subjected to localised blast loading: Part I-experimental observations. International Journal of Impact Engineering 34, 1202-1222. 2007.

(36) Jacob N., Nurick G.N., Langdon G.S. The effect of stand-off distance on the failure of fully clamped circular mild steel plates subjected to blast loads. Engineering Structures 29, 2723-2736. 2007.

(37) Chung Kim Yuen S., Nurick G.N. Experimental and numerical studies on the response of quadrangular stiffened plates -Part I- subjected to uniform blast load. International Journal of Impact Engineering 31, 55-83. 2005.

(38) Jones N.: Structural Impact. Cambridge University Press. 1989.

(39) Menkes S.B., Opat H.J. Tearing and shear failures in explosively loaded clamped beams. Experimental Mechanics 13, 480-486. 1973.

(40) Teeling-Smith R.G., Nurick G.N. The deformation and tearing of thin circular plates subjected to impulsive loads. International Journal of Impact Engineering 11, 77-91. 1991.

(41) Olson M.D., Fagnan J.R., Nurick G.N. Deformation and rupture of blast loaded square plates - Predictions and experiments. International Journal of Impact Engineering 12, 279-291. 1993.

(42) Nurick G.N., Gelman M.E., Marshall N.S. Tearing of blast loaded plates with clamped boundary conditions. International Journal of Impact Engineering 18, 803-827. 1996.

(43) Houlston R., Slater J.E. A summary of experimental results on square plates and stiffened panels subjected to air-blast loading. 57th Shock and Vibration Symposium, New Orleans, Louisiana, USA, 14-16. 1986.

(44) Nurick G.N., Conolly A.G. Response of clamped single and double stiffened rectangular plates subjected to blast loads. Structures Under Shock and Impact III (SUSI III), Southampton, Computational Mechanics publications , 207-220. 1994.

(45) Chung Kim Yuen S., Nurick G.N. The significance of the thickness of a plate when subjected to localised blast load. 16th International Symposium on Military Aspects of Blast and Shock, (MABS 16), Oxford, UK, 491-499. 2000.

(46) Wierzbicki T., Nurick G.N. Large deformation of thin plates under localised impulsive loading. International Journal of Impact Engineering 18, 899-918. 1996.

(47) Jacob N., Chung Kim Yuen S., Nurick G.N., Bonorchis D., Desai S.A., Tait D. Scaling aspects of quadrangular plates subjected to localised blast loads - experiments and predictions. International Journal of Impact Engineering 30, 1179-1208. 2004.

(48) Bonorchis D., Nurick G.N. The influence of boundary conditions on the loading of rectangular plates subjected to localised blast loading - importance in numerical simulations. International Journal of Impact Engineering 36, 40-52. 2009.

(49) Tollner M.E., Nurick G.N. Predictions of stiffened circular plates subjected to impulsive loads. Structures Under Extreme Loading Conditions, Fluid Structural Interaction, and Structural Mechanics Problems in Reactor Safety PVP 394, ASME, New York. 1999.

(50) Nurick G.N., Lumpp D.M. Deflection and tearing of clamped stiffened circular plates subjected to uniform impulsive blast loads. Structures Under Shock and Impact IV (SUSI IV), Southampton, Computational Mechanics publications, 393-402. 1996.

(51) Veldman R.L, Ari-Gur J., Clum C., DeYoung A., Folkert J. Effects of pre-pressurization on blast response of clamped aluminum plates. International Journal of Impact Engineering 32, 1678-1695. 2006.

(52) Veldman R.L, Ari-Gur J., Clum C. pre-pressurized reinforced plates under blast loading. International Journal of Impact Engineering 35, 240-250. 2008.

(53) Schubak R.B., Olson M.D., Anderson D.L. Rigid-plastic modelling of blast loaded stiffened plates - Part I: one way stiffened plates. Third International Symposium on Structural Crashworthiness and Failure. 1993.

(54) Schubak R.B., Olson M.D., Anderson D.L. Rigid-plastic modelling of blast loaded stiffened plates - Part II: partial end fixity, rate effects and two-way stiffened plates. Third International Symposium on Structural Crashworthiness and Failure. 1993.

(55) Schleyer G.K., Hsu S., White M.D. Blast loading of stiffened plates: experimental, analytical and numerical investigations. Structures Under Extreme Loading Conditions, ASME, New York PVP-Vol361, 237-255. 1998.

(56) Schleyer G.K., Hsu S.S., White M.D., Birch R.S. Pulse pressure loading of clamped mild steel plates. International Journal of Impact Engineering 28, 223-274. 2003.

(57) Pan Y., Louca L.A. Experimental and numerical studies on the response of stiffened plates subjected to gas explosions. Journal of Constructional Steel Research 52, 171-193. 1999.

(58) Schubak R.B., Olson M.D., Anderson D.L. Non-linear rigid-plastic analysis of stiffened plates under blast loads. Structures Under Shock and Impact III (SUSI III), Computational Mechanics Publications, 521-532. 1992.

(59) Wiehahn M.A., Nurick G.N., Bowles H.C. Some insights into the mechanism of the deformation and tearing of thin plates at high strain rates incorporating temperature dependent material properties. Structures Under Shock and Impact VI (SUSI VI), Computational Mechanics Publications, Southampton, UK, 207-220. 2000.

(60) Wiehahn M.A.: Circular plates subjected to localised blast loads-some insights into the mechanism of tearing and the energy required, M.Sc. thesis. University of Cape Town, South Africa, 2002.

(61) Langdon G.S., Chung Kim Yuen S., Nurick G.N. Experimental and numerical studies on the response of quadrangular stiffened plates -Part II- subjected to localised load. International Journal of Impact Engineering 31, 85-111. 2005.

(62) Bonorchis D., Nurick G.N. The analysis and simulation of welded stiffener plates subjected to localised blast loading. International Journal of Impact Engineering 37, 260-273. 2010.

(63) Akus Y., Yildirim O.R. Effects of changing explosion distance and explosive mass on deformation of shock loaded square plates. 11th International Conference on Machine Design and Production. 2004.

(64) Thomas B.M., Nurick G.N. The effect of boundary conditions on thin plates subjected to impulsive loads. The 5th International Symposium on Plasticity and its Current Application, Osaka, Japan, 85-88. 1995.

(65) Bonorchis D., Nurick G.N. The effect of welded boundaries on the response of rectangular hot-rolled mild steel plates subjected to localized blast loading. International Journal of Impact Engineering 34, 1729-1738. 2007.

(66) Johnson W. Impact strength of materials. Edward Arnold Ltd. 1972.

(67) Nurick G.N. An empirical solution for predicting maximum central deflections of impulsively loaded plates. International Conference on Mechanical Properties of Materials at High Rates of Strain, Oxford, UK, 457-464. 1989.

(68) Jones N.: On the dynamic inelastic failure of beams; in: Wierzbicki T, Jones N, (eds). New York, Wiley, 1989.

(69) Jones N. Plastic failure of ductile beams loaded dynamically. Journal of Engineering for Industry-Transactions of the ASME 98, 131-136. 1976.

(70) Radford A.M., Nurick G.N.: Circular plates subjected to localised central blast loads. Transient loading and response of structures. An International Symposium honouring Arnfinn Jenssen, Trondheim, Norway, 503-548. 1998.

(71) Farrow G.H., Nurick G.N., Mitchell G.P. Modelling of impulsively loaded circular plates using the ABAQUS finite element code. Proceeding 13th Symposium Finite Element Methods in South Africa, 186-198. 1995.

(72) Fagnan J.R.: Failure analysis of stiffened and unstiffened mild steel plates subjected to blast loading. Department of Civil Engineering The University of British Columbia, Vancouver, Canada, 1996.

(73) Rudrapatna N.S., Vaziri R., Olson M.D. Deformation and failure of blast loaded stiffened plates. International Journal of Impact Engineering 24, 457-474. 2000.

(74) Rudrapatna N.S., Vaziri R., Olson M.D. Deformation and failure of blast loaded square plates. International Journal of Impact Engineering 22, 449-467. 1999.

(75) Hibbit, Karlsson, Sorensen. User's Manual. Version 5.8. [ABAQUS/Explicit, Inc. Rhode Island, USA]. 1998.

(76) Balden V.H., Nurick G.N. Numerical Simulation of the Post Failure Motion of Steel Plates subjected to Blast Loading. International Journal of Impact Engineering 32, 14-34. 2005.

(77) Nurick G.N., Bryant M.W. Fragmentation damage as a result of an explosion. International Symposium on Plasticity and Impact Mechanics, IMPLAST, 484-498. 1996.

(78) Anderson T.L.: Fracture Mechanics (Fundamentals and Applications). CRC Press, Inc., 1991.

(79) ASM Metals HandBook - Fractography: ASM International, 9th edition, 1987.

(80) Michael Janssen, Jan Zuidema, Russel Wanhill: Fracture mechanics. Taylor & Francis, 2005.

(81) ASM Metals Handbook- Failure Analysis and Prevention: ASM International, 2002.

(82) Thomason P.F.: Ductile Fracture of Metals. Oxford, England, Pergamon Press, 1990.

(83) Das A., Soumitra T. Geometry of dimples and its correlation with mechanical properties in austenitic stainless steel. Scripta Materialia 59, 1014-1017. 2008.

(84) Das A., Das S.K., Sivaprasad S., Tarafder S. Fracture-property correlation in copper-strengthened high-strength low-alloy steel. Scripta Materialia 59, 681-683. 2008.

(85) Das A., Sivaprasad S., Chakarborti P.C., Tarafder S. Correspondence of fracture surface features with mechanical properties in 304LN stainless steel. Materials Science and Engineering A 496, 98-105. 2008.

(86) Backman M., Goldsmith W. The mechanics of penetration of projectiles into targets. International Journal of Engineering Sciences 16, 1-99. 1978.

(87) Corbett G.G., Reid S.R., Johnson W. Impact loading of plates and shells by free-flying projectiles: a review. International Journal of Impact Engineering. 1996.

(88) Goldsmith W. Non-ideal projectile impact on targets. International Journal of Impact Engineering 22, 95-395. 1999.

(89) Zukas J.A.: Impact Dynamics. John Wiley & Sons, Inc, 1982.

(90) Zukas J.A.: High velocity impact dynamics. New York, John Wiley & Sons, Inc, 1990.

(91) Czarnecki G.J. Estimation of the V_{50} using semi-empirical (1-point) procedures. Composites Part B 29, 321-329. 1998.

(92) Chia-Jung H., Pee-Yew L., Jium-Shyong C. Ballistic perforamance and microstructure of modified rolled homogeneous armour steel. Journal of the Chinese Institute of Engineers 25, 99-107. 2002.

(93) Raftenberg Martin N., Krause Claire D. Metallographic observations of armor steel specimens from plates perforated by shaped charge jets. International Journal of Impact Engineering 23, 757-770. 1999.

(94) Rogers H.C., Shastry C.V. Materials factors in adiabatic shear bands in steels. M.A.Meyers and L.E.Murr, editor. Shock Waves and High-Strain-Rate Phenomena in Metals, Plenum Press, New York. 235-298. 1981.

(95) Bai Y., Dodd B.: Adiabatic shear localization. Occurrence, theories and applications. Oxford, Pergamon Press, 1992.

(96) Woodward R.L. The interrelation of failure modes observed in the penetration of metallic targets. International Journal of Impact Engineering 2, 121-129. 1984.

(97) AUTODYN, Theory manual. Horsham, England; Century Dynamics Ltd; 1997.

(98) Ahmad M.S.: Study of ballistic impact resistance of composite armour plates, MS. thesis. Faculty of Materials Science and Engineering, GIK Institute of Engineering Sciences and Technology, Pakistan 2007.

(99) Husain SW., Ahmad MS., Qamar I. Dendritic morphology observed in the solid state precipitation in binary alloys. Metallurgical and Materials Transactions 30A, 1529-1534. 1999.

(100) http://emrtk.uni-miskolc.hu/innovate/public/malta/innovate3/jominy_home.htm. 2011.

(101) ASM Metals HandBook - Heat Treating: ASM International, 9th edition, 1991.

(102) Time-Temperature-Transformation (TTT) diagram, (http://bama.ua.cdu). 2009.

(103) Welding Handbook, Metals and Their Weldability: ed 7th, American Welding Society, 1982.

(104) Swedish Steel (SSAB): http://www.ssab.com, 2010.

(105) Standard test methods for tension testing of metallic materials, ASTM Standards, Designation E 8M-93. 1993.

(106) Dieter G.E: Mechanical Metallurgy. Singapore, McGraw Hill, 1988.

(107) Johnson G.R., Cook W.H. A constitutive model and data for metals subjected to large strain, high strain rates and high temperatures. Proceedings of the 7th Symposium on Ballistic, Hague, Netherlands, 541-547. 1983.

(108) Liang R., Khan A.S. A critical review of experimental results and constitutive models for BCC and FCC metals over a wide range of strain rates and temperatures. International Journal of Plasticity 15, 963-980. 1999.

(109) Von Karman Th, Duwes P. The propagation of plastic deformation in solids. Journal of Applied Physics 21, 987. 1950.

(110) Taylor G.I.: The plastic wave in a wire extended by an impact load. British Ministry of Home Security, Civil Defense Research Committee RC 323 1942.

(111) Cowper G.R., Symonds P.S.: Strain-hardening and strain-rate effects in the impact loading of cantilever beams. Technical Report 28. Division of Applied Mathematics, Brown University, Providence, R.I, 1957.

(112) Manjoine M.J.: Influence of rate of strain and temperature on yield stresses of mild steel. Journal of Applied Mechanics 11, 211-218. 1994.

(113) Marais S.T., Tait R.B., Cloete T.J., Nurick G.N. Material testing at high strain rate using the split Hopkinson pressure bar. Latin American Journal of Solids and Structures 1, 319-338. 2004.

(114) Abramowicz W., Jones N. Dynamic progressive buckling of circular and square tubes. International Journal of Impact Engineering 4, 243-270. 1986.

(115) Masui T, Nunokawa T, Hiramatsu T. Shape correction of hot rolled steel using an on line leveller. Journal of Japan Society for Technology of Plasticity 28, 81-87. 1987.

(116) Langdon G.S, Nurick G.N., Chung Kim Yuen S. The response of stiffened square plates subjected to localised blast loading. 7th International Conference on Structures Under Shock and Impact (SUSI VII), Montreal, Canada, 3-12. 2002.

(117) Chung Kim Yuen S., Nurick G.N. Modelling the deformation and tearing of thin and thick plates subjected to localised blast loads. 8th International Symposium on Plasticity and Impact Mechanics, IMPLAST, New Delhi, India, 729-739. 2003.

(118) Alves M. Material constitutive law for large strains and strain rates. Journal of Engineering Mechanics 126, 215-218. 2000.

(119) Holmquist T.J., Johnson G.R. Determination of constants and comparison of results for various constitutive models. Journal de Physique III 1, 853-860. 1991.

(120) Rule W.K., Jones S.E.: A revised form for the Johnson-Cook strength model. International Journal of Impact Engineering 21, 609-624. 1998.

(121) Zerilli F.J.: Armstrong R.W. Dislocation-mechanics-based constitutive relations for material dynamics calculations. Journal of Applied Physics 61, 1816-1825. 1987.

(122) Zerilli F.J., Armstrong R.W. Description of tantalum deformation behavior by dislocation mechanics based constitutive relations. Journal of Applied Physics 68, 1580-1591. 1990.

(123) Goldthorpe B.D. Constitutive equations for annealed and explosively shocked Iron for application to high strain rates and large strains. Journal de Physique IV, Colloque C3, Supplement au Journal de Physique III 1, 829-835. 1991.

(124) Zerilli F.J., Armstrong R.W. Dislocation mechanics based analysis of material dynamics behavior: enhanced ductility, deformation twinning, shock deformation, shear instability, dynamic recovery. Journal de Physique IV, Colloque C3, Supplement au Journal de Physique III 7, 637-462. 1997.

(125) Zhao H. A constitutive model for metals over a large range of strain rates. Identification for mild-steel and aluminium sheets. Materials Science and Engineering A230, 95-99. 1997.

(126) Bodner S.R., Partom Y. Constitutive equations for elastic-viscoplastic strain-hardening materials. Journal of Applied Mechanics June, 385-389. 1975.

(127) Khan A.S., Huang S. Experimental and theoretical study of mechanical behavior of 1100 aluminum in the strain rate range 10^{-5}-10^{4} S^{-1}. International Journal of Plasticity 8, 397-424. 1992.

(128) Bimha R.E., Nurick G.N., Mitchell G.P. Modelling the deformation of blast-loaded stiffened square plates. Proceedings of the 1st South African Conference on Applied Mechanics (SACAM) 96 Midrand, South Africa[1 - 5 July]. 1996.

(129) Bimha R.E.: Response of Thin Circular Plates to Blast Loading, M.Sc. thesis. University of Cape Town, South Africa, 1996.

(130) Grobbelaar W.P, Nurick G.N. An investigation of structures subjected to blast loads incorporating an equation of state to model the material behaviour of the explosive. Proceedings of the 7th International Symposium on Structural Failure and Plasticity (IMPLAST 2000), Melbourne, Australia, 4-6 October, 185-194. 2005.

(131) Radford A.M.: Thin circular metal plates and subjected to localised impulsive loads, M.Sc. thesis, University of Cape Town, South Africa, 1995.

(132) Kennedy J.E.: Behaviour and utilisation of explosives in engineering design. 12th Annual Symposium, ASME, UNM, Albuquerque, NM 1972.

(133) Balden V.H.: Ductile failure of localised blast loaded circular plates: An experimental and numerical investigation, PhD. thesis. University of Cape Town, South Africa, 2011.

(134) Nurick G.N.: Large deformation of thin plates subjected to impulsive loading, PhD. thesis, University of Cape Town, South Africa, 1987.

(135) Bonorchis D. Analysis and simulation of welded plates subjected to blast loading, PhD thesis, University of Cape Town, South Africa, 2007.

(136) Standard test methods for determining average grain size, ASTM Standard, E 112. 1993.

Appendix A

Theory of ballistic pendulum

The theory of the ballistic pendulum has been established and used for many years [134]. The ballistic pendulum sustains its orientation during its swinging motion due to blast loads. It can therefore be treated as a simple pendulum, which means that the rotational inertia of the pendulum and its wires need not to be considered. The linear equation of motion of the simple pendulum is in Equation A-1.

$$\ddot{\mathbf{x}} + \mathbf{2\beta\dot{x}} + \boldsymbol{\omega}_{\mathbf{n}}^{\mathbf{2}}\,\mathbf{x} = \mathbf{0} \qquad \text{A-1}$$

Where

$$\boldsymbol{\beta} = \frac{\mathbf{C}}{\mathbf{2M}}, \quad \boldsymbol{\omega}_{\mathbf{n}} = \frac{\mathbf{2\pi}}{\mathbf{T}}$$

C is the damping co-efficient; M is the total mass of the pendulum (Test rig, I-beam, balance masses and explosive). T is the natural period of the pendulum motion. The solution of Equation A-1 is given by

$$\boldsymbol{x} = \frac{(e^{-\beta t})\dot{x}_0 \sin \omega_d t}{\omega_d} \qquad \text{A-2}$$

Where

$\dot{\boldsymbol{x}}_{\mathbf{0}}$ is the initial velocity of the pendulum

$$\boldsymbol{\omega}_{\mathbf{d}} = \left(\sqrt{\boldsymbol{\omega}_{\mathbf{n}}^{\mathbf{2}} - \boldsymbol{\beta}^{\mathbf{2}}}\right)$$

Let x_1 be the horizontal displacement at t= T/4 and $-x_2$ be the horizontal displacement at t =3T/4 and substituting into Equation A-2 gives

$$\mathbf{x_1} = \left(\frac{\dot{\mathbf{x}}_{\mathbf{0}}\mathbf{T}}{\mathbf{2\pi}}\,\mathbf{e}^{-\frac{\mathbf{1}}{\mathbf{4}}\boldsymbol{\beta}\mathbf{t}}\right)$$

$$-\mathbf{x_2} = \left(\frac{\dot{\mathbf{x}}_0 \mathbf{T}}{\mathbf{2\pi}} \mathbf{e}^{-\frac{3}{4}\beta t}\right)$$

Hence

$$\frac{\boldsymbol{x_1}}{\boldsymbol{x_2}} = \boldsymbol{e}^{\frac{1}{2}\beta t}$$

This gives

$$\boldsymbol{\beta} = \frac{\mathbf{2}}{\boldsymbol{T}} \boldsymbol{Ln}\left(\frac{x_1}{x_2}\right) \qquad \text{A-3}$$

And

$$\dot{\boldsymbol{x}}_{\mathbf{0}} = \frac{\mathbf{2}\boldsymbol{\pi}}{\boldsymbol{T}} \boldsymbol{x_1} \boldsymbol{e}^{\frac{1}{4}\beta t} \qquad \text{A-4}$$

The impulse can now be calculated as

$$\boldsymbol{I} = \boldsymbol{M}\dot{\boldsymbol{x}}_{\mathbf{0}} \qquad \text{A-5}$$

The horizontal displacement by the pendulum (x_1 and x_2) is measured by the pen in terms of ΔR and ΔL, are different that must be considered. In Figure A-1 the horizontal distance (at rest) from the end of the pendulum to the recording pen is given by

$$\boldsymbol{d_1} = (\boldsymbol{Z^2} - \boldsymbol{a^2})^{1/2}$$

While at peak oscillations the distance d_2 is

$$\mathbf{d_2} = (\mathbf{Z^2} - (\mathbf{a} + \mathbf{y})^2)^{1/2}$$

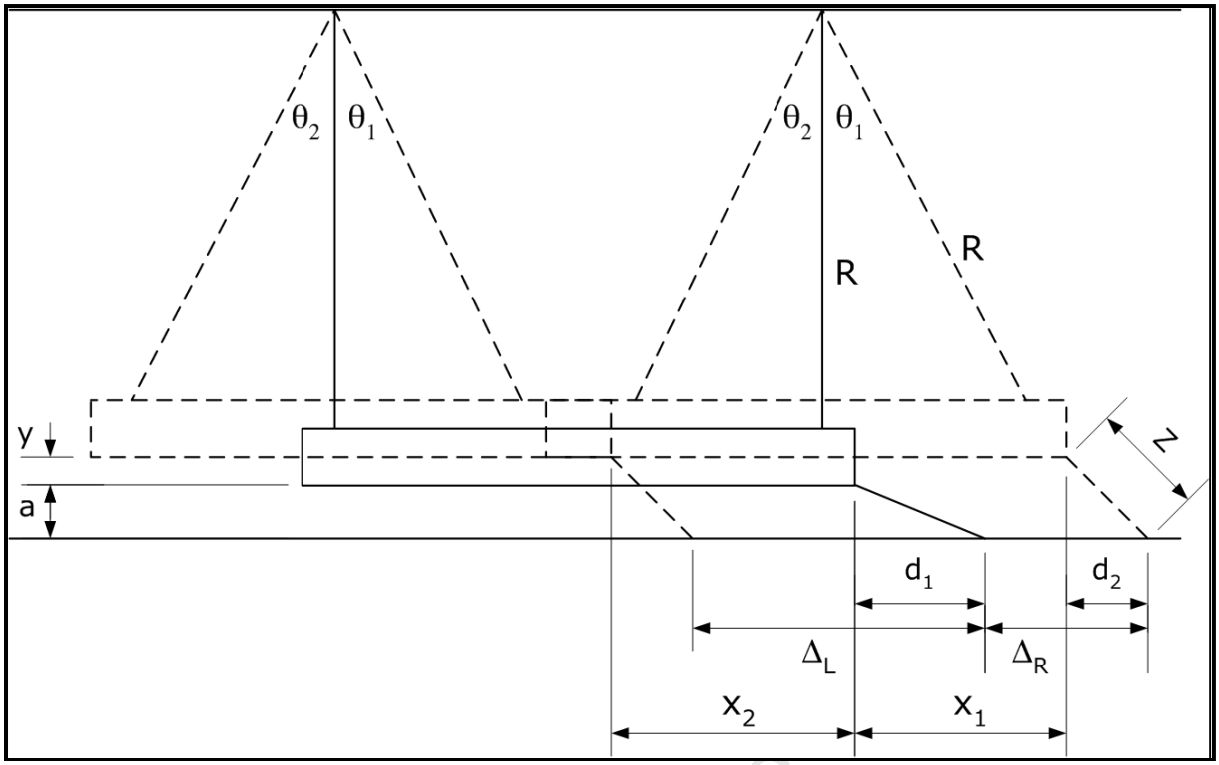

Figure A-1: Geometry of ballistic pendulum [135]

The relationship between the displacements x_1 and y can be obtained as follows

$$(\mathbf{R}-\mathbf{y})^2 = \mathbf{R}^2 - \mathbf{x_1^2} \quad \Rightarrow \quad \mathbf{2Ry} - \mathbf{y^2} = \mathbf{x_1^2}$$

Since the length of the wire R is much larger than the vertical displacement y, the following approximation can be made,

$$\mathbf{R} \gg \Rightarrow \ \mathbf{2Ry} - \mathbf{y^2} \ \approx \mathbf{2Ry} = \mathbf{x_1^2} \Rightarrow \mathbf{y} = \frac{\mathbf{x_1^2}}{\mathbf{2R}}$$

Or alternatively, using the small angle approximation ($\sin\theta \approx \theta$)

$$\mathbf{x_1} \approx \mathbf{R\theta_1} \ \mathbf{and} \ \mathbf{y} \approx \frac{\mathbf{R\theta_1^2}}{\mathbf{2}}$$

Hence

$$\mathbf{y} = \frac{\mathbf{x_1^2}}{\mathbf{2R}} \qquad \text{A-6}$$

From Figure A-1

$$\mathbf{x_1} = \Delta\mathbf{R} + \mathbf{d_1} - \mathbf{d_2}$$

This becomes

$$\boldsymbol{x_1} = \Delta\boldsymbol{R} + (\boldsymbol{Z^2} - \boldsymbol{a^2})^{1/2} - \left(\boldsymbol{Z^2} - \left(\boldsymbol{a} + \frac{\boldsymbol{x_1^2}}{\boldsymbol{2R}}\right)^2\right)^{1/2} \qquad \text{A-7}$$

Similarly

$$\mathbf{x_2} = \Delta\mathbf{L} - \mathbf{d_1} + \mathbf{d_2}$$

Therefore

$$\boldsymbol{x_2} = \Delta\boldsymbol{L} + (\boldsymbol{Z^2} - \boldsymbol{a^2})^{1/2} - \left(\boldsymbol{Z^2} - \left(\boldsymbol{a} + \frac{\boldsymbol{x_1^2}}{\boldsymbol{2R}}\right)^2\right)^{1/2} \qquad \text{A-8}$$

Where (ΔL, ΔR, Z, a and R) are measured physically. The Equation A-7 shows that x_1 is a function of itself and therefore an iterative scheme is required to find a solution. Once x_1 is found, x_2 can be calculated using Equation A-8. β, the initial velocity ($\dot{x}_0$) and finally the impulse (I) are calculated by using Equations A-3, A-4 and A-5 respectively.

The blast experiments were conducted in different batches. The ballistic pendulum was adjusted for each test batch. The details of different parameters of each batch for Domex 550MC and Domex 700MC is given in Table A-1, Table A-2 and in Table A-3. There was a little variation in weight of plates of each size (2mm, 3mm, 4mm and 6mm). The average weight of 6 plates of each thickness was used for calculating the impulse of all experiments.

Table A-1: Shows the pendulum set up details for Domex 550MC

Time Period (s)	3.42	Frame 1 (Kg)	11.94
R (m)	2.945	Frame 2 (Kg)	11.90
Z (m)	0.208	Plate 4 mm(Kg)	5.0
A (m)	0.156	Rods+bolts (4) (Kg)	1.84
		Pendulum plate +4 nuts and bolts (Kg)	20.30
		Total (Kg)	51.50
Domex 550MC		Plate 2 mm (Kg)	2.5
	I-Beam	Test Rig	Counter balance
Pendulum Mass (Kg)	35.56	51.50	51.50
Total Mass (Kg)	138.56		
Note: Extra weight were attached for Impulses (> 45 Ns), (2.9 Kg + 40.18 + 39.48)=107.78Kg			

Table A-2: Shows the pendulum set up details for Domex 700 MC of 4mm configuration

Time Period (s)	3.24	Clamp Back (Kg)= 19.96	66.08 + 4.96
R (m)	2.95	Clamp front (Kg)= 19.88	
Z (m)	0.210	Plate 4mm= 4.96 kg	
A (m)	0.160	All Bolts= 1.3Kg	
		Pendulum plate + attached rods =24.94	
Wt. 2mm Plate	2.48Kg * 2= 4.96	Total (Kg)	71.04
Wt. 4mm Plate	5+5+4.96+4.94+4.94+4.94=29.78/6=4.964		
	I-Beam	Test Rig	Counter balance
Pendulum Mass (Kg)	35.54+40.18+39.92= 115.64	71.04	71.04
Total Mass (Kg)	257.72		

Table A-3: Shows the pendulum set up details Domex 700 MC of 6mm configuration

Time Period (s)	3.24	Clamp Back (Kg)= 19.96	66.08 + 7.42
R (m)	2.95	Clamp front (Kg)= 19.88	
Z (m)	0.210	Plate 4mm= 4.96 kg	
A (m)	0.160	All Bolts= 1.3Kg	
		Pendulum plate + attached rods =24.94	
		Total (Kg)	73.5
Wt. 2mm Plate	2.48Kg * 2= 4.96	Plate 3 mm (Kg)	3.72
Wt. 4mm Plate	5+5+4.96+4.94+4.94+4.94=29.78/6=4.964		
Wt. 6mm plate	7.42 Kg		
	I-Beam	Test Rig	Counter balance
Pendulum Mass (Kg)	35.54+40.18+39.92= 115.64 +39.48 +39.14=194.26	73.5	73.5
Total Mass (Kg)	341.26		

Appendix B

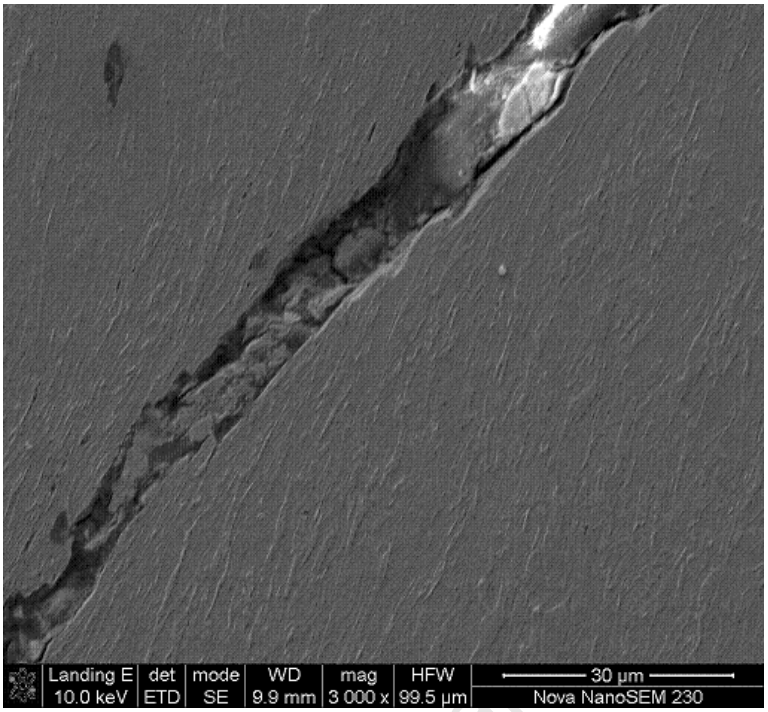

Figure B-1: Microstructure of 4mm thick single plate of Domex 700MC, tested at 33g charge mass (I=68.8 Ns), showing deformed zones near the crack

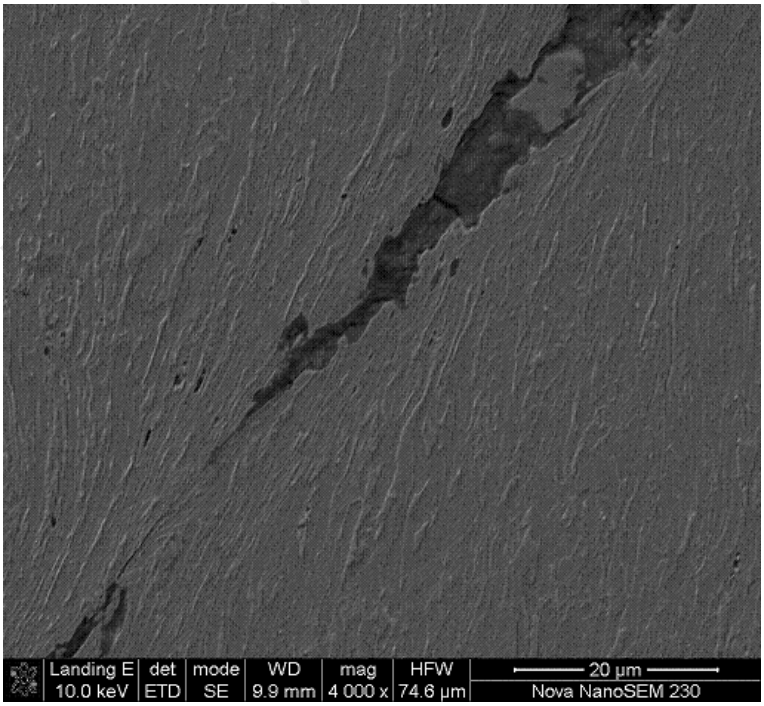

Figure B-2: Microstructure of 4mm thick single plate of Domex 700MC, tested at 33g charge mass (I=68.8 Ns), showing deformed zones near the crack

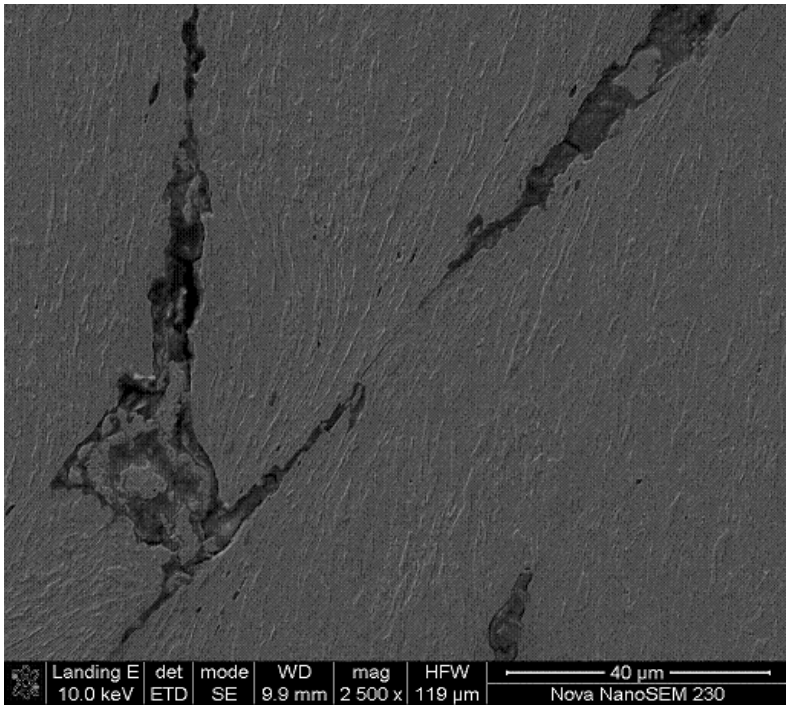

Figure B-3: Microstructure of 4mm thick single plate of Domex 700MC, tested at 33g charge mass (I=68.8 Ns), showing deformed zones near the crack

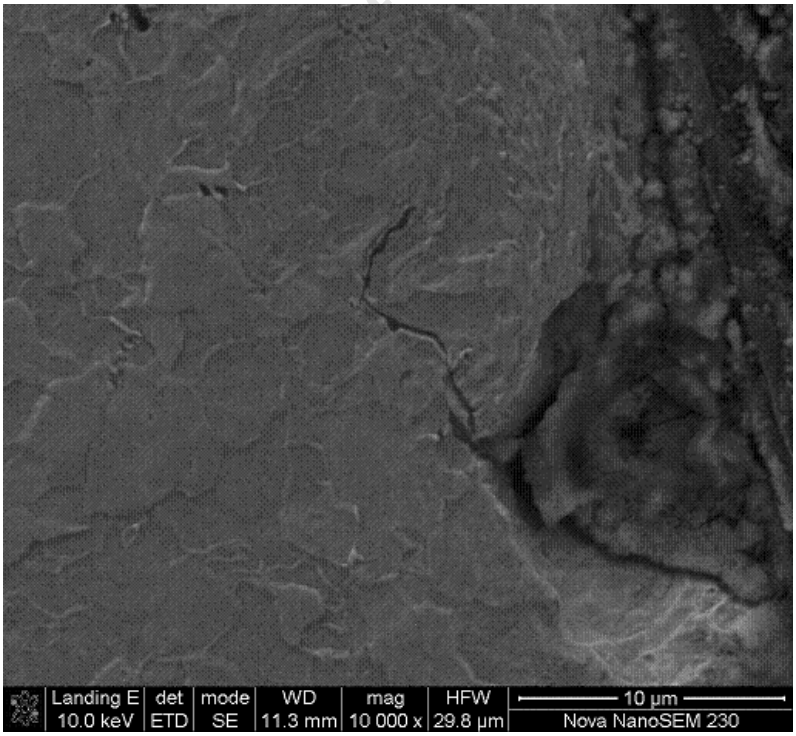

Figure B-4: Microstructure of 6mm thick single plate of Domex 700MC, tested at 56g charge mass (I=103.5Ns), shows inter-granular and trans-granular fracture path

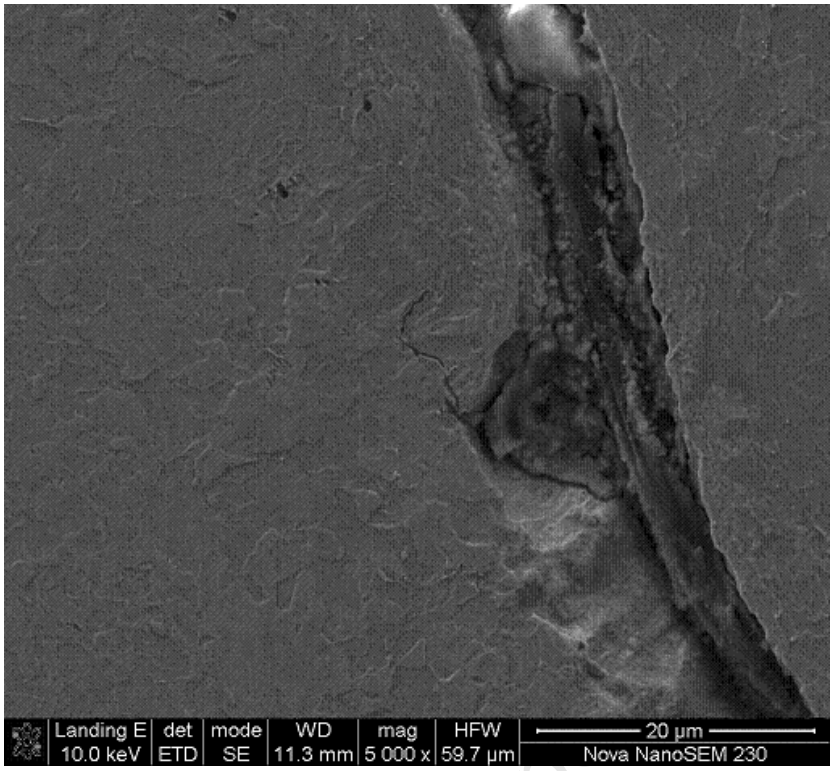

Figure B-5: Microstructure of 6mm thick single plate of Domex 700MC, tested at 56g charge mass (I=103.5Ns), shows inter-granular and trans-granular fracture path

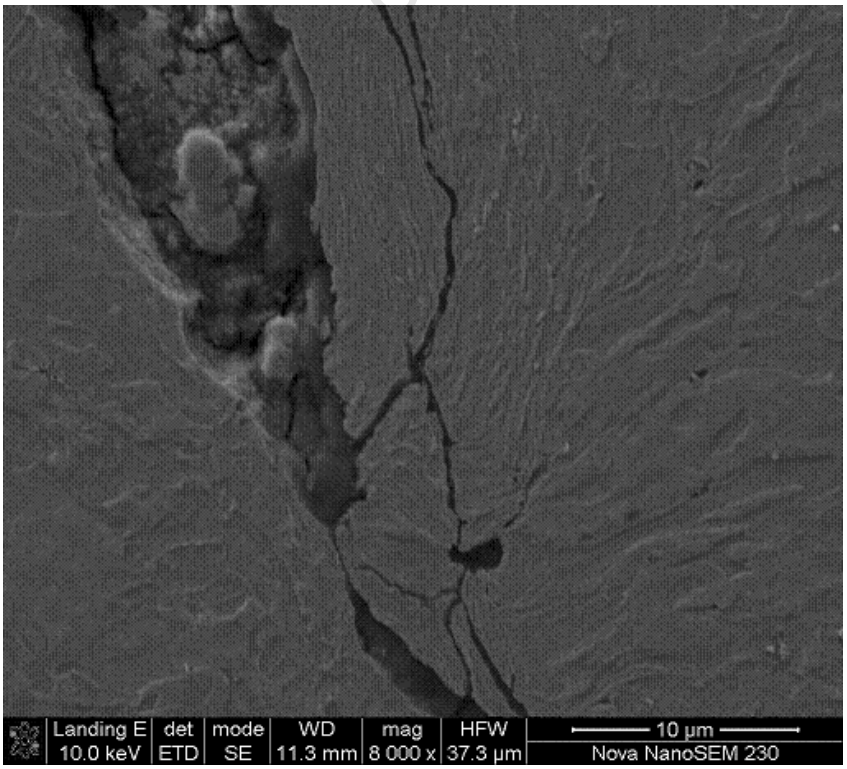

Figure B-6: Microstructure of 6mm thick single plate of Domex 700MC, tested at 56g charge mass (I=103.5Ns), shows deformed grains near the crack

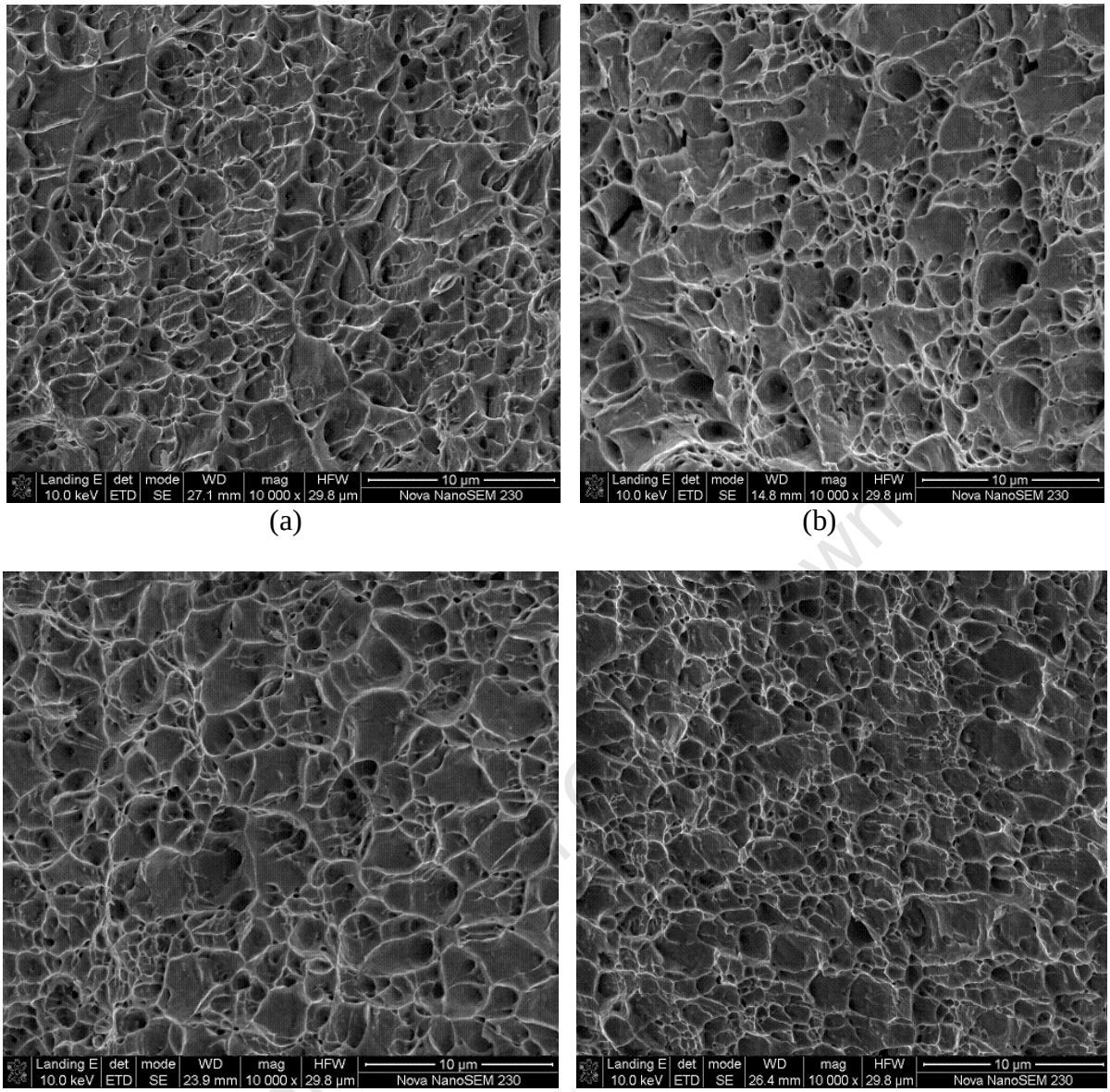

Figure B-7: Fractographs of tensile samples of Domex 700 MC, tested at strain rates of (a) 4.16×10^{-4} S^{-1}, (b) 2.083×10^{-2} S^{-1}, (c) 4.16×10^{-4} S^{-1}, (d) 2.083×10^{-2} S^{-1}, showing equiaxed micro-voids of various sizes

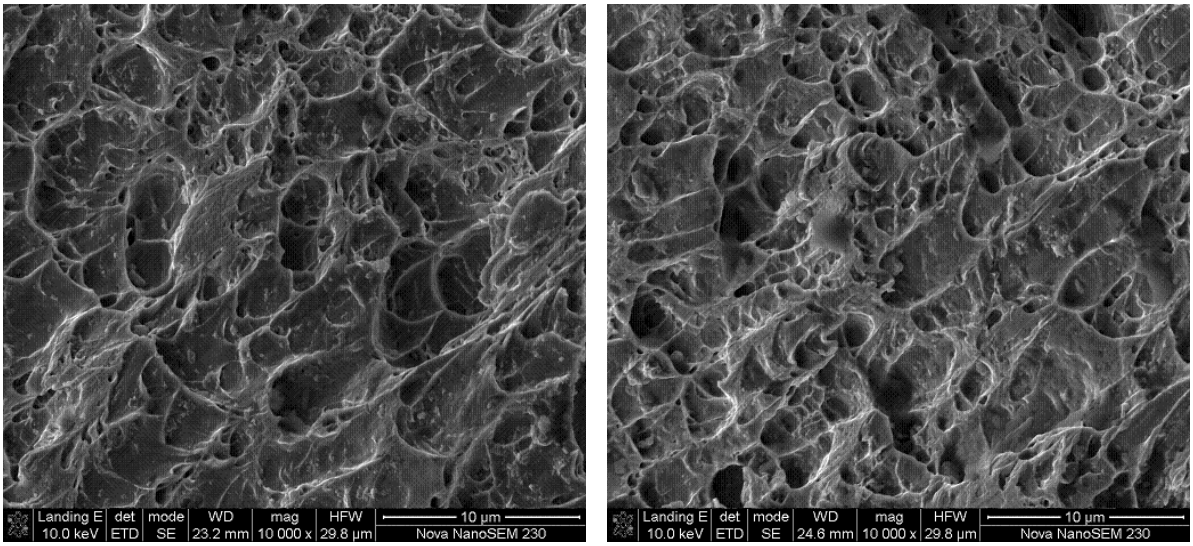

(a) (b)

Figure B-8: Fractographs of 4 mm thick single plates after blast testing at charge mass (a) 38g, 81.7 Ns and (b) 44g, 85.6Ns, showing micro-voids along with a river patterns

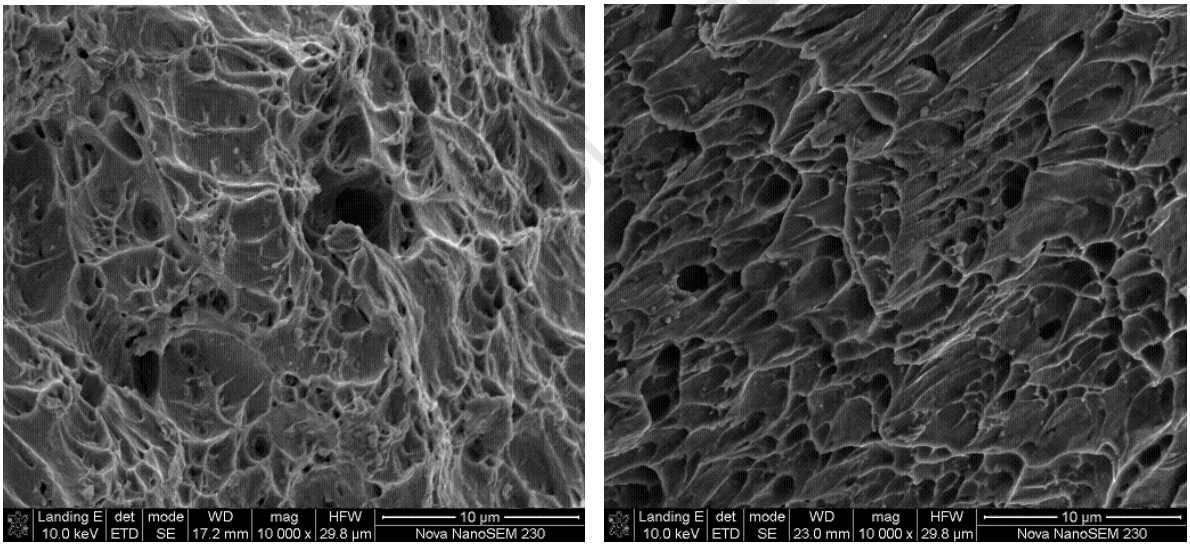

(a) (b)

Figure B-9: Fractographs of double (2+2)mm plates after blast testing at charge=33g, 63.7 Ns (a) front plate and (b) back plate, showing presence of equiaxed dimples in front and elongated dimples in the back plate

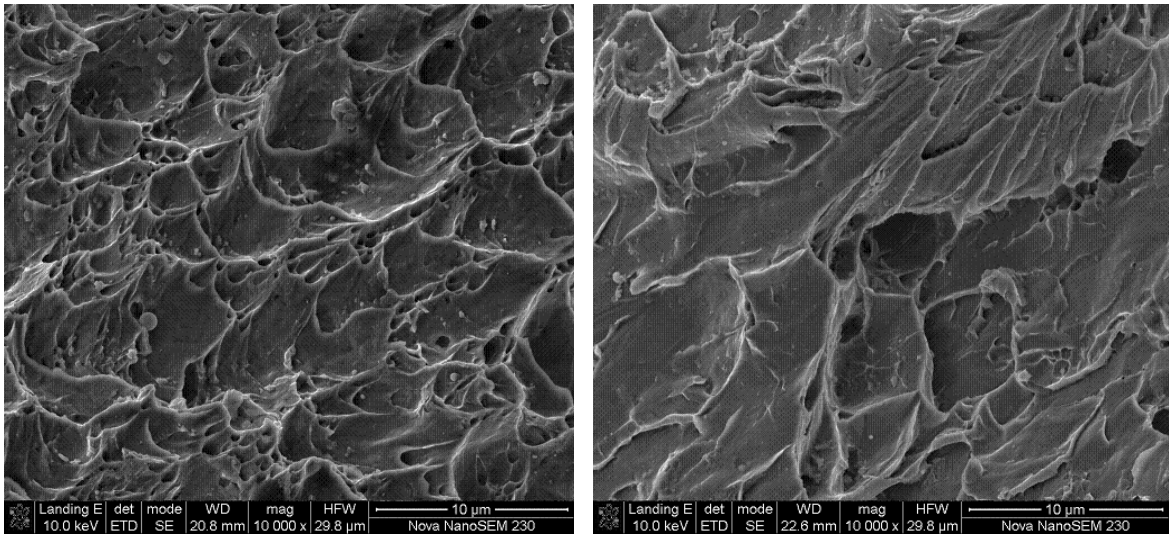

(a) (b)

Figure B-10: Fractographs of 6 mm thick single plates of Domex 700 MC plates after blast testing at a (charge=59g, impulse=109.8 Ns) and b (charge=62g, impulse=108 Ns), showing river patterns

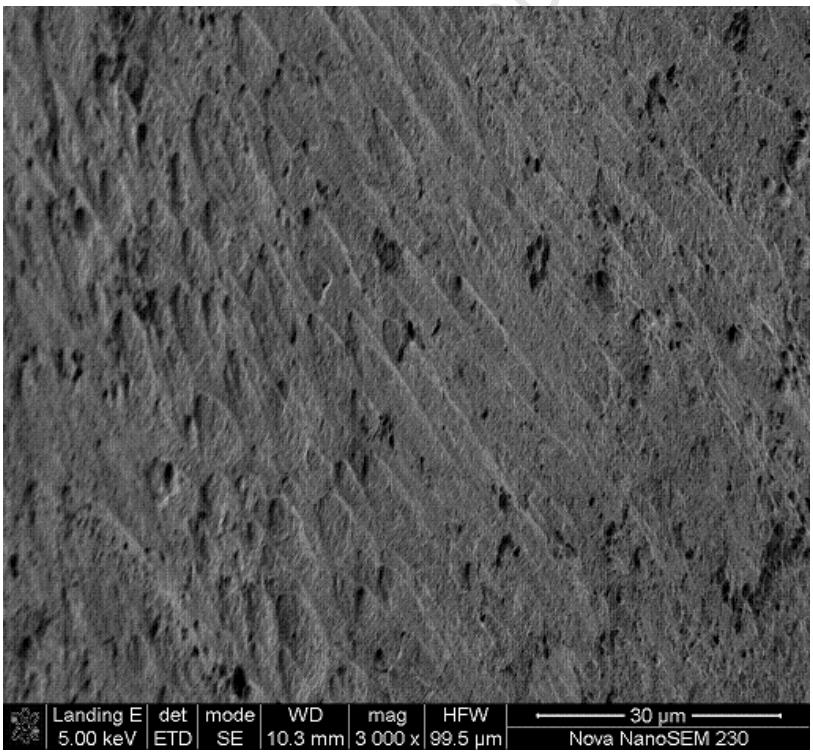

Figure B-11: Fractograph of 6 mm thick single plate after blast testing at charge mass of 62g, 108 Ns, showing river patterns along with the micro-voids

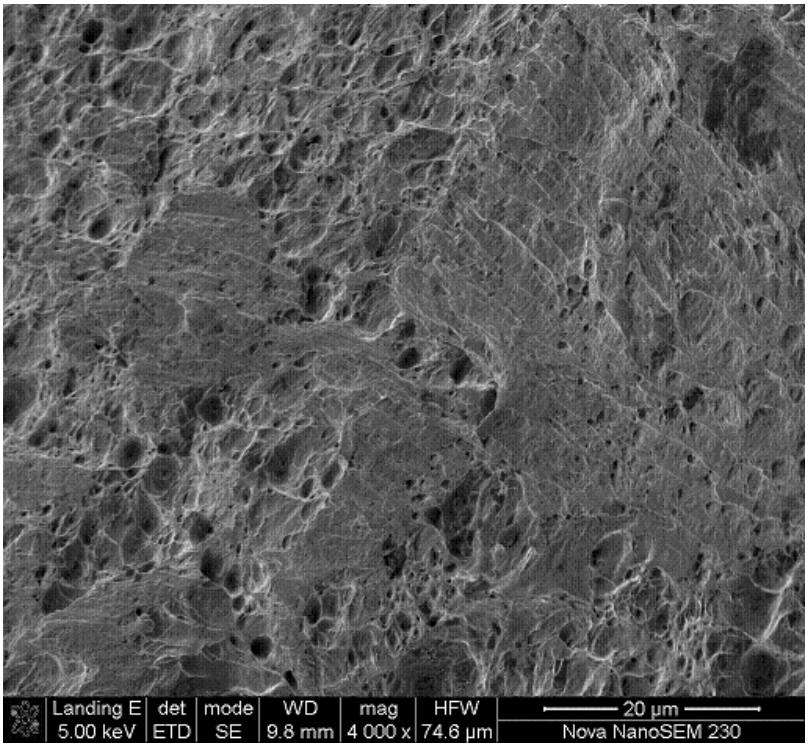

Figure B-12: Fractograph of 6 mm thick single plate after blast testing at charge mass of 62g, 108 Ns, showing river patterns along with the micro-voids

Figure B-13: Stereo-photographs of one side of torn cap of 6 mm thick single plate after blast testing at 62g charge mass, 108 Ns, showing shearing failure

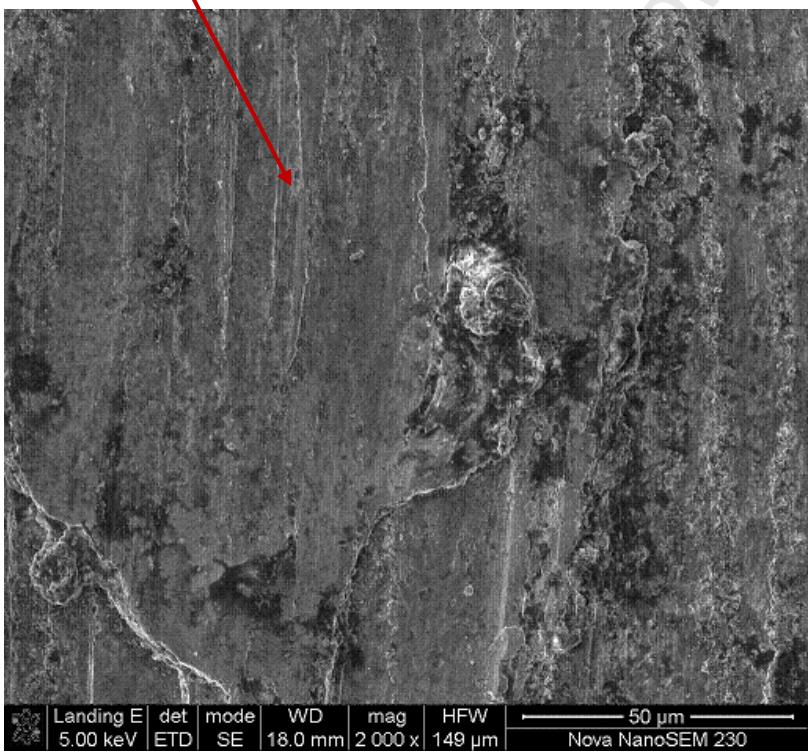

Figure B-14: Fractograph of 6 mm thick single plate after blast testing at charge mass of 62g, 108 Ns, showing featureless surface with no micro-voids

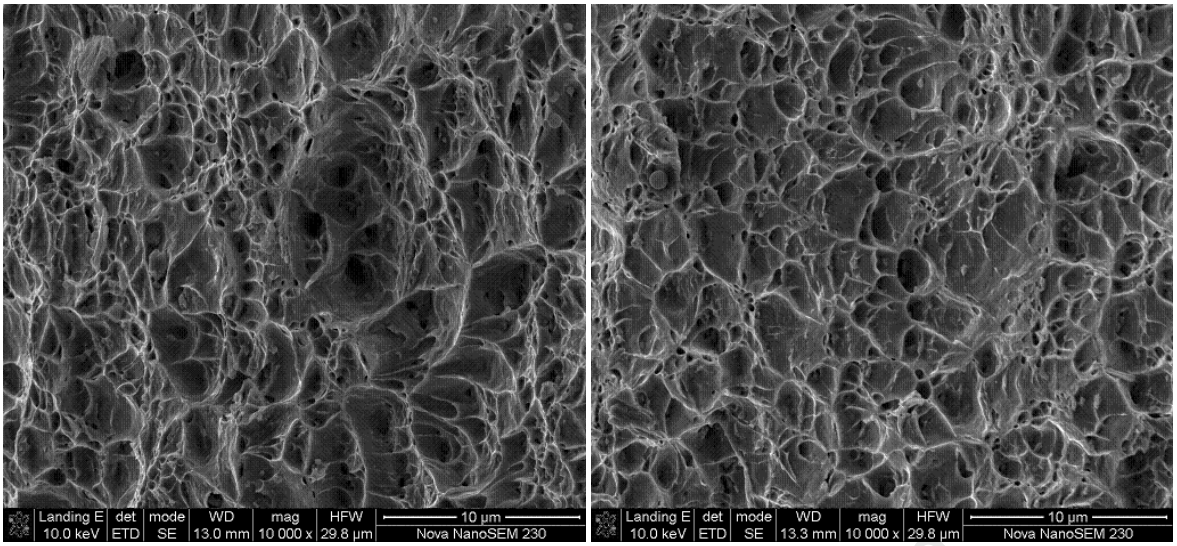

(a) (Front plate) (b) (Back plate)

Figure B-15: Fractographs of the front and back plate of triple (2+2+2)mm configuration after blast testing at a charge mass of 56g, 106 Ns

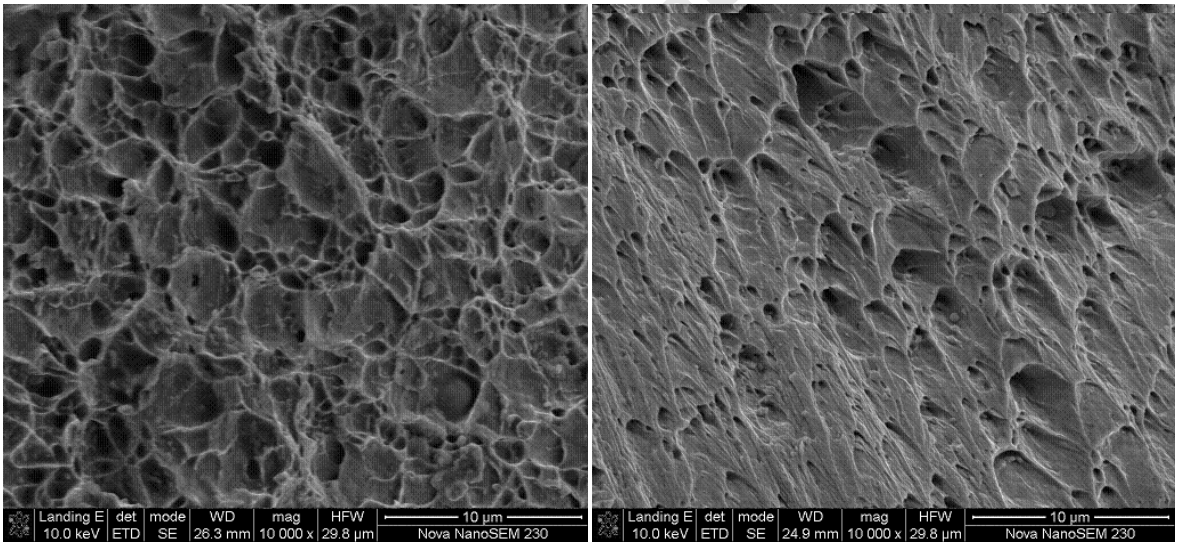

(a) Front plate (b) Back plate

Figure B-16: Fractographs of triple plates (2+2+2)mm after blast testing at a charge mass of 62g, 112.4 Ns (a) front plate and (b) back plate, showing equiaxed dimples in the front plate and elongated dimples in the back plate

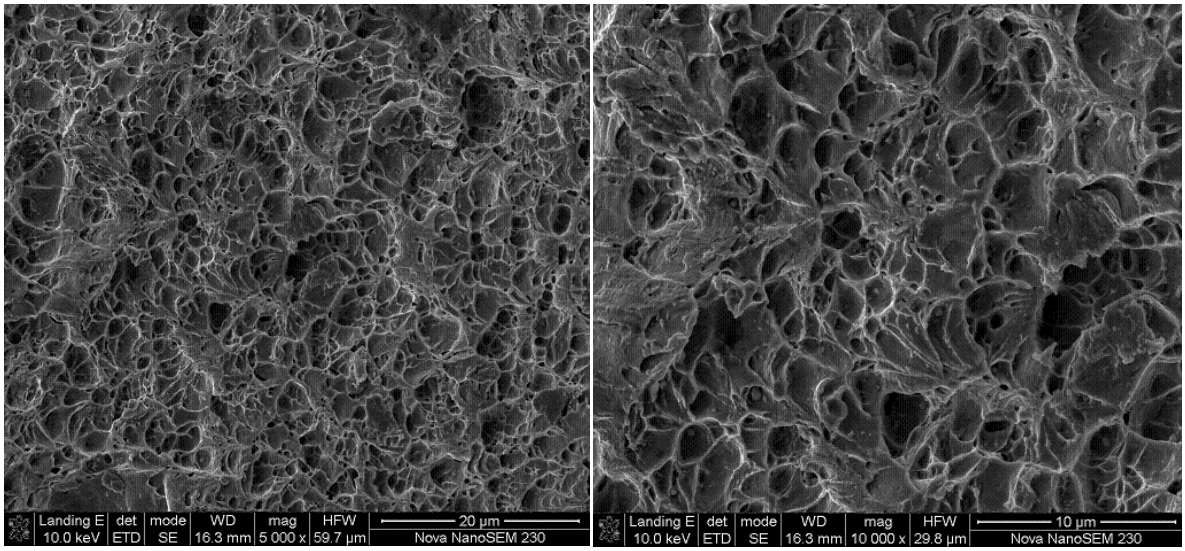

Figure B-17: Fractographs of front plate in triple (2+2+2)mm plate configuration after blast testing at charge mass of 68g, 126.1 Ns, showing equiaxed dimples at various magnifications

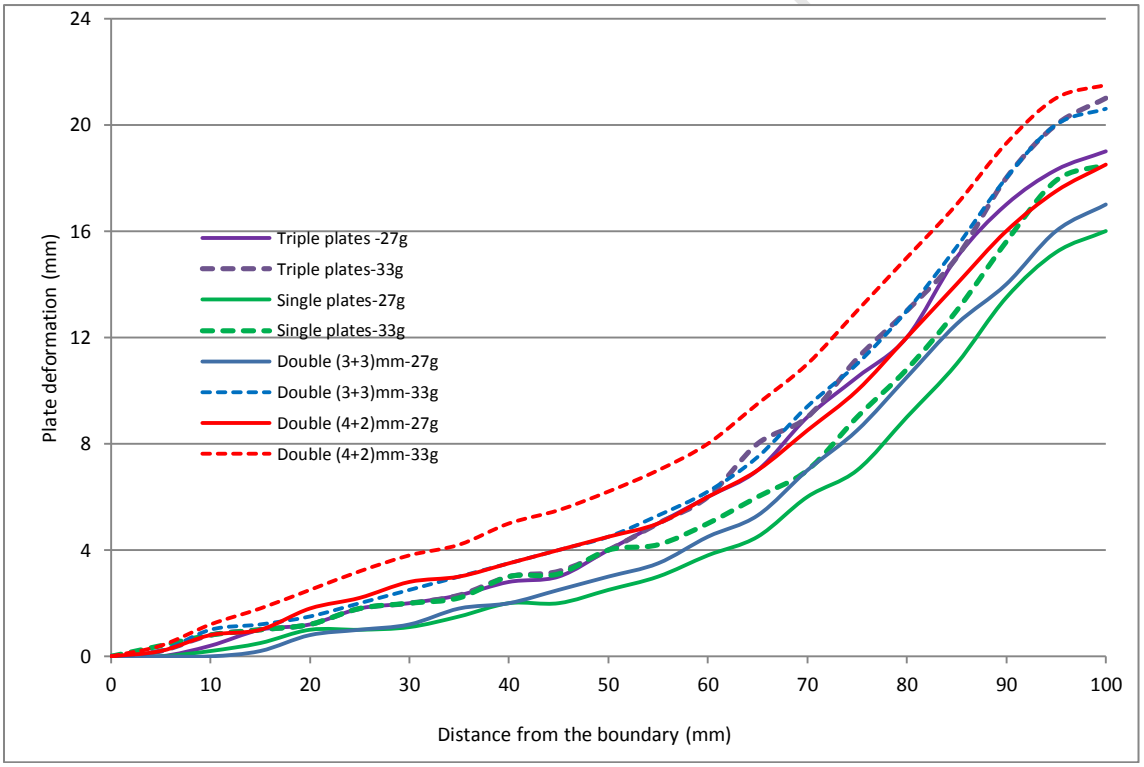

Figure B-18: Comparison of deformation profiles of 6mm configurations at 27g and 33g charge masses

Appendix C

In the appendix C, the user-subroutines “VDLOAD” and the input files of various thicknesses of Domex 550MC and Domex 700MC plates are given used for numerical simulations. The user-subroutine “VDLOAD” is attached to input file of different configurations generated by ABAQUS/Explicit. The parameter like, impulse, plate diameter, charge diameter, blast duration and decay constant (k) is changed for each simulation accordingly. The ABAQUS input files were generated for the thickness of single (4mm, 6mm and 8mm) for Domex 550MC and Domex 700MC plates. The user sub-routine and various input files are given below. The nodal points of input files are deleted here for simplification.

User-subroutines for “VDLOAD”

```
  subroutine vdload (
     1    nblock, ndim, stepTime, totalTime,
     2    amplitude, curCoords, velocity, dircos,
     3    jltyp, sname,
     4    value )
c
      include 'vaba_param.inc'
c
      dimension curCoords(nblock,ndim),
     1          velocity(nblock,ndim),
     2          dircos(nblock,ndim,ndim),
     3          value(nblock)
c
      character*80 sname
c
c-----------------------------------------------------------------------
c       defined user scalars
c-----------------------------------------------------------------------
c23456789
      real impulse, dt
      real r, r0, rb, pi
      real P0, k
c-----------------------------------------------------------------------
      impulse = 57
      dt = 2.6e-6
      r0 = 0.020
      rb = 0.100
      k = 115.72
      pi = 2.*asin(1.d0)
c
      P0 = impulse /
     1 (pi*dt*r0**2.d0+2.d0*pi*dt*(-exp(-k*rb+k*r0)*k*rb-
     2 exp(-k*rb+k*r0)+k*r0+1.d0)/k**2.d0)
c
c       open(unit=110,FILE='Saeed\plates.txt')
c       write (unit=110, fmt=100) totalTime,impulse, k, P0
c  100 FORMAT ('TotalTime= ',e16.8, 'impulse= ',e16.8,' k= ',
c     1         e16.8,'P0= ',e16.8,' Pb= ',e16.8)
c
c-----------------------------------------------------------------------
```

```
c2345678
      do km=1,nblock
       r=curcoords(km,1)
c
       if (r.lt.r0) then
        value(km)=P0
       elseif (r.lt.rb) then
        value(km)=P0*exp(-1.d0*k*(r-r0))
       else
        value(km)=0.0d0
       endif
      end do
      return
      end
c23456
```

Input file for Domex 550MC plates

Single plate of 4mm thickness, diameter 200mm (Domex 550MC)

```
*Heading
** Job name: plate4mm-Rb-100-Ro-16-I-15-SH Model name: Plate-4mm-Rb-100-Ro-10-I-15-StrainHard
** Generated by: Abaqus/CAE Version 6.8-2
*Preprint, echo=NO, model=NO, history=NO, contact=NO
**
** PARTS
**
*Part, name=Clamp
*End Part
**
*Part, name=DomexPlate
*End Part
**
**
** ASSEMBLY
**
*Assembly, name=Assembly
**
*Instance, name=Clamp-1, part=Clamp
        0.,     0.00128,          0.
*Node
     1,       0.125, 0.00400000019,          0.
*Nset, nset=Clamp-1-RefPt_, internal
1,
*Surface, type=SEGMENTS, name=LowerClamp
START,         0.1,          0.
 LINE,         0.1,        0.004
 LINE,        0.15,        0.004
 LINE,        0.15,          0.
 LINE,         0.1,          0.
*Rigid Body, ref node=Clamp-1-RefPt_, analytical surface=LowerClamp
*End Instance
**
*Instance, name=DomexPlate-1, part=DomexPlate
        0.,     0.00528,          0.
*Node

*Surface, type=ELEMENT, name=PlateBottom
_PlateBottom_S2, S2
** Section: SolidSection
*Solid Section, elset=_PickedSet3, material=Domex550

*End Instance
**
*Instance, name=Clamp-2, part=Clamp
        0.,     0.00928,          0.
```

```
*Node
      1,        0.125, 0.00400000019,           0.
*Nset, nset=Clamp-2-RefPt_, internal
1,
*Surface, type=SEGMENTS, name=upperClamp
START,          0.1,          0.
 LINE,          0.1,        0.004
 LINE,         0.15,        0.004
 LINE,         0.15,          0.
 LINE,          0.1,          0.
*Rigid Body, ref node=Clamp-2-RefPt_, analytical surface=upperClamp
*End Instance
**
*Nset, nset=_PickedSet50, internal, instance=DomexPlate-1, generate
    1,  16099,      1
*Elset, elset=_PickedSet50, internal, instance=DomexPlate-1, generate
    1,  15352,      1
*Nset, nset=_PickedSet52, internal, instance=Clamp-1
 1,
*Nset, nset=_PickedSet52, internal, instance=Clamp-2
 1,
*End Assembly
*Amplitude, name=BlastTime
        0.,          1.,      2.2e-06,          1.,     2.21e-06,          0.,          1.,          0.
**
** MATERIALS
**
*Material, name=Domex550
*Density
7850.,
*Elastic
 2.1e+11, 0.33
*Inelastic Heat Fraction
        0.9,
*Plastic
  5.6e+08,    0.
 5.82e+08,  0.01
  6.2e+08,  0.03
 6.42e+08,  0.05
  6.8e+08,  0.08
    7e+08, 0.104
  7.2e+08, 0.132
  7.4e+08, 0.162
*Rate Dependent
40.,5.
*Specific Heat
452.,
**
** INTERACTION PROPERTIES
**
*Surface Interaction, name=Fric3
*Friction
 0.3,
*Surface Interaction, name=NoFric
*Friction
0.,
**
** BOUNDARY CONDITIONS
**
** Name: FixClamp Type: Symmetry/Antisymmetry/Encastre
*Boundary
_PickedSet52, ENCASTRE
**
** PREDEFINED FIELDS
**
** Name: PlateTemp   Type: Temperature
*Initial Conditions, type=TEMPERATURE
_PickedSet50, 298.
** ----------------------------------------------------------------
**
** STEP: Load
**
*Step, name=Load
*Dynamic, Explicit, adiabatic
, 2.2e-06
```

```
*Bulk Viscosity
0.06, 1.2
**
** LOADS
**
** Name: Apply Load on Top   Type: Pressure
*Dsload
DomexPlate-1.LoadSurface, PNU, -1.
**
** INTERACTIONS
**
** Interaction: PlateBottom2Clamp
*Contact Pair, interaction=Fric3, mechanical constraint=PENALTY, cpset=PlateBottom2Clamp
Clamp-1.LowerClamp, DomexPlate-1.PlateBottom
** Interaction: PlateTop2Clamp
*Contact Pair, interaction=Fric3, mechanical constraint=PENALTY, cpset=PlateTop2Clamp
Clamp-2.upperClamp, DomexPlate-1.PlateTop
**
** OUTPUT REQUESTS
**
*Restart, write, number interval=1, time marks=NO
**
** FIELD OUTPUT: F-Output-1
**
*Output, field, variable=PRESELECT
**
** HISTORY OUTPUT: H-Output-1
**
*Output, history, variable=PRESELECT, time interval=1.1e-07
*End Step
** ----------------------------------------------------------------
**
** STEP: LoadConti
**
*Step, name=LoadConti
*Dynamic, Explicit, adiabatic
, 0.0005
*Bulk Viscosity
0.06, 1.2
**
** LOADS
**
** Name: Apply Load on Top   Type: Pressure
*Dsload, op=NEW
**
** OUTPUT REQUESTS
**
*Restart, write, number interval=1, time marks=NO
**
** FIELD OUTPUT: F-Output-1
**
*Output, field, variable=PRESELECT, number interval=60
**
** HISTORY OUTPUT: H-Output-1
**
*Output, history, variable=PRESELECT, time interval=2.5e-05
**
** HISTORY OUTPUT: PlateTip
**
*Output, history, time interval=5e-06
*Node Output, nset=DomexPlate-1.PlateTip
U2, V2
*End Step
```

Input files for Domex 700MC plates

Single plate of 4mm thickness (Domex 700MC)

```
*Heading
 4mm thick Single plate subjected to localized blast loading, charge radius 20mm
** Job name: SinglePlate4mm Model name: SinglePlate-4mm
** Generated by: Abaqus/CAE 6.10-1
*Preprint, echo=NO, model=NO, history=NO, contact=NO
**
** PARTS
**
*Part, name=Clamp
*End Part
**
*Part, name=Domex-Plate
*End Part
**
**
** ASSEMBLY
**
*Assembly, name=Assembly
**
*Instance, name=Clamp-1, part=Clamp
        0.,     0.00208,          0.
*Node
      1,  0.150000006,          0.,          0.
*Nset, nset=Clamp-1-RefPt_, internal
1,
*Surface, type=SEGMENTS, name=LowerClamp
START,          0.1,          0.
 LINE,          0.1,        0.012
 LINE,          0.2,        0.012
 LINE,          0.2,          0.
 LINE,          0.1,          0.
*Rigid Body, ref node=Clamp-1-RefPt_, analytical surface=LowerClamp
*End Instance
**
*Instance, name=Domex-Plate-1, part=Domex-Plate
        0.,     0.01408,          0.
*Node

 Has been deleted


*Surface, type=ELEMENT, name=PlateBottom
_PlateBottom_S2, S2
*End Assembly
*Amplitude, name=BlastTime
        0.,          1.,     2.66e-06,          1.,     2.67e-06,          0.,          1.,          0.
**
** MATERIALS
**
** Material Domex 700 MC
*Material, name=Domex700MC
*Density
7870.,
*Elastic
 2.1e+11, 0.33
*Inelastic Heat Fraction
        0.9,
*Plastic
     8e+08,   0.
   8.2e+08, 0.01
  8.35e+08, 0.02
  8.45e+08, 0.03
  8.63e+08, 0.04
   8.8e+08, 0.05
     9e+08, 0.06
   9.2e+08, 0.08
```

```
 9.45e+08,  0.1
  9.6e+08, 0.11
  9.7e+08, 0.12
  9.8e+08, 0.13
  9.9e+08, 0.14
    1e+09, 0.15
 1.005e+09, 0.16
*Rate Dependent
3110., 2.23
*Specific Heat
452.,
**
** INTERACTION PROPERTIES
**
*Surface Interaction, name=Fric30
*Friction
 0.3,
*Surface Interaction, name=Fric90
*Friction
 0.9,
**
** BOUNDARY CONDITIONS
**
** Name: FixedBoundary Type: Symmetry/Antisymmetry/Encastre
*Boundary
BothClamps, ENCASTRE
**
** PREDEFINED FIELDS
**
** Name: Temp   Type: Temperature
*Initial Conditions, type=TEMPERATURE
AllPlate, 298.
** ----------------------------------------------------------------
**
** STEP: Load
**
*Step, name=Load
Apply load for 2.66 micro seconds
*Dynamic, Explicit, adiabatic
, 2.66e-06
*Bulk Viscosity
0.06, 1.2
**
** LOADS
**
** Name: Apply load on top   Type: Pressure
*Dsload
ExposedSurface, PNU, 1.
**
** INTERACTIONS
**
** Interaction: LowerClamp2Plate
*Contact Pair, interaction=Fric90, mechanical constraint=KINEMATIC, cpset=LowerClamp2Plate
PlateBottom, Clamp-1.LowerClamp
** Interaction: UpperClamp2Plate
*Contact Pair, interaction=Fric90, mechanical constraint=KINEMATIC, cpset=UpperClamp2Plate
Clamp-2.UpperClamp, PlateTop
**
** OUTPUT REQUESTS
**
*Restart, write, number interval=1, time marks=NO
**
** FIELD OUTPUT: F-Output-1
**
*Output, field, variable=PRESELECT
**
** HISTORY OUTPUT: H-Output-1
**
*Output, history, variable=PRESELECT
*End Step
** ----------------------------------------------------------------
**
** STEP: ContiLoad
**
*Step, name=ContiLoad
```

```
Continue for 500 micro seconds
*Dynamic, Explicit, adiabatic
, 0.0005
*Bulk Viscosity
0.06, 1.2
**
** LOADS
**
** Name: Apply load on top   Type: Pressure
*Dsload, op=NEW
**
** INTERACTIONS
**
** Interaction: LowerClamp2Plate
*Contact Pair, op=DELETE, cpset=LowerClamp2Plate
PlateBottom, Clamp-1.LowerClamp
*Contact Pair, interaction=Fric90, mechanical constraint=KINEMATIC, cpset=LowerClamp2Plate
PlateBottom, Clamp-1.LowerClamp
** Interaction: UpperClamp2Plate
*Contact Pair, op=DELETE, cpset=UpperClamp2Plate
Clamp-2.UpperClamp, PlateTop
*Contact Pair, interaction=Fric90, mechanical constraint=KINEMATIC, cpset=UpperClamp2Plate
Clamp-2.UpperClamp, PlateTop
**
** OUTPUT REQUESTS
**
*Restart, write, number interval=1, time marks=NO
**
** FIELD OUTPUT: F-Output-1
**
*Output, field, variable=PRESELECT
**
** HISTORY OUTPUT: H-Output-1
**
*Output, history, variable=PRESELECT
**
** HISTORY OUTPUT: PlateTip
**
*Output, history, time interval=1.25e-06
*Node Output, nset=PlateTip
U2, V2
*End Step
```

Single plate of 6mm thickness (Domex 700MC)

```
*Heading
 Single plate of 6mm thickness subjected to blast loading at 20 mm radius
** Job name: SinglePlate6mm Model name: SinglePlate-6mm
** Generated by: Abaqus/CAE 6.10-1
*Preprint, echo=NO, model=NO, history=NO, contact=NO
**
** PARTS
**
*Part, name=Clamp
*End Part
**
*Part, name=Domex-Plate
*End Part
**
**
** ASSEMBLY
**
*Assembly, name=Assembly
**
*Instance, name=Clamp-1, part=Clamp
         0.,      0.00252,           0.
*Node
      1,  0.150000006,           0.,           0.
*Nset, nset=Clamp-1-RefPt_, internal
1,
*Surface, type=SEGMENTS, name=LowerClamp
START,          0.1,           0.
```

```
 LINE,         0.1,        0.012
 LINE,         0.2,        0.012
 LINE,         0.2,          0.
 LINE,         0.1,          0.
*Rigid Body, ref node=Clamp-1-RefPt_, analytical surface=LowerClamp
*End Instance
**
*Instance, name=Domex-Plate-1, part=Domex-Plate
        0.,     0.01452,          0.
*Node
     Has been deleted


*Surface, type=ELEMENT, name=PlateTop
_PlateTop_S4, S4
*End Assembly
*Amplitude, name=BlastTime
        0.,          1.,     2.66e-06,          1.,     2.67e-06,          0.,          1.,          0.
**
** MATERIALS
**
** Material Domex 700 MC
*Material, name=Domex700MC
*Density
7870.,
*Elastic
 2.1e+11, 0.33
*Inelastic Heat Fraction
        0.9,
*Plastic
     8e+08,   0.
   8.2e+08, 0.01
  8.35e+08, 0.02
  8.45e+08, 0.03
  8.63e+08, 0.04
   8.8e+08, 0.05
     9e+08, 0.06
   9.2e+08, 0.08
  9.45e+08,  0.1
   9.6e+08, 0.11
   9.7e+08, 0.12
   9.8e+08, 0.13
   9.9e+08, 0.14
     1e+09, 0.15
 1.005e+09, 0.16
*Rate Dependent
3110., 2.23
*Specific Heat
452.,
**
** INTERACTION PROPERTIES
**
*Surface Interaction, name=Fric30
*Friction
 0.3,
*Surface Interaction, name=Fric90
*Friction
 0.9,
**
** BOUNDARY CONDITIONS
**
** Name: FixedBoundary Type: Symmetry/Antisymmetry/Encastre
*Boundary
BothClamps, ENCASTRE
**
** PREDEFINED FIELDS
**
** Name: Temp   Type: Temperature
*Initial Conditions, type=TEMPERATURE
AllPlate, 298.
** ----------------------------------------------------------------
**
** STEP: Load
**
*Step, name=Load
```

```
Apply load for 2.66 micro seconds
*Dynamic, Explicit, adiabatic
, 2.66e-06
*Bulk Viscosity
0.06, 1.2
**
** LOADS
**
** Name: Apply load on top   Type: Pressure
*Dsload
ExposedSurface, PNU, 1.
**
** INTERACTIONS
**
** Interaction: LowerClamp2Plate
*Contact Pair, interaction=Fric90, mechanical constraint=KINEMATIC, cpset=LowerClamp2Plate
PlateBottom, Clamp-1.LowerClamp
** Interaction: UpperClamp2Plate
*Contact Pair, interaction=Fric90, mechanical constraint=KINEMATIC, cpset=UpperClamp2Plate
Clamp-2.UpperClamp, PlateTop
**
** OUTPUT REQUESTS
**
*Restart, write, number interval=1, time marks=NO
**
** FIELD OUTPUT: F-Output-1
**
*Output, field, variable=PRESELECT
**
** HISTORY OUTPUT: H-Output-1
**
*Output, history, variable=PRESELECT
*End Step
** ----------------------------------------------------------------
**
** STEP: ContiLoad
**
*Step, name=ContiLoad
Continue for 500 micro seconds
*Dynamic, Explicit, adiabatic
, 0.0005
*Bulk Viscosity
0.06, 1.2
**
** LOADS
**
** Name: Apply load on top   Type: Pressure
*Dsload, op=NEW
**
** INTERACTIONS
**
** Interaction: LowerClamp2Plate
*Contact Pair, op=DELETE, cpset=LowerClamp2Plate
PlateBottom, Clamp-1.LowerClamp
*Contact Pair, interaction=Fric90, mechanical constraint=KINEMATIC, cpset=LowerClamp2Plate
PlateBottom, Clamp-1.LowerClamp
** Interaction: UpperClamp2Plate
*Contact Pair, op=DELETE, cpset=UpperClamp2Plate
Clamp-2.UpperClamp, PlateTop
*Contact Pair, interaction=Fric90, mechanical constraint=KINEMATIC, cpset=UpperClamp2Plate
Clamp-2.UpperClamp, PlateTop
**
** OUTPUT REQUESTS
**
*Restart, write, number interval=1, time marks=NO
**
** FIELD OUTPUT: F-Output-1
**
*Output, field, variable=PRESELECT
**
** HISTORY OUTPUT: H-Output-1
**
*Output, history, variable=PRESELECT
**
** HISTORY OUTPUT: PlateTip
```

**
*Output, history, time interval=1.25e-06
*Node Output, nset=PlateTip
U2, V2
*End Step

Single plate of 8mm thickness (Domex 700MC)

*Heading
 Single plate of 8mm thickness subjected to blast loading, radius 20mm
** Job name: SinglePlate8mm Model name: SinglePlate-8mm
** Generated by: Abaqus/CAE 6.10-1
*Preprint, echo=NO, model=NO, history=NO, contact=NO
**
** PARTS
**
*Part, name=Clamp
*End Part
**
*Part, name=Domex-Plate
*End Part
**
**
** ASSEMBLY
**
*Assembly, name=Assembly
**
*Instance, name=Clamp-1, part=Clamp
        0.,   0.00296,   0.
*Node
      1, 0.150000006,   0.,   0.
*Nset, nset=Clamp-1-RefPt_, internal
1,
*Surface, type=SEGMENTS, name=LowerClamp
START,   0.1,   0.
 LINE,   0.1,   0.012
 LINE,   0.2,   0.012
 LINE,   0.2,   0.
 LINE,   0.1,   0.
*Rigid Body, ref node=Clamp-1-RefPt_, analytical surface=LowerClamp
*End Instance
**
*Instance, name=Domex-Plate-1, part=Domex-Plate
        0.,   0.01496,   0.
*Node

Has been deleted

*Surface, type=ELEMENT, name=PlateTop
_PlateTop_S4, S4
*End Assembly
*Amplitude, name=BlastTime
        0.,   1.,   2.66e-06,   1.,   2.67e-06,   0.,   1.,   0.
**
** MATERIALS
**
** Material Domex 700 MC
*Material, name=Domex700MC
*Density
7870.,
*Elastic
 2.1e+11, 0.33
*Inelastic Heat Fraction
        0.9,
*Plastic
     8e+08,   0.
   8.2e+08, 0.01
  8.35e+08, 0.02
  8.45e+08, 0.03
  8.63e+08, 0.04
   8.8e+08, 0.05

```
   9e+08, 0.06
  9.2e+08, 0.08
 9.45e+08,  0.1
  9.6e+08, 0.11
  9.7e+08, 0.12
  9.8e+08, 0.13
  9.9e+08, 0.14
    1e+09, 0.15
1.005e+09, 0.16
  1.3e+09,  0.3
*Rate Dependent
3110., 2.23
*Specific Heat
452.,
**
** INTERACTION PROPERTIES
**
*Surface Interaction, name=Fric30
*Friction
 0.3,
*Surface Interaction, name=Fric90
*Friction
 0.9,
**
** BOUNDARY CONDITIONS
**
** Name: FixedBoundary Type: Symmetry/Antisymmetry/Encastre
*Boundary
BothClamps, ENCASTRE
**
** PREDEFINED FIELDS
**
** Name: Temp   Type: Temperature
*Initial Conditions, type=TEMPERATURE
AllPlate, 298.
** ----------------------------------------------------------------
**
** STEP: Load
**
*Step, name=Load
Apply load for 2.66 micro seconds
*Dynamic, Explicit, adiabatic
, 2.66e-06
*Bulk Viscosity
0.06, 1.2
**
** LOADS
**
** Name: Apply load on top   Type: Pressure
*Dsload
ExposedSurface, PNU, 1.
**
** INTERACTIONS
**
** Interaction: LowerClamp2Plate
*Contact Pair, interaction=Fric90, mechanical constraint=KINEMATIC, cpset=LowerClamp2Plate
PlateBottom, Clamp-1.LowerClamp
** Interaction: UpperClamp2Plate
*Contact Pair, interaction=Fric90, mechanical constraint=KINEMATIC, cpset=UpperClamp2Plate
Clamp-2.UpperClamp, PlateTop
**
** OUTPUT REQUESTS
**
*Restart, write, number interval=1, time marks=NO
**
** FIELD OUTPUT: F-Output-1
**
*Output, field, variable=PRESELECT
**
** HISTORY OUTPUT: H-Output-1
**
*Output, history, variable=PRESELECT
*End Step
** ----------------------------------------------------------------
**
```

```
** STEP: ContiLoad
**
*Step, name=ContiLoad
Continue for 500 micro seconds
*Dynamic, Explicit, adiabatic
, 0.0005
*Bulk Viscosity
0.06, 1.2
**
** LOADS
**
** Name: Apply load on top   Type: Pressure
*Dsload, op=NEW
**
** INTERACTIONS
**
** Interaction: LowerClamp2Plate
*Contact Pair, op=DELETE, cpset=LowerClamp2Plate
PlateBottom, Clamp-1.LowerClamp
*Contact Pair, interaction=Fric90, mechanical constraint=KINEMATIC, cpset=LowerClamp2Plate
PlateBottom, Clamp-1.LowerClamp
** Interaction: UpperClamp2Plate
*Contact Pair, op=DELETE, cpset=UpperClamp2Plate
Clamp-2.UpperClamp, PlateTop
*Contact Pair, interaction=Fric90, mechanical constraint=KINEMATIC, cpset=UpperClamp2Plate
Clamp-2.UpperClamp, PlateTop
**
** OUTPUT REQUESTS
**
*Restart, write, number interval=1, time marks=NO
**
** FIELD OUTPUT: F-Output-1
**
*Output, field, variable=PRESELECT
**
** HISTORY OUTPUT: H-Output-1
**
*Output, history, variable=PRESELECT
**
** HISTORY OUTPUT: PlateTip
**
*Output, history, time interval=1.25e-06
*Node Output, nset=PlateTip
U2, V2
*End Step
```

Appendix D

Zerilli-Armstrong (ZA) constitutive relation

The models of Zerilli and Armstrong are more specialized for military applications due to involvement of very high strain rates, high temperature and high hydro-pressure. Zerilli-Armstrong (ZA) constitutive relation [121] is based on the dislocation theory while the J-C constitutive relation is purely empirical [107]. The effects of strain hardening, strain-rate hardening, and thermal softening based on the thermal activation analysis have been incorporated into a constitutive relation. The relation has a relatively simple expression compared to other dislocation based constitutive models. One of the main points proposed is that each material structure type (FCC, BCC, and HCP) will have a different constitutive behavior based on the different rate-controlling mechanism for that particular structure. Therefore, there are two different constitutive relations for FCC and BCC materials. The formulation is based on the idea of thermally activated motion of dislocations. For BCC metals, the dislocation motion is governed mainly by the interaction with the overall lattice potential (the Peierls-Nabarro stress). The thermally activated motion is not dependent on the strain, so the strain hardening becomes independent of temperature and strain rate.

$$\boldsymbol{\sigma_{eq}=\Delta\sigma_G^{`}+Kl^{-1/2}+C_1\exp\left(-C_3+C_4T\ln\dot{\varepsilon}_{eq}\right)+C_5\varepsilon_{eq}^{n}} \qquad \text{D-1}$$

The first two terms in this equation ($\Delta\sigma_G^{`}$ *and* $Kl^{-1/2}$) take care of the effects of initial dislocation density and grain size, and C_1,C_2,C_3,C_4 and C_5 and n are material constants. Since the first two terms are not dependent on the strain, strain rate or temperature, Zerilli and Armstrong [122] turned the constitutive relation into a simpler form by combining these terms into one material constant σ_a in Equation D-1.

$$\boldsymbol{\sigma_{eq}=\sigma_a+B\exp(-\beta T)+A\varepsilon_{eq}^{n}} \qquad \text{D-2}$$

Where

$$\boldsymbol{\beta=\beta_o-\beta_1 ln\dot{\varepsilon}_{eq}}$$

The BCC model has six material constants σ_a, B, β_0, β_1, A and n (note that A, B and n are not the same parameters as in the J-C constitutive relation and σ_a is termed as c_0 by Zerilli and Armstrong [122]. Goldthorpe [123] modified the strain hardening term of the BCC constitutive relation to make it temperature dependent. The development was based on experimental results for annealed and explosively shocked iron. The modified equation reads

$$\boldsymbol{\sigma_{eq}=C_1+C_2\exp\left(C_3+C_4\ln\dot{\varepsilon}_{eq}\right)T+(C_5\varepsilon_{eq}^{n}+C_6)\frac{\mu_T}{\mu_{298}}} \qquad \text{D-3}$$

where C_1, C_2, C_3, C_4, C_5, C_6 and n are material constants, μ_T is the shear modulus at the prevailing temperature and μ_{293} the shear modulus at 293 K.

For FCC metals, the thermally activated motion is produced by dislocation intersections which are leading to temperature and strain-rate dependent strain hardening.

$$\boldsymbol{\sigma_{eq=\Delta\sigma_G^{`}+Kl^{-1/2}+C_2\varepsilon_{eq}^{1/2}\exp(-C_3T+C_4T\ln\dot{\varepsilon}_{eq}}}) \quad \text{D-4}$$

Where, and C_1, C_2, C_3, and C_4 are material constants. Equation D-1 may be rewritten in the same manner that was done with the bcc model in Equation D-3

$$\boldsymbol{\sigma_{eq=\sigma_a+A\varepsilon_{eq}^{n}\exp(-\alpha T)}} \quad \text{D-5}$$

Where

$$\boldsymbol{\alpha = \alpha_o - \alpha_1 \ln\dot{\varepsilon}_{eq}}$$

The FCC model includes five material constants, σ_a, α_0, α_1, *A* and *n*, where n = ½ in Equation (D-3).

HCP metals have a stress-strain behaviour falling somewhere between BCC and FCC metals. Zerilli and Armstrong [124] proposed a constitutive relation for HCP materials and steel alloys. In order to describe the intermediate behaviour, both the predominant interaction in the BCC model and the predominant interaction in the FCC model are introduced a single Equation D-6.

$$\boldsymbol{\sigma_{eq=\sigma_a+\beta\exp(-\beta T)+A\varepsilon_{eq}^{n}\exp(-\alpha T)}} \quad \text{D-6}$$

By excluding some of the parameters one can either return to the original BCC model or the original FCC model. The Zerilli-Armstrong model presumes that the work hardening rate is independent of the temperature and strain rate. For most metals, work-hardening behaviours are actually dependent on the temperature and strain rate. Therefore, the Zerilli-Armstrong model is not a good candidate for modeling the work-hardening behaviors of materials with strong temperature and strain-rate dependences.

Zhao

A phenomenological model is presented to describe the mechanical behaviour for metals and alloys over a large range of strain rates. This model partially relies on physical considerations

and is specially developed for an easy application in explicit finite element method (FEM) codes. Zhao [125] presented a phenomenological model to describe the mechanical behaviour of metals and alloys over a large range of strain rates. It is an elasto-plastic model with a strain rate and temperature-sensitive yield stress. The model seeks to capture physical behaviours such as a decrease in rate sensitivity with an increase in strain while still being relatively simple to characterize. The model format is given in Equation D-7

$$\boldsymbol{\sigma} = \left[\mathbf{A} + \mathbf{B}\varepsilon_{\mathbf{p}}^{\mathbf{n}} + \left(\mathbf{C} - \mathbf{D}\varepsilon_{\mathbf{p}}^{\mathbf{m}}\right)\mathbf{log}\left(\frac{\dot{\varepsilon}}{\dot{\varepsilon}_{\mathbf{0}}}\right) + \mathbf{E}\dot{\varepsilon}^{\mathbf{k}}\right] + [\mathbf{1} - \boldsymbol{\mu}\Delta\mathbf{T}\,] \qquad \text{D-7}$$

Where A, B, C, D, E, k, m, n and ϵ_o are coefficients of the model. Parameters D and m describe the variation of rate sensitivity as a function of strain. This model is not limited to the uniaxial case as with most empirical models. It can be easily generalized to three-dimensional cases (for an FEM-code application) using equivalent stress and strain in the sense of the Von Mises criterion.

Bodner-Partom (BP) model

A set of constitutive equations was presented by Bodner and Partom [126] to represent elastic-viscoplastic strain-hardening material behaviour for large deformations and arbitrary loading histories. An essential feature of the formulation is that the total deformation rate is considered to be separable into elastic and inelastic components, which are functions of state variables at all stages of loading and unloading. The formulation is independent of any yield criteria or loading and unloading conditions. The deformation rate components are determinable from the current state, which permits an incremental formulation of problems. Strain hardening is considered in the equations by introducing plastic work as the representative state variable. The assumptions of isotropy and isothermal conditions are maintained in this formulation, although strain hardening is known to induce anisotropy. The Bodner-Partom model, in its original form, is not very sensitive to the strain rate. It can be seen as a constant work-hardening model when the strain rate change is minor. The BP model also does not take the temperature effect into consideration. Many modifications have been made to the model that adds more material constants.

Khan-Huang (KH) model

Khan and Huang [127] proposed a new constitutive model that can predict the experimental results in a very large strain-rate range including the high work-hardening region. Direct disc impact technique was used to study the mechanical behaviour of aluminum (1100 and 1100-0) in the strain rate range 10^{-5}–10^{4} s^{-1}. The experimental results showed that fully annealed aluminium (1100) was negligibly strain rate sensitive and its behaviour at high strain rates can be described by Bell's parabolic equation, while aluminium (1100-0) was quite strain rate sensitive and a rate dependent theory has to be used to describe its behaviour. A new viscoplastic model was proposed which can predict the experimental results in a very large strain rate range, 10^{-5}–10^{4} s^{-1}, including the high work hardening region. Based on similar assumption as that of the BP model, the KH model proposed a new relation to describe the dependence of work hardening behaviour on strain and strain rate. The KH model is more

capable of predicting the strong work hardening behaviour in a large strain-rate range than that of the BP model.

Appendix E

Simulation results of 4mm thick single plates (Domex550MC) (R=100mm, a=10mm)

The finite element simulation results of the 4mm thick single plates subjected to explosive load diameter of 20mm are given in Table E-1. Permanent midpoint deflection increases on increasing the impulse. The plates failed at an impulse of 75Ns as indicated in Table E-1. Thinning was found after an impulse of 45Ns. Decrease in thickness of plate over a charge diameter was observed as shown in Figure E-1 and Figure E-2 at an impulse of 45Ns and 60Ns respectively.

The 4mm thick single plates failed with a cap diameter of 28mm at an impulse of 75Ns and 90Ns as shown in Figure E-3 and Figure E-4 respectively.

Table E-1: Midpoint displacement predictions from simulations of 4mm thick single plates (R = 100mm, a = 10mm)

Impulse (Ns)	Maximum deflections (mm)
	a = 10mm
15	8.6
30	20
45	32
60	45 Necking
75	Cap Ø= 28mm

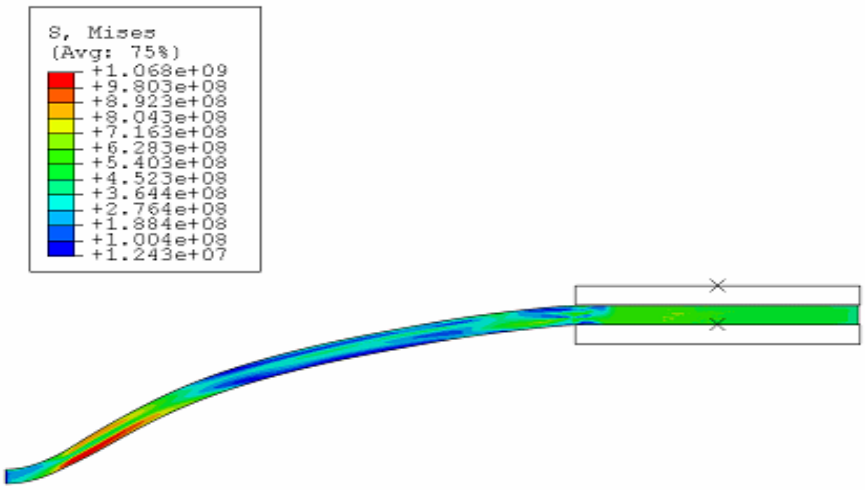

Figure E-1: FE predictions of 4mm thick plate of Domex 550MC subjected to an impulse of 45Ns and a charge diameter of 20mm

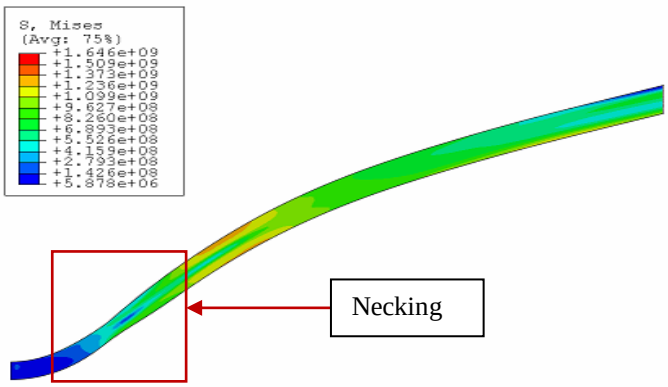

Figure E-2: FE predictions of 4mm thick plate of Domex 550MC subjected to an impulse of 60Ns and a charge diameter of 20mm

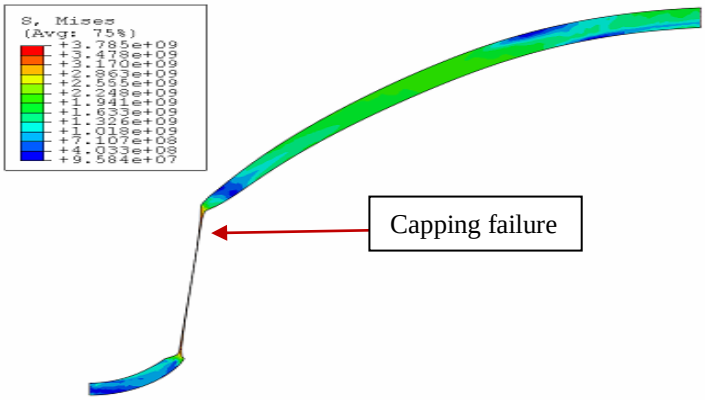

Figure E-3: FE predictions of 4mm thick plate of Domex 550MC subjected to an impulse of 75Ns and a charge diameter of 20mm, cap diameter 28mm

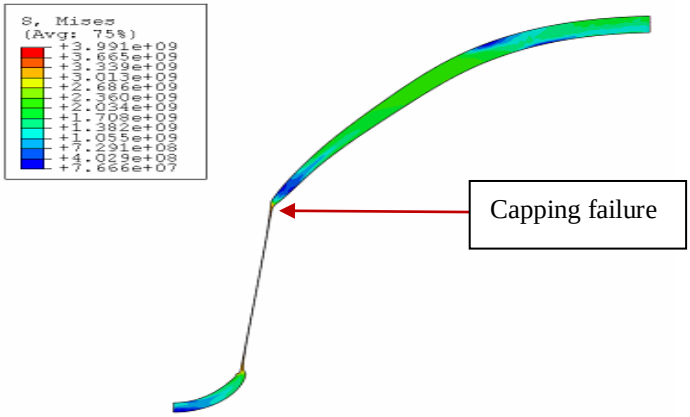

Figure E-4: FE predictions of 4mm thick plate of Domex 550MC subjected to an impulse of 90 Ns and a charge diameter of 20mm

Simulation results of 4mm thick single plates of Domex 550MC tested at charge diameter of 30mm

The thinning in single plates of 4mm thickness subjected to a load diameter of 30mm was started at an impulse of 45Ns as shown in Figure E-5. Necking was observed at an impulse of 60Ns and 75Ns as indicated in Figure E-6 and Figure E-7 respectively. These plates were capped at an impulse of 100Ns as depicted in Figure E-8, with a cap diameter of 37mm.

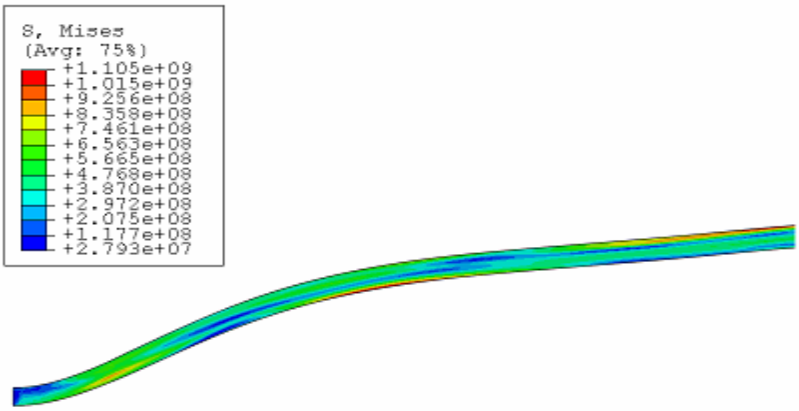

Figure E-5: FE predictions of 4mm thick plate of Domex 550MC subjected to an impulse of 45 Ns and a charge diameter of 30mm

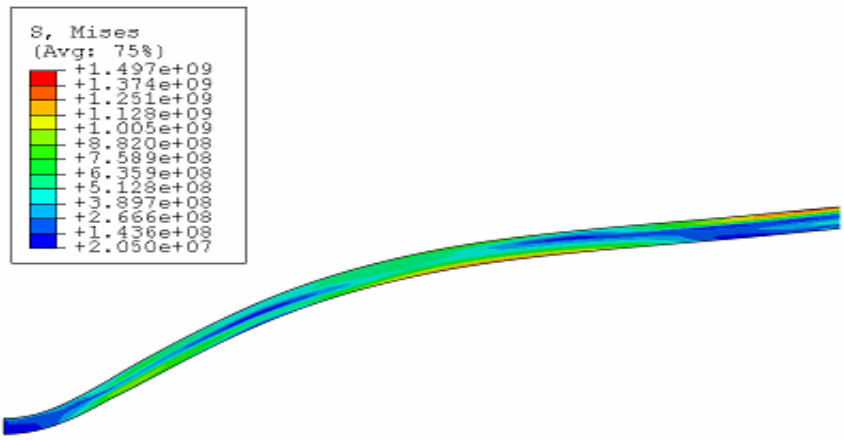

Figure E-6: FE predictions of 4mm thick plate of Domex 550MC subjected to an impulse of 60 Ns and a charge diameter of 30mm

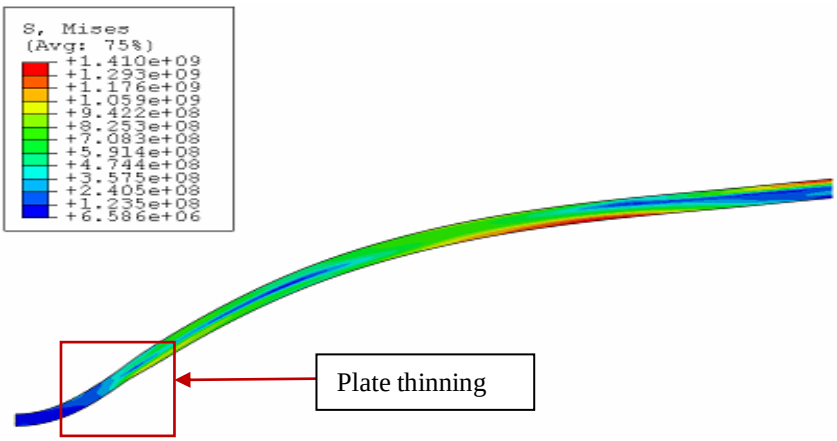

Figure E-7: FE predictions of 4mm thick plate of Domex 550MC subjected to an impulse of 75 Ns and a charge diameter of 30mm

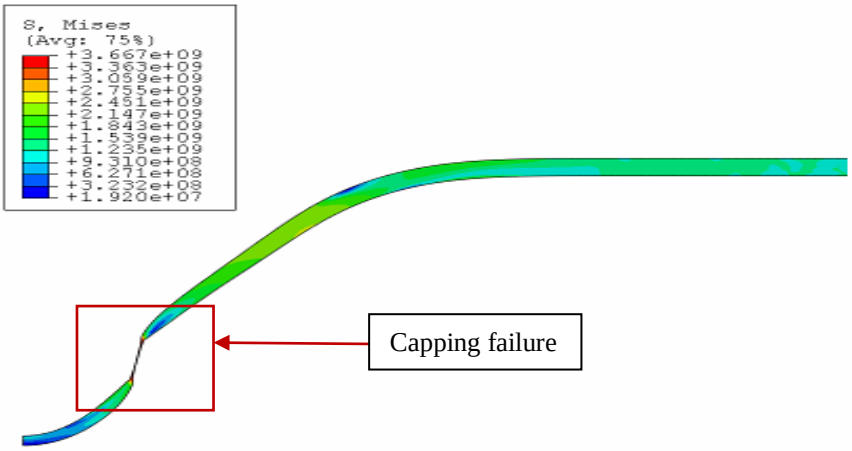

Figure E-8: FE predictions of 4mm thick plate of Domex 550MC subjected to an impulse of 100 Ns and a charge diameter of 30mm

Simulation results of 4mm single plates of Domex 550MC tested at a charge diameter of 50mm

The single plates of diameter of 300mm and thickness 4mm subjected to localized blast load of charge diameter of 50mm did not fail up to an impulse of 125Ns. The plates were plastically deformed up to an impulse of 60Ns as shown in Figure E-9 and Figure E-10. Thinning over a charge diameter at an impulse of 75Ns, 100Ns and 125Ns are shown in Figure E-11, Figure E-12 and Figure E-13 respectively.

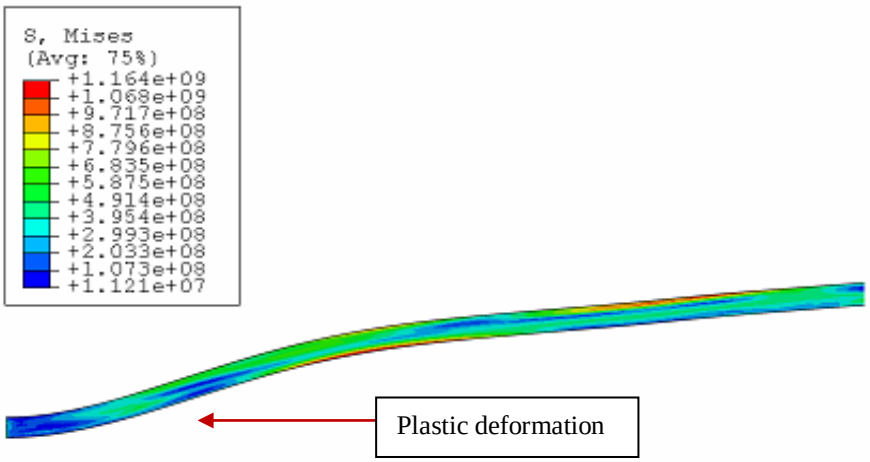

Figure E-9: FE predictions of 4mm thick plate of Domex 550MC subjected to an impulse of 45 Ns and a charge diameter of 50mm

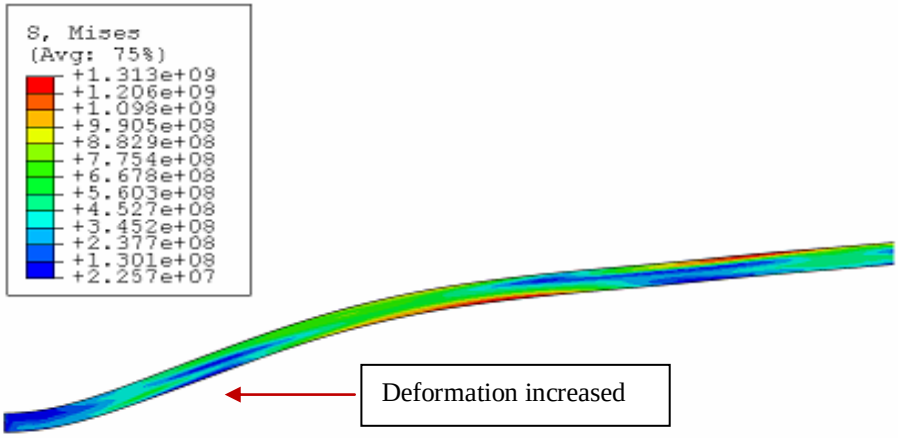

Figure E-10: FE predictions of 4mm thick plate of Domex 550MC subjected to an impulse of 60 Ns and a charge diameter of 50mm

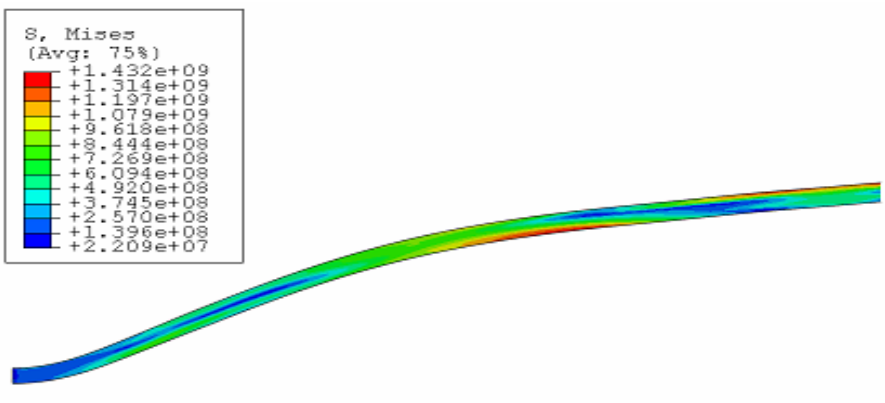

Figure E-11: FE predictions of 4mm thick plate of Domex 550MC subjected to an impulse of 75 Ns and a charge diameter of 50mm

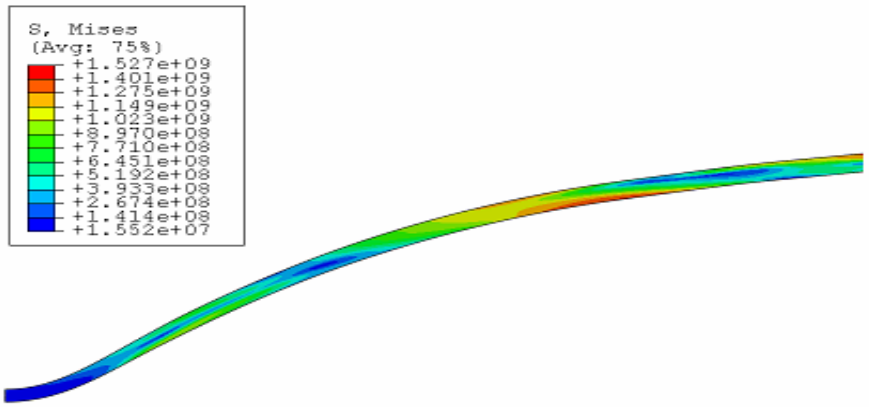

Figure E-12: FE predictions of 4mm thick plate of Domex 550MC subjected to an impulse of 100 Ns and a charge diameter of 50mm

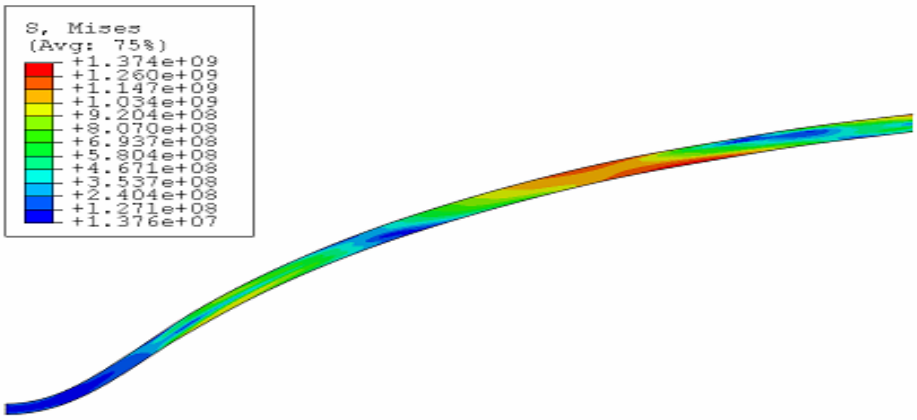

Figure E-13: FE predictions of 4mm thick plate of Domex 550MC subjected to an impulse of 125 Ns and a charge diameter of 50mm

Simulation results of 6mm thick single plates of Domex 550MC subjected to a charge diameter of 30mm

The single plates of 300mm diameter and 6mm thickness subjected to charge diameter of 30mm deformed plastically up to an impulse of 60Ns as shown in Figure E-14. On increasing impulse, thickness of the plate decreased over a charge diameter at an impulse of 75Ns and 100Ns as indicated in Figure E-15 and Figure E-16 respectively. The necking on a charge diameter appeared at an impulse of 125Ns as indicated in Figure E-17.

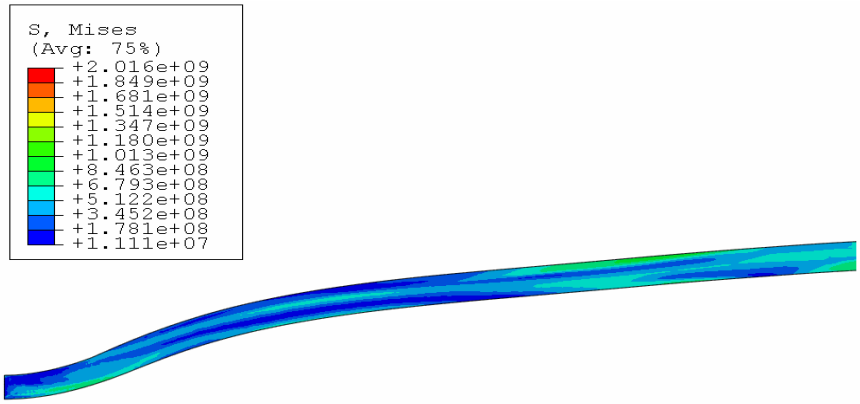

Figure E-14: FE predictions of 6mm thick plate of Domex 550MC subjected to an impulse of 60 Ns and a charge diameter of 30mm

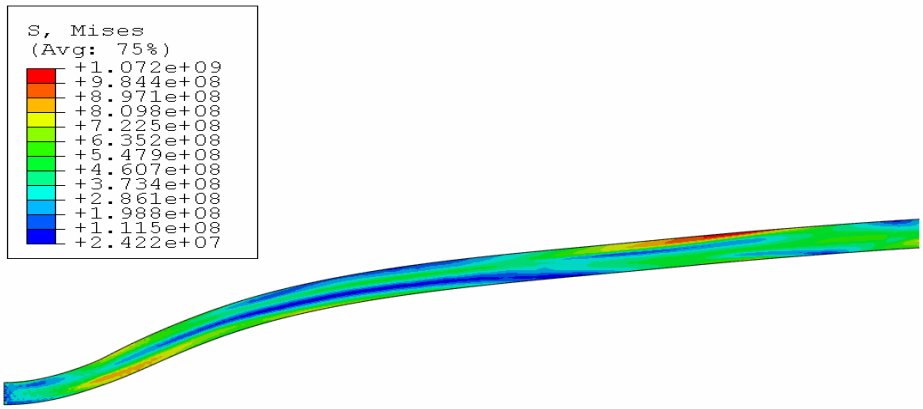

Figure E-15: FE predictions of 6mm thick plate of Domex 550MC subjected to an impulse of 75 Ns and a charge diameter of 30mm

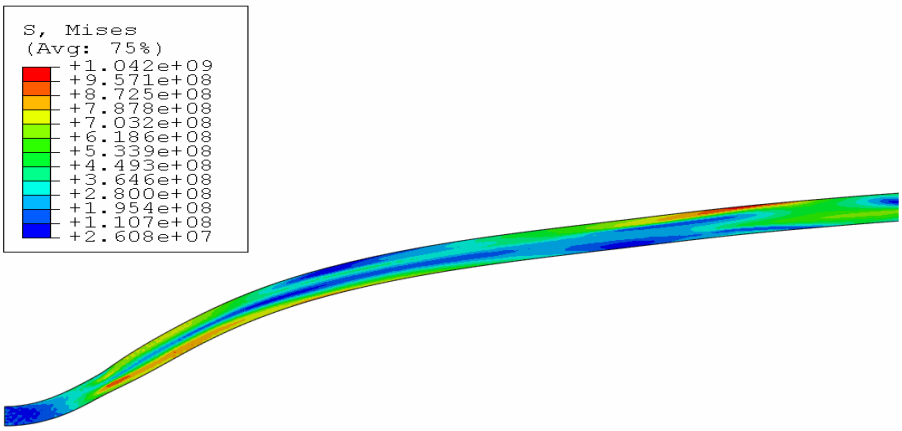

Figure E-16: FE predictions of 6mm thick plate of Domex 550MC subjected to an impulse of 100 Ns and a charge diameter of 30mm

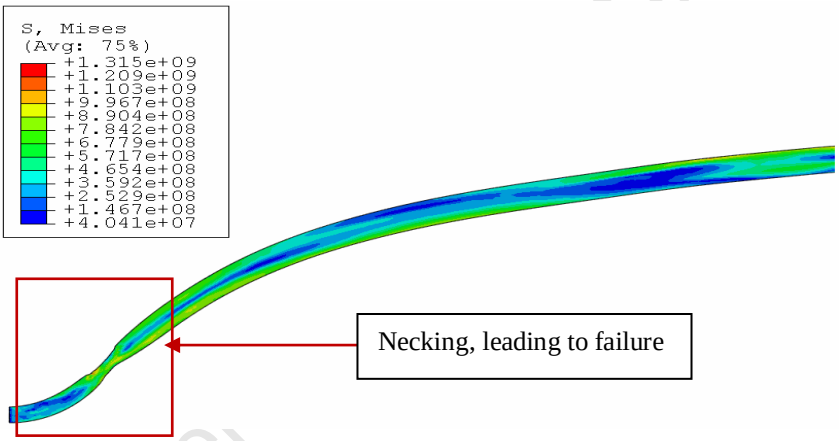

Figure E-17: FE predictions of 6mm thick plate of Domex 550MC subjected to an impulse of 125 Ns and a charge diameter of 30mm

Simulation results of 6mm thick single plates of Domex 550MC subjected to a charge diameter of 50mm

Single plates of 300mm diameter and 6mm thickness subjected to charge diameter of 50mm were deformed plastically up to an impulse of 75Ns as shown in Figure E-18 and Figure E-19. Minor thinning in thickness was observed at an impulse of 100Ns and at 125Ns as indicated in Figure E-20 and Figure E-21. These plates were not capped up to an impulse of 125Ns.

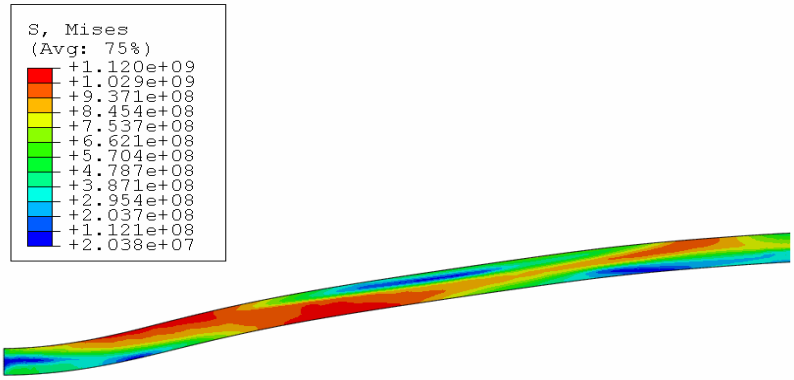

Figure E-18: FE predictions of 6mm thick plate of Domex 550MC subjected to an impulse of 60 Ns and a charge diameter of 50mm

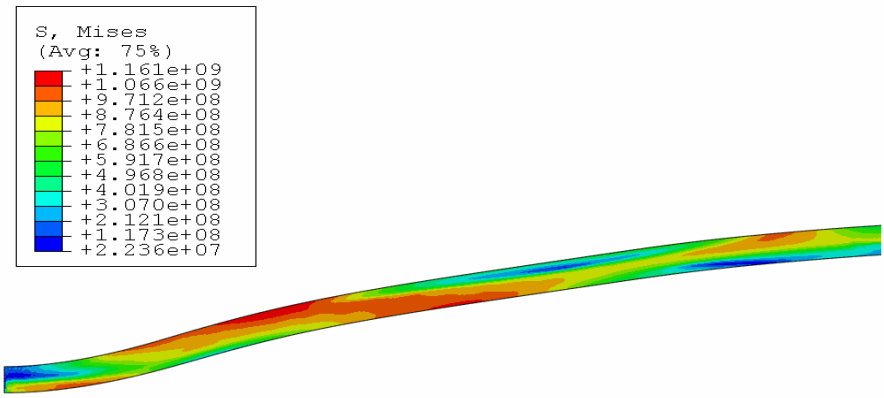

Figure E-19: FE predictions of 6mm thick plate of Domex 550MC subjected to an impulse of 75 Ns and a charge diameter of 50mm

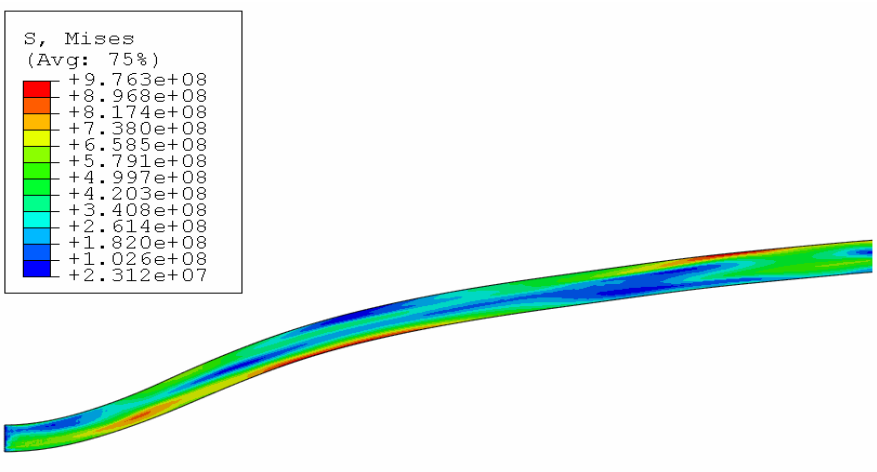

Figure E-20: FE predictions of 6mm thick plate of Domex 550MC subjected to an impulse of 100 Ns and a charge diameter of 50mm

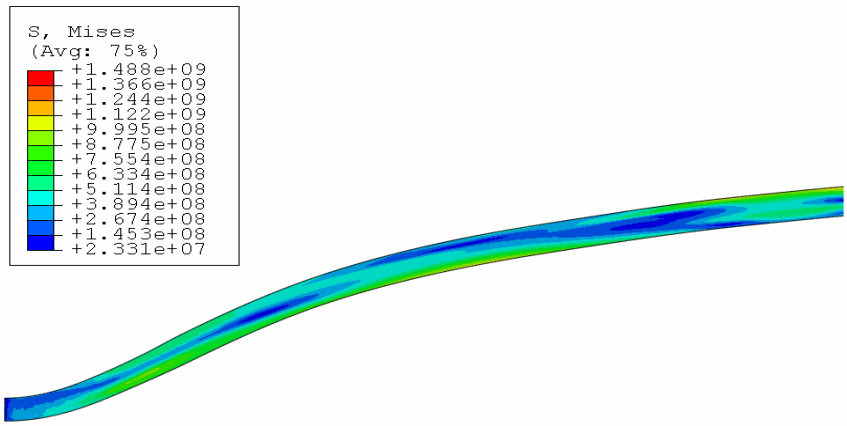

Figure E-21: FE predictions of 6mm thick plate of Domex 550MC subjected to an impulse of 125 Ns and a charge diameter of 50mm

Simulation results of 8mm thick single plates of Domex 700MC subjected to a charge diameter of 40mm, using J-C parameters

Domex 700MC single plates of 8mm thickness subjected to charge diameter of 40mm were deformed plastically up to an impulse of 85Ns. Decrease in thickness of the plate was initiated when subjected to an impulse of 100Ns as shown in Figure E-22. Further decrease in thickness was noted in the plates tested at an impulse of 110Ns and 120Ns as shown in Figure E-23 and Figure E-24 respectively. Necking in the plate tested at an impulse of 130Ns is shown in Figure E-25. The plate was almost failed at an impulse 130Ns.

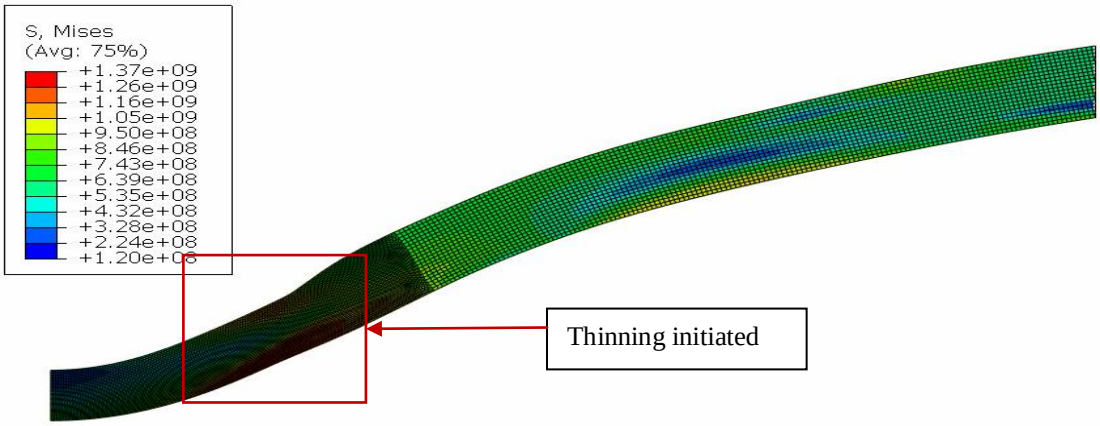

Figure E-22: FE predictions of 8mm thick plate of Domex 700MC subjected to an impulse of 100 Ns and a charge diameter of 20mm

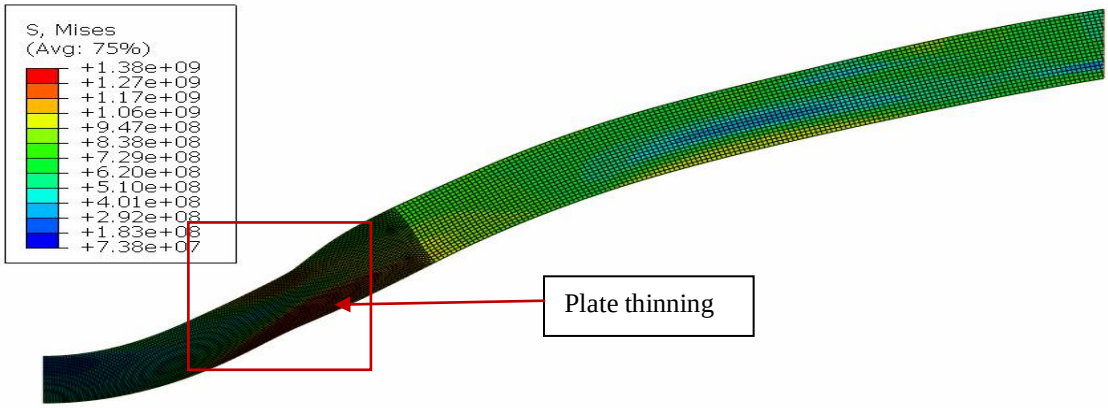

Figure E-23: FE predictions of 8mm thick plate of Domex 700MC subjected to an impulse of 110 Ns and a charge diameter of 20mm

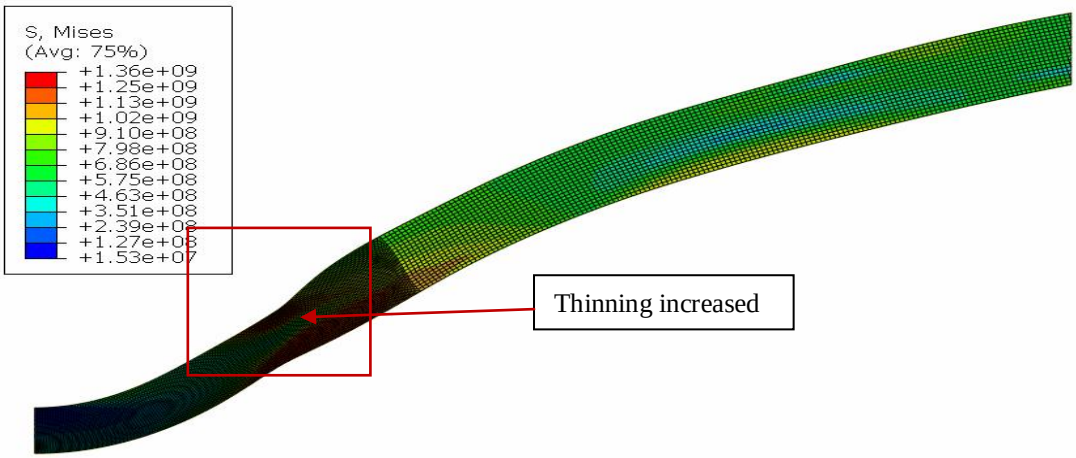

Figure E-24: FE predictions of 8mm thick plate of Domex 700MC subjected to an impulse of 120 Ns and a charge diameter of 20mm

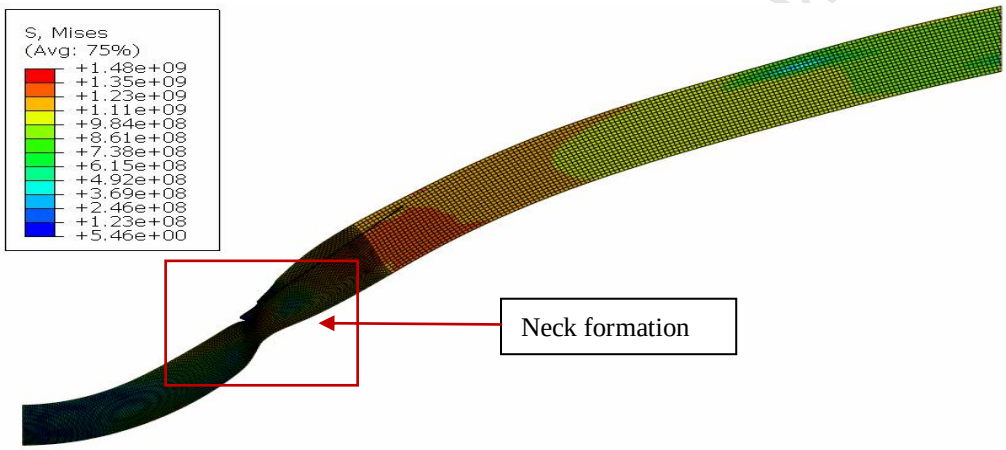

Figure E-25: FE predictions of 8mm thick plate of Domex 700MC subjected to an impulse of 130 Ns and a charge diameter of 20mm

Simulation results of 4mm, 6mm and 8mm thick single plates of Domex 700MC, using Cowper-Symonds relationship

The single plates of 4mm thickness were analyzed up to impulse of 85Ns and these plates did not fail. The increase in midpoint deflections with the increase in impulse is shown in Figure E-26. The change in deformation profile of the plates simulated at various impulses is shown in Figure E-27.

The 6mm thick single plates were analyzed up to an impulse of 140Ns. The deformation profiles of 6mm single plates at various impulses are given in Figure E-28. Minor thinning was observed at an impulse of 130Ns and 140Ns as indicated in Figure E-29 and Figure E-30 respectively. The increase in midpoint deflections is shown in graph of displacement versus impulse in Figure E-31. These plates did not show capping failure in the numerical simulation up to an impulse of 140 Ns.

Domex 700MC single plates of 8 mm thickness were also analyzed up to an impulse of 140Ns. The changes in the deformation profiles at various impulses are shown in Figure E-32. The increase in midpoint deflection with impulse is shown in Figure E-33. This configuration did not fail up to 140Ns impulse.

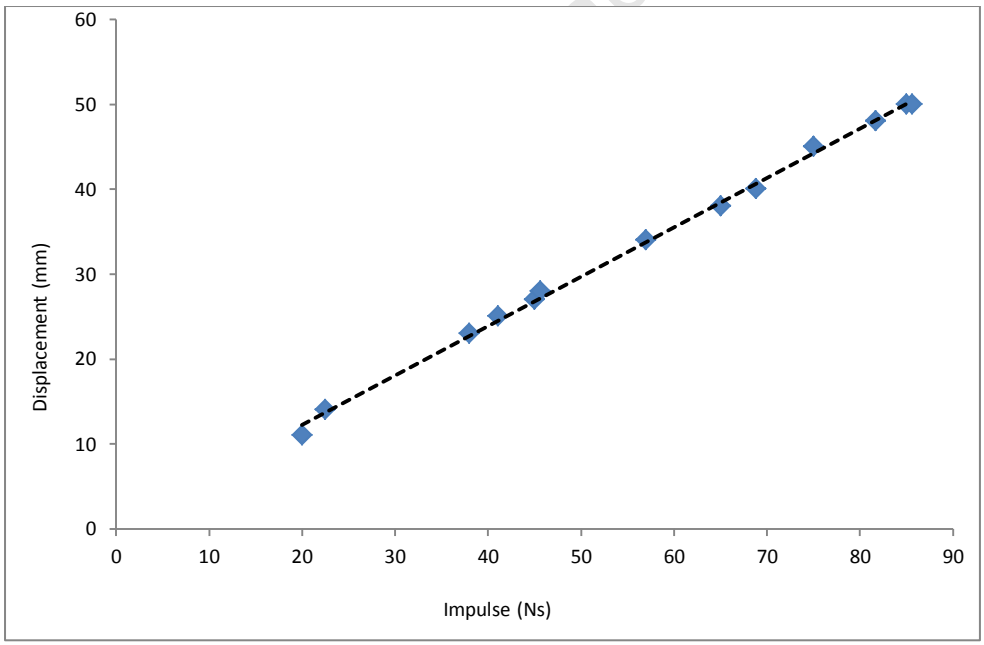

Figure E-26: Graph to show the theoretical deformation versus impulse of blast loaded 4mm thick single plates

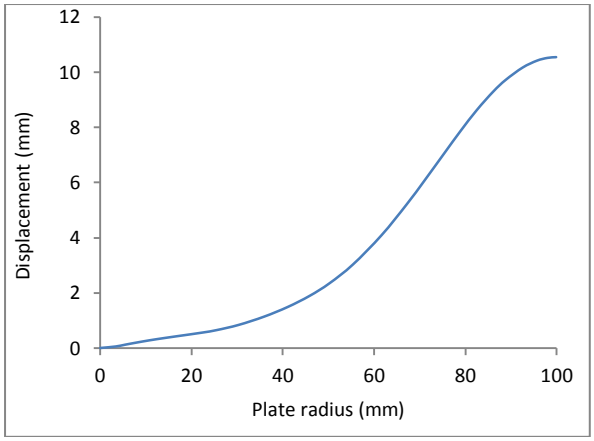

(a) I= 20Ns

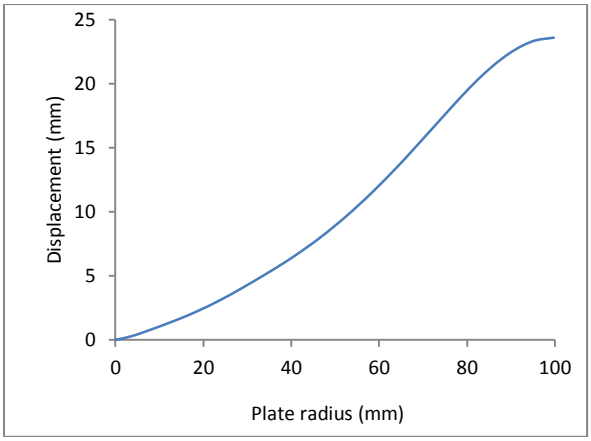

(c)) I=38Ns

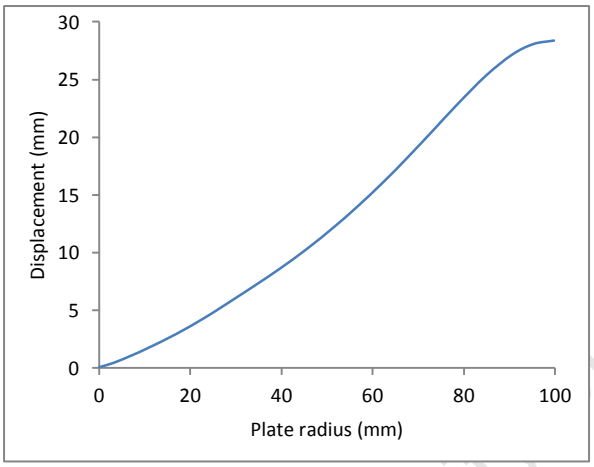

(e) I=45 Ns

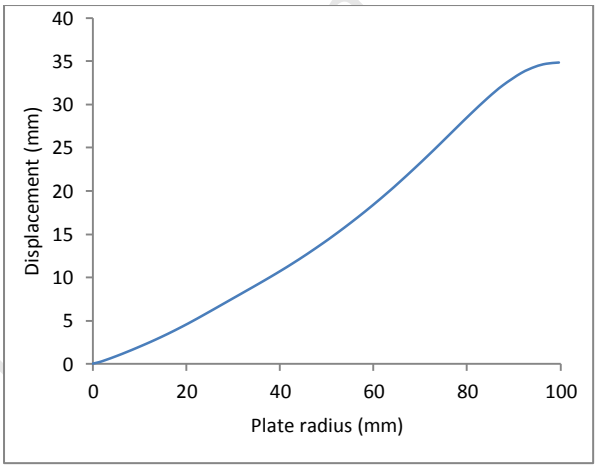

(g) I=57 Ns

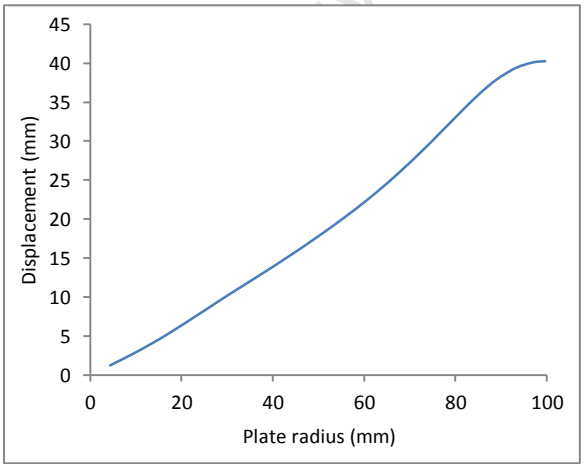

(h) I=65Ns

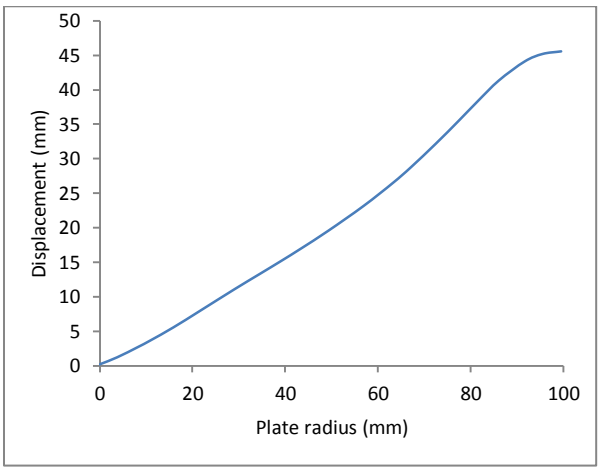

(j) I=75 Ns

Figure E-27: Graph to show the theoretical deformation profiles of blast loaded 4mm thick single plates at different impulses

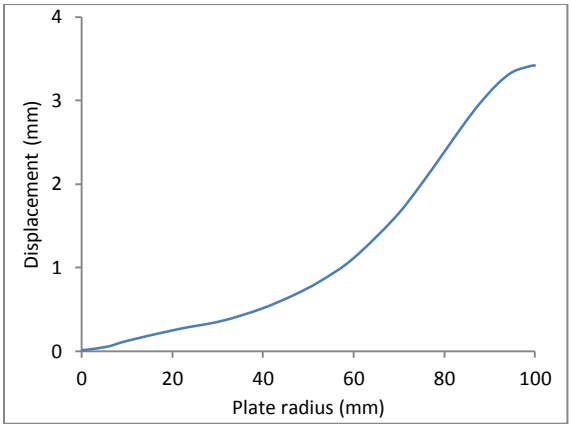

(a) I= 20Ns

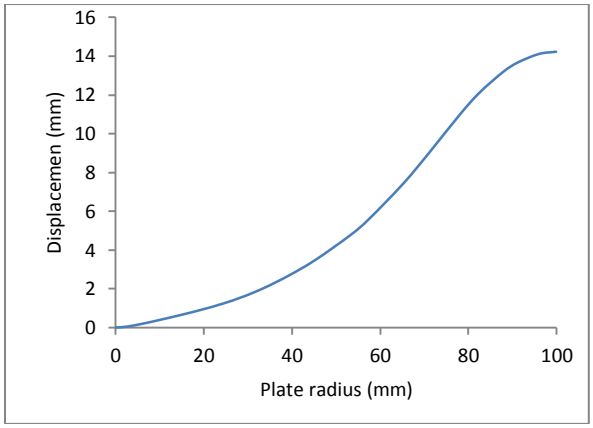

(b) I= 38Ns

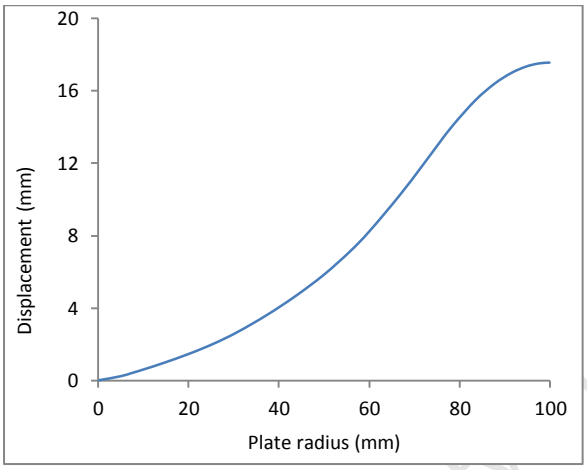

(c) I=45Ns

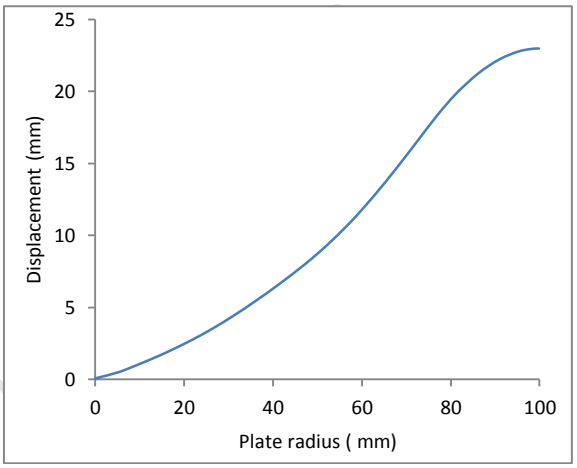

(d) I= 57Ns

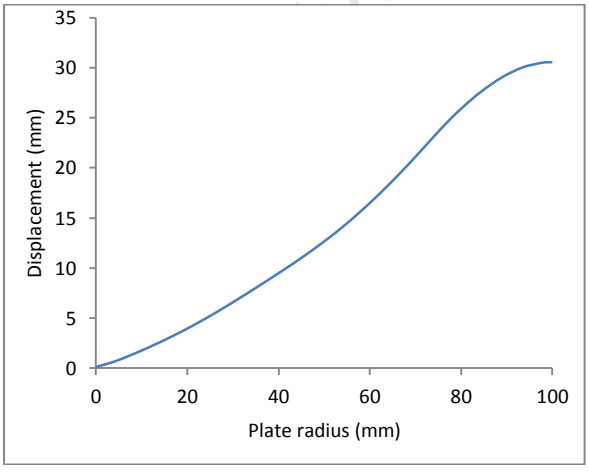

(e) I= 75Ns

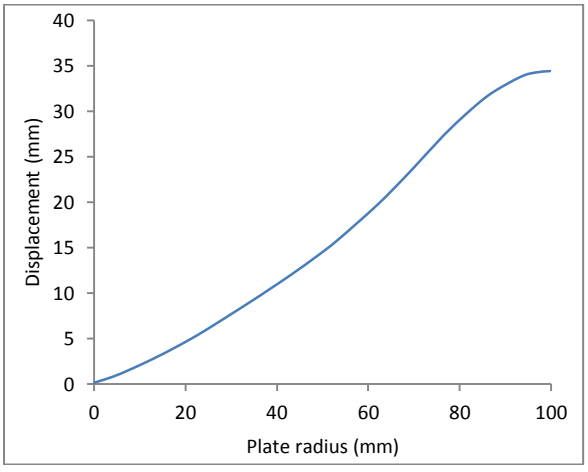

(f) I= 85Ns

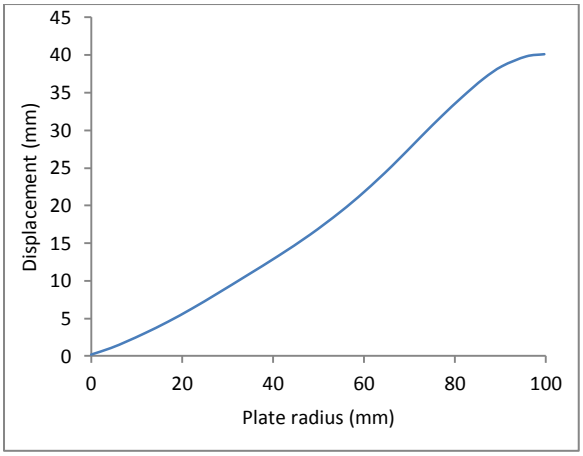

(g) I= 100Ns

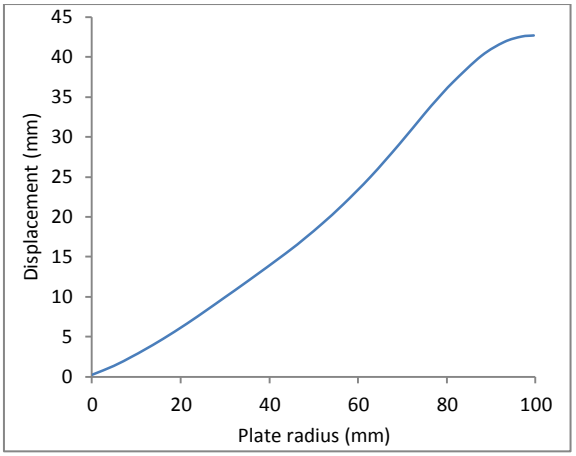

(h) I= 110Ns

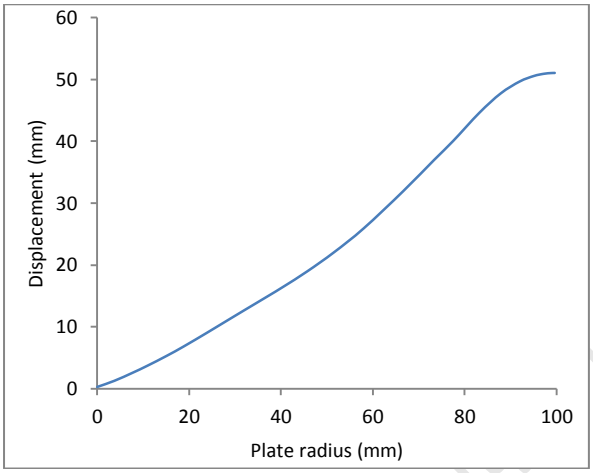

(i) I= 130Ns

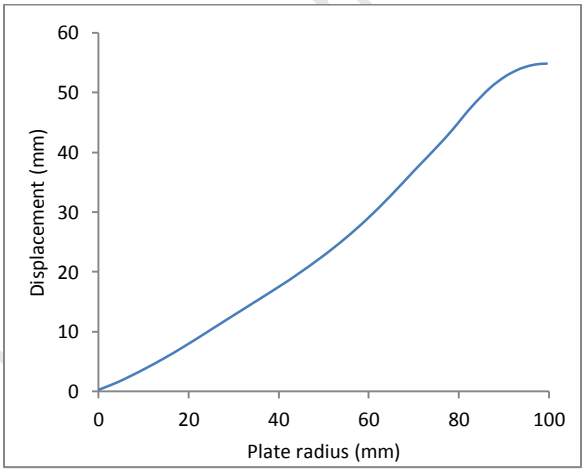

(j) I=140Ns

Figure E-28: Graph to show the theoretical deformation profiles of 6mm thick single plates at various impulses

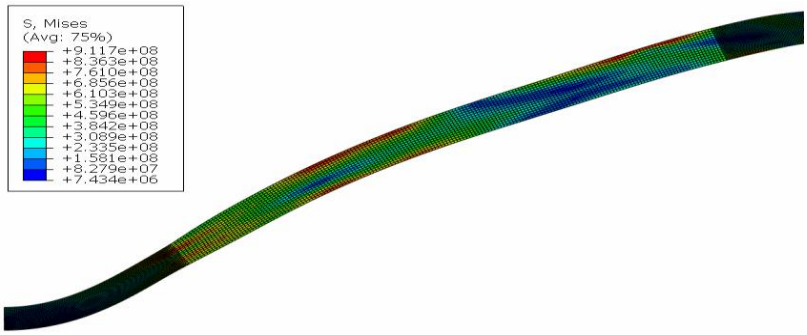

Figure E-29: FE predictions of 6mm thick plate of Domex 700MC subjected to an impulse of 130 Ns and a charge diameter of 20mm

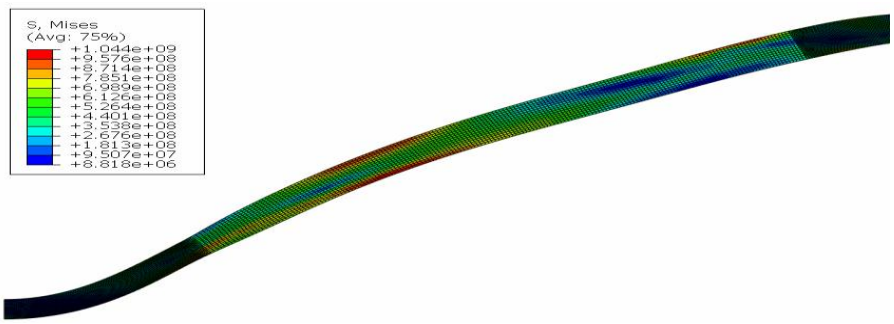

Figure E-30: FE predictions of 6mm thick plate of Domex 700MC subjected to an impulse of 140 Ns and a charge diameter of 20mm

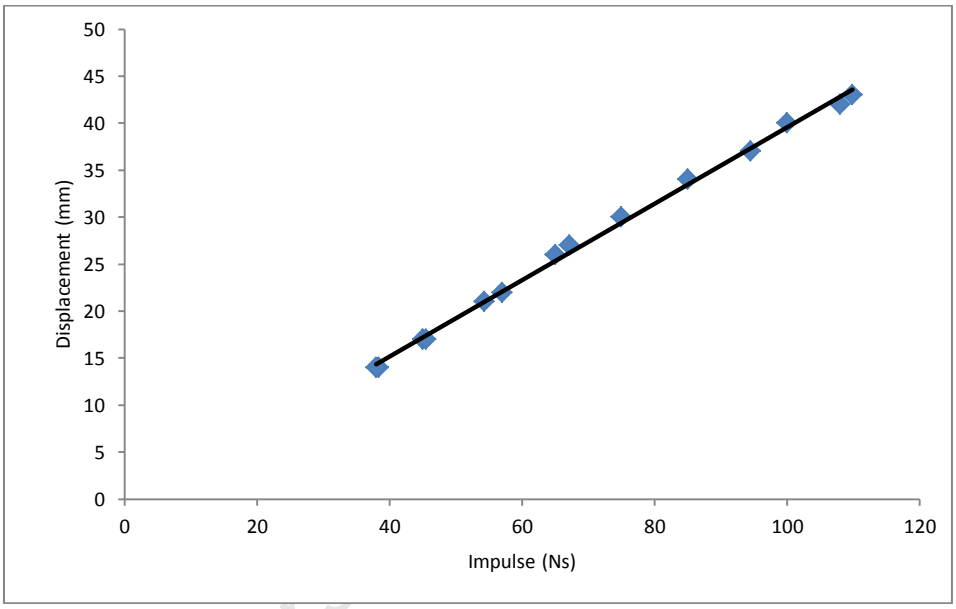

Figure E-31: Graph to show the theoretical deformation versus impulse 6mm thick single plates

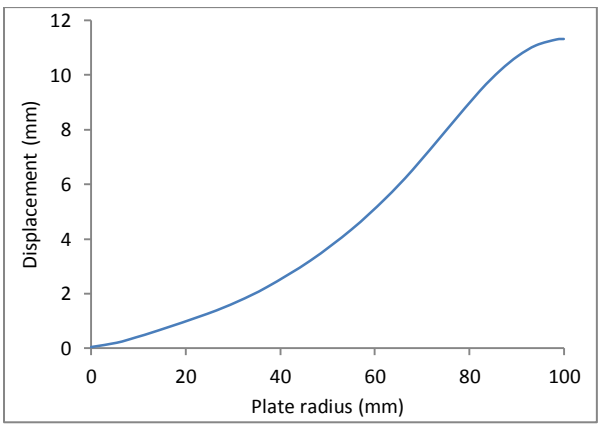

(a) I= 45Ns

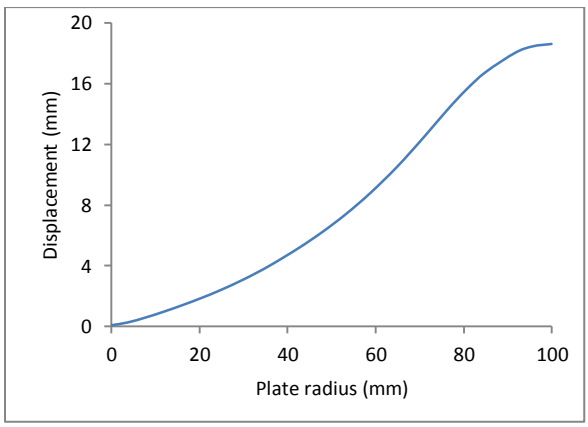

(b) I= 65Ns

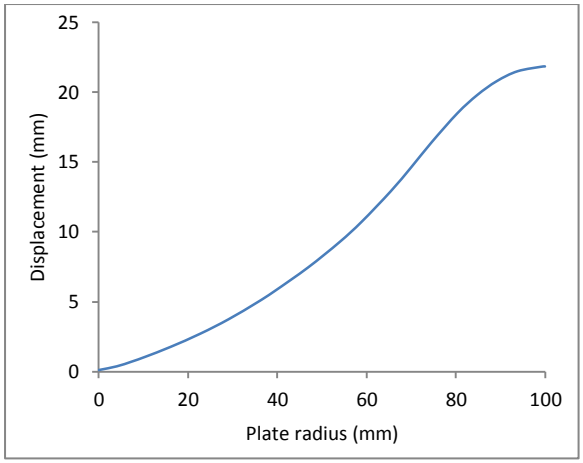

(c) I=75Ns

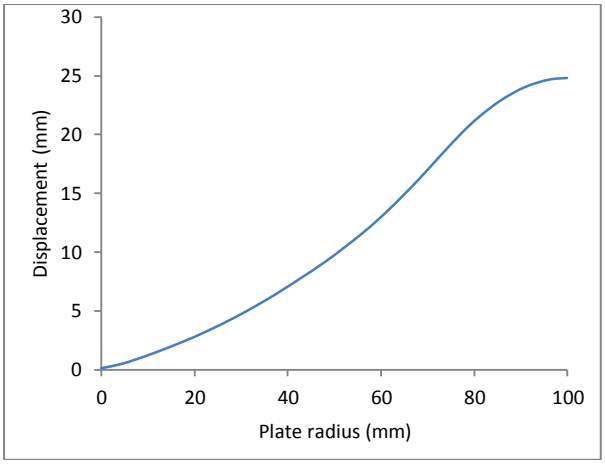

(d) I=85Ns

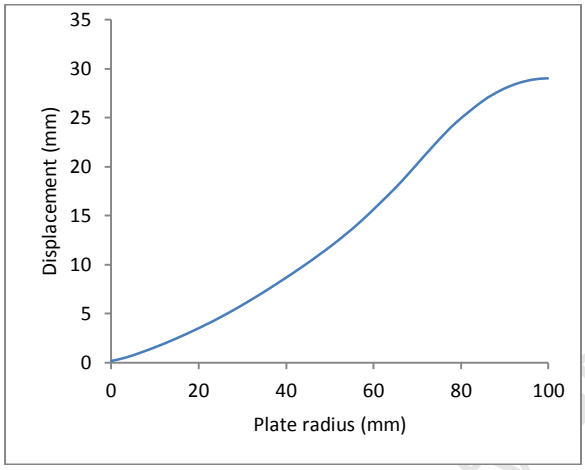

(e) I=100Ns

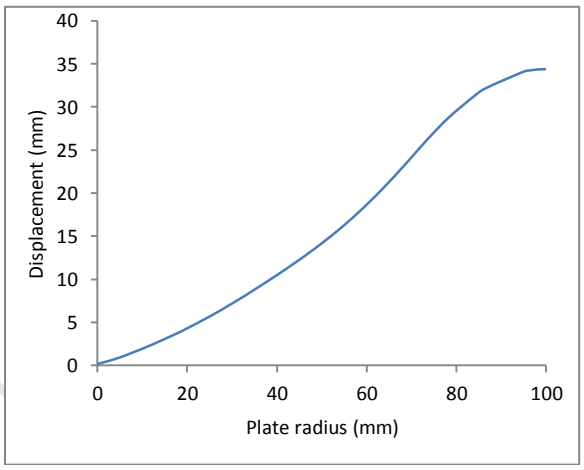

(f) I=120Ns

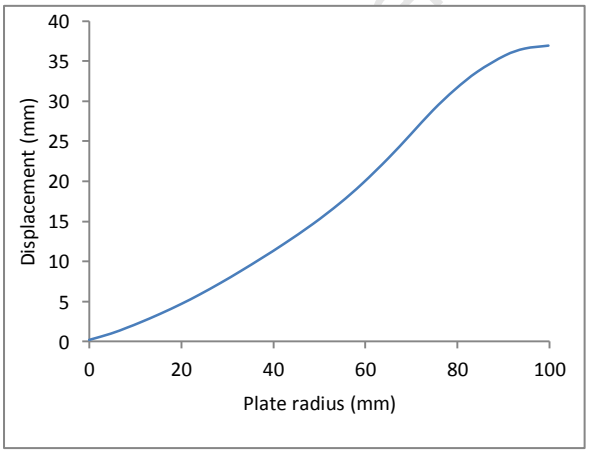

(g) I= 130 Ns

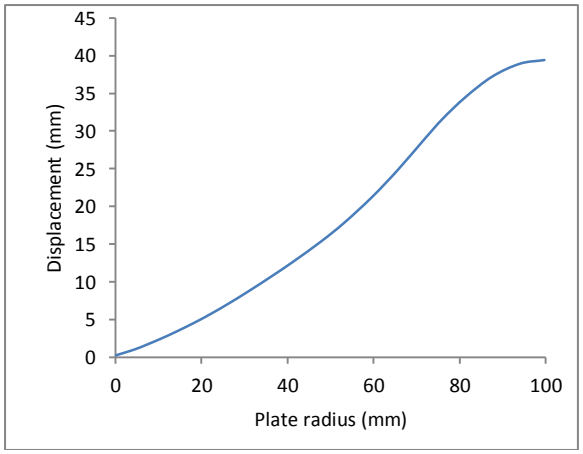

(h) I= 140Ns

Figure E-32: Graph to show the theoretical deformation profiles of 8mm thick single plates at various impulses

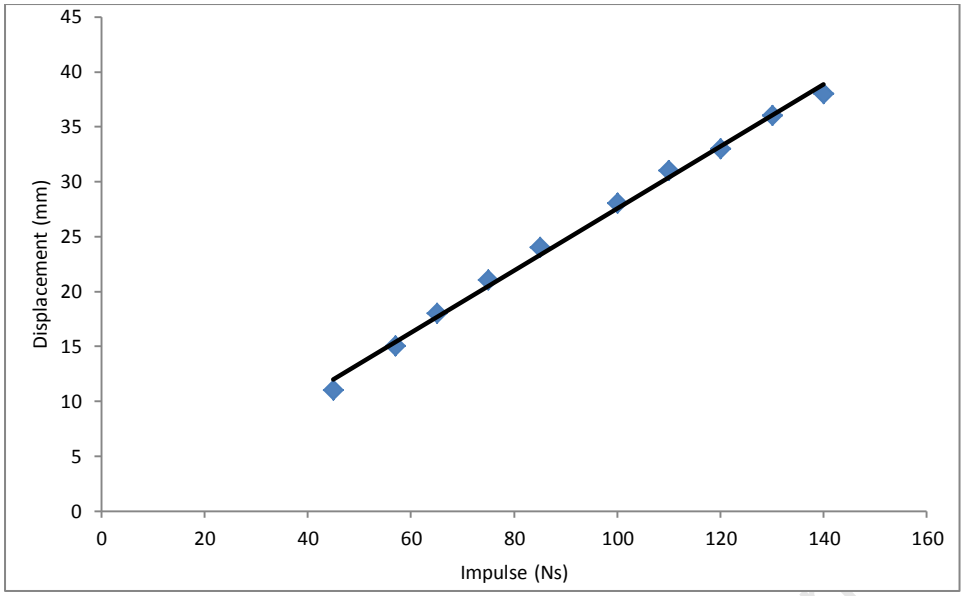

Figure E-33: Graph to show the theoretical deformations versus impulse of 8mm thick single plates

Table E-2: Effect of impulse on strain over a charge diameter (at 50micrseconds)

Impulse (Ns)	**Strain**
20	0.03
38	0.065
45	0.08
57	0.11
75	0.17